Dissertation Thesis

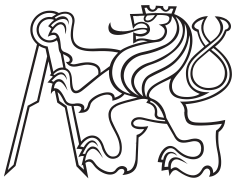

Czech Technical University in Prague

Faculty of Nuclear Sciences and Physical Engineering
Department of Physics

Ultra-Peripheral Collisions at ALICE

Looking inside lead ions

Roman Lavička

Supervisor: prof. Jesús Guillermo Contreras Nuño, Ph.D.
Supervisor–specialist: Mgr. Michal Broz, Ph.D.
Field of study: Nuclear Engineering
May 2021

Albertovi.

Acknowledgements

I would like to express my gratitude to my supervisor prof. Jesús Guillermo Contreras Nuño, Ph.D. for his invaluable advice and support during the realization of this work. You were right, it is possible to measure it!

I would also like to thank Mgr. Michal Broz, Ph.D for his preparation of the Monte Carlo simulations and his quick helps with programming difficulties.

I am infinitely happy that I could grow under their supervision. Thank you for everything.

I would also like to thank prof. Martino Gagliardi for his offer to work with him on the topics of ALICE trigger coordination. Thanks to the collaboration with him, I was able to learn much about physics event triggering and luminosity calculation and understand how to become a complete scientist.

I would also like to thank my family for their inexhaustible moral, financial and loving support without which I would have never been able to succeed.

Declaration

Prohlašuji, že jsem tuto práci vypracoval samostatně a použil jsem pouze podklady (literaturu, projekty, SW atd...) uvedené v přiloženém seznamu.

Nemám závažný důvod proti použití tohoto školního díla ve smyslu § 60 Zákona č. 121/200 Sb., o právu autorském, o právech souvisejících s právem autorským a o změně některých zákonů (autorský zákon).

V Praze, 25. 5. 2021

Abstract

There are several different predictions for the behaviour of the gluon distribution in nuclei at small Bjorken-x and experimental data are needed to chose among them. This is achieved by measuring the cross section of processes specially sensitive to this parton distribution. This work focuses on ultra-peripheral collisions of lead-lead nuclei producing a J/ψ meson. The main task is to calculate the rapidity and $|t|$ dependence of the cross section, where the $|t|$ is the square of the momentum transferred between the incoming and outgoing target nucleus. ALICE data from the Run 2 period, specifically from the year 2018, are used in this thesis. The results proof the existence of nuclear shadowing effects, and put new constraints on available theoretical models in the form of a more precise measurement and in this context the newly measured dependence of the cross section on $|t|$.

Keywords: Ultra-peripheral collisions, momentum transfer, unfolding, luminosity

Supervisor: prof. Jesús Guillermo Contreras Nuño, Ph.D.

Supervisor–specialist: Mgr. Michal Broz, Ph.D.

Abstrakt

Pro popis chování rozložení gluonů v jádře při malých Bjorkenovo-x existuje několik různých předpovědí. Abychom mezi nimi mohli vybrat tu správnou, potřebujeme experimentální data. Na nich se naměří účinný průřez procesů, které jsou zvlášť citlivé na tuto partonovou distribuci. Tato práce se zaměřuje na ultraperiferální srážky jader olova, které produkují J/ψ mezon. Hlavním úkolem je spočítat závislost účinného průřezu na rapiditě a $|t|$, odmocnině z hybnosti přenesené mezi vstupním a výstupním stavem měřeného jádra. Data z experimentu ALICE z období Run 2, konkrétně z roku 2018, jsou použita v této práci. Výsledky dokazují existenci efektu známého jako "nuclear shadowing" a také umožňují vylepšit dosavadní teoretické modely pomocí tohoto nového přesnějšího měření a v tomto kontextu prvně změřené závislosti účinného průřezu na $|t|$.

Klíčová slova: Ultraperiferní srážky, přenesená hybnost, unfolding, luminozita

Překlad názvu: Ultraperiferní srážky na experimentu ALICE

Contents

Preface

One of the main goals of physics is to give an answer to the question *what are we made of?* As technology improves we are able to study smaller and smaller pieces of our world, revealing that matter is made of atoms, atoms are made of their nuclei and electrons and so on. Nowadays modern detectors give us an opportunity to measure the distribution of quarks and gluons inside hadrons and nuclei. The goal of these doctoral studies is to use data from ALICE to measure a process which is expected to be specially sensitive to the gluon distribution in lead nuclei.

The HERA accelerator legacy [1] has taught us that hadrons are mainly composed of gluons when we look deeply inside them. LHC provides highly energetic beams of protons and lead ions [2] which allow us to study their gluonic structure, giving rise to the question *can the nucleon structure be scaled to describe nuclear structure?* The phenomenon called nuclear shadowing [3] groups effects, like gluon saturation, which modify the relation between nucleon and the nucleus. A good description of shadowing is the goal of many models attempting to understand the nuclear structure.

The results from the data taking session called Run 1 (2010-2013) at $\sqrt{s_{\mathrm{NN}}} = 2.76$ TeV [4–6] have already demonstrated the possibility to use ultra-peripheral collisions (UPCs) of Pb–Pb beams at the LHC to study the structure of lead nuclei. The next data taking session called Run 2 (2015-2018) brought the beams to higher energies: the lead ions collided at $\sqrt{s_{\mathrm{NN}}} = 5.02$ TeV. Together with the detector and event-triggering software upgrade it was possible to record ten times more data, which allowed us to perform more precise measurements.

This thesis is mainly focused on a unique measurement of the $|t|$ dependency of the photonuclear cross section for the production of a J/ψ meson. The muon decay channel of the J/ψ was found to be the best opportunity for a precise measurement. First, the UPC, meaning the interaction Pb+Pb→Pb+Pb+J/ψ, cross sections in different p_{T}^2 intervals[1] are measured. Then, an unfolding technique is used (i) to take into account the resolution of the ALICE apparatus and (ii) to find a relation between the p_{T}^2 and $|t|$

[1] p_{T} represents the transverse momentum of the J/ψ.

cross sections. In the end, the photonuclear, meaning γ+Pb$\rightarrow$ J/ψ+Pb, cross section is calculated, which is an intrinsic input to physics theories: the $|t|$ dependence is related by a 2D Fourier transform to the distribution of gluons, in the impact-parameter plane, of the nucleus.

An overview of the physics relevant for this thesis measurement is given in Chapter 1 where the ultra-peripheral collisions, the J/ψ particle, the kinematic variables used and the current theoretical models are briefly presented. In the next chapter, which is focused on the ALICE apparatus, the several subdetectors and triggers used in this work are described. Chapter 3 is dedicated to the luminosity calculation. In Chapter 4 methods of data unfolding are introduced, and in Chapter 5 the cross section calculation is described. All the results are presented and discussed in Chapter 6. The next chapter contains a summary and an outlook for this topic. A summary of the author's research activities is presented in the last chapter.

Chapter 1

Introduction

1.1 The structure of matter

The world around us is made of various fundamental particles, which can be combined together to create the atoms we are familiar with. These fundamental particles are divided according to their spin into so-called bosons (integer spin) and fermions (half-integer spin). An important difference between them is that bosons are allowed to occupy the same quantum state, which is not the case for two identical fermions [7].

The current knowledge about matter is described in the Standard Model. There, the photon which propagates the electromagnetic field; Z and $W^{\pm}$ responsible for the weak interaction; and the gluon connected with the strong force are identified as the elementary gauge bosons. According to this theory, one more boson is necessary to give mass to the Z and $W^{\pm}$ bosons. The famous Higgs boson recently discovered at the LHC [8, 9]. The elementary fermions are divided into leptons (electrons, muons, taus and their corresponding neutrinos and antiparticles) and quarks, which exhibit six flavours in Nature [10].

Within the Standard Model, the theory which describes the strong interaction is called quantum chromodynamics (QCD) [11]. This theory is a non-abelian gauge theory based on the symmetry group SU(3) [12, 13]. As the electromagnetic force has the familiar electric charge, a colour charge is found in QCD, which has three types, normally called red, blue and green. Each of them can take "positive" and "negative" values; the "negative" values are called anti-red, anti-blue and anti-green. The gluons are particles, which carry a pair of colour and anti-colour. The symmetry of the SU(3) group yields eight possible configurations of gluons.

Unfortunately, QCD produces equations that are not solved in the general case, yet. In particular, the equations for the dynamics of the interaction of quarks and gluons, nor how they interact to form bound states are not solved. Luckily, a tool called perturbative QCD (pQCD) can set up equations which tell how the structure of hadrons change when the energy of the interaction

used to probe the structure is changed. These equations are only valid in the regime where it can be considered that the quarks and gluons are free during the interaction. Hence the interest in the study of the structure of bound states. The process investigated in this thesis is specially sensitive to the gluonic structure of hadrons.

1.2 Small-x physics

Parton distribution functions (PDF) describe the distribution of the longitudinal component (in a light-cone frame) of the momentum of quarks and gluons (partons) in matter at a given energy scale given by the interaction. Before turning on the LHC facility in 2009 the proton PDFs were well known in a large kinematic domain for the so-called Bjorken-x and scale Q^2 as they were measured with high precision at HERA in Hamburg [14]. There it was found that the gluon distribution in the proton grows very fast for decreasing x at small values of x. QCD predicts that this growth would eventually result in many gluons which start overlapping and interacting among themselves. The moment of equilibrium between gluon creation and annihilation is called saturation. With the LHC an opportunity to study the gluon distribution of lead nuclei at small values of x for perturbative scales Q^2 appeared. As there are many more gluons in the nucleus than in the proton one could be more sensitive to saturation effects if they are already present at LHC energies.

1.2.1 Bjorken x

In the infinite-momentum frame the Bjorken-x is related to the fraction of momentum carried by a gluon or a quark in the nucleon (nucleus) to the total momentum of the nucleon (nucleus). A powerful tool for studying PDFs at small-x is deep inelastic scattering (DIS). Here, in the high-energy limit, x is related to the transferred momentum via the centre-of-mass energy s as $s \sim \frac{Q^2}{x}$. From this equation it is clearly seen that small values of x correspond to large energies. Distribution functions for quarks and gluons in the proton for fixed Q^2 are shown in Fig. 1.1. The strong rise of the gluon distribution at small-x is clearly seen.

1.2.2 The gluon distribution function

The reason to study the coherent production of J/ψ is its connection with the gluon distribution function in Pb, where the scale of the interaction is related to the mass of the J/ψ as $Q^2 \sim \frac{M^2_{J/\psi}}{4}$ [15] and thus it is expected to be in the perturbative regime. This distribution cannot be obtained by rescaling the proton distribution function according to the nucleus nucleon number N and proton number Z. For Bjorken-x below 0.1 the so-called shadowing appears and the ratio of the structure function of the nucleus

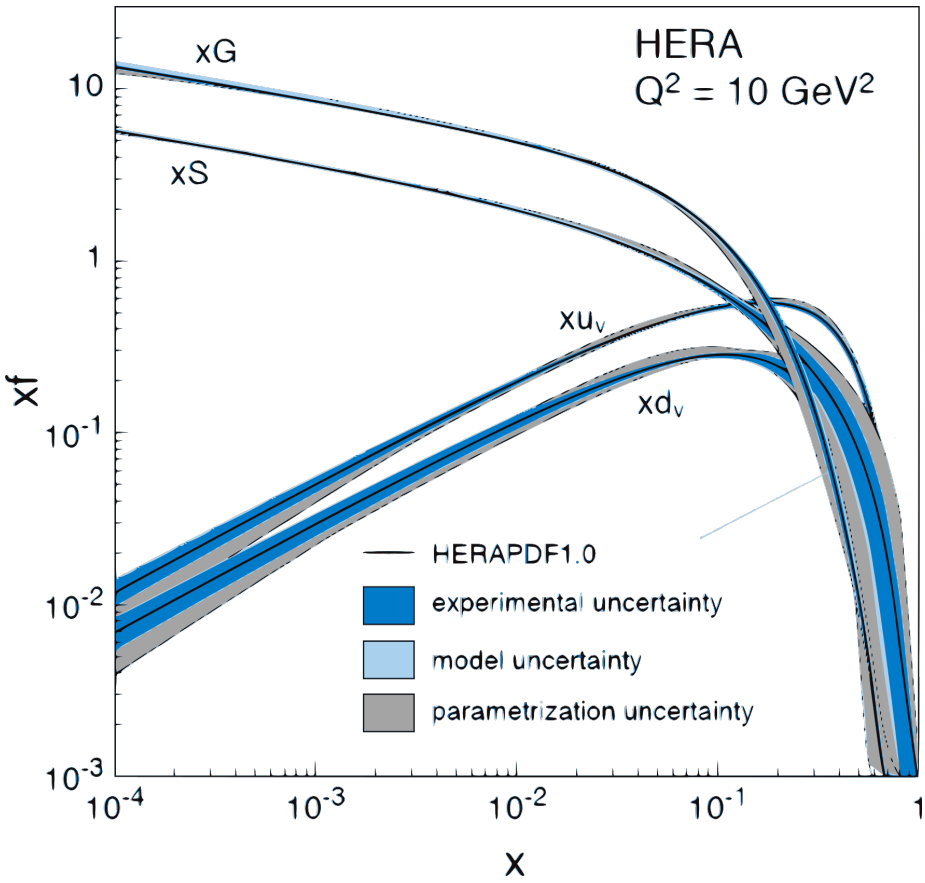

Figure 1.1: Parton distribution functions for different partons in the proton. Taken from Ref. [1] (colours are modified).

to the structure function of the proton decreases. This is an experimental fact and the measurement performed during the author's doctoral studies provided new data at a previously unexplored kinematic region, which helps to understand better this phenomenon.

The LHC provides collisions at higher energies than ever before in the laboratory, which gives us a larger range in x for a fixed value of Q^2. The rapidity of the coherently produced J/ψ is related to the Bjorken-x of the pomeron. At midrapidity the process is sensitive to $x \sim 10^{-3}$ for Run 1 energies and $x \sim 6 \times 10^{-4}$ for Run 2 energies. The collinear PDFs do not carry information about the distribution of gluons in the plane transverse to the interaction, the so called impact-parameter plane. Saturation models predict interesting signatures in this plane [16]. To access this information, it is also needed to measure the $|t|$ dependence of the cross section at a given rapidity. As it will be discussed later, the J/ψ meson is an ideal particle to study this distribution.

Table 1.1: Properties of the J/ψ particle. Taken from Ref. [19].

J/ψ **properties**	
Type	meson
Composition	charm quark and antiquark
Discovered	1974, BNL [17] and SLAC [18]
Mass	(3096.900 $\pm$ 0.006) MeV/c^2
Full width	(92.9 $\pm$ 2.8) keV/c^2
J^{PC}	1^{--}
Charmness	0 (hidden charm)

Table 1.2: The main decay channels of the J/ψ particle. Taken from Ref. [19].

J/ψ **decay channels**	
Mode	Fraction (%)
hadrons	87.7 $\pm$ 0.5
e^+e^-	5.971 $\pm$ 0.032
$\mu^+\mu^-$	5.961 $\pm$ 0.033

1.3 The J/ψ particle

The J/ψ is a vector meson. Its main attributes are listed in Tab. 1.1. States, which are composed of $c\bar{c}$ quarks, are called charmonium and the J/ψ is the lowest vector state. The whole family can be seen in Fig. 1.2. The ground state for this family is $\eta_c(1S)$. The decay channels of the J/ψ, interesting for this thesis, are listed in Tab. 1.2. The decays to hadrons are the most probable. The probabilities of decays to di-leptons are almost the same (with a little bit higher chance for e^+e^-). Unfortunately, decays to hadrons are quite complicated and it is difficult to reconstruct them. This work focus mainly on the $\mu^+\mu^-$ channel, because when muons propagate through detectors, they do not radiate as easily as electrons do and therefore a better resolution in $|t|$ is achieved.

The beauty of this meson is the sharp peak in the invariant-mass distribution, which can be found around 3.1 GeV/c^2. This can be compared with other vector mesons in Fig. 1.3. The mass of the J/ψ gives a scale that makes possible to use perturbative QCD at small-x. Adding the fact of the very narrow peak and the possibility to trigger on the leptonic decay channels in UPCs at the LHC, the J/ψ is an ideal particle for the analysis.

1.4 Mandelstam variables

To study the kinematics of high-energy collisions it is useful to define kinematic variables. Some of them are the so-called Mandelstam variables [22]. These

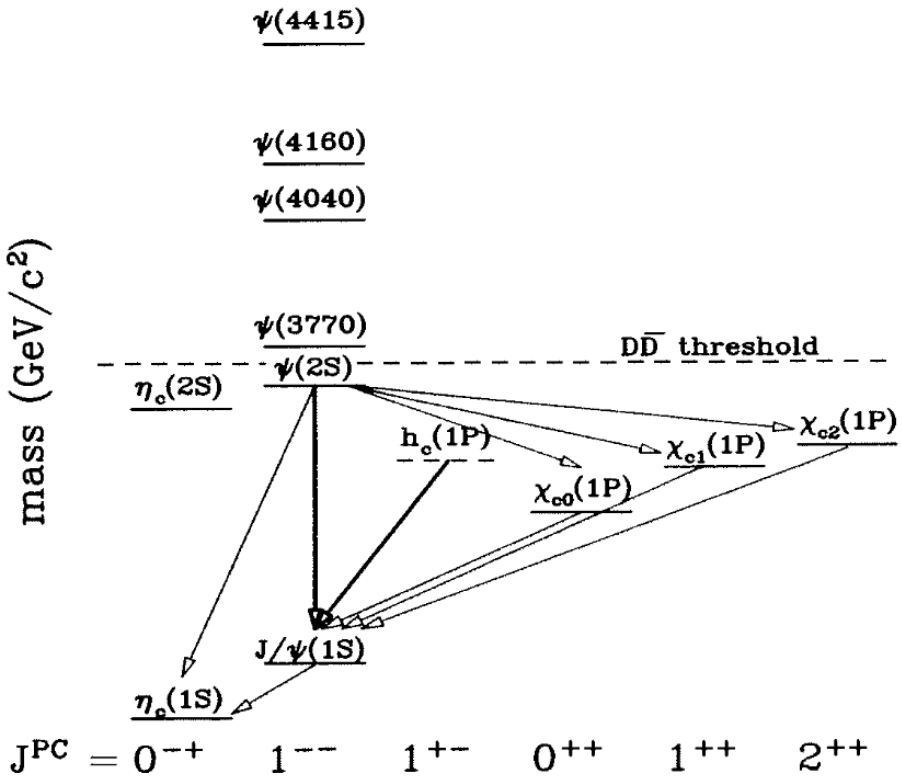

Figure 1.2: The charmonium family. Note, that $\psi(2S)$ is an alternative notation of ψ'. Taken from Ref. [20].

are mostly used in scattering experiments, where there are 2 particles before an interaction and 2 particles after it (γ+Pb$\rightarrow$ J/ψ+Pb in the case of this measurement). For high-energy interactions, the variables, which are labelled as channels (see Fig. 1.4), are defined by Eq. (1.1). Their advantage is that they are Lorentz invariant. Also in the centre-of-mass system they have a clear interpretation. The s-channel represents the square of the total energy of the incoming particles. The t-channel reflects the momentum transfer between incoming and outgoing particles. Fig. 1.5 shows the diagram of the process to be measured and depicts the t variable in this case.

$$\begin{aligned} s &= (p_1 + p_2)^2 = (p_3 + p_4)^2, \\ t &= (p_1 - p_3)^2 = (p_2 - p_4)^2, \\ u &= (p_1 - p_4)^2 = (p_2 - p_3)^2. \end{aligned} \tag{1.1}$$

1.5 Ultra-peripheral collisions

Ultra-peripheral collisions (UPCs) are defined as a collision, where two projectiles with radii R_A and R_B pass by with an impact parameter b larger

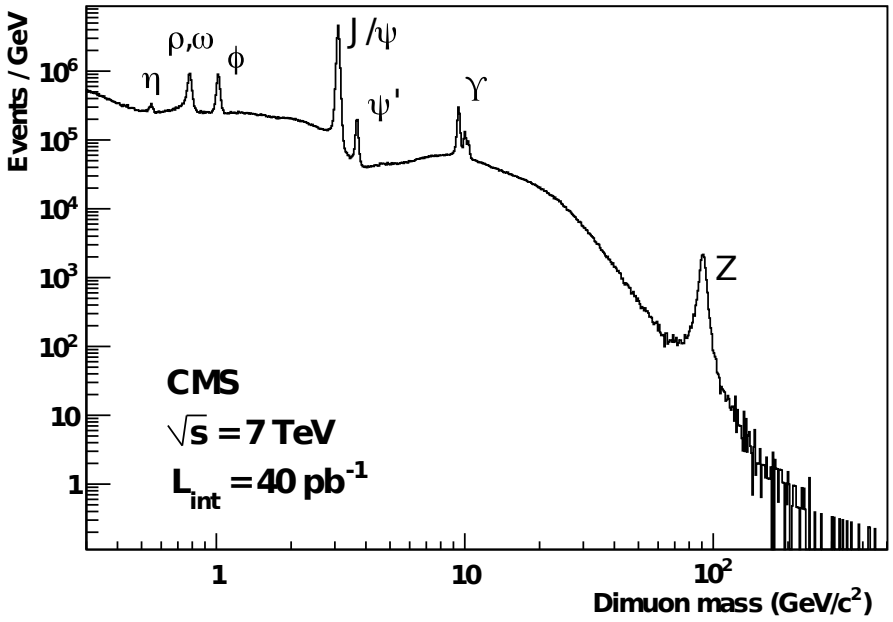

Figure 1.3: Dimuon mass distribution showing mesons popping up in the continuum. Taken from Ref. [21].

than the sum of these radii [15, 23–25]. A sketch of such collision is shown in Fig. 1.6. The LHC uses ions with radius of a few femtometres. Because in the UPCs case the impact parameter minus the sum of the radii is larger than the range of the strong interactions (their range is around or less than a femtometre) and because the weak and the gravitational interactions are very weak in comparison with other forces, UPCs are mediated by electromagnetic interactions. When the projectiles are ultra-relativistic, these collisions can be imagined as an interaction of clouds of quasi-real photons, which surround the projectiles.

Any charged particle can be used as a projectile for UPCs. The number of surrounding photons depends on the atomic number Z, with the intensity of the interaction growing with Z^2. From this condition the advantage of using heavy-ion collisions for UPCs is obvious. Nowadays, the physics of UPCs is studied at the RHIC and LHC facilities using a variety of projectiles.

In general, two types of UPCs can occur at the LHC. One is called photon-photon collision and in this case photons from the mother nuclei interact with each other. As a result new particles appear (e.g. $\mu^+\mu^-$ pairs or $q\overline{q}$ pairs). However, due to the law of conservation of total angular momentum the creation of one vector meson cannot happen. For this we need more photons in the interaction or the second type of collision; photon-nucleus collision. A diagram for such process is shown in Fig. 1.5. Here one nucleus emits the photon. The situation is interpreted in the rest frame of the target nucleus. The photon fluctuates into a virtual $q\overline{q}$ pair. This pair is a colour dipole, which interacts strongly with the second nucleus to produce a vector meson.

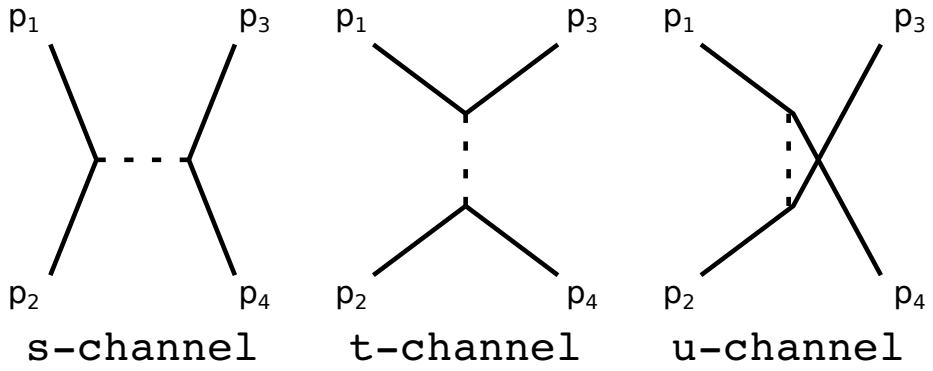

Figure 1.4: The s- t- and u- channels of scattering processes.

This work is interested in the case of the vector meson being a J/ψ particle. The second nucleus contributes to the momentum for the created J/ψ particle. This contribution comes from the transferred momentum $|t|$ between the initial and final nucleus acting as target. The main goal of this thesis is to evaluate the measurement of the cross section of J/ψ photoproduction as a function of $|t|$ at midrapidity using the ALICE detector. The integration over $|t|$ of this cross section yields the cross section at midrapidity. In practice, $|t|$ is not measured directly, but the transverse momentum p_{T} of the vector meson, which is connected with the transferred momentum as $|t| \sim p_{\mathrm{T}}^2$, where the difference is caused by the photon momentum. Therefore, the cross section dependency on p_{T}^2 is measured and the result is transformed to $\mathrm{d}\sigma/\mathrm{d}t$.

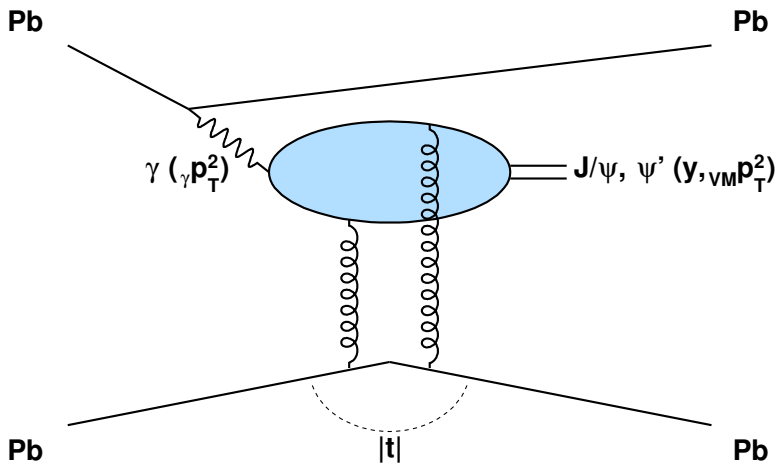

Figure 1.5: A Feynmann diagram of a lead-lead ultra-peripheral collision, which produces a J/ψ particle. The $|t|$ stands for the square of the transferred momentum. The γ is a quasi-real photon emitted from the Pb nucleus.

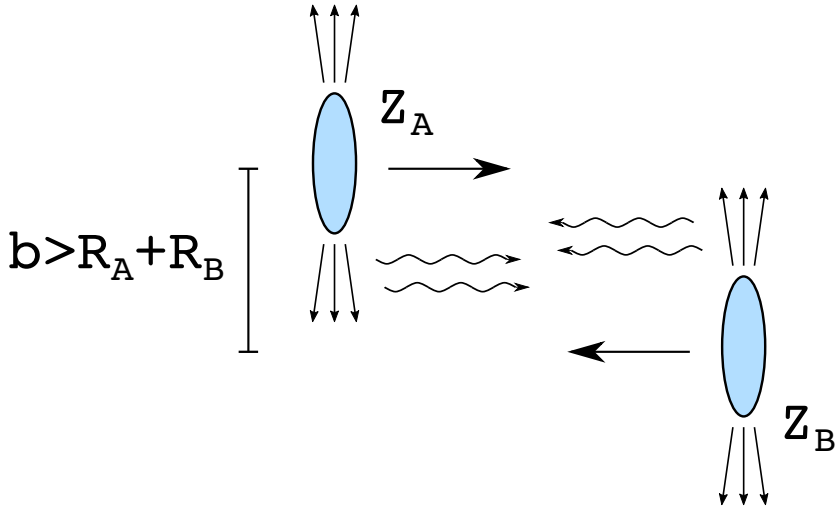

Figure 1.6: A diagram of an ultra-peripheral collision of two ions (proton number Z) with impact parameter b.

1.6 Exclusive photoproduction of J/ψ mesons

1.6.1 Description of photonuclear production

There are several models, which can predict the cross section for photonuclear production at LHC energies [15, 23]. All models are based on Eq. (1.2)

$$\frac{\mathrm{d}\sigma_{\mathrm{PbPb}}(y)}{\mathrm{d}y} = N_\gamma(y, M)\sigma_{\gamma\mathrm{Pb}}(y) + N_\gamma(-y, M)\sigma_{\gamma\mathrm{Pb}}(-y), \tag{1.2}$$

where N_γ is the photon flux, M is the mass of the produced vector meson, $y = \ln 2k/M$ is the rapidity (with k being the momentum of the photon) and $\sigma_{\mathrm{PbPb}/\gamma\mathrm{Pb}}$ are the corresponding cross sections. Each term in the sum represents one incoming nucleus.

In the semi-classical description [26] the photon flux per unit area can be written as

$$n(k, b) = \frac{\alpha Z^2}{\pi^2 b^2}\chi^2\left[K_1^2(x) + \frac{K_0^2(x)}{\gamma}\right], \tag{1.3}$$

with α standing for the fine-structure constant, Z for the electric charge, $K_{0,1}$ are Bessel functions and $\chi = \frac{kb}{\gamma}$. This formula is approximated with the hard sphere model or it is integrated with the convolution of the probability of no hadronic interaction [15] in the models.

1.6.2 List of models

Many attempts to describe photonuclear reactions were made in the past. A representative set of models was chosen in the measurements relevant for this thesis. The alphabetical summary of the models:

- **b-BK:** A model by Bendova, Cepila, Contreras and Matas [27–29],
- **BGK-I:** A model by Łuszczak and Schäfer [30],
- **EPS09 LO:** A model by Guzey, Kryshen and Zhalov [31, 32],
- **GG-HS:** A model by Cepila, Contreras, Krelina and Tapia Takaki [33],
- **LTA:** A model by Guzey, Kryshen and Zhalov [31, 34],
- **IIM BG:** A model by Gonçalves and Machado [35, 36],
- **Impulse approximation:** A model by Guzey, Kryshen, Strikman and Zhalov [37],
- **IPsat:** A model by Lappi and Mäntysaari [38, 39],
- **STARlight:** A model by Klein and Nystrand [40–42].

Further in the text, these models are described more. In particular, the STARlight [42] prediction, which is used widely in the measurements, is described in detail.

STARlight

The Monte Carlo generator used in this thesis is called STARlight [42]. This generator employs a model introduced by Klein and Nystrand [40, 41]. This model is based on the generalized vector meson dominance model (GVMD) [43]. In general, the GVMD relates the process $\gamma + \mathrm{Pb} \to \mathrm{V} + \mathrm{Pb}$ to $\mathrm{V} + \mathrm{Pb} \to \mathrm{V} + \mathrm{Pb}$, where V stands for the vector meson.

The total cross section for nuclei depends on the slope of the $\mathrm{d}\sigma/\mathrm{d}t$ and is dominated by the nuclear form factor $F(t)$ [40]. The photonuclear cross section then can be expressed as

$$\sigma(\gamma + \mathrm{Pb} \to \mathrm{V} + \mathrm{Pb}) = \left.\frac{\mathrm{d}\sigma(\gamma + \mathrm{Pb} \to \mathrm{V} + \mathrm{Pb})}{\mathrm{d}t}\right|_{t=0} \int_{t_{min}}^{\infty} \mathrm{d}t |F(t)|^2. \quad (1.4)$$

Making use of the optical theorem and the eikonalisation technique [15] it can be found that the cross section relates to the nuclei as

$$\left.\frac{\mathrm{d}\sigma(\gamma + \mathrm{Pb} \to \mathrm{V} + \mathrm{Pb})}{\mathrm{d}t}\right|_{t=0} = \frac{\alpha\sigma_{tot}^2\,(\mathrm{V} + \mathrm{Pb})}{4f_v^2}. \quad (1.5)$$

Here f_v is the vector meson-photon coupling. From a classical Glauber model [44]

$$\sigma_{tot}\,(\mathrm{V} + \mathrm{Pb}) = \int \mathrm{d}^2b \left(1 - e^{[-\sigma_{tot}(\mathrm{V+p})T_{\mathrm{Pb}}(b)]}\right), \quad (1.6)$$

where T_{Pb} is the nuclear thickness function, b is the impact parameter and for $\sigma^2_{tot}\,(\mathrm{V}+\mathrm{p})$ the optical theorem at the nucleon level yields

$$\sigma^2_{tot}\,(\mathrm{V}+\mathrm{p}) = 16\pi \left.\frac{\mathrm{d}\sigma(\mathrm{V}+\mathrm{p}\to\mathrm{V}+\mathrm{p})}{\mathrm{d}t}\right|_{t=0}. \tag{1.7}$$

Using GVMD leads to

$$\left.\frac{\mathrm{d}\sigma(\mathrm{V}+\mathrm{p}\to\mathrm{V}+\mathrm{p})}{\mathrm{d}t}\right|_{t=0} = \frac{f_V^2}{4\pi\alpha} \left.\frac{\mathrm{d}\sigma(\gamma+\mathrm{p}\to\mathrm{V}+\mathrm{p})}{\mathrm{d}t}\right|_{t=0}, \tag{1.8}$$

where the elementary cross section can be parametrised with the results from the measurement made at HERA [45]

$$\left.\frac{\mathrm{d}\sigma(\gamma+\mathrm{p}\to\mathrm{V}+\mathrm{p})}{\mathrm{d}t}\right|_{t=0} = b_V(XW^{\epsilon}+YW^{-\eta}), \tag{1.9}$$

where W is the centre-of-mass energy and the rest are constants, which were determined from fits to data and can be found in Table II in Ref. [41]. The first term with X represents the pomeron exchange and the Y is the meson exchange.

STARlight takes the form factor as the Woods-Saxon distribution approximated as a convolution of a hard sphere and a Yukawa potential. Then the form factor looks like

$$F(q=\sqrt{|t|}) = \frac{4\pi\rho_0}{Aq^3}\left[\frac{\sin(qR_A)-qR_A\cos(qR_A)}{1+a^2q^2}\right], \tag{1.10}$$

where A is the atomic number, ρ_0 is the nuclear density of the hard sphere, R_{A} is the radius of the nucleus and a is the range of the Yukawa potential. STARlight takes as input numbers $a = 0.7$ fm and $R_{\mathrm{A}} = 6.62$ fm [42].

Putting all things together the photonuclear cross section used has the form

$$\frac{\mathrm{d}\sigma(\gamma+\mathrm{Pb}\to\mathrm{V}+\mathrm{Pb})}{\mathrm{d}t} = \mathrm{NORM}|F(t)|^2 \tag{1.11}$$

with NORM standing for the normalisation of the fit function used later in this work in Sec. 5.5.1.

Impulse Approximation

The Impulse Approximation (IA) is a calculation of the photoproduction cross section, where all nuclear effects, except coherence, are neglected [37]. That means the cross section is estimated as

$$\sigma(\gamma+\mathrm{Pb}\to\mathrm{J}/\psi+\mathrm{Pb}) = \left.\frac{\mathrm{d}\sigma(\gamma+\mathrm{p}\to\mathrm{J}/\psi+\mathrm{p})}{\mathrm{d}t}\right|_{t=0} \int_{t_{min}}^{\infty} \mathrm{d}t|F(t)|^2, \tag{1.12}$$

where $\mathrm{d}\sigma(\gamma+\mathrm{p}\to\mathrm{J}/\psi+\mathrm{p})/\mathrm{d}t$ is taken from a measurement of the corresponding interaction and $F(t)$ is an elastic-nuclear form factor, which defines

the $|t|$ distribution. The form factor is estimated using a nuclear density distribution well-known from elastic scattering experiments [46, 47].

This cross section is based on experimental data and hence can serve for a model-independent comparison of nuclear structure to single-nucleon structure.

The concept of the impulse approximation is very old (can be tracked back into 19th century books) and in the classical scattering theory it refers to the case when one of the forces exerted on a scattering particle acts for a short time and is much greater than any other force present. So one can effectively ignore other forces (see Sec. 5.4. in Ref. [48]). In nuclear collision theory, the "impulse approximation" term was introduced by G. F. Chew and G. C. Wick [49, 50]. In brief, this approximation refers to the case when one can ignore nuclear forces between nucleons when a particle scatters off a nucleus. So the scattering off a nucleus is considered as a superposition of scatterings on individual nucleons. What is more important for the case of this thesis is that in the IA one also ignores multiple scattering that is at the origin of shadowing effects and in that sense it was firstly used in Ref. [37].

EPS09 LO

This calculation [31] is based on the leading logarithmic approximation of perturbative QCD (LO pQCD) [51]. The exclusive photoproduction cross section of J/ψ, as the charm quark anti-quark in the lowest Fock state, off a proton was firstly introduced in Ref. [52] and is depicted in Eq. (1.13)

$$\left.\frac{\mathrm{d}\sigma(\gamma + \mathrm{p} \to \mathrm{V} + \mathrm{p})}{\mathrm{d}t}\right|_{t=0} = C_{\mathrm{p}}\left(\mu^2\right)\left[\alpha_s\left(\mu^2\right) x g_{\mathrm{p}}\left(x, \mu^2\right)\right]^2, \tag{1.13}$$

where C_{p} is a normalisation factor, α_s is the strong coupling constant and xg_{p} is the gluon distribution of the proton. Here, a non-relativistic approximation of the J/ψ wave function is taken into account. The gluon distributions of the proton are taken from HERA measurements.

The step from proton to nuclear cross section is shown in Eq. (1.14) and connects the gluon distributions in the proton and the lead through α_s. The nuclear gluon density function of lead (xg_{Pb}) is taken from the EPS09 nuclear parton distribution functions [32].

$$\begin{aligned}
&\sigma(\gamma + \mathrm{Pb} \to \mathrm{J}/\psi + \mathrm{Pb}) \\
&= C_{\mathrm{Pb}}\left(\mu^2\right)\left[\alpha_s\left(\mu^2\right) x g_{\mathrm{Pb}}\left(\mu^2\right)\right]^2 \int_{t_{min}}^{\infty} \mathrm{d}t |F(t)|^2, \\
&= C\left(\mu^2\right) \left.\frac{\mathrm{d}\sigma(\gamma + \mathrm{p} \to \mathrm{V} + \mathrm{p})}{\mathrm{d}t}\right|_{t=0} \left[\frac{x g_{\mathrm{Pb}}\left(\mu^2\right)}{A_{\mathrm{Pb}} x g_{\mathrm{p}}\left(\mu^2\right)}\right]^2 \int_{t_{min}}^{\infty} \mathrm{d}t |F(t)|^2.
\end{aligned} \tag{1.14}$$

This calculation is rather a parametrisation of existing data than a theory derived from first principles, but the gluon-distributions ratio term of Eq. (1.14) directly introduces the nuclear gluon shadowing factor into the calculations, which is an advantage of this model.

LTA

The Leading Twist Approximation (LTA) models nuclear-shadowing phenomena combining the Gribov-Glauber theory [53, 54], QCD factorisation theorems [55] and the data from lepton deep-inelastic scatterings off protons at HERA [14]. The Gribov-Glauber theory serves as a prescription of transformation from photon-proton cross sections to photon-lead cross sections, the factorisation theorems describes the nuclear structure function as a convolution of some hard scattering coefficients with the parton distribution functions (PDFs) of the target and the PDFs are taken from the experimental data. The computation is detailed in Ref. [34].

GG-HS

The energy-dependent hot-spot model with the Gribov-Glauber formalism (GG-HS) [33] uses the idea of the proton having subnucleonic degrees of freedom, which group into regions of high density of gluons (hot spots). Here, the impact-parameter plane is described by an energy-dependent hot-spot profile. The extension to the nuclear case is done with the Gribov-Glauber theory, which describes the nucleus as a sum of nucleon wave functions belonging to the nucleus [53, 54].

The gluon saturation [56] is a non-linear QCD effect which modifies the cross section. With increasing energy, more gluons appear as a result of gluon creation. However, the probability of gluon recombination is expected to balance the gluon creation at the LHC energies and the number of gluons should saturate. An effect, which simulates the saturation, is incorporated into this hot-spot model [57]. With increasing energy, the number of hot spots in the impact-parameter plane grows. Also the dipole cross section grows following the Golec-Biernat, Wüsthoff model [58] that includes saturation explicitly.

b-BK

The b-dependent Balitsky-Kovchegov equation (b-BK) model is based on the colour dipole approach, which imagines the photon-proton interaction through the interaction of the quark-antiquark pair, and the development of the scattering amplitude by solving the Balitsky-Kovchegov equation (see Ref. [59, 60]) to obtain its dependency on impact parameter b, which is directly related to the Mandelstam t.

This solution utilises nuclear-like initial conditions. Here, the balance of gluon creation and annihilation, is turned on at some saturation scale, which is an input to the model. Assuming a nucleus has more gluons and has a larger diameter than a single proton, the nuclear-like initial conditions are represented by Woods-Saxon profiles and have a different saturation scale in the model than for the single-proton case.

BGK-I

The Bartels, Golec-Biernat and Kowalski (BGK) [30, 61] based model calculates the dipole cross section with the saturation scale taken into account in the eikonal approximation with the saturation radius related to the gluon density. The evolution of the gluon density is driven by the DGLAP evolution [62, 63]. The parameterisation is obtained by fitting HERA data [14]. The transformation from photon-proton to photon-lead cross section is done via the Gribov-Glauber theory briefly described above.

IIM BG

The Iancu-Itakura-Munier (IIM) model [64] improved with the b-dependent Colour Glass Condensate (b-CGC) model [65] creates the IIM BG. The scattering amplitude is built by joining limiting solutions to the BFKL equation [66, 67] and the CGC frameworks. The saturation is introduced via a simplified BK equation in this model.

The description of the nucleus scattering amplitude adopts a simple model from Ref. [68], which again employs the Gribov-Glauber theory parametrised with data.

IPsat

The Impact Parameter Dipole Saturation Model [69] (IPsat) uses the Color Glass Condensate inspired dipole cross section fit to HERA data [14]. The eikonalised gluon distribution is evolved using the DGLAP equation.

The nuclear scattering amplitude is obtained as an average over the positions of the nucleons in the nucleus, which follows the Woods-Saxon distribution.

Chapter 2

Experimental set-up

The Large Hadron Collider (LHC) is a scientific facility located beneath the France-Switzerland border near Geneva, Switzerland. Its circumference of 27 kilometres granted it the title of the largest particle collider in the world. It was built to accelerate protons and lead ions to relativistic energies and to collide them at four crossings, where the four main LHC experiments are situated: ALICE, ATLAS, CMS and LHCb.

From its start in 2009 to a pause in 2013 it produced a huge amount of proton-proton, proton-lead and lead-lead collisions. This epoch is called Run 1. After it, an almost two-year Long Shutdown 1 proceeded to give scientists an opportunity to upgrade systems and prepare the collider to deliver higher energy and luminosity. At the beginning of 2015 the epoch called Run 2 was started and the LHC established a new world record in the energy of collided particles to 13 TeV for pp and $\sqrt{s_{\mathrm{NN}}} = 5.02$ TeV per nucleon pair for Pb–Pb collisions. New p–Pb/Pb–p collisions were conducted at energies 5.02 and 8.16 TeV per nucleon pair in the year 2016. The programme of Run 2 data taking continued until 2018, where towards the end of the year the last Pb–Pb collisions were recorded.

In ALICE terminology, the last heavy-ion period is tagged as LHC18q and LHC18r. The difference between these periods is in the polarity of the solenoid magnet used for particle tracking. The data analysis of this thesis is based on Pb–Pb data collected in 2018. A smaller data-taking time unit is called run and confines a time period between one start and one corresponding stop of actual data taking. The runs tagged as "physics" are used in the analysis. The smallest time frame is the so-called bunch crossing (BC), a time window when two slots of each beam crosses in the interaction area. One BC can contain from none to many events.

2.1 The ALICE apparatus

One of the experiments, which is using the LHC machine, is ALICE [70, 71]. In contrast to the other experiments, this one was designed to look for the

state of matter called quark gluon plasma (QGP) and to measure some of its properties. Because large volumes with high energy densities are needed to create the QGP, beams of lead ions are used at the LHC. As it is mentioned in Sec. 1.5, these beams of lead ions are also used for UPCs. The ALICE detector consists of 18 sub-detectors (See Fig. 2.1). For the UPC trigger only AD, TOF, V0 and ITS are needed, while the measurement requires ITS, TPC, TOF, V0, AD and ZDC. The central barrel detectors are immersed in an homogeneous field along the beam direction of 0.5 T.

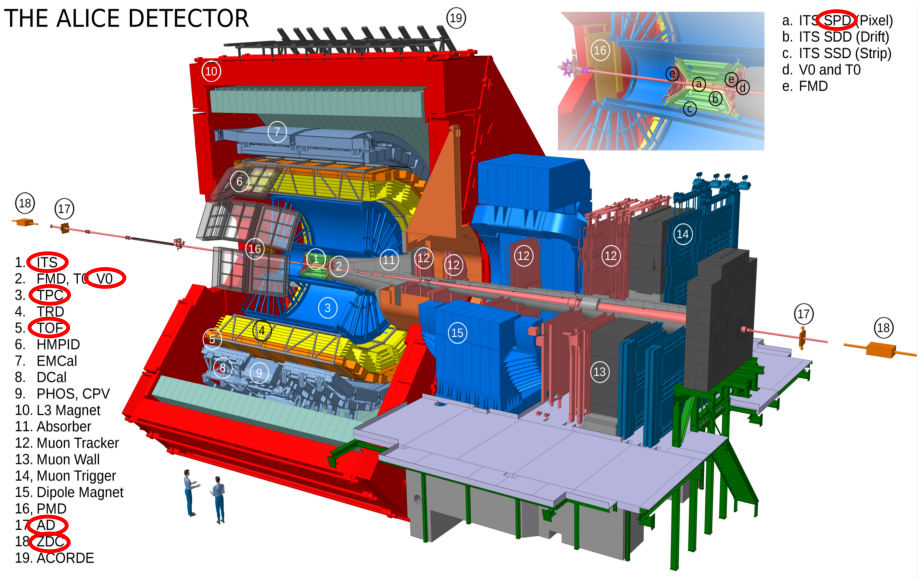

Figure 2.1: Scheme of the ALICE detector. Detectors used for UPC triggering at midrapidity and analysis are in the red ellipsis. Taken from Ref. [72].

2.1.1 Inner Tracking System

The Inner Tracking System (ITS) detector is located in the central part of ALICE. Its main tasks are to localise the primary and secondary vertices, to track and identify particles with low momentum and reconstruct particles traversing dead regions of the main tracking detector, the TPC. The ITS itself is a silicon based detector and it is divided in three parts each consisting of two cylinders of detectors using different technologies: SPD, SDD and SSD.

For triggering in UPCs only the SPD is used, where the abbreviation stands for the Silicon Pixel Detector. This is the innermost layer of the ITS. A sketch of the SPD is in Fig. 2.2. The SPD itself consists of the inner and outer layer, which are divided in so-called staves in the azimuthal angle. The inner (outer) layer has 20 (40) staves. Each stave is made of four ladders. Each ladder has 5 pixel chips and each of them contains 8192 readout cells. Together we have 1200 active chips in the SPD. Each chip provides a trigger signal which is on if any of the readout cells have a signal above threshold.

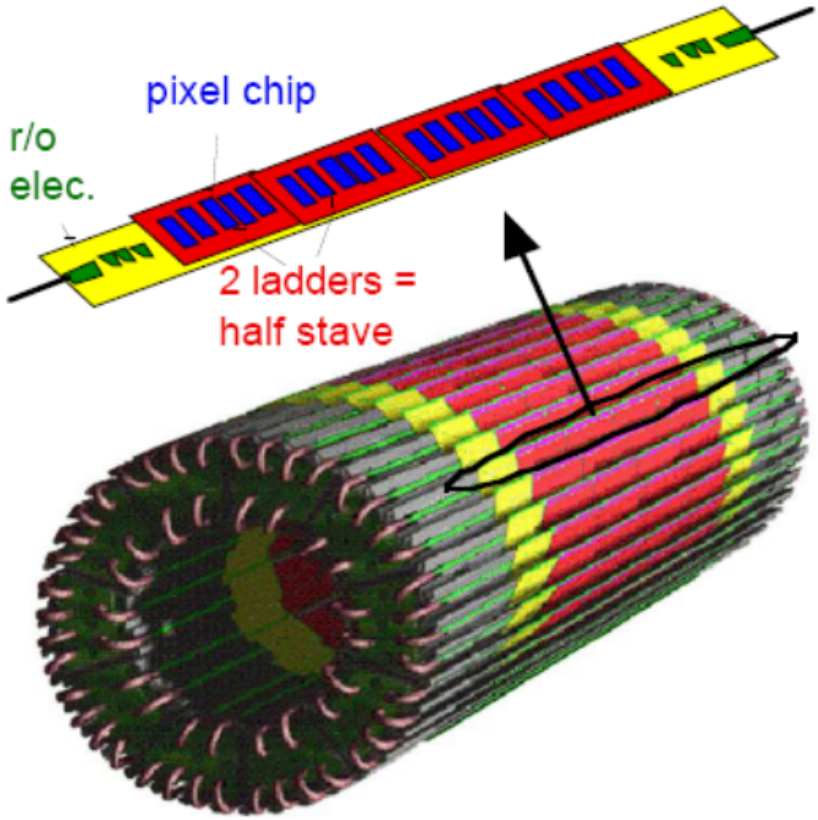

Figure 2.2: Scheme of the SPD sub-detector. Taken from Ref. [73]

The SPD is 282 mm long in the direction of the beam and 39 (76) mm in the radius of the inner (outer) layer, covering the pseudorapidity intervals $|\eta| < 2$ ($|\eta| < 1.4$). A chip has a size of 13.5 mm with an average spacing of 0.6 mm.

2.1.2 Time Projection Chamber

The Time Projection Chamber (TPC) detector is another central-barrel detector which is placed right after the ITS in radial distance. Its main purpose is to track particles and provide charged-particle momentum measurements with good two-track separation, vertex determination and particle identification. The TPC coverage in pseudorapidity is $|\eta| < 0.9$ for tracks with full radial length and in azimuth it has full coverage. It offers good momentum resolution in a large transverse momentum of the track (p_{T}) range from 0.1 GeV/c to 100 GeV/c.

The TPC has a cylindrical shape. Its active volume goes from 848 mm to 2466 mm in radius and 5000 mm along the beam direction. It is split in the radial direction in two chambers and the readout of each is divided into 18 sectors in azimuth. In addition, the TPC is split up in the longitudinal

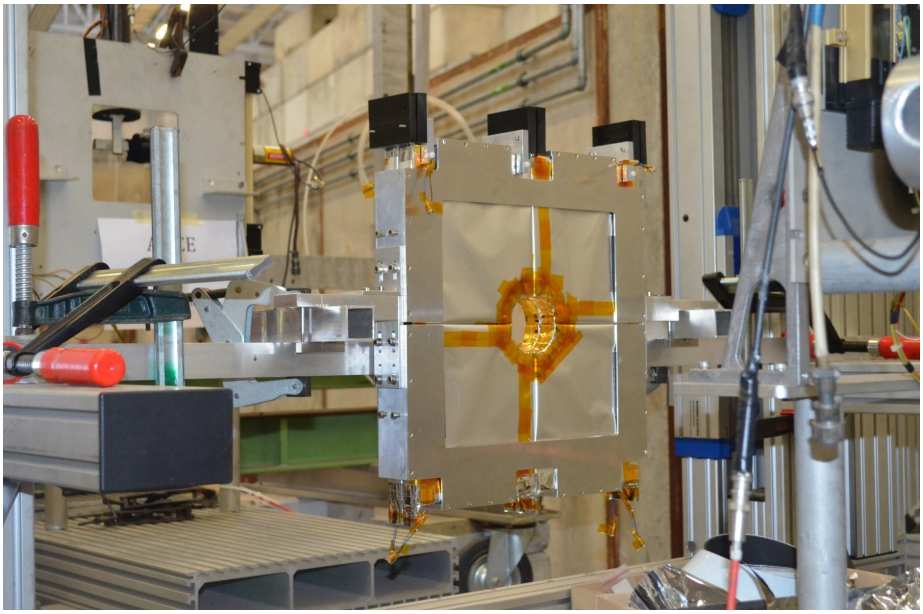

Figure 2.3: A prototype of the AD detector. Taken from Ref. [74]

direction at the middle by a central electrode (positioned vertically). Together it gives 72 chambers, which are read out on both ends of the detector.

The TPC is a gaseous detector filled with a mixture of neon and carbon oxide in Run 1 and a mixture of argon and carbon oxide in Run 2. When a particle propagates through the gas mixture, it ionises its surroundings. Because this happens in an electric field, electrons from the ionisation drift to electrodes at both ends of the detector, where charge is collected. Crucial here is the drift time, which for the neon mixture is ~ 90 μs. The speed of data collecting is then limited by the drift time, so when the interaction rate is large, a new event appears in the TPC in the moment when the old one is still not read out. Also, the charge particle multiplicity density increases with the energy of collision, which makes the operation of the detector in Run 2 more difficult.

2.1.3 Time-Of-Flight

The Time-Of-Flight (TOF) detector is a gaseous detector which covers the central pseudorapidity region for particle identification in the intermediate momentum range and helps ITS and TPC to track low momentum particles. The TOF is built of Multi-gap Resistive-Plate Chambers (MRPC) [75]. The advantage of this method is the high, uniform electric field over the full volume. A traversing charged particle causes a gas avalanche process and therefore the drift time is not a problem any more.

The TOF has a length of 741 cm and an internal (external) radius of 370 (399) cm. It is divided in 18 sectors in azimuthal angle and five segments in the beam direction. The fast response of the MRPC, the large area covered

at $|\eta| < 0.8$ and the high segmentation make the TOF a good option for the triggering of UPCs events in the midrapidity region.

2.1.4 V0

The V0 is a scintillator based detector, which is made of two counters V0A and V0C installed on both sides of the ALICE nominal interaction point [76]. Its purpose is to measure particles in the forward region (particles, which left the interaction point under a small angle). V0A (V0C) is located 340 (90) cm on the side heading away from (towards) the muon spectrometer (see Fig. 2.1). It covers the pseudorapidity range $2.8 < \eta < 5.1$ ($-3.7 < \eta < -1.7$). Both counters are segmented in four rings in the radial direction, each ring divided into eight parts in azimuth.

The V0 is the most frequently used detector for triggering. Since it consists of two parts, it can work in two modes: AND and OR. The AND mode is used for example for the Minimum Bias trigger. When looking for J/ψ photoproduction at midrapidity in UPCs, the OR mode is negated, because it is desirable to have nothing in any of the V0 arrays: if there is something in V0A or V0C, the event does not trigger the readout detectors.

2.1.5 Zero Degree Calorimeter

The Zero Degree Calorimeter (ZDC) detector is a forward detector designed to detect spectator nucleons, which can be used to calculate the number of participants in a collision. It can also identify the centrality of a collision, which can be used for triggering particular centrality classes of events. In addition, the ZDC is used for the determination of luminosity as explained in Sec. 3.3.

The ZDC is made of two sets of hadronic scintillators located 112.5 meters on each side of the interaction point. The sets are made of two calorimeters, where the ZN (ZP) is situated between (outside) the beam pipes and measures neutrons (protons). The protons feel the magnetic fields of the LHC and deviate, while the neutrons fly at zero degrees. In addition, electromagnetic calorimeters ZEM are placed seven meters from the interaction point at positive rapidities. These help to distinguish between very central and very peripheral events, where the signal in ZN is very similar. In addition, the ZDC detects neutrons emitted in the very forward region, for example neutrons produced following electromagnetic dissociation [77].

2.1.6 ALICE Diffractive

The ALICE Diffractive detector (AD) is another system installed in the forward pseudorapidity region of ALICE [78, 79]. The system itself consists of two scintillator stations situated in two different places. The stations

are called according to the side they are located as ADA and ADC. The ADA (ADC) is 16 (19) metres from the interaction point and covers the pseudorapidity range $4.8 < \eta < 6.3$ ($-7.0 < \eta < -4.9$).

This sub-detector was added to ALICE during the Long Shutdown 1 and it was commissioned with the first pp collisions in Run 2. In Run 1, the forward detectors were able to select about 30% of single diffractive events. With AD the selection significantly improves for diffracted mass below 10 GeV/c^2 [74]. For UPCs this new detector system means that the capabilities to veto the presence of particles is increased substantially and thus, for the measurements presented in this thesis, it is expected even less background when using the AD system.

2.2 UPC triggers

The LHC is designed to collide projectiles with a frequency of 40 MHz for protons and ∼8 MHz for ion beams [2]. However, the ALICE detectors need some time to read out electrical signals, which is in order of μs. Therefore it is not possible to save every single event, but the events, which have signs for the physics we are interested in, have to be carefully picked. This is done with a so-called trigger. The ALICE trigger system is briefly described in Sec. 3.1.

For ultra-peripheral collisions, several triggers were designed. In the next lines, those focusing on the photoproduction of the J/ψ at midrapidity are described to demonstrate the time evolution of the design.

During Run 1 the detectors SPD, TOF and V0 were used to build trigger signals. The CCUP4 trigger was used to collect data in 2011 Pb–Pb collisions at $\sqrt{s_{\mathrm{NN}}} = 2.76$ TeV. This trigger consists of the following conditions:

- **!V0$_{\mathbf{OR}}$:** Nothing was detected in the V0 detector,
- **0OMU:** More than one hit and less than seven hits in the TOF detector + at least two of the hits with an opening angle $> 150°$,
- **0SM2:** More than one hit in the outer layer of the SPD.

Data collected in 2015 used the trigger called CCUP8 to retrieve events with photoproduction of the J/ψ from Pb–Pb at the higher energy, $\sqrt{s_{\mathrm{NN}}} = 5.02$ TeV. This trigger already employs the new AD detector and has slightly different conditions and higher performance with respect to the CCUP4 trigger. The conditions are:

- **!0VB$_{\mathbf{OR}}$:** Nothing was detected in the V0 detector,
- **!0UB$_{\mathbf{OR}}$:** Nothing was detected in the AD detector,

- **0STP:** Less than eight hits in the outer layer of SPD detector + opening angle of at least two tracklets[1] $> 150°$,
- **0OMU:** More than one hit and less than seven hits in the TOF detector + at least two of the hits with an opening angle $> 150°$.

In this thesis, data from 2018 Pb–Pb collisions at $\sqrt{s_{\mathrm{NN}}} = 5.02$ TeV are analysed. The latest evolution of a central barrel UPC trigger, the CUP31 trigger, was designed to pick up these events. The CCUP31 is defined as:

- **!0VB$_{\mathbf{OR}}$:** Nothing was detected in the V0 detector,
- **!0UB$_{\mathbf{OR}}$:** Nothing was detected in the AD detector,
- **0STG:** Less than eight hits in the outer layer of SPD detector + opening angle of at least two tracklets $> 36^{\mathrm{o}}$ for runs before run 295753 and opening angle $> 144^{\mathrm{o}}$ for the other runs,
- **0OMU:** More than one hit and less than seven hits in the TOF detector + at least two of the hits with an opening angle $> 150^{\mathrm{o}}$.

In addition, due to high rate of collisions in some runs of 2018 data taking, the past-future protection[2] was active in this trigger to prevent from ambiguity of the SPD trigger signal with respect to signals from the TOF detector.

In other words, all these triggers are looking for two back-to-back leptons in an otherwise empty detector. For Run 2, the veto in the forward region was extended by the newly added AD detector and the condition on the back-to-back tracks was fine-tuned resulting in (together with a higher collision energy) an increase of the data sample by a factor of ten with respect to the data recorded during Run 1.

2.3 Data flow

The extraction of data from a collision to a TTree ready for an analysis is a rather long process. When two lead ions collide a selection starts with online triggers. The UPC triggers are described in Sec. 2.2. Only a small portion of events passes these criteria not just because of the physics condition, but also due to the occupancy of the readout detectors for example. In fact, there are several trigger levels. When a positive decision is made, detector signals are stored as RAW data in the ALICE computing clusters, where the data are compressed. Detector settings are saved as well. These settings are then used to reconstruct physics events from the RAW data, which are stored

[1] In the ALICE nomenclature, tracklet is defined as pair of matching clusters in the two layers of SPD [71].

[2] The past-future protection is an electronic veto on trigger due to signals coming from collisions from a different time frame than desired.

again at so-called ESD level. The last step is to use a physics selection on the ESD data, which rejects some background and focuses on interesting physics signatures. These data are called AOD and are further used to create objects, which can be used in an analysis. In the case of this thesis, this last step of the process takes the form of a file with ROOT trees and histograms [80], which is produced by the official LEGO train of the PWG-UD analysis group [81].

2.4 Data samples

To study the cross section for the production of a vector meson in UPCs good data have to be chosen. An opportunity to measure such events at the nowadays highest possible energies appeared in 2011, 2015 and 2018. Those years several runs with Pb-Pb collisions had active triggers for ultra-peripheral collisions. The data we analyse were prepared using the LEGO train framework of the PWG-UD. The LEGO train ran over several millions of triggers and made a first pre-selection of events with only two tracks. The requirements for the tracks (Sec. 2.4.2) were quite relaxed and were strengthened by the selection described in Sec. 2.4.3.

Besides these data, also Monte Carlo simulations (MC) were used. Several different processes were generated with the STARlight 2.2.0 MC generator [42]. The channel with a dimuon pair coming from the J/ψ decay (J/$\psi \to \mu^+\mu^-$) was generated twice. Once for the coherent production of J/ψ and once for the incoherent production of J/ψ. Another channel that was generated corresponds to the reaction of two photons producing two muons ($\gamma\gamma \to \mu^+\mu^-$). This process represents the main irreducible background to our measurement. Another generated channel is the decay of the ψ' meson to pions and muons ($\psi' \to \mu^+\mu^- + \pi^+\pi^-$). Both coherent and incoherent productions were generated in this case. The last generated channel is the decay of the ψ' meson into muons only ($\psi' \to \mu^+\mu^-$). Then, the paths of all particles in the generated events through ALICE were simulated. GEANT 3.21 [82] was used to reproduce the response of the detector and the simulated data were reconstructed with the same software as the real ones, accounting for the actual data-taking conditions.

2.4.1 Data selection

In order to find out the right events for the measurement with 2018 data, additional selection criteria were applied to online triggered data.

2.4.2 Pre-selection of the ESD sample

A data sample for detailed analysis is selected from ESD files. The physics pre-selection applied to these files is listed in this set of conditions:

- Minimum number of TPC crossed rows is 70,
- minimum ratio of TPC crossed rows to findable clusters is 0.8,
- maximum ITS (TPC) fit χ^2 per ITS (TPC) cluster is 36(4),
- both ITS and TPC refits required,
- maximum distance of closest approach (DCA) to the vertex in XY plane according to:

$$\mathrm{DCA_{XY}} < \frac{0.0105 + 0.0350}{p_{\mathrm{T}}^{1.1}}, \tag{2.1}$$

- maximum DCA to vertex in Z is 2 cm,
- at least one hit in SPD and each track has at least one hit in the inner and the outer layer of the ITS detector,
- one vertex within 15 cm from the interaction point in beam direction.

Each event has to have exactly two tracks that pass all the previous criteria related to tracks.

2.4.3 Selection of the pre-selected data sample

In order to find out the right events for the measurement with 2018 data, the following additional selections were used:

- the event is from a run approved by ALICE Data Preparation Group [83],
- the event has been triggered with the CCUP31 trigger (see Sec. 2.2),
- offline version of the 0STG trigger input,
- all (two, back-to-back) remaining tracks surviving the previous criteria are more likely to be muons than electrons in the units of significance σ, representing the distance from the measured ionisation energy loss of the track and the expectation of a Bethe model, expressed in units of the standard deviation of the measurement,
- the invariant mass is between 2.2 GeV/c^2 and 4.5 GeV/c^2,
- there is nothing in either of AD and V0 according to the offline processing,
- the rapidity of the $\mu^+\mu^-$ pair is within (-0.8,0.8).
- the pseudorapidity η of each track is within (-0.8,0.8).
- the tracks have opposite charge,
- $p_{\mathrm{T}}^{\mu\mu} < 0.11$ GeV/c.

Table 2.1: Effects of selection criteria on data sample. For details see the text.

Data	
Selection	No. events
Total no. of events	2441424
DPG official run list	2441424
CCUP31 trigger	2204763
SPD cluster matches FOhits	791510
$\mathrm{PID}^{\mathrm{muon}}_{\mathrm{TPC}}(\sigma^2_{\mathrm{trk1}}+\sigma^2_{\mathrm{trk2}}) < \mathrm{PID}^{\mathrm{electron}}_{\mathrm{TPC}}(\sigma^2_{\mathrm{trk1}}+\sigma^2_{\mathrm{trk2}})$	694970
Mass $\in$ (2.2,4.5) GeV/c^2	28767
ADA offline veto	28684
ADC offline veto	28629
V0A offline veto	25247
V0C offline veto	22975
Rapidity $\in$ (-0.8,0.8)	22643
Track $\eta \in$ (-0.8,0.8)	18540
Tracks have opposite charge	16782
$p_{\mathrm{T}}^{\mu\mu} < 0.11$ GeV/c	11219
Mass $\in$ (3.0,3.2) GeV/c^2	3605

The effect of these criteria on the data sample is reported in Tab. 2.1 and Fig. 2.4. The effect of the mass $\in$ (3.0,3.2) GeV/c^2 selection is only for a better imagination of the total number of signal+background events. In order to obtain the yield of J/ψ (see Sec. 5.2), the analysis is started with the number of selected events in the last line of Tab. 2.1.

The upper bound on $p_{\mathrm{T}}^{\mu\mu}$ was set to first, significantly reduce contamination from incoherent J/ψ decay (see Fig. 2.4, the increase of events above $\approx$ 0.2 GeV/c is due to prevailing incoherent J/ψ production) and second, to avoid the dip in the p_{T} spectrum (see Fig. 2.6), which can be troublesome when converting the cross section of J/ψ from p_{T}^2 to $|t|$. In the end, the shape of the $|t|$ spectrum and its projection to $|t| = 0$ is the interesting input for theoretical calculations.

For MC simulations there are two different selection criteria. One for generated particles and the second one for reconstructed particles. For the generated sample these criteria were used:

- at least 2 generated particles,
- the rapidity of $\mu^+\mu^-$ is within (-0.8,0.8).

The same criteria as for measured data were applied on MC reconstructed particles, because the MC simulation are used to train the unfolding method and revert the detector effects. Effects of these selections on the MC sample are in Fig. 2.5.

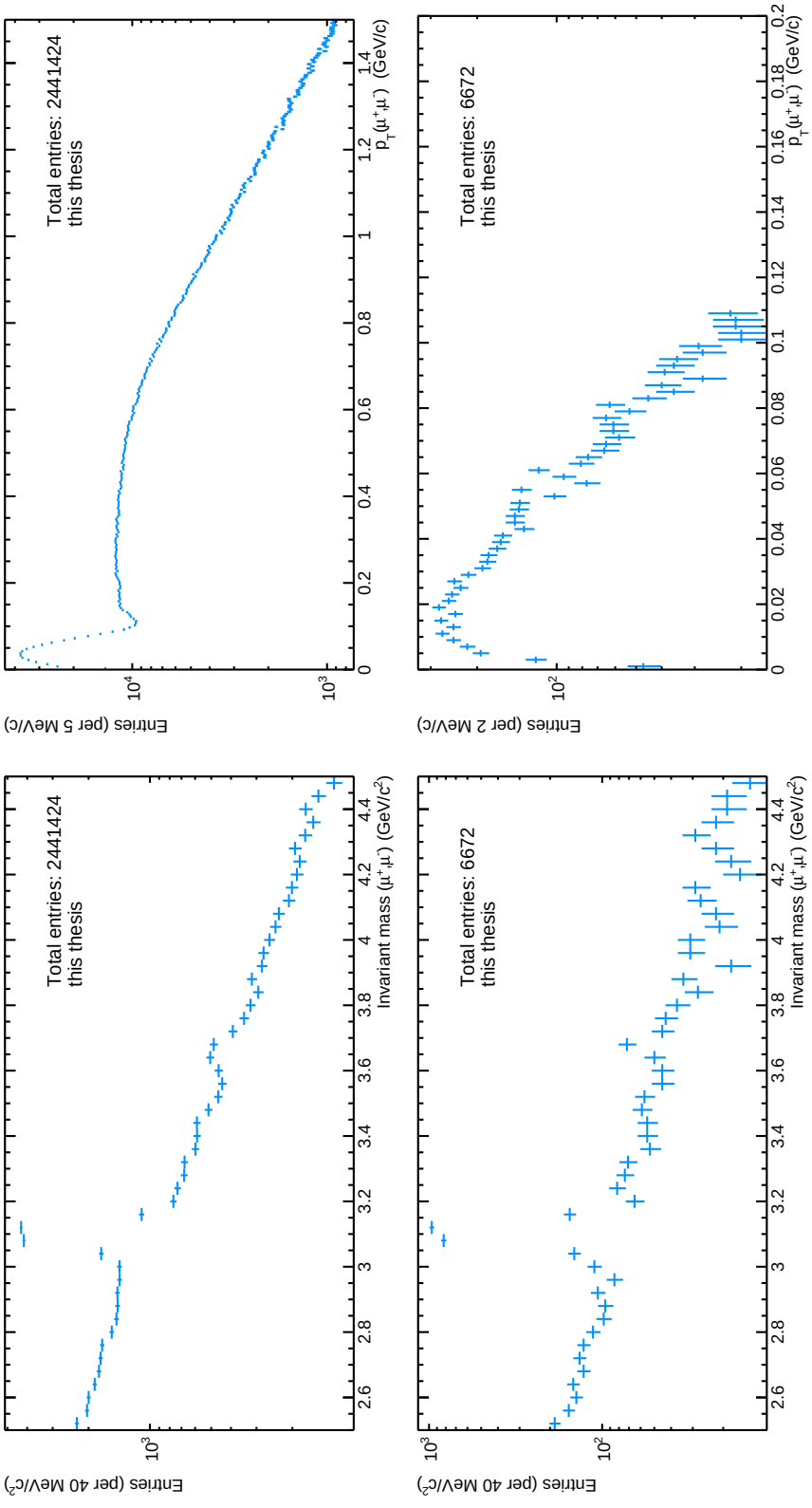

Figure 2.4: Measured data: Invariant mass (left) and p_T (right) spectra before (top) and after (bottom) applying the selection criteria mentioned in Sec. 2.4.1.

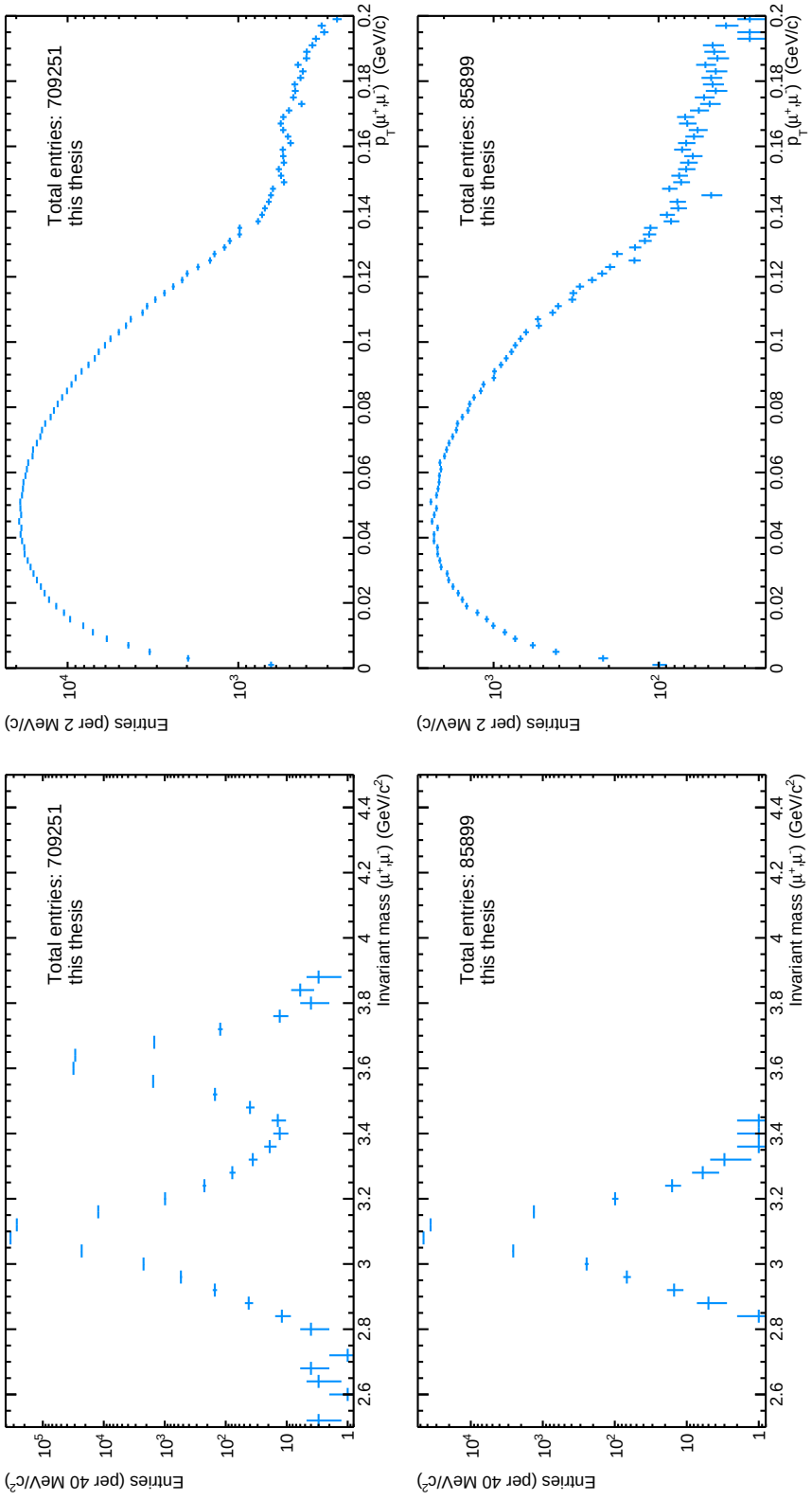

Figure 2.5: Monte Carlo: Invariant mass (left) and p_T (right) spectra before (top) and after (bottom) applying the selection criteria mentioned in Sec. 2.4.1.

Table 2.2: Definition of p_{T}^2 intervals and their connection to the bin numbering.

p_{T}^2 interval (GeV^2/c^2)	bin numbering
$(0; 0.00072)$	1
$(0.00072; 0.0016)$	2
$(0.0016; 0.0026)$	3
$(0.0026; 0.004)$	4
$(0.004; 0.0062)$	5
$(0.0062; 0.012)$	6

2.4.4 p_{T}^2 intervals decision

The analysis presented in this thesis is split in six p_{T}^2 intervals, which can be found in Tab. 2.2. The decision on the size of the p_{T}^2 intervals and the number of bins is described in Sec. 5.5.1.

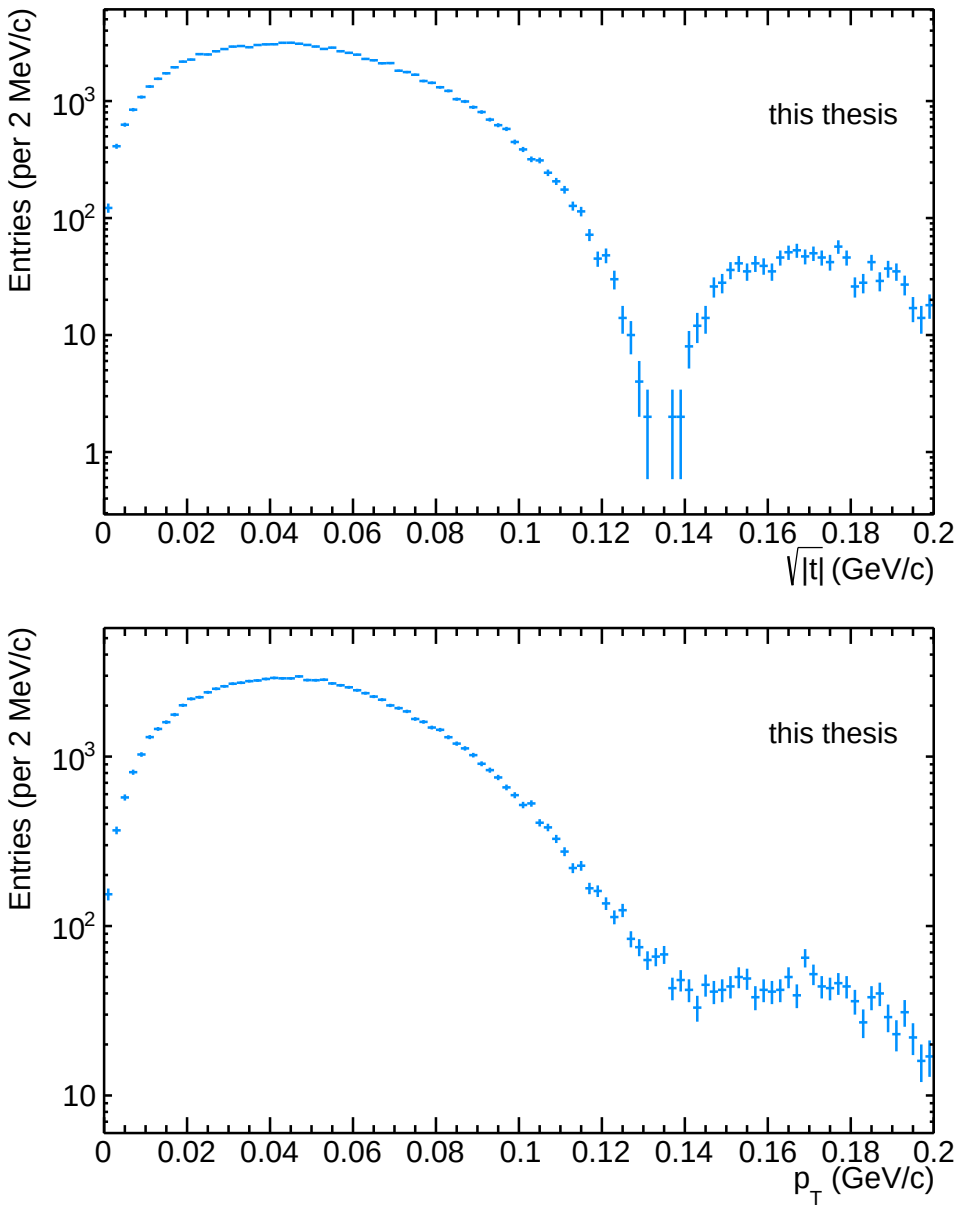

Figure 2.6: (Top panel) The p_{T} spectrum of pomeron as predicted by STARlight [42]. The pomeron p_{T} directly corresponds to the transferred momentum $|t|$ of the target nucleus and together with the photon momentum coming from the other nucleus creates the p_{T} of J/ψ. (Bottom panel) The p_{T} spectrum of J/ψ as calculated by STARlight.

Chapter 3

Luminosity

The world has seen many different physics experiments which are looking for answers to physics questions. They observe a certain process and quantify what they see. The credibility of modern science is based on the reproducibility of the process and the more independent observations are made, the smaller is the chance of a mistake. Current experiments deliver the observed processes using particle accelerators, whose frame-independent parameter describing the ability to repeat the experiment is called luminosity.

The instantaneous (or relative) luminosity [84, 85] is defined as

$$\mathcal{L}_{\text{inst}} = \frac{R_{\text{evts}}}{\sigma_{\text{proc}}}, \tag{3.1}$$

where σ_{proc} is the cross section of the process and R_{evts} the event rate. To express the absolute luminosity $\mathcal{L}_{\text{abs}}$ [86], the event rate is turned into the number of the events N_{evt} per time t and the correction for the efficiency of detected events $(\text{Acc} \times \epsilon)_{\text{evts}}$ is added to the yield

$$\mathcal{L}_{\text{abs}} = \frac{\mathrm{d}N_{\text{evts}}}{\mathrm{d}t} \frac{(\text{Acc} \times \epsilon)_{\text{evts}}}{\sigma_{\text{proc}}}. \tag{3.2}$$

Integrating $\mathcal{L}_{\text{abs}}$ over time one can obtain the integrated luminosity $\mathcal{L}_{\text{int}}$, which is a fundamental input for the measurement of cross sections.

3.1 Determination of the recorded luminosity

To understand the calculation of the recorded-data luminosity, the ALICE trigger system [87] has to be described. The main part of the system is the Central Trigger Processor (CTP), which receives signals (input) from triggering detectors, makes a decision and sends a signal to readout detectors. There are 4 levels of decisions, called LM, L0, L1 and L2. The application of each of them depends on the speed of propagation of the signal from the triggering detectors to the CTP. Each level has two sets of counters. First, the CTP counts the number of events, LXB, satisfying logical combinations

of trigger inputs in a predefined subset of bunch crossings (BC-mask). Then an electronic veto is applied and results are stored as LXA. Note, that A(B) stands for after(before) veto and X for the level of decision. The veto is issued mainly due to busy detectors or downscaling, which is an artificial stochastic prohibition to enforce a predefined readout bandwidth distribution for processes of the ALICE physics programme.

3.1.1 Reference luminosity

Equation (3.1) tells that in addition to the trigger counts the cross section of the process is also needed. Usually, this is not known and often it is the target of the measurement. Hence, a reference to a known process with a known cross section is needed. The analysis described in this thesis used V0-based trigger conditions (called V0M) which select ∼50% most central hadronic events. The reference luminosity $\mathcal{L}_{\text{ref}}$ is then calculated as

$$\mathcal{L}_{\text{ref}} = \frac{L_{\text{0B}}^{\text{V0M, corrected}}}{\sigma^{\text{V0M}}} \, \text{corr}_{\text{pile-up}}^{\text{V0M}}, \tag{3.3}$$

where $L_{\text{0B}}^{\text{V0M, corrected}}$ are corrected V0M trigger counts before the CTP veto, σ^{V0M} is an experimentally measured reference cross section and $\text{corr}_{\text{pile-up}}^{\text{V0M}}$ is a correction for possible pile-up of interactions in one recorded event. In Eq. (3.4), the V0M trigger counts are corrected for background ($\text{corr}_{\text{background}}^{\text{V0M}}$) and satellite ($\text{corr}_{\text{satellites}}^{\text{V0M}}$) events.

$$L_{\text{0B}}^{\text{V0M, corrected}} = L_{\text{0B}}^{\text{V0M}} \, \text{corr}_{\text{background}}^{\text{V0M}} \, \text{corr}_{\text{satellites}}^{\text{V0M}}. \tag{3.4}$$

Pile-up correction

The distribution of pile-up events follows the Poisson distribution [88]. The correction (Eq. 3.5) is calculated as the probability of having at least one trigger in a bunch crossing.

$$\text{corr}_{\text{pile-up}}^{\text{V0M}} = \frac{\mu_{\text{V0M}}}{1 - \exp(-\mu_{\text{V0M}})}. \tag{3.5}$$

The average number of visible collisions per bunch crossing, μ_{V0M}, is calculated as

$$\mu_{\text{V0M}} = -\ln\left(1 - \frac{L_{\text{0B}}^{\text{V0M, corrected}}}{N_{\text{bcs}}}\right), \tag{3.6}$$

where N_{bcs} is the total number of beam-beam bunch crossings over the whole data taking.

Background correction

The reference V0M trigger counts may be polluted by random noise or interactions of the beam with residual gas in the interaction area (IA).

Control triggers were setup for bunch-crossing time windows, where no beam was present in the IA (designated as E mask; empty bunch crossing) or only one beam coming from A- or C-side was present in the IA (A/C mask; anticlockwise/clockwise side). The probability of such an event is calculated using the corresponding $L_{0B}^{\text{X mask}}$ counts and $N_{bcs}^{\text{X mask}}$ mask bunch crossings as

$$\text{corr}_{\text{background}}^{\text{class}} = 1 - \left(\frac{L_{0B}^{\text{A mask}}}{N_{bcs}^{\text{A mask}}} + \frac{L_{0B}^{\text{C mask}}}{N_{bcs}^{\text{C mask}}} - \frac{L_{0B}^{\text{E mask}}}{N_{bcs}^{\text{E mask}}} \right) / \frac{L_{0B}^{\text{B mask}}}{N_{bcs}^{\text{B mask}}}. \quad (3.7)$$

The negative sign of the random noise probability term shows up because this term has to be extracted from the beam-gas terms as well. Equation (3.7) shows the simplest possible notation of such case.

Satellite subtraction

The particle beam at the LHC is made of bunches, each containing tens of millions lead ions [2]. These bunches are distributed into 25 ns large time windows along the diameter of the LHC that provides a collision rate up to 40 MHz. Each bunch is accelerated in superconducting radio-frequency (RF) electromagnetic cavities [89] with a frequency of 400 MHz, forming an electromagnetic wave with 2.5 ns between two amplitudes. Ideally, the bunch is dragged with only one of these waves, but when the bunch is not longitudinally focused enough, the late or early particles are caught by adjacent waves and are torn out of the main bunch, forming so-called satellite bunches.

The reference cross section measurement is done with events from collisions of two main bunches. Therefore, the trigger counts have to be corrected for events from main-satellite or satellite-satellite collisions. The fraction of these events can be estimated using timing information in the ZDC detectors, as shown in Fig. 3.1. ZDC, in particular the ZNA and ZNC hodoscopes, measure neutrons from V0M triggered events. Those arriving in the $(-2.5, 2.5)$ ns time interval are tagged as coming from collisions of main bunches, others are tagged as satellite events. The ratio of the amounts of these two cases is taken as the correction.

Van der Meer scan

The luminosity $\mathcal{L}_{\text{head-on}}$ for head-on collisions can be determined as

$$\mathcal{L}_{\text{head-on}} = \frac{N_1 \; N_2 \; \nu}{h_x \; h_y}, \quad (3.8)$$

where $N_{1,2}$ are beam intensities, ν is the frequency of beam circulation and $h_{x,y}$ are effective widths of the beam overlap regions in x- and y-directions defining the transverse plane. The overlap region is measured using a technique called the van der Meer scan [91–93]. In these scans, the beams are moved across

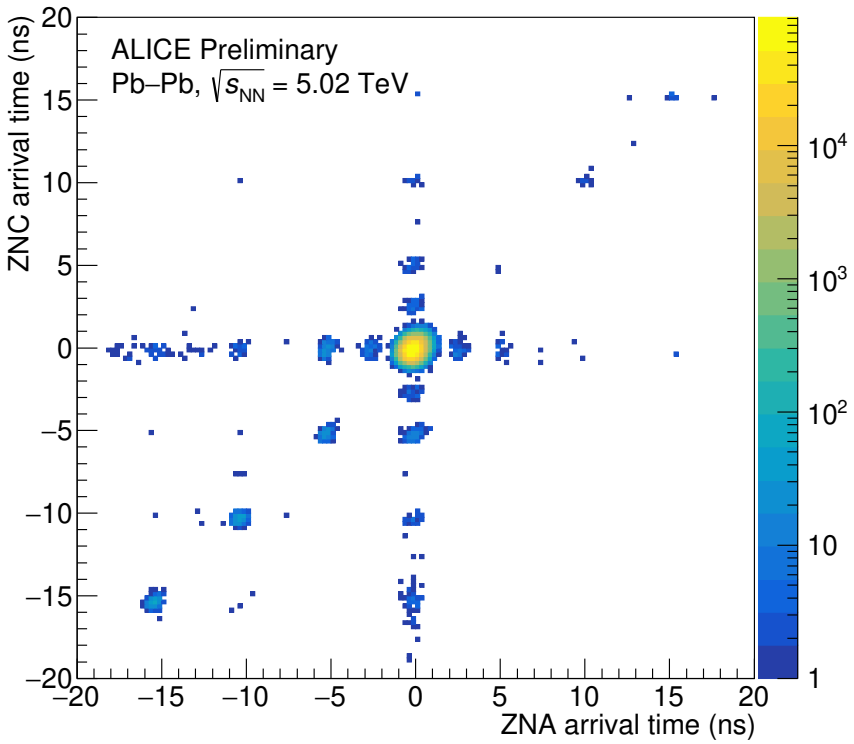

Figure 3.1: Arrival times of neutrons in ZDC located on A/C-side (ZNA/C) of the experiment. Taken from Ref. [90].

each other in the x- and y- directions separately, while the beams remain head-on in the non-scanned direction, and the rate of a reference process (V0M in the case of this thesis) is being recorded resulting in two rates curves $R(\Delta x, 0), R(0, \Delta y)$. The $h_{x,y}$ can then be determined as the area under the corresponding rate curve divided by the head-on rate, $R(0, 0)$. From the knowledge of the head-on rate and the $\mathcal{L}_{\text{head-on}}$, the σ^{V0M} of Eq. 3.3 can be estimated as

$$\sigma^{\text{V0M}} = \frac{R(0,0)}{\mathcal{L}_{\text{head-on}}}. \tag{3.9}$$

The measurement of the V0M reference cross section in Pb–Pb collisions is published in [90] and the contribution of the author of this thesis to this paper is mentioned in Sec. 3.3.

3.1.2 Trigger classes

A well-arranged organisation of the trigger signals is crucial for handling these data. Objects, which group readout detectors, are called *clusters*. These have various names and due to hardware conditions we can have only 6 of them

per run. Other objects called *classes* group trigger information like descriptor (logical combination of trigger inputs), BC-mask or cluster name. Each class contains information about L_{XY} counters, which is used for the luminosity calculation.

$$\mathcal{L}_{\mathrm{class}} = \mathcal{L}_{\mathrm{ref}}\ LT_{\mathrm{class}}. \tag{3.10}$$

Equation 3.10 shows the formula that is used for the calculation of luminosity of a given trigger class. The reference cross section $\mathcal{L}_{\mathrm{ref}}$ is calculated according to Eq. 3.3 and LT_{class} is the live-time of the trigger class. The live-time is defined as the fraction of the total time when the cluster corresponding to the trigger class is ready to readout data (and do so). This is calculated via the L_{XY} counters as

$$LT = \prod_{\mathrm{X=M,0,1,2}} \frac{L_{\mathrm{XA}}}{L_{\mathrm{XB}}}, \tag{3.11}$$

where the product is used to reflect the fact that the classes can obtain the CTP decision at different levels. The connection between the reference cross section and the actual trigger class cross section is visible by comparing Eq. 3.3 and Eq. 3.11, where L_{XB} counters of the reference trigger and the analysed trigger stand in a ratio.

The trigger counts can occasionally be spoiled by after-pulses in the trigger detectors and hence the live-time calculation of Eq. 3.11 can be inaccurate. The live-time of the trigger classes belonging to the same cluster are the same by definition. Therefore it is ideal to pick one cluster-representative trigger class, which is not affected by after-pulses, and use its trigger counts to obtain the live-time. In this case, the downscaling factors (DS) of both classes have to be taken into account as these in principle can be different. The live-time of the analysed classes is then computed as

$$LT_{\mathrm{class}} = LT_{\mathrm{cluster}}\ \frac{DS_{\mathrm{class}}}{DS_{\mathrm{cluster}}}. \tag{3.12}$$

3.2 Analysed luminosity

Despite the maximum effort of all ALICE teams involved in data reconstruction, this process is not fully effective. The road from recorded data to final sample used in an analysis is mentioned in Sec. 2.3. In order to estimate the luminosity of the analysed sample, the number of triggers of the sample is compared to actual number of triggers as recorded during the data taking. The ratio of these two numbers is taken as a scaling factor for the calculated recorded luminosity as explained in Sec. 3.1. Such analyses of the data sample of different periods used in this thesis are shown in Fig. 3.2 and Fig. 3.3. In this case, the total efficiency of the data availability is 94%.

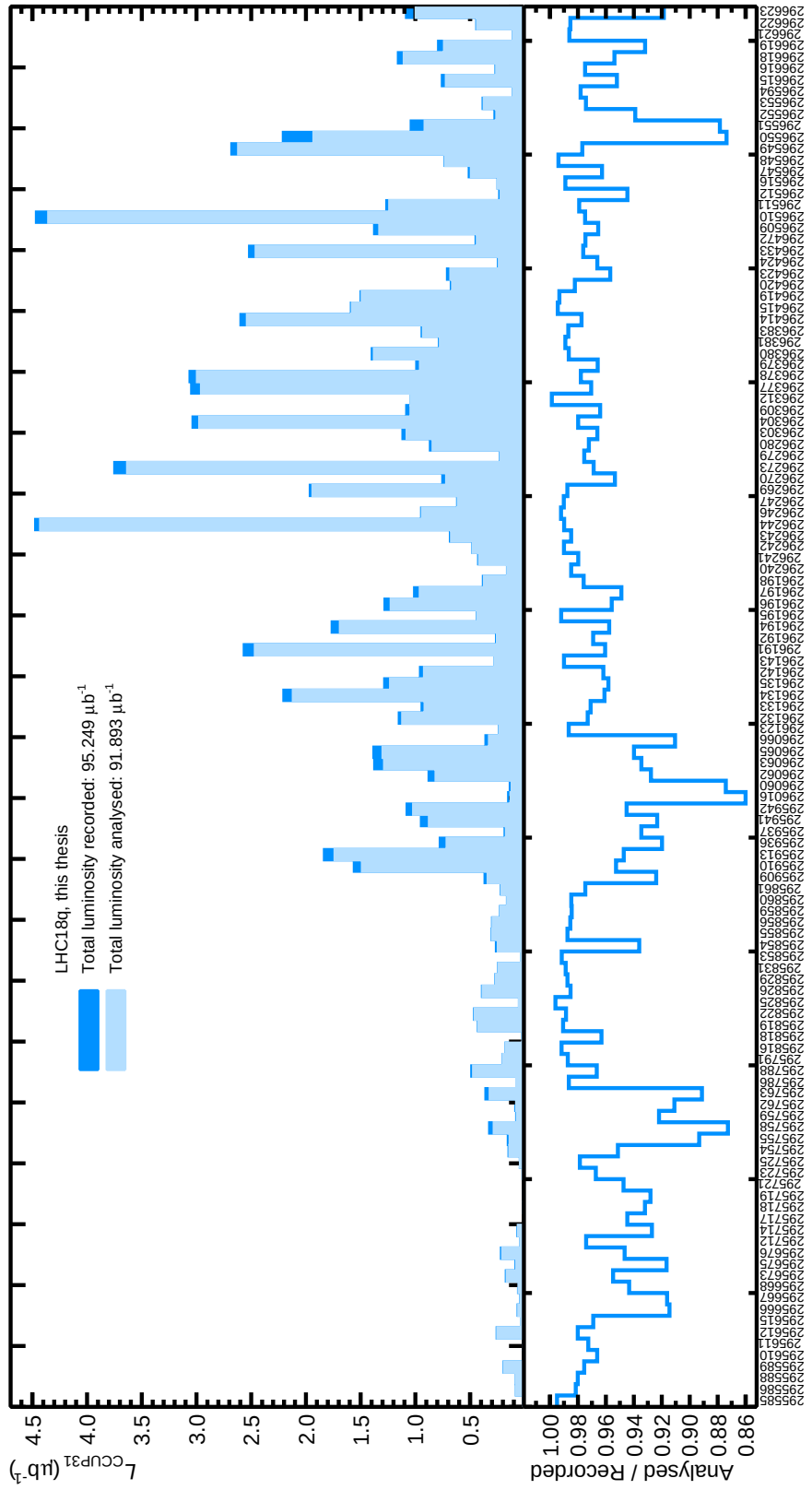

Figure 3.2: Analysed and recorded integrated luminosity of the CCUP31 trigger class per data taking run for the LHC18q period.

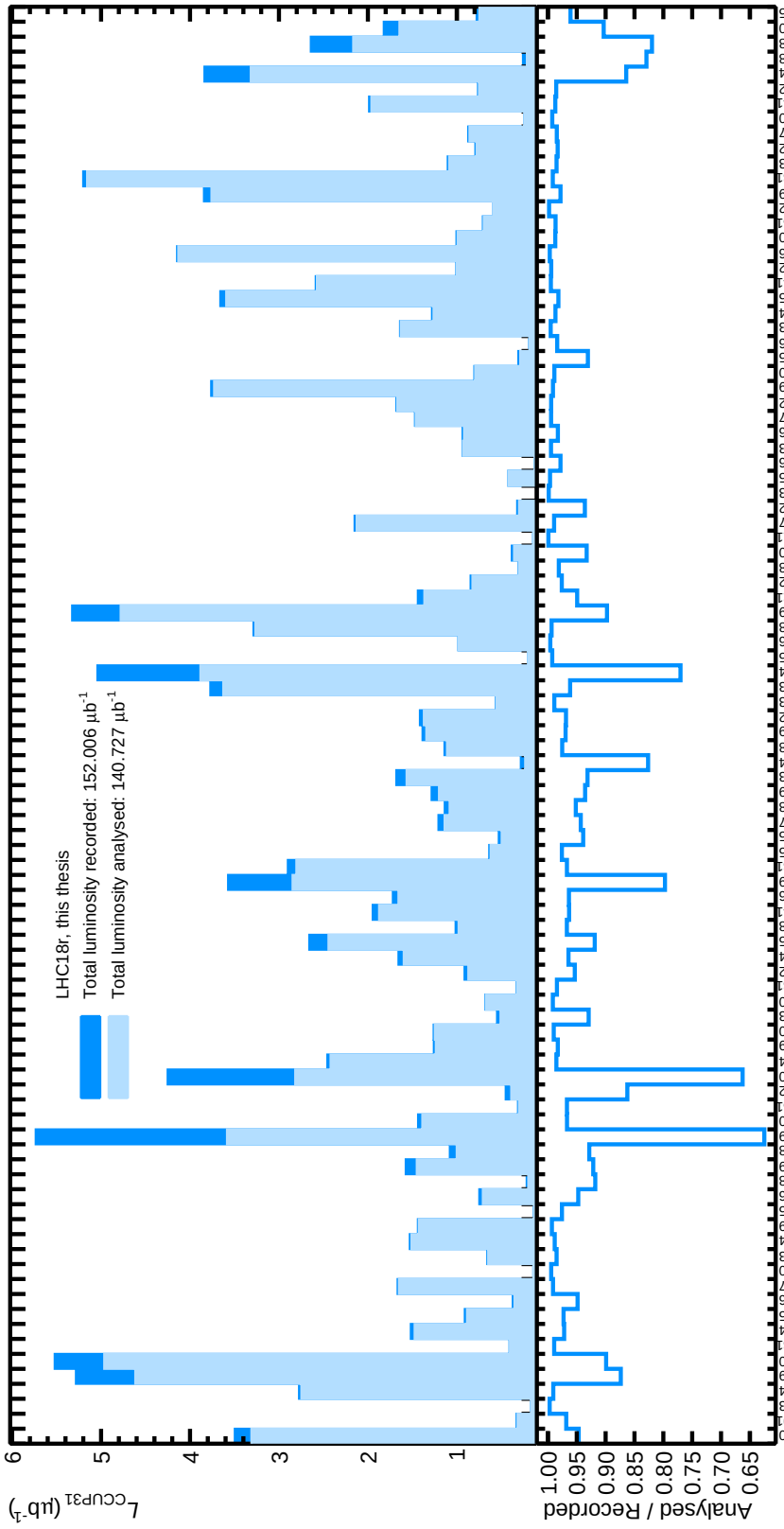

Figure 3.3: Analysed and recorded integrated luminosity of the CCUP31 trigger class per data taking run for the LHC18r period.

3.3 Stability of the visible-luminosity calculation

The reference cross section calculation is an implicit input to the luminosity calculation. The determination of this visible cross section is described in App. C or Ref. [90]. The contribution of the author of this thesis to this published work is described in the next lines.

The methodology of the reference cross section calculation using the van der Meer scan technique is explained in Sec. 3.1.1. The stability of the extrapolation of the van der Meer scans results to all other runs is investigated by measuring the visible cross section using two different trigger classes; V0M, which relies on the V0 calorimeters, and ZED[1], which utilises the ZDC detectors. Then, the visible luminosity can be calculated using Eq. 3.3.

The ratio of the V0M-based luminosity $\mathcal{L}_{\mathrm{V0M}}$ to the ZED-based luminosity $\mathcal{L}_{\mathrm{ZED}}$ was calculated for each run used for physics analyses. The time dependency of this ratio, for the period relevant for the studies presented in this thesis, is depicted in Fig. 3.4.

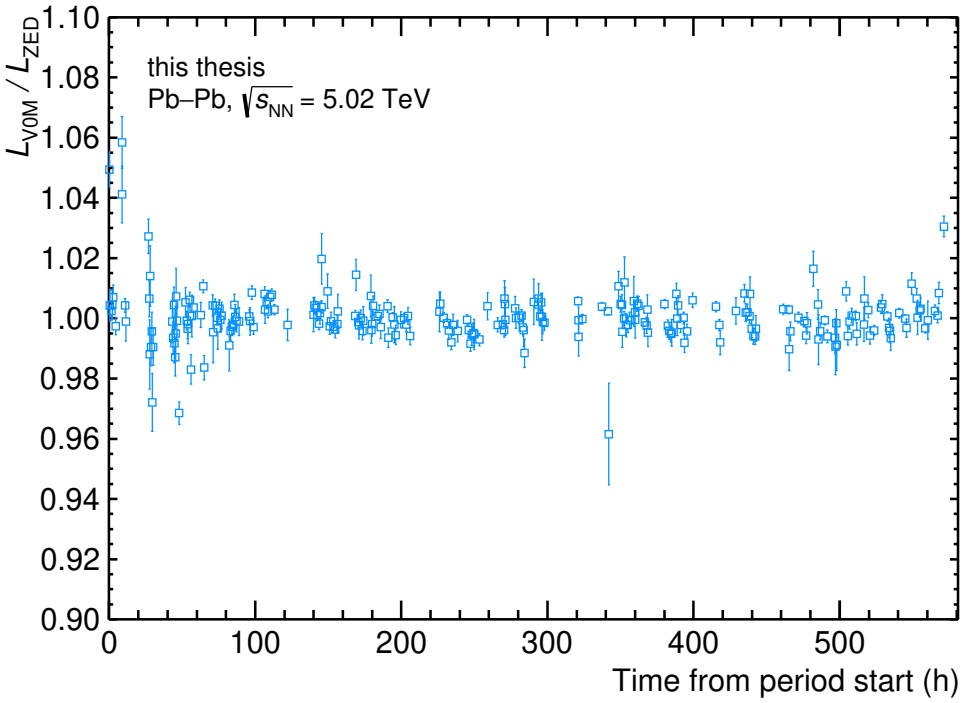

Figure 3.4: Luminosity ratios of V0M- to ZED-based calculations for the 2018 Pb–Pb data taking period as a function of time since the start of the period.

The ZED trigger is a so-called Level 1 trigger, which means that the decision in the CTP is made after the short time that the machinery needs to receive the trigger signal from the triggering detector. Hence, the $L_{\mathrm{0B}}^{\mathrm{ZED}}$

[1]ZED is defined as a signal in the ZNA or ZNC and originally it was designed to select the electromagnetic dissociation.

counters do not show reality as the CTP ignores this step for ZED. Instead, L_{1B}^{ZED} shows the actual number of events which may be triggered by the ZED trigger. Level 0 and Level 1 counters can differ due to the rejection of the event for other reasons. To calculate a Level 0-equivalent input to Eq. 3.3, the following equation is used:

$$L_{0B\text{ equivalent}}^{ZED} = L_{0B}^{ZED}\ \frac{L_{1B}^{ZED}}{L_{0A}^{ZED}}. \tag{3.13}$$

The uncertainty of $\mathcal{L}_{V0M}$ is estimated from the uncertainty of the measured cross section and the uncertainty of the trigger counts as dictated by the Poisson distribution, $\sigma_{L_{0B}}^{V0M} = \sqrt{L_{0B}^{V0M}}$. The $\mathcal{L}_{ZED}$ uncertainty is a bit more delicate in the sense that the trigger counts are obtained via Eq. 3.13. L_{0B}^{ZED} is typically a large number with respect to Level 1 counters and hence the statistical error origination from this number is neglected. Then, the uncertainty is treated following Binomial statistics [94] as

$$\sigma_{L_{0B\text{ equivalent}}}^{ZED} = L_{0B\text{ equivalent}}^{ZED}\ \frac{\sigma_{L_{1B}}^{ZED}}{L_{0A}^{ZED}} \Big/ \frac{L_{1B}^{ZED}}{L_{0A}^{ZED}}, \tag{3.14}$$

where

$$\sigma_{L_{1B}}^{ZED} = \sqrt{L_{0A}^{ZED}\ \frac{L_{1B}^{ZED}}{L_{0A}^{ZED}} \left(1 - \frac{L_{1B}^{ZED}}{L_{0A}^{ZED}}\right)}. \tag{3.15}$$

The variation of the luminosity ratios is calculated as the weighted mean quadratic difference from unity of the ratios distribution, where the calculated luminosity is taken as a weight for each run. This was estimated to be 0.5% in the 2018 data taking periods.

Chapter 4

Unfolding

This chapter contains a definition of the unfolding problematic and an outline of possible methods with their description. The expected $|t|$ distribution of this measurement is very peaked at values close to zero (See Fig. 4.1), which puts extra requirements on the methods themselves. In addition, the resolution of the central barrel detectors is not good enough to avoid large migrations in this measurement, making a bin-to-bin correction to the measurement unfeasible.

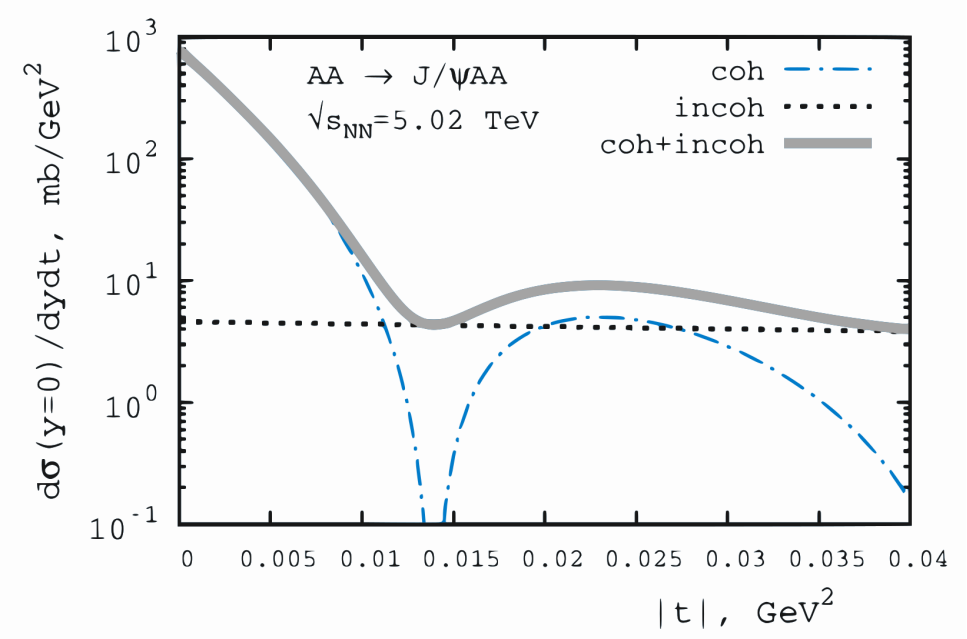

Figure 4.1: Example of a shape of a $|t|$ distribution. Taken from Ref. [95] (colours are modified).

4.1 Definition of the problem

The goal of every physics measurement is to revel the true behaviour of the process of interest. These measurements usually use detectors for this purpose. Every detector built up-to-now is imperfect in some of its attributes (volume acceptance, efficiency of detection, resolution...). Therefore every measurement smears the value to be measured. If the measurement is intended to be compared with theory or other experiments, these effects need to be corrected. This problem is in general defined in Eq. (4.1), where $f_{\text{meas}}(y)$ is a measured distribution, $f_{\text{true}}(x)$ is a true distribution and $R(x, y)$ is a response function containing all smearing effects.

$$f_{\text{meas}}(y) = \int R(x, y) f_{\text{true}}(x) dx. \tag{4.1}$$

Real measured spectra are not continuous, but discreet, in particle physics. Therefore,the problem can be rewritten to Eq. (4.2), where y is a measured vector, x is a truth vector and R is a response function in the form of a matrix.

$$y_i = R_{ij}\, x_j \quad \Longrightarrow \quad x_j = R^{-1}_{ji}\, y_i \tag{4.2}$$

Here, the solution of the problem can be depicted to a simple inversion of the response matrix.

4.1.1 Matrix inversion limitation

One of the important attributes is the resolution of the detector. When the resolution is better than a chosen binning, then the response matrix is diagonal, as shown for an example in Eq. (4.3) (inheriting notation from Eq. (4.2)).

$$\begin{gathered} \begin{pmatrix} 1 \\ 2 \\ 3 \end{pmatrix} = \begin{pmatrix} 0.8 & 0 & 0 \\ 0 & 1 & 0 \\ 0 & 0 & 0.9 \end{pmatrix} \cdot \begin{pmatrix} ? \\ ? \\ ? \end{pmatrix} \quad \Longrightarrow \\ \begin{pmatrix} 1.25 & 0 & 0 \\ 0 & 1 & 0 \\ 0 & 0 & 1.111 \end{pmatrix} \cdot \begin{pmatrix} 1 \\ 2 \\ 3 \end{pmatrix} = \begin{pmatrix} 1.25 \\ 2 \\ 3.333 \end{pmatrix} \end{gathered} \tag{4.3}$$

The inversion of a diagonal matrix is an easy task and generates a correct result. Unfortunately, the binning is usually more granular than the resolution in particle physics (which is also the case of the measurements presented in this thesis). This means that the detector does not always measure an event in a correct bin. This leads to a non-diagonal response matrix, as illustrated in Eq. (4.4), where calculated errors are added to stress out the problem (the errors correspond to standard deviations and the method of their calculation

can be found in [96]).

$$R = \begin{pmatrix} 0.5 & 0.3 & 0 \\ 0.3 & 0.4 & 0.3 \\ 0 & 0.4 & 0.5 \end{pmatrix} \implies \begin{pmatrix} -16 & 30 & -18 \\ 30 & -50 & 30 \\ -24 & 40 & -22 \end{pmatrix} \cdot \begin{pmatrix} 1 \\ 2 \\ 3 \end{pmatrix} = \begin{pmatrix} -10 \pm 293 \\ 20 \pm 382 \\ -10 \pm 338 \end{pmatrix} \tag{4.4}$$

Clearly, the mathematically correct operation returns physically incorrect and oscillating result with large variance. This situation gives rise to the development of several methods described in Sec. 4.2.

4.2 Unfolding methods

Several unfolding methods on how to deal with ill-posed problems have been developed [97]. In general, they modify the response matrix by introducing some bias into the process. Monte Carlo simulations are often use as a source of bias. The list of the methods is the following:

- Without regularisation:
  - Response matrix inversion [96],
  - Method of correction factors [96].
- With regularisation:
  - Direct regularisation (likelihood or χ^2 test) [98].
  - Singular Value Decomposition (SVD) [99].
- Iterative:
  - Bayes by D'Agostiny [100–102].

The difficulties with a simple matrix inversion were already mentioned before in Sec. 4.1.1. The method of correction factors is based on the calculation of each element of the inversed response matrix directly from the Monte Carlo simulation and therefore is strongly biased and not a good candidate for a scientific field. To find the best trade-off between bias and variance of the results is the goal. Other methods, which are described in the subsections below, were designed for this purpose.

This work uses two different tools for testing of the best unfolding method for the measurements in this thesis. The first one, TUnfold [103], is a C++ class in ROOT [80] which allows us to easily handle distributions and input/output parameters of the regularisation method. The second one, RooUnfold [104], is a tool wrapping few methods together with a friendly

interface. This tool is used to operate with the SVD method and the Bayes' method.

Monte Carlo simulations are used to retrieve the response matrix. Some of the methods (using regularisation) contain features that yield unrealistically optimistic results in case the response matrix is squared [105]. The literature recommends to use twice as much bins for the input measured MC distribution than for the input truth MC distribution. This rule is used in this study when it is needed.

4.2.1 Regularisation

To solve Eq. (4.2), the maximum log-likelihood or χ^2-minimisation methods [96] can be used. The standard χ^2 prescription reads

$$\chi^2 = (y - Rx)_i V_{ij}^{-1} (y - Rx)_j, \tag{4.5}$$

where V is the covariance matrix of the quantity y. As stated before, the inversion of this leads to large oscillations of the result due to its large variance. Therefore an additional term, called regularisation, is added. This term brings the bias which tames the oscillations and can have many variants [96]. The Tikhonov type regularisation [106] was chosen in this study as this one is implemented in the software package TUnfold. Then the χ^2 equation takes the form

$$\chi^2 = (y - Rx)_i V_{ij}^{-1} (y - Rx)_j + \tau^2 \|S \cdot x\|^2, \tag{4.6}$$

where τ is the strength of the regularisation and S is the regularisation function. The general definition of the Tikhonov regularisation function [106] is

$$S[f_{\text{true}}(x)] = -\int \left(\frac{d^k f_{\text{true}}(x)}{dx^k} \right)^2 dx, \tag{4.7}$$

which is a discrete derivative of k-th order. The first and the second order are tested in this work, which are the standard options of the TUnfold class [103],

$$k = 1 : S(x) = -\sum_{i=1}^{M-1} (x_i - x_{i+1})^2, \tag{4.8}$$

$$k = 2 : S(x) = -\sum_{i=1}^{M-2} (-x_i + 2x_{i+1} - x_{i+2})^2 \tag{4.9}$$

and are called derivative and curvature respectively.

The parameter τ represents the trade-off between bias and variance. To find its optimal value is a key task. TUnfold offers two approaches to find it: L-curve scan and Global correlation coefficient scan ($\overline{\rho}$ vs. $\log \tau$) [103]. In this analysis, the second approach is used, which computes a global correlation coefficient ρ_i for each bin using Eq. (4.10)

$$\rho_i = \sqrt{1 - \frac{1}{V_{ii} V_{ii}^{-1}}}, \tag{4.10}$$

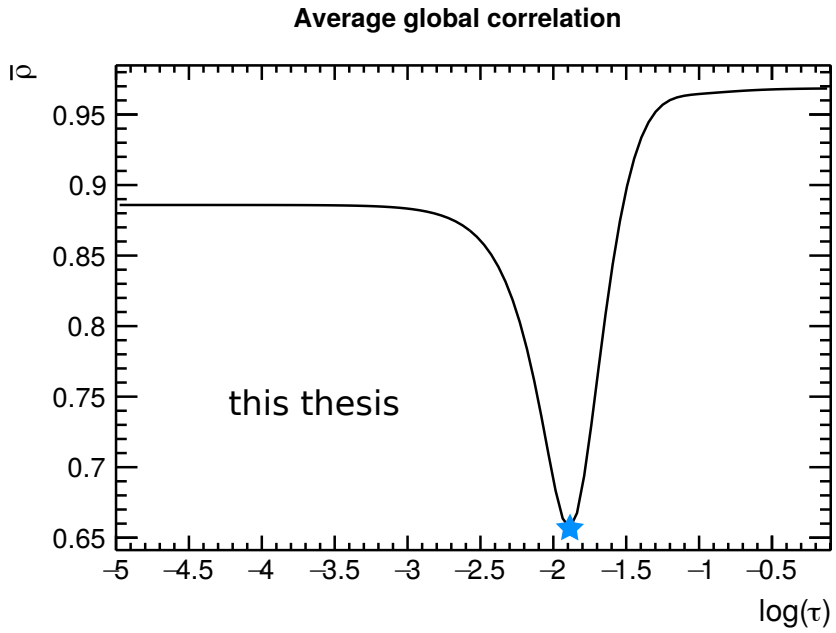

Figure 4.2: An example of a τ determination with Global correlation coefficient scan. The blue star indicates the best τ.

where $V_{ii}V_{ii}^{-1} = \sigma^2$ is the variance of the bin, and calculates an average over all bins. This is done for several τ values and plotted. The minimum of this graph points to the best τ. An example of this method is in Fig. 4.2.

4.2.2 Singular Value Decomposition

One of the methods, which is implemented in RooUnfold, is Singular Value Decomposition (SVD) [99]. This method inverts the m×n dimensional response matrix R by factorising it into the form

$$R = USV^{\mathsf{T}}, \tag{4.11}$$

where U is an m×m orthogonal matrix, V is an n×n orthogonal matrix and S is an m×n diagonal matrix with non-negative diagonal elements s_i [107]. These elements are called singular values of the response matrix R and the columns of U and V are called the left and right singular vectors. Inserting this into Eq. (4.2) (and swapping sides) produces the forms

$$USV^{\mathsf{T}} \times x = y, \tag{4.12}$$

$$S\underbrace{V^{\mathsf{T}} \times x}_{z} = \underbrace{U^{\mathsf{T}} \times y}_{d}. \tag{4.13}$$

Due to the orthogonality properties of the used matrices Eq. (4.12) is rewritten into a set of separate equations for each bin i as

$$s_i z_i = d_i \quad \Longrightarrow \quad z_i = \frac{d_i}{s_i}. \tag{4.14}$$

The variables z_i in Eq. (4.14) build the desired truth distribution. The whole process is more complex than shown in the last lines. For a more detailed description one can read [99]. For the purpose of this thesis it is important to know that

- binning should be chosen wisely as it can decrease variation,
- x and y in Eq. (4.12) need not to have the same binning,
- use test MC samples with the same statistics as data [107].

4.2.3 Based on Bayes' theorem

The last method mentioned here, proposed by D'Agostini, is a procedure based on the Bayes' theorem [100]. The Bayes' theorem is stated in Eq. (4.15) [108] and reads

$$P(\mathrm{A}|\mathrm{B}) = \frac{P(\mathrm{B}|\mathrm{A})P(\mathrm{A})}{P(\mathrm{B})}, \tag{4.15}$$

where A|B (B|A) is the conditional probability that event A (B) happened if event B (A) occurred and $P(\mathrm{A})$ ($P(\mathrm{B})$) is the standard likelihood of event A (B). This equation is then rewritten for the purpose of unfolding as

$$P(x_i|y_j) = \frac{P(y_i|x_j)P(x_j)}{\sum_l^{\text{n bins}} P(y_i|x_l)P(x_l)}, \tag{4.16}$$

where x_i is a truth event in bin i, y_j is a measured event in bin j and the rest follows the notation of Eq. (4.15). The left-sided conditional probability is basically an element of the inverted response matrix, because it represents the portion of events originally produced in bin i, but were measured in bin j. The right-sided conditional probability stands for the portion of events measured in bin i that were generated in bin j. These elements are known from MC and are usually called the response matrix, when they are put together. The last term, $P(x)$, is the portion of truth events in each bin. Here, information from MC generated events is taken as a first guess, but because this unfolding method is iterative and these terms are changing with each iteration, the first choice does not matter much. Actually, this procedure embodies great freedom in the first guess and a uniform distribution of initial probabilities is also a good start, according to tests, at the price of more iterations [100]. Luckily, this method needs only few iterations to converge in the case of this thesis, hence the influence of the choice of the initial distribution does not affect much the computational speed.

The unfolding method based on the Bayes' theorem is an iterative method. The steps are:

1. Choose first $P(x_j)$.
2. Do the Bayes estimation and get the number of true events.

$$n(x_j) = \sum_{l}^{\text{n bins}} n(y_l) P(x_j|y_l). \tag{4.17}$$

3. Do a χ^2 test.
4. If the convergence condition is not fulfilled, repeat with a new truth probability estimation

$$P(x_j) = \frac{n(x_j)}{\sum_{l}^{\text{n bins}} n(y_l)}. \tag{4.18}$$

The number of iterations represents the trade-off between bias and variance for this method. With increasing number of iterations, the influence of MC is lowered, but the variance of the results is growing. This situation is shown in Fig. 4.3. The choice of the optimal number with respect to all parameters of the measurement (errors, fit parameters...) is the intrinsic task.

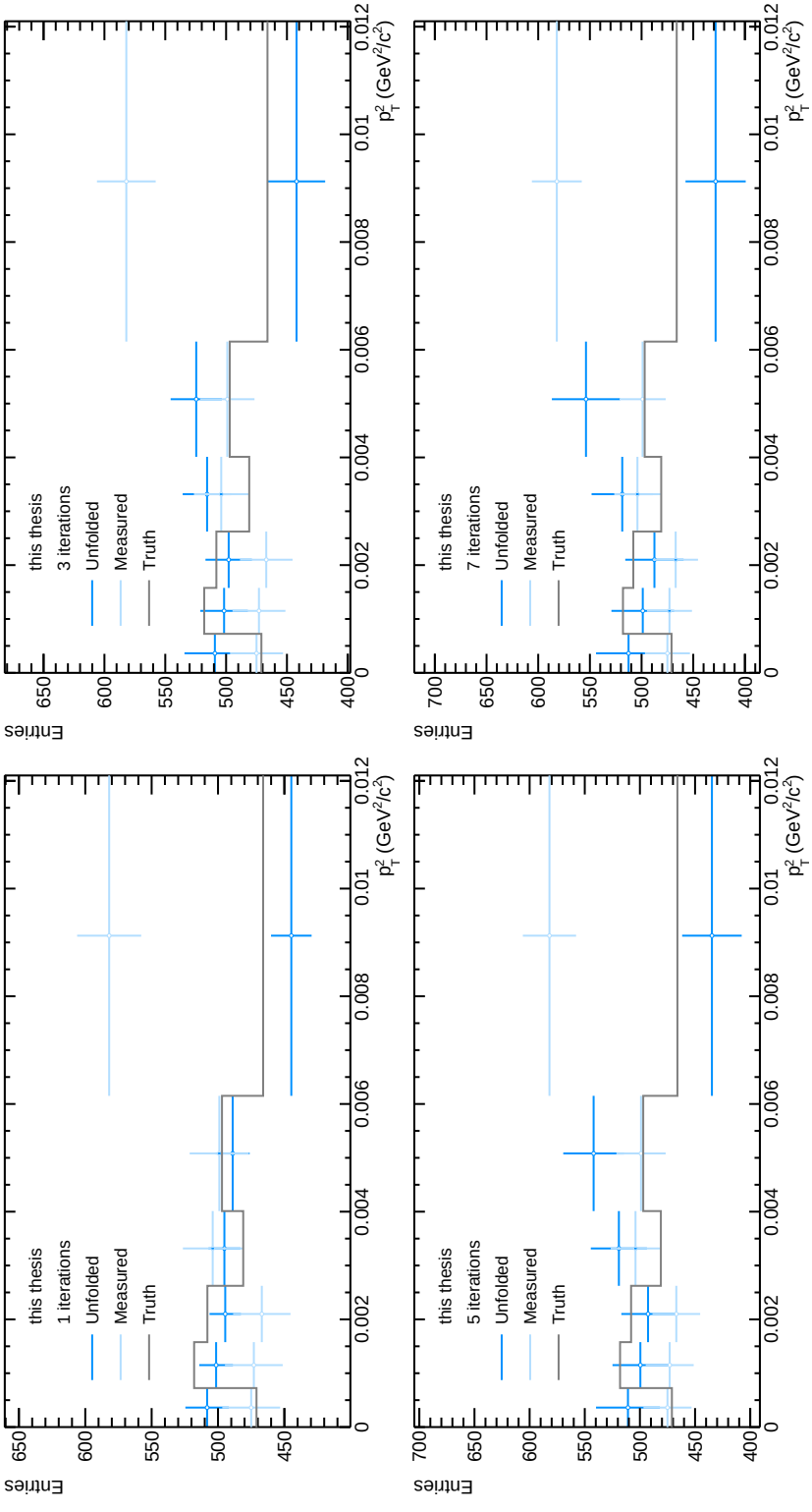

Figure 4.3: Example of results of Bayes unfolding for different number of iterations. A MC sample with an amount of events corresponding to the data sample analysed in this thesis.

Chapter 5

Measurement of the UPC cross section

A measure of the probability, that an interaction occurs when a probing projectile appears in the target's area, is called the cross section. Its unit is called barn [b], and corresponds to $10^{-28}\mathrm{m}^2$ and it is a classical physics joke originating in the early era of nuclear scattering experiments, when physicists were trying to hit a uranium nucleus with a neutron. The nucleus was "big as a barn" in comparison to a ball-size neutron [109]. The rate of balls successfully hitting the barn is the cross section.

In physics, the cross section serves as a connection between measurement and theory, as it can be clearly defined in the observation and all useful theories should be able to compute the occurrence of the predicted phenomenon. However, experiments are usually limited to a certain kinematic region and also the total cross section of the phenomenon does not reveals all physics. Therefore a differential cross section is quite often reported.

This work focuses on a measurement of the cross section differential in rapidity y and transferred momentum $|t|$. While the rapidity limitation originates in the capable-detectors coverage of the interaction products, the $|t|$ dependency has a physics essence. At ALICE, $|t|$ cannot be directly determined, hence the experimental differential cross section is determined through the p_{T}^2 dependency instead. The connection between $|t|$ and p_{T}^2 is described in Sec. 5.5.2.

All ingredients needed to compute the differential cross section together read

$$\frac{\mathrm{d}^2\sigma_{\mathrm{J}/\psi}^{\mathrm{coh}}}{\mathrm{d}y\mathrm{d}p_{\mathrm{T}}^2} = \frac{{}^{\mathrm{unf}}_{\mathrm{axe}}N_{\mathrm{J}/\psi}^{\mathrm{coh}}}{\epsilon^{\mathrm{VETO}}\ \epsilon^{\mathrm{EMD}}\ \mathrm{BR}_{\mathrm{J}/\psi\to\mu^+\mu^-}\ \mathcal{L}_{\mathrm{int}}\ \Delta\mathrm{p}_{\mathrm{T}}^2\ \Delta\mathrm{y}}, \tag{5.1}$$

where the correction factors ϵ^{VETO} and ϵ^{EMD} are introduced in Secs. 5.4.2 and 5.4.3, $\mathrm{BR}_{\mathrm{J}/\psi\to\mu^+\mu^-}$ is the branching ratio taken from Ref. [19], $\mathcal{L}_{\mathrm{int}}$ is the total integrated luminosity of the data sample calculated following the information from Chapter 3, and Δp_{T}^2 and Δy are the sizes of the kinematic interval where the measurements were performed. The ${}^{\mathrm{unf}}_{\mathrm{axe}}N_{\mathrm{J}/\psi}^{\mathrm{coh}}$ is the number

of coherent J/ψ candidates after unfolding the results given by

$$ {}_{\text{axe}}N^{\text{coh}}_{\text{J}/\psi} = \frac{N^{\text{coh}}_{\text{J}/\psi}}{(\text{Acc} \times \epsilon)^{\text{coh}}_{\text{J}/\psi}}. \tag{5.2} $$

The number of coherent J/ψ candidates $N^{\text{coh}}_{\text{J}/\psi}$ is obtained according to methodology described in Sec. 5.1. This number is corrected by an acceptance times efficiency $(\text{Acc} \times \epsilon)^{\text{coh}}_{\text{J}/\psi}$ factor (see Sec. 5.4.1).

5.1 Sample contamination

The goal of this thesis is to measure the cross section of coherent J/ψ production, which embodies a certain diffraction pattern in the p^2_{T} spectrum. There are other processes, which produce a similar signal in the detector and cannot be distinguished from the signal of our interest.

The first is the production of incoherent J/ψ, where the projectile does not interact with the whole target and therefore its complete structure is not probed in the transverse plane (and the diffraction pattern in p^2_{T} spectrum is not visible, see Fig. 5.1). These events are first rejected with the selection criterion on $p^{\mu\mu}_{\text{T}}$ to be smaller than 0.11 GeV/c. However, about 5% of all incoherent events appear also in this p_{T} region. The correction on the rest of the events is done with Monte Carlo simulations anchored to measured data and the method is described in Sec. 5.3.1.

The second process contaminating the sample is the decay of ψ' to J/ψ plus anything, where the 'anything' is not detected for some reason. The J/ψ then decays in the same way as the coherently produced J/ψ. The correction on these events is also done with Monte Carlo simulations anchored to the measured data and the method is described in Sec. 5.2.1.

The existence of incoherent events N^{inc} and feed-down events $N^{\text{feed down}}$ alongside the coherent events N^{coh} can be expressed in one equation as

$$ N^{\text{measured}} = N^{\text{coh}} + N^{\text{inc}} + N^{\text{feed down}}, \tag{5.3} $$

where N^{measured} is the number of measured events. The feed-down stands for the decay of ψ' into J/ψ + anything. In terms of N^{coh}, both can be written as

$$ N^{\text{inc}} = f_{\text{I}}\, N^{\text{coh}}; \quad N^{\text{feed down}} = f^{\text{neutrals}}_{\text{D}}\, N^{\text{coh}} + f^{\text{charged}}_{\text{D}}\, N^{\text{coh}}, \tag{5.4} $$

where $f_{I,D}$ are the fractions of the unwanted contributions. Here, f_{D} is split into events, where the J/ψ is accompanied by neutral particles, which have low p_{T} and are undetectable by ALICE, and the events where the J/ψ is accompanied by two pions with opposite charge. The second can also be undetected by ALICE and therefore mimic the coherent J/ψ production.

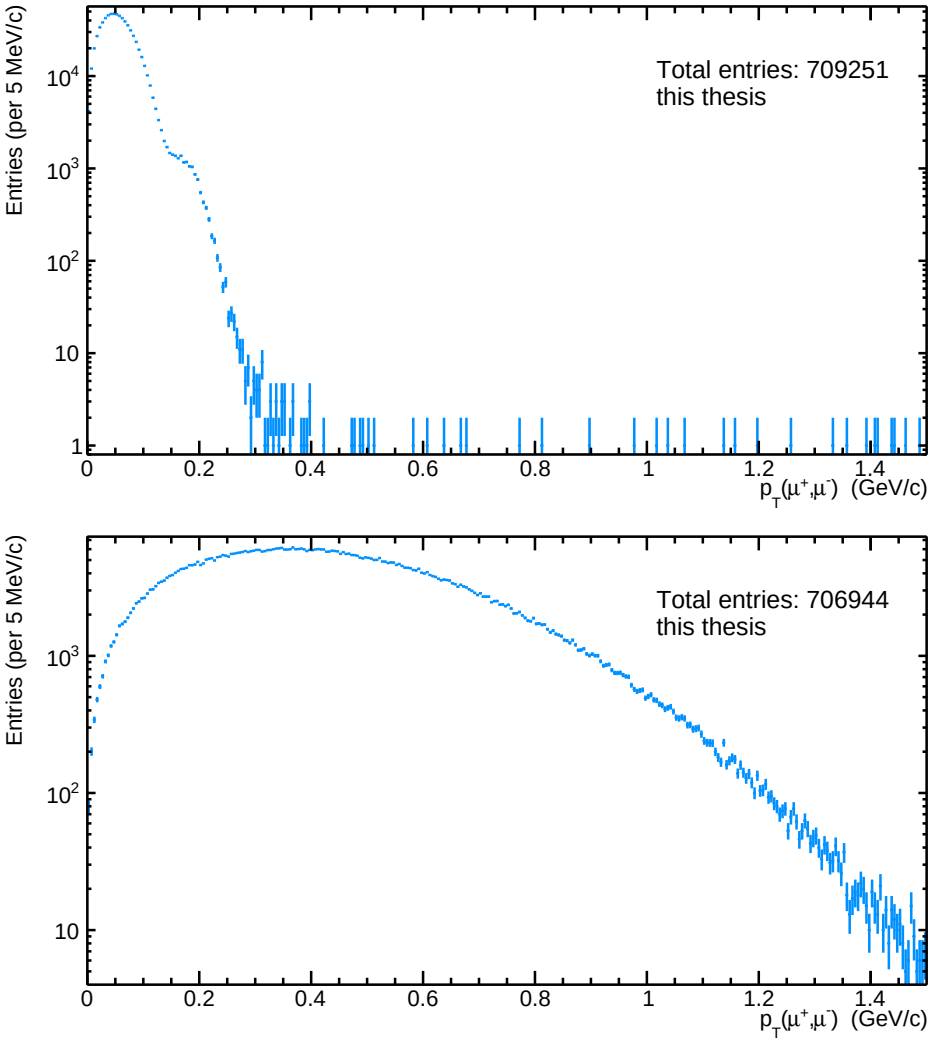

Figure 5.1: Example of p_{T} spectra for coherent (top panel) and incoherent (bottom panel) J/ψ production from the generated MC sample. The occurrence of a diffraction pattern is clear in the upper panel.

A simple rearrangement

$$N^{\mathrm{measured}} = N^{\mathrm{coh}}(1 + f_{\mathrm{I}} + f_{\mathrm{D}}^{\mathrm{neutrals}} + f_{\mathrm{D}}^{\mathrm{charged}}) \tag{5.5}$$

leads to

$$N_{\mathrm{J}/\psi}^{\mathrm{coh}} = \frac{N^{\mathrm{measured}}}{1 + f_{\mathrm{I}} + f_{\mathrm{D}}^{\mathrm{neutrals}} + f_{\mathrm{D}}^{\mathrm{charged}}}, \tag{5.6}$$

which is put into Eq. (5.2). N^{measured} from Eq. (5.6) is the yield of coherent J/ψ candidates as obtained from the invariant mass fit described in Sec. 5.2.

5.2 Invariant mass spectrum

The method of signal extraction chosen in this thesis is an extended maximum likelihood fit of the un-binned invariant mass spectrum. The model used to fit data consists of three templates. One Crystal-Ball function [110] (CB) is used to describe the J/ψ peak in the mass range (3.0,3.2) GeV/c^2, a second Crystal-Ball function is used to describe the ψ' peak in the mass range (3.6,3.8) GeV/c^2 and an exponential function is used to describe the continuum background.

The exponential function parameters were left free. An integral of this exponential in the mass ranges of the resonances is used to determine the number of background events.

The CB parameters, α and n, describing the tails of the distributions are estimated from a fit to the invariant mass of the associated Monte Carlo simulation and are fixed when the data sample is fit. The other parameters are left free.

Results of the fit of the data sample selected according to criteria from Sec. 2.4.3 are shown in Fig. 5.2. It was found that the background corresponds to 20% of the data sample in the region of the J/ψ invariant-mass peak. The last line of Tab. 2.1 shows the amount of sample events in this region. Taking away the background, one would get a result which corresponds to a simple bin-counting method. The result of 2 884 J/ψ candidates is compatible with the fit within fit uncertainties.

To obtain the number of J/ψ particles in each p_{T}^2 interval, all events which survived the selection criteria until the $p_{\mathrm{T}}^{\mu\mu}$ cut (No. of selected events in Tab. 2.1) are taken and are split accordingly. Each p_{T}^2-interval is fit separately and the corresponding figures can be found in Appendix A.

5.2.1 Feed-down contamination

The feed-down contribution to the yield is calculated from the fits of ψ' and J/ψ of the invariant mass spectrum. In general, the feed-down fraction is

$$f_{\mathrm{D}} = \frac{N_{\psi'\to \mathrm{J}/\psi}}{N_{\mathrm{J}/\psi}} = \frac{\sigma_{\psi'}}{\sigma_{\mathrm{J}/\psi}} \times \frac{(\mathrm{Acc}\times\epsilon)_{\psi'\to \mathrm{J}/\psi}}{(\mathrm{Acc}\times\epsilon)_{\mathrm{J}/\psi}} \times \frac{\mathrm{BR}_{\psi'\to \mathrm{J}/\psi+\mathrm{pions}}\ \mathrm{BR}_{\mathrm{J}/\psi\to\mu^+\mu^-}}{\mathrm{BR}_{\mathrm{J}/\psi\to\mu^+\mu^-}} \times \frac{\mathcal{L}}{\mathcal{L}}. \tag{5.7}$$

Cancelling the equal terms a general term

$$f_{\mathrm{D}} = \frac{\sigma_{\psi'}}{\sigma_{\mathrm{J}/\psi}} \times \frac{(\mathrm{Acc}\times\epsilon)_{\psi'\to \mathrm{J}/\psi}}{(\mathrm{Acc}\times\epsilon)_{\mathrm{J}/\psi}}\ \mathrm{BR}_{\psi'\to \mathrm{J}/\psi+\mathrm{pions}} \tag{5.8}$$

is obtained. Both Acc $\times\ \epsilon$ are taken from dedicated Monte Carlo simulations and the ratio $\sigma_{\psi'}/\sigma_{\mathrm{J}/\psi}$ is calculated from the ψ' and J/ψ yields of the fits of

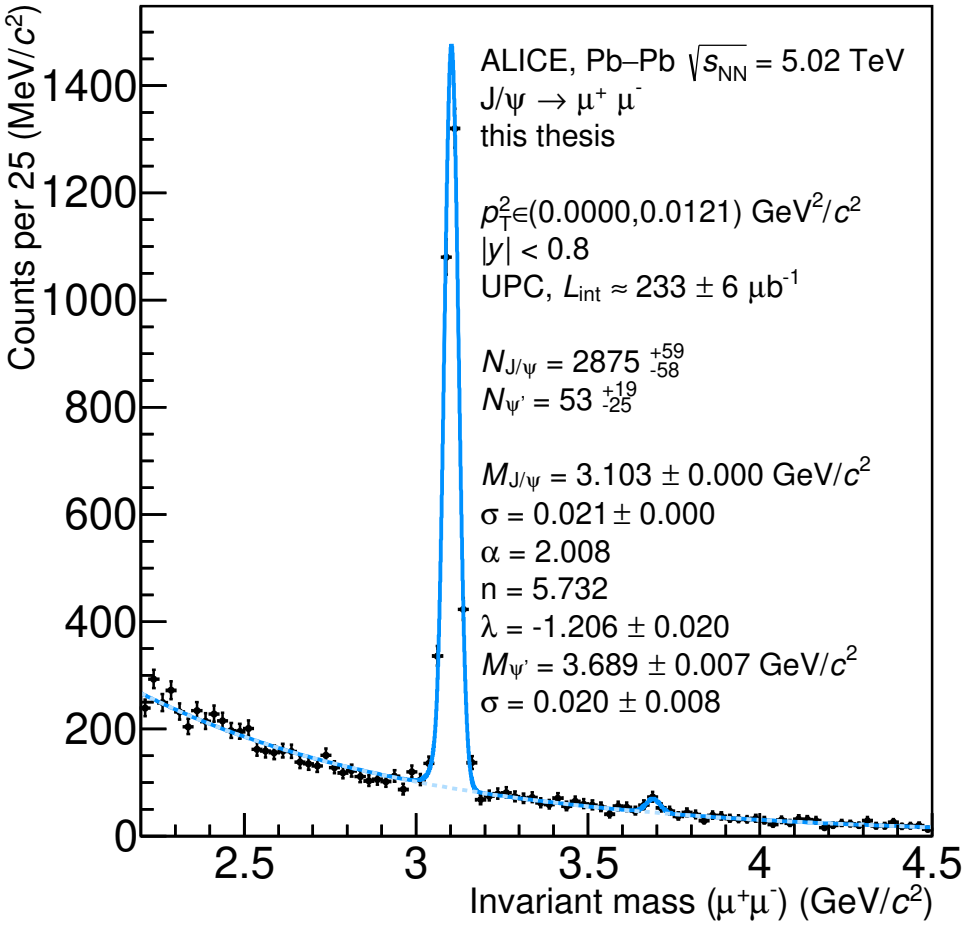

Figure 5.2: Invariant mass spectrum of data after selections from Sec. 2.4.3. The model, which fits the data, is marked with the full line (*blue colour*). The dashed line (*light blue colour*) marks the exponential background.

the invariant mass spectrum. The ratio of these yields, $R_{\mathrm{N}} = N^{\mathrm{yield}}_{\psi'}/N^{\mathrm{yield}}_{\mathrm{J}/\psi}$, can be expressed in other way as

$$R_{\mathrm{N}} = \frac{N_{\psi'\to\mu^+\mu^-}}{N_{\mathrm{J}/\psi\to\mu^+\mu^-} + N_{\psi'\to\mathrm{J}/\psi\to\mu^+\mu^-}}, \tag{5.9}$$

$$\begin{aligned} N_{\psi'\to\mu^+\mu^-} &= \sigma_{\psi'}\ (\mathrm{Acc}\times\epsilon)_{\psi'\to\mu^+\mu^-}\ \mathrm{BR}_{\psi'\to\mu^+\mu^-}, \\ N_{\mathrm{J}/\psi\to\mu^+\mu^-} &= \sigma_{\mathrm{J}/\psi}\ (\mathrm{Acc}\times\epsilon)_{\mathrm{J}/\psi\to\mu^+\mu^-}\ \mathrm{BR}_{\mathrm{J}/\psi\to\mu^+\mu^-}, \\ N_{\psi'\to\mathrm{J}/\psi\to\mu^+\mu^-} &= \sigma_{\psi'}\ (\mathrm{Acc}\times\epsilon)_{\psi'\to\mathrm{J}/\psi}\ \mathrm{BR}_{\psi'\to\mathrm{J}/\psi}\ \mathrm{BR}_{\mathrm{J}/\psi\to\mu^+\mu^-}. \end{aligned}$$

Reorganizing the equations above the ratio $\sigma_{\psi'}/\sigma_{\mathrm{J}/\psi}$ is obtained as

$$\frac{\sigma_{\psi'}}{\sigma_{\mathrm{J}/\psi}} = \frac{R_{\mathrm{N}}\ (\mathrm{Acc}\times\epsilon)_{\mathrm{J}/\psi\to\mu^+\mu^-}\ \mathrm{BR}_{\mathrm{J}/\psi\to\mu^+\mu^-}}{D_1 - D_2}, \tag{5.10}$$

$$\begin{aligned} D_1 &= (\mathrm{Acc}\times\epsilon)_{\psi'\to\mu^+\mu^-}\ \mathrm{BR}_{\psi'\to\mu^+\mu^-}, \\ D_2 &= R_{\mathrm{N}}\ (\mathrm{Acc}\times\epsilon)_{\psi'\to\mathrm{J}/\psi}\ \mathrm{BR}_{\psi'\to\mathrm{J}/\psi}\ \mathrm{BR}_{\mathrm{J}/\psi\to\mu^+\mu^-}. \end{aligned}$$

Bin dependent derivation

The scope of this study is the dependence of the cross section as a function of $|t|$. Therefore, Eq. 5.8 has to be modified to reflect the different yield of events in different bins. The bins are correlated. This is treated with unfolding after the yield is corrected for unwanted events. That means, no attention on it is needed here.

The Acc $\times\, \epsilon$ in each bin can be simply taken as

$$ {}^{\text{ibin}}(\text{Acc} \times \epsilon) = \frac{{}^{\text{ibin}}_{\text{rec}}\text{N}}{{}^{\text{ibin}}_{\text{gen}}\text{N}}, \tag{5.11} $$

where the index rec stands for reconstructed events and the index gen represents generated particles. In this analysis, the events are selected according to the description in Sec. 5.4.1 and are taken from the Monte Carlo samples mentioned in Sec. 2.4. In the case of $\psi' \to \mu^+\mu^-$, the selection on both daughter particles being muons according to the PDG code in the MC was added to diminish wrongly identified pions.

The cross section is also different for each $|t|$ bin and thus the ratio can differ. However, dividing data into $|t|$ bins means less events in each bin, which especially because of the very small number of ψ' events in each bins causes a large uncertainty of the calculated cross section ratio. Therefore the ratio obtained from the $|t|$-integrated sample is scaled using the STARlight prediction by comparing the number of generated particles in a certain $|t|$ range corresponding to the full data (here without top left index) and the binned cross section is calculated as

$$ {}^{\text{ibin}}\sigma = \frac{{}^{\text{ibin}}_{\text{gen}}N}{{}_{\text{gen}}N}\ \sigma. \tag{5.12} $$

With all these ingredients, everything together is put into (omitting the branching ratio term in order to shorten the notation)

$$ \begin{aligned} {}^{\text{ibin}} f_{\text{D}} &= \frac{{}^{\text{ibin}}\sigma_{\psi'}}{{}^{\text{ibin}}\sigma_{\text{J}/\psi}} \times \frac{{}^{\text{ibin}}(\text{Acc} \times \epsilon)_{\psi'}}{{}^{\text{ibin}}(\text{Acc} \times \epsilon)_{\text{J}/\psi}} \\ &= \frac{{}^{\text{ibin}}_{\text{gen}}N_{\psi'}\ \sigma_{\psi'}\ {}_{\text{gen}}N_{\text{J}/\psi}}{{}_{\text{gen}}N_{\psi'}\ \sigma_{\text{J}/\psi}\ {}^{\text{ibin}}_{\text{gen}}N_{\text{J}/\psi}} \times \frac{{}^{\text{ibin}}_{\text{rec}}N_{\psi'}\ {}^{\text{ibin}}_{\text{gen}}N_{\text{J}/\psi}}{{}^{\text{ibin}}_{\text{gen}}N_{\psi'}\ {}^{\text{ibin}}_{\text{rec}}N_{\text{J}/\psi}} \end{aligned} \tag{5.13} $$

and after a few simple adjustments, the final form for the feed-down correction of each bin (returning the branching ratio term) reads

$$ {}^{\text{ibin}} f_{\text{D}} = \frac{\sigma_{\psi'}\ {}_{\text{gen}}N_{\text{J}/\psi}}{\sigma_{\text{J}/\psi}\ {}_{\text{gen}}N_{\psi'}} \times \frac{{}^{\text{ibin}}_{\text{rec}}N_{\psi'}}{{}^{\text{ibin}}_{\text{rec}}N_{\text{J}/\psi}}\ \text{BR}_{\psi' \to \text{J}/\psi + \text{pions}}. \tag{5.14} $$

In Eq. (5.4), f_{D} is split into two separate process. The case of the decay of ψ' into J/ψ and two opposite charged pions can be written as

$$ {}^{\text{ibin}} f_{\text{D}}^{\text{charged}} = \frac{\sigma_{\psi'}\ {}_{\text{gen}}N_{\text{J}/\psi}}{\sigma_{\text{J}/\psi}\ {}_{\text{gen}}N_{\psi'}} \times \frac{{}^{\text{ibin}}_{\text{rec}}N_{\psi'}}{{}^{\text{ibin}}_{\text{rec}}N_{\text{J}/\psi}}\ \text{BR}_{\psi' \to \text{J}/\psi + \pi^+\pi^-}. \tag{5.15} $$

The version for the decay into J/ψ and neutral particles is

$$ {}^{\text{ibin}} f_{\text{D}}^{\text{neutrals}} = \frac{\sigma_{\psi'\ \text{gen}} N_{\text{J}/\psi}}{\sigma_{\text{J}/\psi\ \text{gen}} N_{\psi'}} \times \frac{{}^{\text{ibin}}_{\text{rec}} N_{\psi'}}{{}^{\text{ibin}}_{\text{rec}} N_{\text{J}/\psi}} \text{BR}_{\psi' \to \text{J}/\psi + \text{neutrals}}. \tag{5.16} $$

The ${}_{\text{gen}}N_X$ factors are taken from dedicated Monte Carlo simulations. The corresponding branching ratios are $\text{BR}_{\psi' \to \text{J}/\psi + \pi^+\pi^-} = (34.68 \pm 0.30)\%$ and $\text{BR}_{\psi' \to \text{J}/\psi + \text{neutrals}} = (25.38 \pm 0.32)\%$ according to [19].

5.3 p_T spectrum

The p_T and p_T^2 spectra in the mass range of the J/ψ after all selections, except the $p_T^{\mu\mu}$ cut, are in Fig. 5.3. In theory, the coherent photoproduction should show a certain diffraction pattern, as for example in Fig. 5.1. Unfortunately, no such clear pattern is visible in the measured data due to the detector resolution and the presence of background.

The events in the p_T spectrum of the selected data sample does not origin from the coherent J/ψ photoproduction only; it is a mixture of multiple processes indistinguishable with a simple selection criteria. A detailed knowledge of the p_T spectrum allows us to precisely identify the unwanted processes and to extract the amount of sample contamination by each process. This thesis uses the p_T-distribution study to unveil the fraction of incoherent events (see Sec. 5.3.1) f_I, which enters Eq. (5.6).

5.3.1 Incoherent contamination

The incoherent contamination cannot be described with a similar method as the feed-down contamination (see Sec. 5.2.1) due to the incoherent J/ψ photoproduction accompanied by nucleon dissociation (dissociative J/ψ further in the text), for which no Monte Carlo simulations were produced for this thesis. Instead, a model of the p_T distribution is created to imitate the data. The model consists of six templates; coherent J/ψ photoproduction, incoherent J/ψ photoproduction, incoherent J/ψ photoproduction with nucleon dissociation, coherent ψ' photoproduction, incoherent ψ' photoproduction and continuum dimuons from the $\gamma\gamma \to \mu^+\mu^-$ process. The templates of all, but dissociative J/ψ and continuum dimuons, are taken from dedicated Monte Carlo simulations. The proportions to data of both ψ' photoproduction processes are fixed in the model and are calculated as in Sec. 5.2.1 with the modification that the $p_T^{\mu\mu}$ criterion was released and a selection on the invariant mass was added (see Tab. 5.1). Other proportions are left free for the fit. The normalisation of the continuum for the fit is set from an invariant mass fit (see Sec. 5.2) as the number of background events in the mass range of the J/ψ. Then, the model is fit with an extended maximum likelihood to un-binned measured data. The result is depicted in Fig. 5.4.

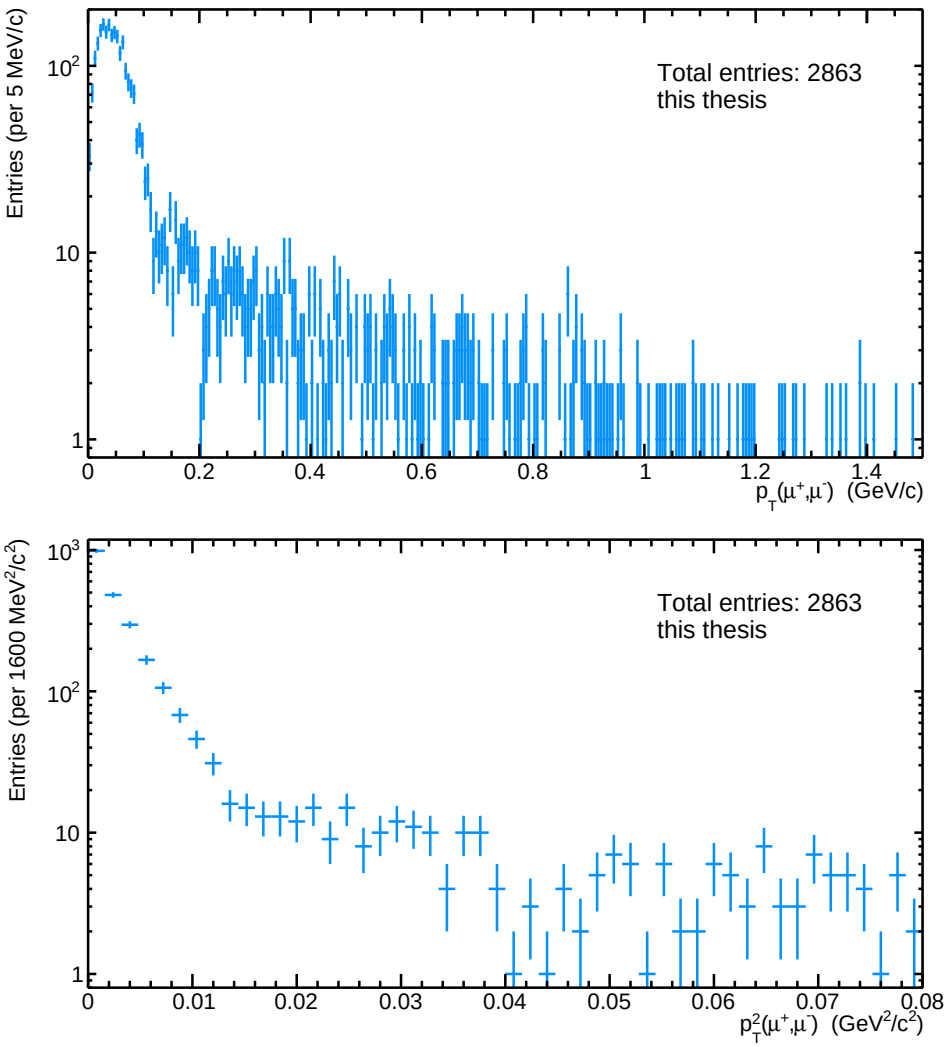

Figure 5.3: (Top panel) The p_{T} spectrum of the selected data sample. (Bottom panel) The p_{T}^2 spectrum of the selected data sample. All events are from the dimuon invariant mass range (3.0,3.2) GeV/c^2.

Coherent J/ψ

The template for the coherent J/ψ photoproduction is taken from the dedicated Monte Carlo simulation based on STARlight model. However, the middle plot of Fig. 5.4 shows slight disagreement between data and the model at low p_{T}. Therefore, instead of using events generated by STARlight for the template of coherent J/ψ, directly a formula

$$\frac{\mathrm{dN}_{\mathrm{J}/\psi}}{\mathrm{d}p_{\mathrm{T}}} = a\ p_{\mathrm{T}}\ e^{-bp_{\mathrm{T}}^2}, \tag{5.17}$$

where the parameter a is a normalisation and the parameter b is left free, was used for comparison. This is the actual formula used by STARlight to generate the p_{T} shape, but with fixed b. Using Eq. (5.17), the fitting

Table 5.1: Feed down corrections f_{D} used to fix coherent and incoherent ψ' fit templates.

	coherent $\mu^+\mu^-$ channel	incoherent $\mu^+\mu^-$ channel
f_{D} (-)	0.0698	0.0732

procedure finds the best b which ends in the best description of data (see bottom plot of Fig. 5.4).

Continuum dimuons

The shape of the background, which is tagged as dimuons from the $\gamma\gamma \rightarrow \mu^+\mu^-$ process, is not described by Monte Carlo correctly. Instead, measured data outside the J/ψ mass region, so called side-bands, were studied. It was found that the mass region bellow 3.0 GeV/c^2 is contaminated by J/ψ mesons with a photon as part of the decay products, or a photon radiated by one of the muons while traversing the detector. Thus, the p_{T} shape of data measured in the mass region $(3.3, 4.5)$ GeV/c^2 is taken as the background in the model of the p_{T} spectrum.

Nucleon dissociation

The dissociative J/ψ process was introduced in order to describe the high-p_{T} tail of the spectrum. The template is based on the H1 parametrisation [111] and is defined as

$$\frac{\mathrm{d}N}{\mathrm{d}p_{\mathrm{T}}} \sim p_{\mathrm{T}} \left(1 + \frac{b_{\mathrm{pd}}}{n_{\mathrm{pd}}}\, p_{\mathrm{T}}^2\right)^{n_{\mathrm{pd}}}. \tag{5.18}$$

The fit parameters are fixed to $b_{\mathrm{pd}} = 1.7$ (GeV/c)$^{-2}$ and $n_{\mathrm{pd}} = 3.56$. These numbers are taken as mean of values obtained by the H1 Collaboration, which provided two sets of measurements with different centre-of-mass energies.

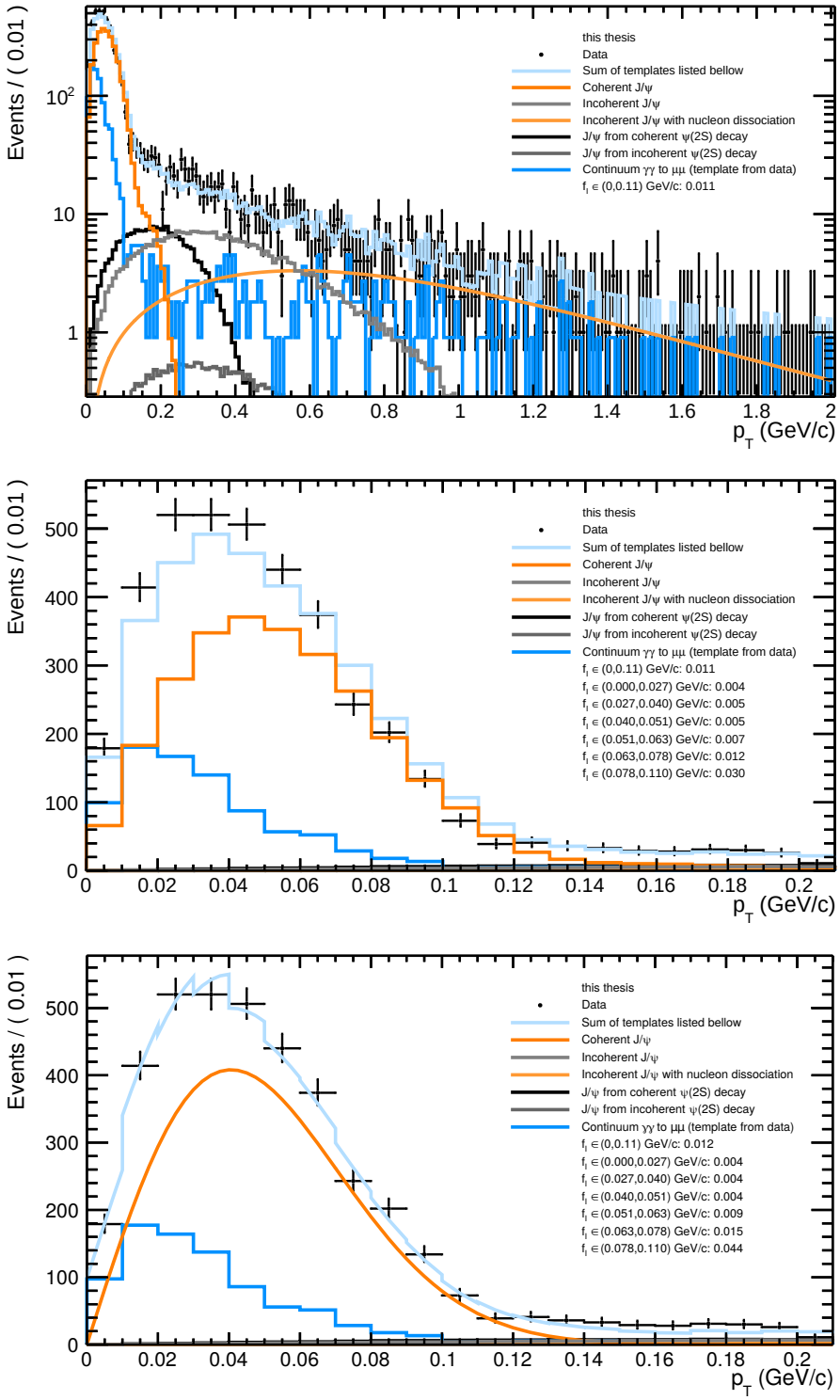

Figure 5.4: (All panels) p_{T} spectra of measured data (*black points*) and templates of various processes (*colour lines*) contributing to the model (*light blue line*), which is fit to data. (Middle and bottom panels) Difference at low p_{T} when using different coherent J/ψ templates as discussed in Sec. 5.3.1.

5.4 Efficiencies and inefficiencies

The route from a collision to data for the analysis is full of technicalities, whose purpose is to translate the physics event into human-readable form. These technologies are usually fascinating state-of-the-art machines/methods, but not perfect. The (in)efficiencies of these techniques have to be investigated. The problematic systems identified for the analysis performed in this thesis are described in this section.

5.4.1 Acceptance times efficiency

The phase-space acceptance and reconstruction efficiency of the detector and the readout systems (Acc $\times$ ϵ) significantly reduce the amount of data available for the analysis. The strategy to calculate Acc $\times$ ϵ is simple. The Monte Carlo sample is restricted only to events in the rapidity range (-0.8,0.8) and with $p_{\mathrm{T}}^{\mu\mu} < 0.11$ GeV/c. These generated events are then checked whether they were reconstructed or not and than we apply all selection criteria mentioned in Secs. 2.4.2 and 2.4.3 on these reconstructed events. This efficiency for each bin is in Fig. 5.5 and is increasing with p_{T} in general. Fig. 5.6 shows the Acc $\times$ ϵ in the $p_{\mathrm{T}}^{\mu\mu} \in (0, 0.11)$ GeV/c for each analysed run and a plot of the Acc $\times$ ϵ dependency on the azimuthal angle. The slight dependence in the azimuth Acc $\times$ ϵ was studied and it was found that this effect is described by the Monte Carlo simulation. These plots show stable results over the whole run period.

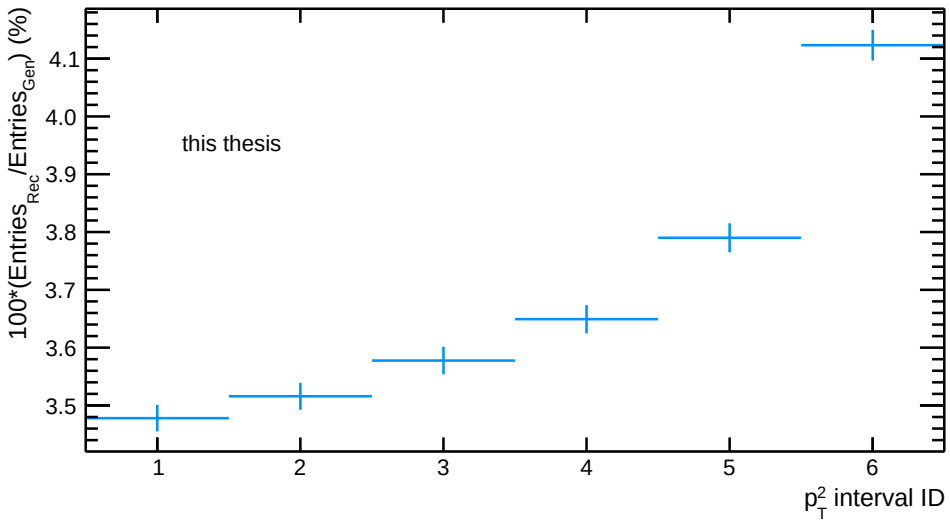

Figure 5.5: Acc $\times$ ϵ for each analysed p_{T}^2 interval.

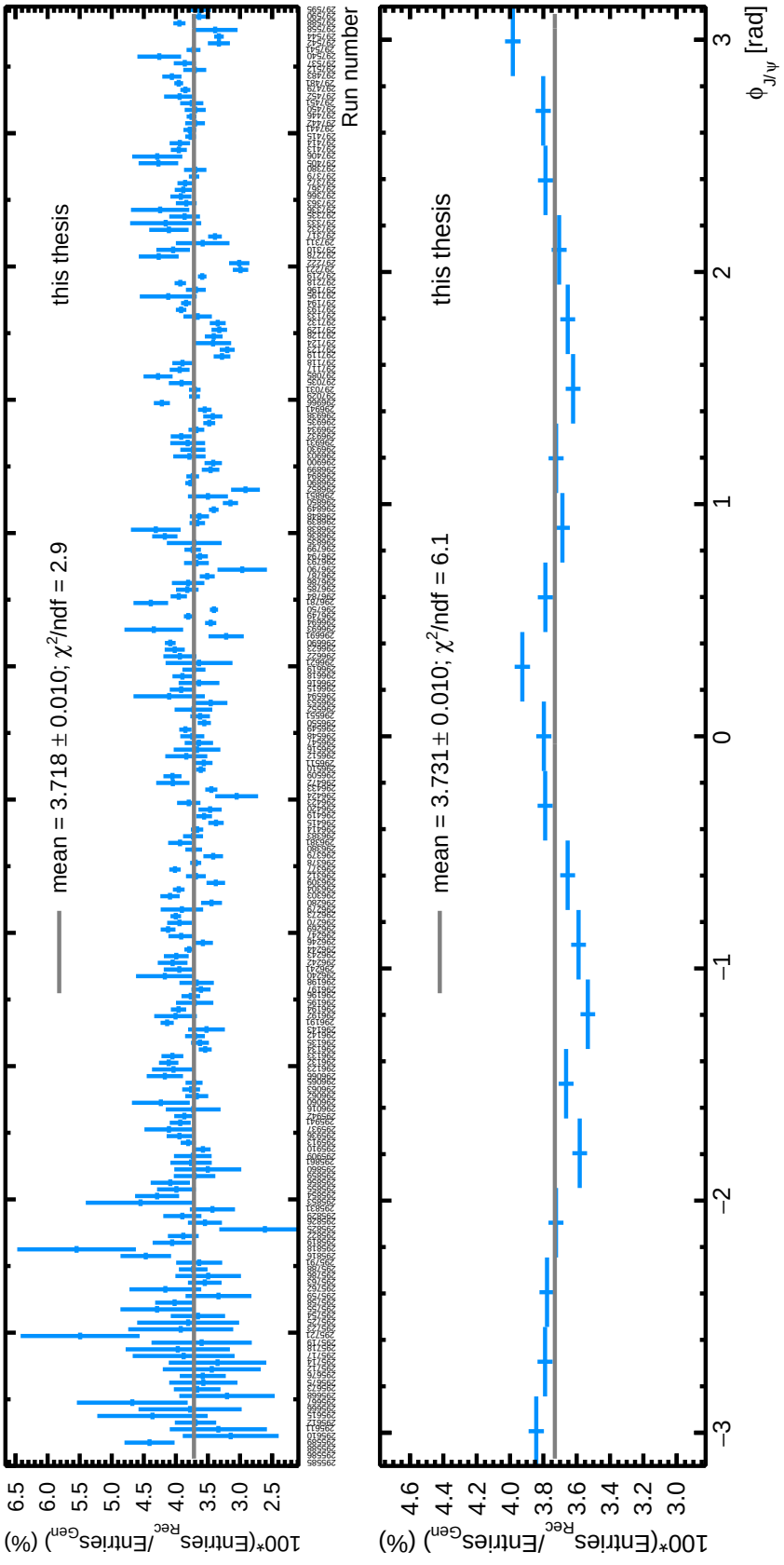

Figure 5.6: Acc $\times \epsilon$ for each analysed run (top). Acc $\times \epsilon$ dependence on azimuthal angle φ (bottom).

Table 5.2: Inefficiencies for different VETO trigger inputs. The uncertainties are calculated using three standard deviations of the fit.

	online decision	offline decision
V0A	0.0157 ± 0.0003	0.0379 ± 0.0004
V0C	0.0052 ± 0.0002	0.0185 ± 0.0003
ADA	0.0005 ± 0.0001	0.0009 ± 0.0001
ADC	0.0002 ± 0.0001	0.0005 ± 0.0001

5.4.2 Forward VETO triggers inefficiencies

The forward detectors AD and V0 are used to apply vetoes on activity at forward rapidities. The efficiency of these detectors suffer from random overlap with signals from other collisions, which yield fake signals and result in the rejection of potentially interesting events (so-called trigger inefficiency). This effect is calculated as the probability of having one of the vetoing triggers fired in an otherwise empty event using an unbiased trigger, which records data from the detectors when the beams from the both directions are presented in the interaction area (beam-beam window) and no other conditions on the event are required.

The vetoes are applied on two levels of the analysis. First on the online level, where it was a part of the CCUP31 trigger as trigger inputs 0V(U)BA(C) (see Sec. 2.2). The trigger input is fired when there is a signal over a predefined threshold in the corresponding detector in the beam-beam window. Second application is on the offline level, where a more complex algorithm is used for the offline data selection (0V(U)DA(C)). This algorithm returns several possible states of the detectors, one of them is that the detector is empty. The fake detector signal is considered when the flag is everything else but not empty.

The probability of not having this effect is taken from a Poisson distribution as $p_0 = \exp(\lambda)$, where λ stands for the expected number of wrongly fired detector to all empty events. Figures 5.7 and 5.8 show linear fits of the probability dependency on inelastic pile-up. These fits have fixed intercept term to zero, representing the expected behaviour of not having fake signals when there is no pile-up. The λ is calculated using the linear fit parameter as $\lambda_i = a\ \mu_{\mathrm{INEL},i}$ for each analysed run. The average probability is then calculated as $p_0 = \sum w_i p_{0,i} / \sum w_i$, where the weights are originating from the analysed luminosity of the CCUP31 trigger. The vetoing-trigger inefficiencies are then calculated as $\epsilon_{\mathrm{XXX}} = 1 - p_0$ and are collected in Tab. 5.2. The total trigger efficiency used in Eq. (5.1) is calculated with Eq. (5.19), where only the correction on the offline decision is made, as the online decision is a subset of the offline decision.

$$\epsilon^{\mathrm{VETO}} = (1 - \epsilon_{\mathrm{VDA}})\ (1 - \epsilon_{\mathrm{VDC}})\ (1 - \epsilon_{\mathrm{UDA}})\ (1 - \epsilon_{\mathrm{UDC}}). \tag{5.19}$$

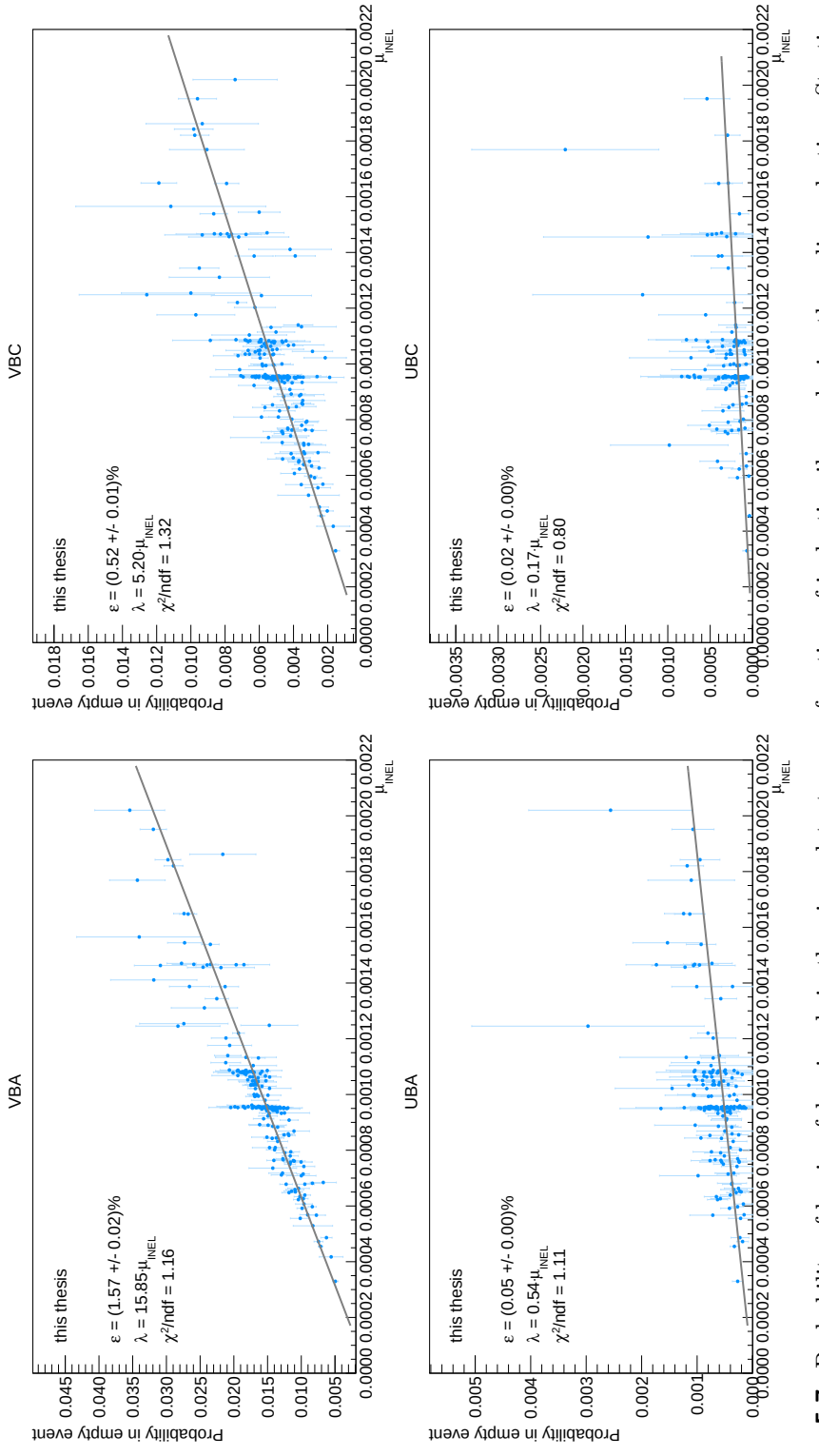

Figure 5.7: Probability of having fake signals in the given detector as a function of inelastic pile-up during the online selection. Starting from the top left in a clockwise direction: V0A, V0C, ADA, ADC.

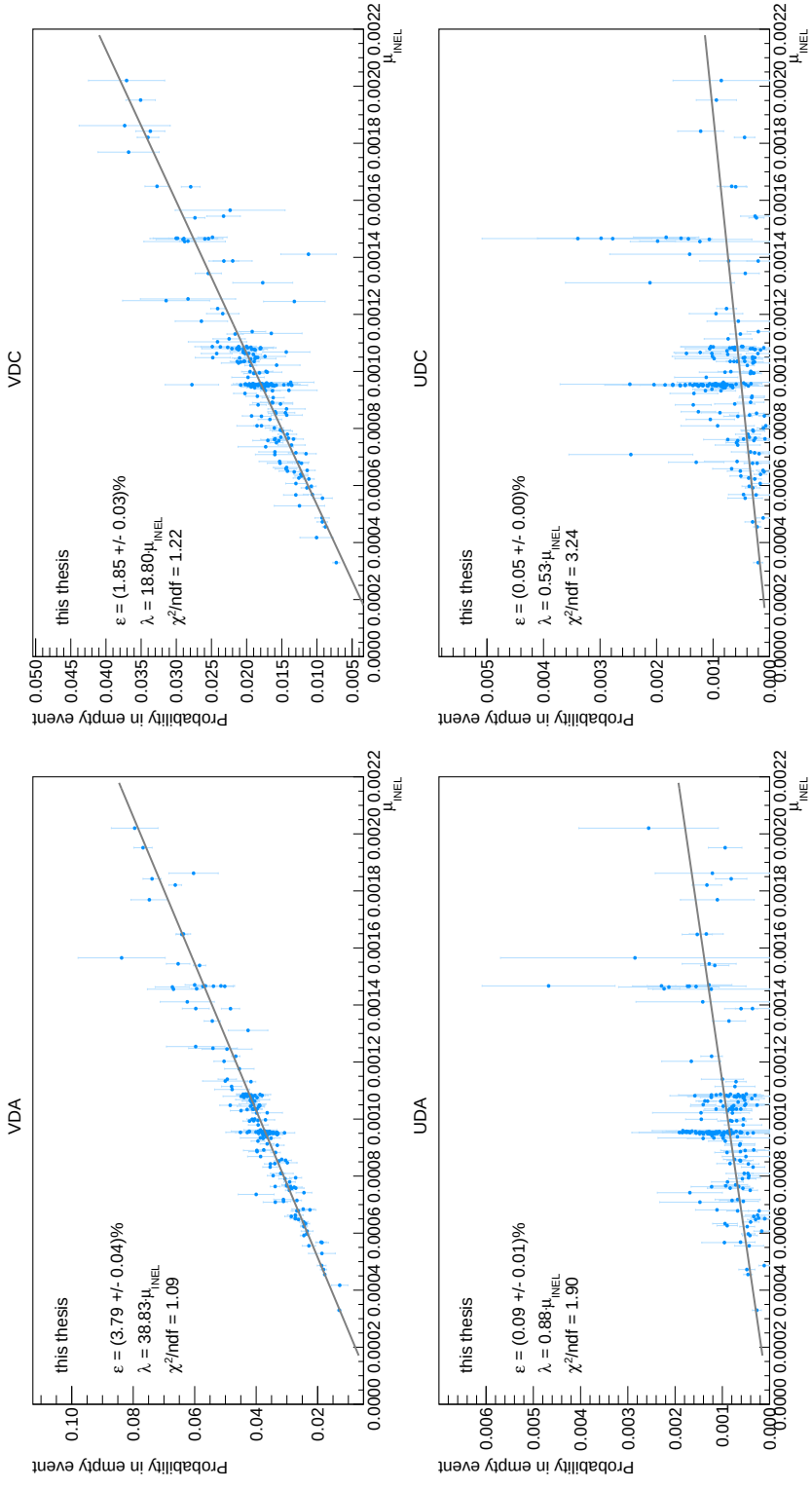

Figure 5.8: Probability of having fake signals in the given detector as a function of inelastic pile-up during the offline selection. Starting from the top left in a clockwise direction: V0A, V0C, ADA, ADC.

5.4.3 Inefficiencies due to electromagnetic dissociation

Electromagnetic dissociation (EMD) is another unwanted process, which can occur when one or more photons excite one or both interacting nuclei. Upon de-excitation one or more neutrons are emitted. Sometimes, other charged particles are emitted as well at forward rapidities [112, 113]. These particles can yield fake veto signal in V0 and AD. This correction amounts to 0.92 and was determined centrally by the group working on ultra-peripheral collisions in ALICE.

5.5 Unfolding usage

The unfolding is a technique, which finds its assertion when an original distribution of data is somehow smeared. A discussion of this topic can be found in Chapter 4. This thesis measurement uses unfolding at two different analysis stages. First, when the p_{T}^2 distribution is blurred due to the detector resolution and second, when the momentum of the probing photon has to be extracted from the measured p_{T} distribution to obtain the dependency on $|t|$.

5.5.1 p_{T}^2 unfolding

The investigation of the $|t|$ dependency requires to split events into several p_{T}^2 intervals (bins). The number and the size of the intervals is dictated by several contradictory conditions which have to be balanced. These conditions are:

- More bins means more detailed dependency description,
- statistical uncertainty of the bin at the level of systematic uncertainty,
- measurement uncertainties reasonably low,
- detector resolution at the level of the interval size.

The resolution smearing of the detector can be reverted using unfolding, but at the price of an additional systematic uncertainty which grows with smearing-effect severity. In addition, more bins means less events in each p_{T}^2 interval and hence larger statistical uncertainty. Hence, studying the ideal number and size of the p_{T} bins is crucial for a successful measurement.

The collected number of events allows for splitting into regions, which are slightly smaller than the resolution of ALICE detectors. A STARlight simulation of this effect can be seen in Fig. 5.9. Using the number of J/ψ events in each bin it was estimated that around 45% of all events were reconstructed in the wrong p_{T}^2 interval. To revert this effect the Bayesian unfolding was determined as the best method for the case of this thesis, with the use of the SVD method to cross-check.

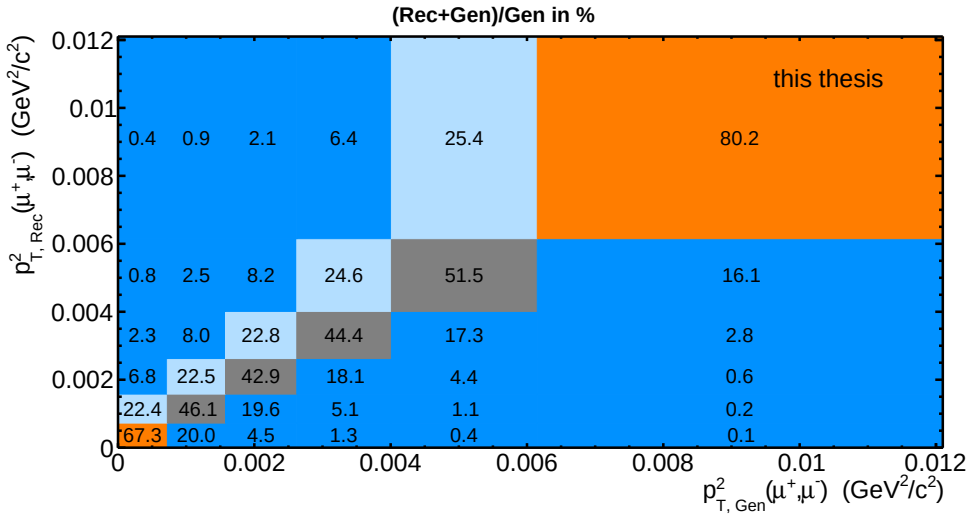

Figure 5.9: Migration across p_T^2 bins as simulated by GEANT.

The Monte Carlo sample used for unfolding contained several hundreds of thousand events. 80% of these events were used to train the response matrix that is responsible for unfolding the truth distribution from the measured distribution. A test of this matrix, where the result of the training is applied on the rest 20% of the events of the Monte Carlo simulation which represent an independent sample, was highly evincing and tells that the response matrix is correctly trained.

The Bayesian unfolding is an iterative method, therefore, besides the investigation on the number of p_T^2 bins, the result depends on the number of iterations used. These two parameters can be tuned using Monte Carlo simulations.

The evolution of the relative statistical error of unfolding is in Tab. 5.3. In addition, the evolution of the relative difference between unfolded results between i iterations and $i+1$ iterations is also in the table. With more iterations this difference decreases as the method converges. Conversely, the computed average statistical uncertainty, originating in the statistical errors of the data sample, is increasing with the number of iterations. The final choice on the number of iterations is determined from these observations, where a difference of less than 1% is considered to be small enough for the price of a still relatively small statistical error. It can be read from Tab. 5.3 that three to five iterations is ideal. Following the decision on the p_T^2 interval constitution, four iterations were used in this analysis.

At the end, the result should be comparable with theory. The events for the Monte Carlo sample are generated with STARlight which uses a model based on the Vector Meson Dominance model (VMD). Three parameters in this model can be tested; normalisation, range of Yukawa potential a and size of nucleus R_A. The generator is set with $a = 0.7$ fm and $R_A = 6.67$ fm. Results and errors of fit parameters of the unfolded MC sample for different

Table 5.3: Relative unfolding result differences to previous iteration (Av. Rel. Diff.) and relative statistic errors (Av. Stat. Err.) for different number of bins and number of iterations.

Iteration:	1	2	3	4	5	6	7	8
Number of bins: 5								
Av. Rel. Diff. (%)		4.38	1.68	0.83	0.52	0.38	0.32	0.28
Av. Stat. Err. (%)	2.81	3.74	4.43	4.99	5.45	5.85	6.20	6.52
Number of bins: 6								
Av. Rel. Diff. (%)		4.69	1.89	0.89	0.54	0.39	0.31	0.28
Av. Stat. Err. (%)	2.70	3.62	4.33	4.89	5.37	5.79	6.17	6.51
Number of bins: 7								
Av. Rel. Diff. (%)		4.66	1.90	1.15	0.82	0.65	0.56	0.55
Av. Stat. Err. (%)	2.94	3.99	4.79	5.44	5.99	6.48	6.93	7.34
Number of bins: 8								
Av. Rel. Diff. (%)		4.65	1.81	0.83	0.52	0.36	0.27	0.21
Av. Stat. Err. (%)	2.99	4.09	4.94	5.63	6.23	6.77	7.25	7.70
Number of bins: 9								
Av. Rel. Diff. (%)		4.61	1.83	0.85	0.51	0.41	0.38	0.36
Av. Stat. Err. (%)	3.03	4.16	5.04	5.77	6.40	6.96	7.48	7.96

number of bins and count of iterations are in Tab. 5.5. The parameter a, which is strongly correlated with R_{A}, is fixed to the generator value to prevent plateau trapping when fitting data. Table 5.5 informs that R_{A} agrees with the model within the uncertainty. The error of the normalisation is increasing with the number of iterations, which is expected, since the statistical errors of the fitted points are increasing as well. An increase on the number of bins is decreasing the uncertainty of the normalisation, which is also expected. All fits are good assuming the $\chi^2/\mathrm{ndf} < 2.5$ is an acceptable fit.

The decision, which p_{T}^2 interval constitution is used, is made by analysing the statistical uncertainty of the last bin of the spectrum, which is expected to have the largest relative error due to the lowest amount of events in this last bin. The first step is to design the p_{T}^2 intervals to contain a similar portion of events in each bin. Several such interval constitution were made with respect to different number of bins. All considered interval constitutions were unfolded using the ideal number of iterations found in Tab. 5.3. The results of the relative statistical errors for each bin are in Tab. 5.4. Out of these, the six-bin configuration was chosen, where the error of the last bin is smaller than in the case of more-bin configurations, while the fit parameters errors (see Tab. 5.5) are comparable.

Table 5.4: Relative statistic errors for each bin for each bin configuration after the use of the ideal number of iterations found in Tab. 5.3.

Bin number:	1	2	3	4	5	6	7	8	9
Number of iterations: 4									
Stat. Err. (%)	5	4	4	5	7				
Number of iterations: 4									
Stat. Err. (%)	5	4	4	4	5	7			
Number of iterations: 5									
Stat. Err. (%)	6	5	5	5	5	7	9		
Number of iterations: 4									
Stat. Err. (%)	6	4	5	4	5	5	6	9	
Number of iterations: 4									
Stat. Err. (%)	6	5	5	4	5	5	6	7	10

Table 5.5: Fit parameters of the VMD model for different number of bins and different number of iterations. The parameter a, which is strongly correlated with R_A, is fixed to prevent plateau trapping when fitting data.

Iteration:	1	2	3	4	5	6	7	8
Number of bins: 5								
Norm. fit err. (%)	3.24	4.28	4.92	5.36	5.69	5.94	6.15	6.32
a (fm)	0.70 ± 0.00	0.70 ± 0.00	0.70 ± 0.00	0.70 ± 0.00	0.70 ± 0.00	0.70 ± 0.00	0.70 ± 0.00	0.70 ± 0.00
R_A (fm)	6.81 ± 0.05	6.80 ± 0.06	6.80 ± 0.07	6.80 ± 0.08	6.80 ± 0.09	6.80 ± 0.09	6.80 ± 0.09	6.80 ± 0.10
χ^2/ndf	1.97	1.58	1.42	1.35	1.33	1.33	1.35	1.38
Number of bins: 6								
Norm. fit err. (%)	3.10	4.16	4.84	5.32	5.69	5.99	6.23	6.43
a (fm)	0.70 ± 0.00	0.70 ± 0.00	0.70 ± 0.00	0.70 ± 0.00	0.70 ± 0.00	0.70 ± 0.00	0.70 ± 0.00	0.70 ± 0.00
R_A (fm)	6.78 ± 0.05	6.76 ± 0.06	6.76 ± 0.07	6.76 ± 0.08	6.76 ± 0.09	6.76 ± 0.09	6.77 ± 0.09	6.77 ± 0.10
χ^2/ndf	1.47	1.21	1.04	0.91	0.82	0.75	0.69	0.64
Number of bins: 7								
Norm. fit err. (%)	2.96	4.02	4.73	5.24	5.65	5.97	6.24	6.47
a (fm)	0.70 ± 0.00	0.70 ± 0.00	0.70 ± 0.00	0.70 ± 0.00	0.70 ± 0.00	0.70 ± 0.00	0.70 ± 0.00	0.70 ± 0.00
R_A (fm)	6.75 ± 0.04	6.72 ± 0.06	6.72 ± 0.07	6.72 ± 0.08	6.73 ± 0.08	6.73 ± 0.09	6.73 ± 0.09	6.74 ± 0.10
χ^2/ndf	2.18	1.86	1.67	1.54	1.44	1.37	1.31	1.26
Number of bins: 8								
Norm. fit err. (%)	2.80	3.85	4.56	5.11	5.56	5.93	6.25	6.53
a (fm)	0.70 ± 0.00	0.70 ± 0.00	0.70 ± 0.00	0.70 ± 0.00	0.70 ± 0.00	0.70 ± 0.00	0.70 ± 0.00	0.70 ± 0.00
R_A (fm)	6.75 ± 0.04	6.73 ± 0.06	6.73 ± 0.07	6.73 ± 0.08	6.74 ± 0.08	6.74 ± 0.09	6.75 ± 0.09	6.76 ± 0.10
χ^2/ndf	2.46	1.91	1.67	1.52	1.42	1.35	1.30	1.25
Number of bins: 9								
Norm. fit err. (%)	2.69	3.72	4.43	4.98	5.44	5.82	6.16	6.45
a (fm)	0.70 ± 0.00	0.70 ± 0.00	0.70 ± 0.00	0.70 ± 0.00	0.70 ± 0.00	0.70 ± 0.00	0.70 ± 0.00	0.70 ± 0.00
R_A (fm)	6.72 ± 0.04	6.70 ± 0.06	6.70 ± 0.07	6.70 ± 0.07	6.70 ± 0.08	6.71 ± 0.09	6.71 ± 0.09	6.72 ± 0.10
χ^2/ndf	2.31	1.69	1.42	1.26	1.15	1.08	1.02	0.99

5.5.2 γPb extraction unfolding

Finally, the dependence of the cross section on the transferred momentum of the lead projectile $|t|$ is the goal of the thesis. What is actually measured is the ${}_{\mathrm{J}/\psi}p_{\mathrm{T}}^2$ of the J/ψ particle. In fact, ${}_{\mathrm{J}/\psi}p_{\mathrm{T}}^2$ is the sum of $|t|$ and ${}_{\gamma}p_{\mathrm{T}}^2$, where the second corresponds to the transverse momentum squared of the quasi-real photon (See Fig. 1.5).

To study, if the momentum of the photon is negligible, it is necessary to understand the tool that was used to create the simulations: STARlight. STARlight itself proceeds as follow: First, it generates the momenta of the photon and the so-called pomeron which mediates the strong interaction, and then it calculates the momentum of the created J/ψ. A 2D histogram of pomeron $|t|$ vs. J/ψ p_{T}^2 can be found in the top part of Fig. 5.10. The spread of events outside the ideal case, $p_{\mathrm{T}}^2 = |t|$, tells us that the photon p_{T} has to be subtracted from the measured p_{T}^2 spectrum.

The relation between p_{T}^2 and $|t|$ points was found with the Bayesian unfolding of the p_{T}^2 spectrum, where as the truth $|t|$ and training p_{T}^2 distributions were taken spectra from the following: (*i*) STARlight prediction; 500 000 events of the coherent photoproduction of the J/ψ particle were generated and for each event saved $|t|$ and ${}_{\mathrm{J}/\psi}p_{\mathrm{T}}^2$. (*ii*) Pomeron $|t|$ from data; for each event, which survived the selection criteria described in Sec. 2.4.1, one hundred photon p_{T} were calculated according to Ref. [114] and the azimuthal angle between J/ψ and photon was randomly assigned. Then 2D vectors of the J/ψ and the photon representing their momenta in the azimuthal plane were built. Then the photon vector was subtracted from the J/ψ vector, resulting in the pomeron p_{T} 2D vector. The squared magnitude of the pomeron vector is the $|t|$ used for building the truth distribution. This way a response matrix made of 360 500 events was obtained. A 2D histogram of pomeron $|t|$ vs. J/ψ p_{T}^2 for the case (*ii*) can be found in bottom part of Fig. 5.10.

An average of results of unfolding with (*i*) and (*ii*) are taken as a result of going from p_{T}^2 to $|t|$.

5.6 Theoretical corrections

The extraction of the γ contribution from Sec. 5.5.2 is not the only correction needed to convert the dependency on p_{T}^2 to a dependency on $|t|$. The other steps are described in the next lines.

5.6.1 Interference of the amplitudes

In UPCs, there are two potential photon sources, so in principle both amplitudes have to be added and will produce an interference. This was studied for the first time in Ref. [40] and later measured for the case of ρ^0 coherent photoproduction by the STAR Collaboration [115]. To account for this effect,

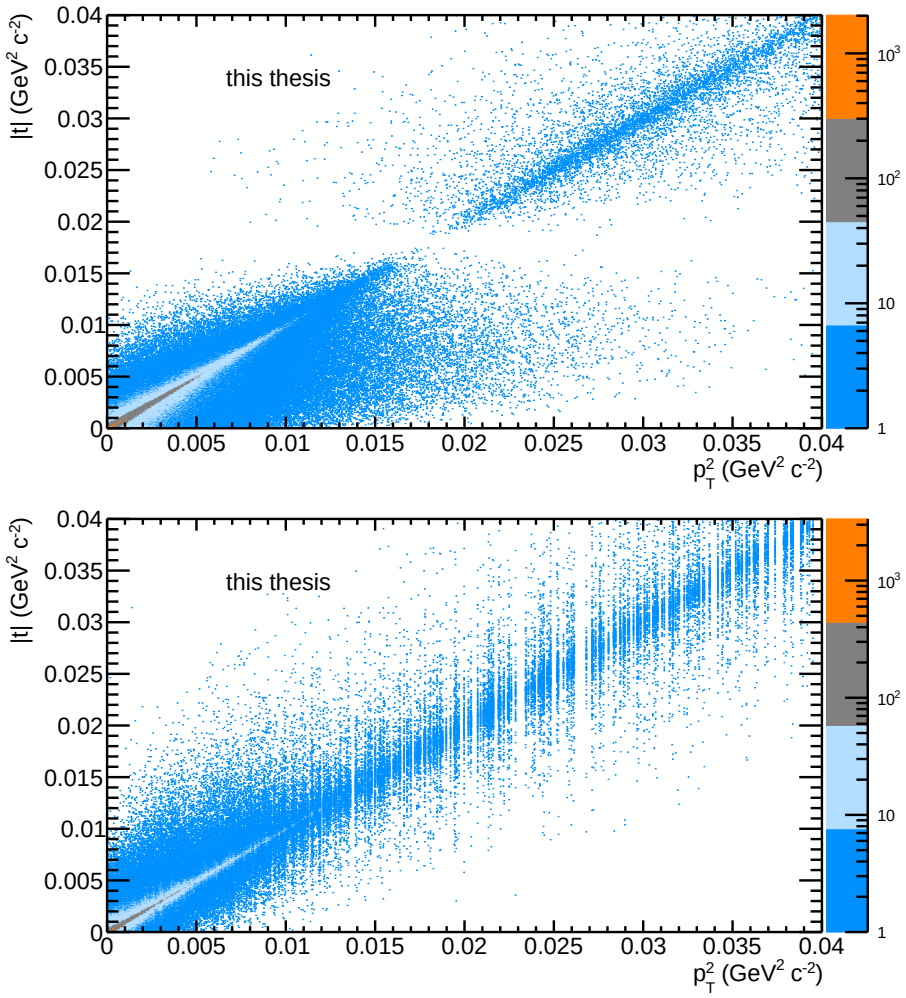

Figure 5.10: p_{T}^2 of J/ψ vs. $|t|$ of pomeron as predicted by STARlight (top panel), and data + photon flux as in Ref. [114] (bottom panel).

the STARlight program, which includes the interference of both amplitudes, was used. The comparison of the STARlight generated p_{T}^2 distribution is in Fig. 5.11. One can see that the interference is important only at very small values of $|t|$. Unfortunately, with interference ON, it is not possible to decide which pomeron produced the final state J/ψ. Hence, it is not possible to generate a response matrix for unfolding as described in Sec. 5.5.2, (i) case. Therefore the ratio of both histograms is taken, rebinned to the six-p_{T}^2-intervals, and the measured p_{T}^2 distribution is scaled before the p_{T}^2 to $|t|$ correction is applied, see Tab. 6.1.

5.6.2 Going from the Pb–Pb to the γPb cross section

Theory computations of the γPb process are done at fixed energies. At midrapidity the UPC cross section corresponds to the γPb cross section

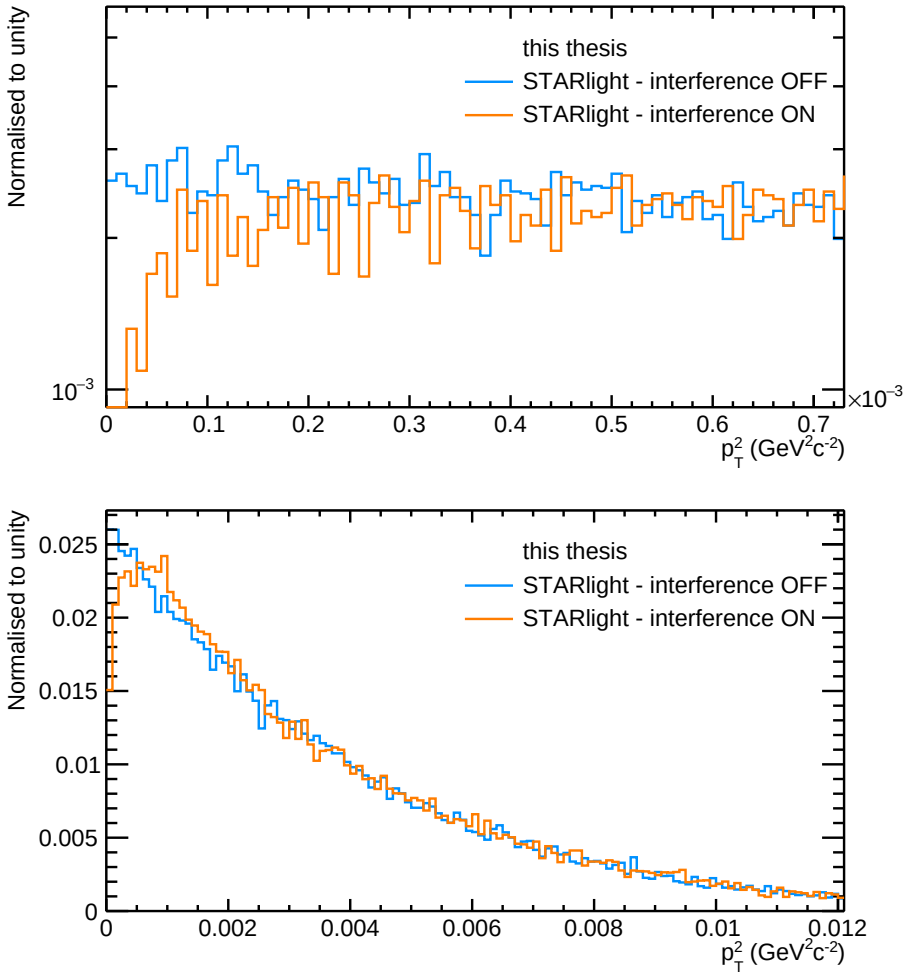

Figure 5.11: p_{T}^2 of J/ψ as calculated by STARlight with interference effect ON (*orange line*) or OFF (*blue line*). The upper panel is a zoom in the low-p_{T}^2 region to highlight the difference.

multiplied by twice the photon flux ($n_{\gamma\mathrm{Pb}}(y)$)

$$\left.\frac{\mathrm{d}^2\sigma^{\mathrm{coh}}_{\mathrm{J}/\psi}}{\mathrm{d}y\mathrm{d}p_{\mathrm{T}}^2}\right|_{y=0} = 2n_{\gamma\mathrm{Pb}}(y=0)\frac{\mathrm{d}^2\sigma_{\gamma\mathrm{Pb}}}{\mathrm{d}|t|}. \tag{5.20}$$

The photon flux was computed following the prescription detailed in [116] and amounts to 84.9. Finally, noticing that the rapidity dependence of the UPC cross section in the rapidity range studied here is fairly flat the measurements are taken to represent the value at $y = 0$.

Mean of $|t|$ bin

While converting from p_{T}^2- to $|t|$-dependent cross section, also the event $|t|$-distribution in each p_{T}^2-interval changes and hence the mean $|t|$ point with respect to the corresponding mean p_{T}^2 value, which could be evaluated directly from data. The pomeron $|t|$-distribution was estimated as described in Sec. 5.5.2, case (ii). The input ${}_{\mathrm{J}/\psi}p_{\mathrm{T}}^2$ are the p_{T}^2 of all measured events which survived the selection criteria as mentioned in Sec. 2.4.1 with the additional restriction on the mass to be in the range $(3.0, 3.2)$ GeV/c^2. For each p_{T}^2 input, one hundred of possible pomeron $|t|$ $({}_{\mathrm{pom}}p_{\mathrm{T}}^2)$ were calculated with ${}_{\gamma}p_{\mathrm{T}}$ chosen randomly according to a prescription for photon p_{T}-distribution found in [114] and φ_γ also taken randomly following an uniform distribution of $(0,2\pi)$. The calculated p_{T} spectrum of pomeron can be found in Fig. 5.12. The resulting weighted mean $|t|$-points based on the calculated pomeron distribution are used in the final cross section $|t|$ dependency.

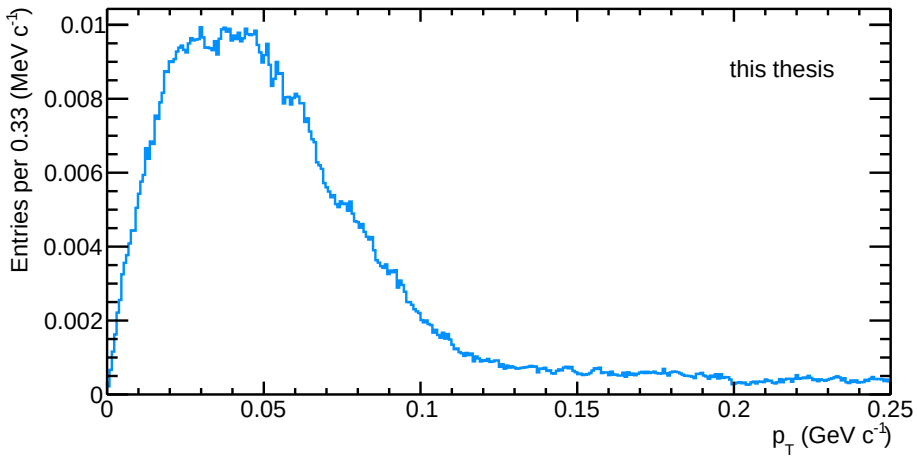

Figure 5.12: Distribution of $|t|$ of pomeron as calculated according to the description in Sec. 5.5.2, case (ii). Photon p_{T} calculated according to Ref. [114].

5.7 Systematic uncertainties

Every measurement employs methods, which generate systematic uncertainty for the measurement. Ten experimental uncertainties and three additional uncertainties, coming from theoretical corrections, were identified. The methodology of their computation is explained in this section.

5.7.1 Experimental systematic uncertainties

In this section, the systematic uncertainties, which are applied to the measurement itself, are described.

Table 5.6: Systematic uncertainties from the invariant mass fit for each p_{T}^2 interval.

p_{T}^2 interval (GeV^2/c^2)	uncertainty (%)
$(0; 0.00072)$	2.2
$(0.00072; 0.0016)$	0.9
$(0.0016; 0.0026)$	0.7
$(0.0026; 0.004)$	1.2
$(0.004; 0.0062)$	1.2
$(0.0062; 0.012)$	0.8

Signal extraction

The signal extraction is described in Sec. 5.2. The used Crystal-Ball function is defined as

$$\mathrm{CB}(m) = \begin{cases} \exp\left[-(\bar{m}-m)^2/(2\sigma_m)^2\right] & , \; m \geq m_1 \\ \\ A\left[\sigma_m/(m'-m)\right]^n & , \; m < m_1, \end{cases} \tag{5.21}$$

where the parameters m_1, A and m' are fixed by the continuity requirement:

$$\begin{aligned} m_1 &= \bar{m} - \alpha\sigma_m \\ A &= (n/\alpha)^n \; \exp\left(-\alpha^2/2\right) \\ m' &= \bar{m} + \sigma_m \left(n/\alpha - \alpha\right). \end{aligned} \tag{5.22}$$

This leaves us with two possible variables, which influence the fit: parameter n and parameter α. In addition, the bottom boundary and the top boundary of the fitted invariant mass spectrum were also investigated. Varying these parameters and boundaries, and comparing yields the systematic uncertainty of the signal extraction was deduced. Meanwhile the placement of boundaries had negligible effects on the final result, the parameter n varied the result within 0.4% and the parameter α showed differences within 2%. The setting with the largest difference in the calculation of the cross section for each p_{T}^2 interval was used. Differences to results with the default setting are taken as systematic uncertainties from the invariant mass fitting. They can be found in Tab. 5.6.

Feed down contamination

The calculation of the correction for the feed down effect is described in Sec. 5.2.1. The main source of uncertainty is coming from the ratio of total cross sections of both processes, $\sigma_{\psi'}^{\mathrm{coh}}/\sigma_{\mathrm{J}/\psi}^{\mathrm{coh}}$. In STARlight, this ratio is set to 0.201 and is used in this analysis. To revel the uncertainty, a result of ALICE [117], where this ratio was measured to be $(0.150 \pm 0.018(\mathrm{stat.}) \pm 0.021(\mathrm{syst.}) \pm 0.007(\mathrm{BR}))$, was employed. Comparing both inputs we get a systematic uncertainty for each bin. The results are in Tab. 5.7.

Table 5.7: Systematic uncertainties from the feed down correction f_D for each p_T^2 interval.

p_T^2 interval (GeV$^2/c^2$)	uncertainty (%)
$(0; 0.00072)$	0.1
$(0.00072; 0.0016)$	0.1
$(0.0016; 0.0026)$	0.2
$(0.0026; 0.004)$	0.3
$(0.004; 0.0062)$	0.4
$(0.0062; 0.012)$	0.5

Table 5.8: Uncertainty of p_T fit and relative difference of cross sections for each p_T^2 interval.

p_T^2 interval (GeV$^2/c^2$)	fit (%)	template diff. (%)	total (%)
$(0; 0.00072)$	1.0	0.2	1.1
$(0.00072; 0.0016)$	1.2	0.2	1.3
$(0.0016; 0.0026)$	1.2	0.3	1.3
$(0.0026; 0.004)$	1.3	0.3	1.4
$(0.004; 0.0062)$	1.4	0.2	1.5
$(0.0062; 0.012)$	1.8	1.5	2.3

Incoherent contamination

The calculation of the correction for the incoherent effect is described in Sec. 5.3.1. The strategy is to obtain the systematic uncertainty from two sources. The first one is the error from the p_T fit of the incoherent fraction (see Fig. 5.4). The second one is a modification of the fitting model. Instead of using events generated by STARlight, for the template of coherent J/ψ, Eq. (5.17) was used, where the parameter b is left free. The total systematic uncertainty is the quadratic sum of both results. The results are in Tab. 5.8.

Unfolding

To reveal the systematic error from the unfolding technique described in Sec. 5.5.1, 45 samples each with 3115 events to simulate data statistics were prepared from the part of the Monte Carlo sample that was not used to train the response matrix.

The method is the following. On each sample, both, Bayes' theorem technique and SVD technique, were applied and stored in a distribution of the relative difference of the results for each bin. The RMSs of these distributions determine the systematic uncertainties of the unfolding for each bin. The relative systematic errors are shown in Tab. 5.9.

Table 5.9: Systematic errors from unfolding for each p_{T}^2 interval.

p_{T}^2 interval (GeV$^2/c^2$)	uncertainty (%)
$(0; 0.000724)$	0.6
$(0.000724; 0.001577)$	1.1
$(0.001577; 0.002623)$	0.9
$(0.002623; 0.004011)$	1.1
$(0.004011; 0.006151)$	1.4
$(0.006151; 0.0121)$	2.3

Luminosity

The systematic uncertainty from luminosity is made of two contributions. The first is the uncertainty on the V0M visible cross section calculated from dedicated van der Meer scans [90] and amounts to 2.2%. The second comes from the determination of the live-time of the UPC trigger and has an additional uncertainty of 1.5%. The total relative systematic uncertainty of the integrated luminosity is thus 2.7%.

V0 and AD veto

The systematic uncertainty from the V0 and AD vetoes was estimated as the relative change in the measured J/ψ cross section before and after imposing them and correcting for the losses. It amounts to 3%.

Electromagnetic dissociation

The relative systematic uncertainty of 2% is given by the statistical uncertainty from the control sample.

ITS-TPC tracking

The relative systematic uncertainty from tracking, which takes into account the track quality selection and the track propagation from the TPC to the ITS, was estimated from a comparison of data and Monte Carlo simulation. The combined uncertainty to reconstruct both tracks is 2.8%.

SPD and TOF trigger inputs efficiency

The relative systematic uncertainty from the SPD and TOF trigger amounts to 1.3%, which was estimated using a data-driven method by changing the requirements on the probe tracks.

Branching ratio uncertainty

The uncertainties of the branching ratios used in this analyses origin from PDG live tables [19]. These are combined statistical errors and systematic uncertainties of various measurements. Therefore, they are added as a separate term in the final result. Adding all branching ratio uncertainties in quadrature result in a total uncertainty of 0.5%.

5.7.2 Theoretical systematic uncertainties

In this section uncertainties, which come from the application of corrections to the photonuclear cross section, are described. That means all uncertainties, which come on top of the experimental result.

Photon flux at $y = 0$ uncertainty

The uncertainty of the photon flux correction is taken as a variation of the geometry of lead ion and is 2% [116].

p_{T}^2 to $|t|$ conversion

Two response matrices for unfolding are used for this correction, one based on STARlight and one based on the pomeron $|t|$ calculated directly from data and a theoretical photon flux calculation. Each unfolding provides slightly different result. Half of the difference is taken as an uncertainty for each bin and varies from 0.1% to 5.7%.

Amplitude interference

The STARlight program provides prediction with interference of amplitudes of both possible processes (γ coming from one Pb and scanning the second Pb or vice versa). The strength of the interference can be modified. $p_{\mathrm{T}}^2 \rightarrow |t|$ unfolding outputs with interference on 100% and 75% were produced to simulate a possible amplitude variation. The resulting uncertainties for each bin vary from 0.3% to 1.2%.

5.7.3 p_{T} correlation of systematic uncertainties

Some of identified systematic uncertainties can be correlated amongst p_{T}^2 bins, which means that a change of the uncertainty of the method would lead to a similar change in every bin. In contradiction to this, one can imagine an example of an uncorrelated uncertainty: statistical fluctuation. Different number of events in one bin and hence different uncertainty in this bin, will not affect other bins. The list of all uncertainties are in Tab. 5.10. The only

Table 5.10: List of identified systematic uncertainties.

Source	Uncertainty (%)
Signal extraction	(0.7,2.2)
f_{D}	(0.1,0.5)
f_{I}	(1.1,2.3)
p_{T}^2 migration unfolding	(0.6,2.3)
Luminosity	2.7
V0 and AD veto	3
EM dissociation	2
ITS-TPC tracking	2.8
SPD and TOF efficiency	1.3
Branching ratio	0.5
Variations in interference strength	(0.3,1.2)
Value of the photon flux at $y = 0$	2
$p_{\mathrm{T}}^2 \rightarrow \lvert t \rvert$ unfolding	(0.1,5.7)

identified uncorrelated uncertainty is the signal extraction, which comes from the fit of the invariant-mass distribution in certain p_{T}^2 interval and hence a change in one interval will not affect the others.

Chapter 6

Physics results and discussion

The previous pages have introduced the methodology of cross section computation of UPCs in the scope of a measurement using the ALICE apparatus. Results of the analysis of data collected in 2018 in Pb–Pb collisions at $\sqrt{s_{\mathrm{NN}}} = 5.02$ TeV are presented and discussed in this section. These results were also published, see Ref. [118, 119].

6.1 $|t|$-differential cross section

The cross section was calculated using Eq. (5.1). The analysed sample is based on a luminosity of $\mathcal{L}_{\mathrm{int}} = 233\ \mu$b, the inefficiency correction factors are set to $\epsilon^{\mathrm{EMD}} = 0.92$ and $\epsilon^{\mathrm{VETO}} = 0.94$, the branching ratio is 5.961%. Other $|t|$-dependent input variables are mentioned in Tab. 6.1. The mean value $\langle p_{\mathrm{T}}^2 \rangle$ in each point is calculated as a weighted average of the p_{T}^2 of measured events after selection (Sec. 2.4.1) in each bin. The description of the calculation of the mean value $\langle |t| \rangle$ is given in Sec. 5.6.2.

The statistical uncertainty of each bin comes from the error from the invariant mass fit. This number is corrected on sample contamination (see Sec. 5.1) and then propagated through the unfolding process to obtain a statistical uncertainty related to the unfolded result. The calculation of systematic uncertainties is described in Sec. 5.7. Statistical uncertainties, quadrature sums of correlated systematic uncertainties and quadrature sums of correlated systematic uncertainties for each p_{T}^2 interval are in Tab. 6.1. The correlation of uncertainties is discussed in Sec 5.7.3.

The calculated photonuclear cross sections are depicted in Fig. 6.1 and compared with selected models. Experimental and theoretical uncertainties are shown separately. The uncorrelated uncertainty is merged in quadrature with the statistical uncertainty.

Three models are chosen according to their availability of $|t|$ predictions and representativity of certain group of QCD dynamical effects. STARlight has no explicit introduction of nuclear shadowing, which is very similar to the impulse approximation, which is usually a reasonable baseline for the

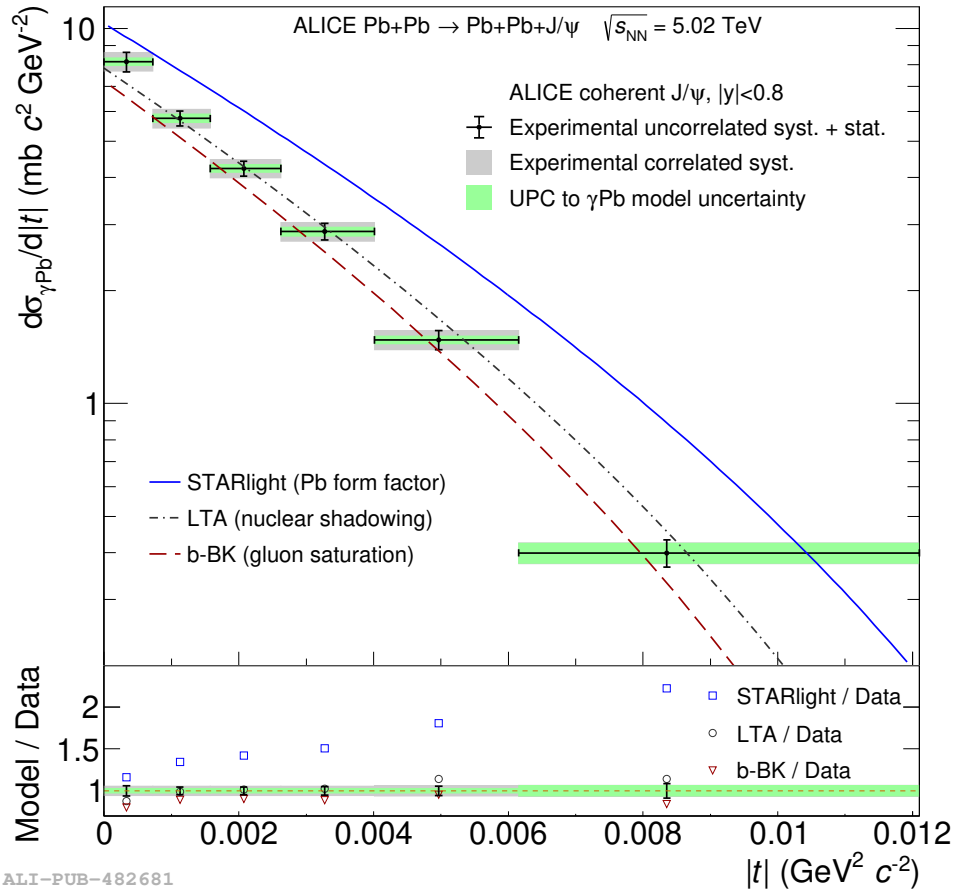

Figure 6.1: Cross section dependency on $|t|$ compared with selected models. Taken from Ref. [118].

study of the shadowing phenomena. The LTA models nuclear shadowing and is parameterised with HERA data on inclusive diffraction. It offers two predictions; one called *high shadowing* and the other *low shadowing*. The last model is b-BK, which represents the set of models including gluon saturation effects. A brief description of the models can be found in Sec. 1.6.2.

The slope predicted by STARlight does not describe data points very well. The reason is the shape dictated by Eq. (5.17), where one of the parameters is fixed by the authors of the model. It is possible to find a set of parameters for the form factor in STARlight which would describe these data better, but then many other previous results, used to fixed this parameter, would not be correctly described. The cross sections magnitude is overestimated by STARlight suggesting the existence of gluon shadowing.

The low shadowing prediction of LTA is shown in Fig. 6.1. The shape obtained from this model is similar to that of the data and describes the cross section within experimental uncertainties. As shown in Fig. 3 of [95], the high-shadowing version of the model has a similar shape but the overall normalisation is smaller by a factor around 1.7.

The model including gluon saturation, b-BK, is able to describe the data quite well in both, the slope and the magnitude.

The model comparison clearly indicates the existence of non-linear QCD effects in the interaction, supporting the idea of the cross section measurement in $|t|$ being a good tool to explore these effects.

6.2 $|t|$-integrated cross section

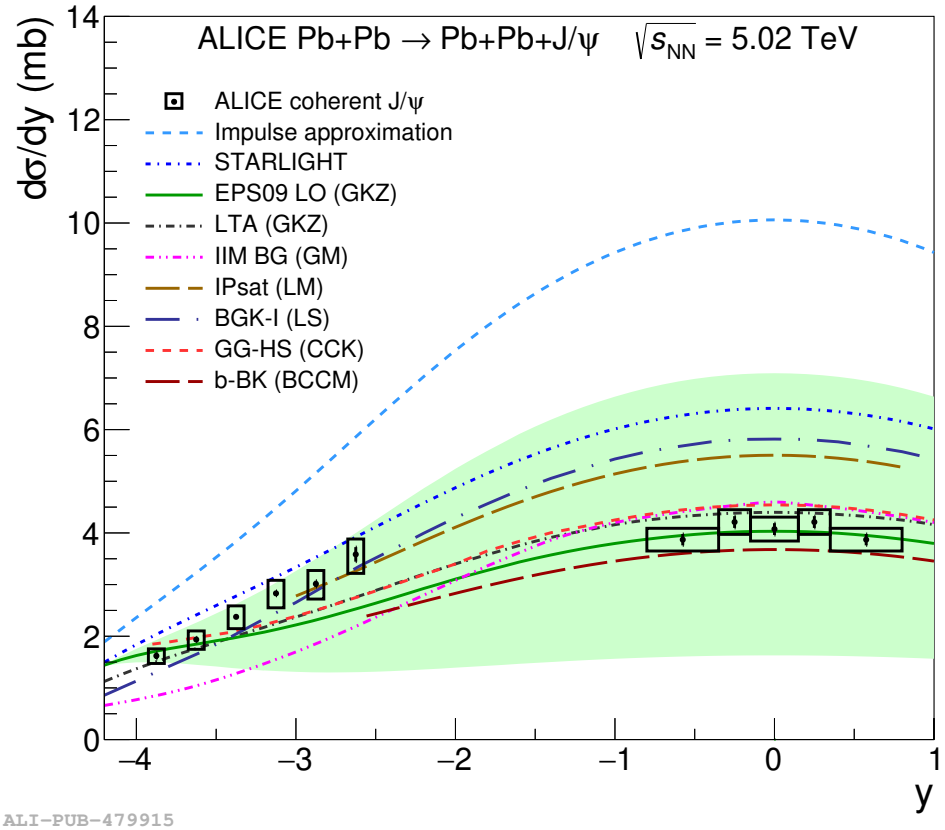

Figure 6.2: Cross section dependency on y compared with selected models. Taken from Ref. [119].

This thesis extends an inclusive analysis, where the calculated cross section is integrated over the complete p_{T}^2 region [119]. There, the ALICE collaboration quotes a cross section of $\mathrm{J}/\psi \to \mu^+\mu^-$ in the rapidity range (-0.8,0.8) to be $\mathrm{d}\sigma^{\mathrm{coh}}_{\mathrm{J}/\psi}/\mathrm{d}y = (4.12 \pm 0.08(\mathrm{stat.}) \pm 0.23(\mathrm{syst.}))$ mb. Integrating the measured p_{T}^2-dependent cross section over p_{T}^2. To achieve this, the sum of cross sections in Tab. 6.1 respecting variable bin widths is made and the result is corrected on the fraction of events with $p_{\mathrm{T}}^{\mu\mu}$ larger than 0.11 GeV/c. This correction is 1.045 and was calculated with the STARlight model. The p_{T}^2-integrated result is $\mathrm{d}\sigma^{\mathrm{coh}}_{\mathrm{J}/\psi}/\mathrm{d}y = 4.21$ mb, which is compatible with the inclusive analysis within uncertainties.

This cross section is split into several y regions and together with ALICE results from data measured at forward rapidity a y dependence can be built. The comparison of these data points with theory predictions is in Fig. 6.2.

There are many models able to calculate the UPC cross section dependency on y. All are further described in Chapter 1. The impulse approximation, which computes the nucleus as a sum of free nucleons, obviously overpredicts the data, giving a strong evidence for the existence of dynamical QCD effects, such as nuclear shadowing and gluon saturation. Other models describe the data with partial success. None of the models is able to fit all data at once. Current predictions explain only a combination of very forward and semi-forward or very forward and central rapidity data.

The measurements presented in this thesis highlight specific regions where models are not able to describe data pointing the way to a deeper understanding of pQCD at the high-energy limit.

Table 6.1: A summary table containing all ingredients for the cross section calculation according to Eq. (5.1), measured cross section in UPC in the different p_{T}^2 intervals as well as the photonuclear cross section in $|t|$ intervals. The mean value of p_{T}^2 and $|t|$ in each interval, and the relevant relative statistical and systematic uncertainties are also shown.

p_{T}^2 or $\lvert t\rvert$ (GeV$^2/c^2$)$\times 10^{-3}$	$(0; 0.72)$	$(0.72; 1.6)$	$(1.6; 2.6)$	$(2.6; 4.0)$	$(4.0; 6.2)$	$(6.2; 12.1)$
$N_{\mathrm{J}/\psi}^{\mathrm{fit}}$	569	551	511	469	388	401
$(\mathrm{Acc} \times \epsilon)_{\mathrm{J}/\psi}^{\mathrm{coh}}$	0.0348	0.0352	0.358	0.365	0.379	0.412
f_{I}	0.0045	0.0047	0.0047	0.0072	0.0120	0.0300
f_{D}	0.0039	0.0046	0.0058	0.0072	0.0110	0.0280
$\langle p_{\mathrm{T}}^2 \rangle$ (GeV$^2/c^2$)	0.00027	0.00110	0.00208	0.00328	0.00497	0.00812
$\langle \lvert t\rvert \rangle$ (GeV$^2/c^2$)	0.00032	0.00113	0.00207	0.00328	0.00498	0.00833
$\mathrm{d}^2\sigma_{\mathrm{J}/\psi}^{\mathrm{coh}}/\mathrm{d}y\mathrm{d}p_{\mathrm{T}}^2$ (mbc^2/GeV^2)	1290	1035	743	465	229	51
$\mathrm{d}^2\sigma_{\mathrm{J}/\psi}^{\mathrm{coh}}/\mathrm{d}y\mathrm{d}\lvert t\rvert$ (mbc^2/GeV^2)	1384	978	719	488	251	68
Interference correction	1.13	0.93	0.95	1.03	0.99	0.96
$\mathrm{d}^2\sigma_{\gamma\mathrm{Pb}}/\mathrm{d}\lvert t\rvert$ (mbc^2/GeV^2)	8.15	5.75	4.23	2.87	1.48	0.40
Stat. (%)	5.7	4.5	4.6	5.0	5.7	8.4
Experimental unco. syst. (%)	2.2	0.9	0.7	1.2	1.2	0.8
Experimental corr. syst. (%)	5.6	5.7	5.7	5.8	5.9	6.4
Theoretical syst. (%)	2.4	2.7	2.4	2.7	2.5	6.1

Chapter 7

Summary

Ultra-peripheral collisions were used to study photoproduction of J/ψ in this thesis. The measurement used the Pb beams delivered by the LHC machine and utilised the ALICE apparatus to record collisions of these beams. The J/ψ decay channel into $\mu^+\mu^-$ was analysed and two results were presented; the $|t|$ dependent photonuclear cross section and the y dependent UPC cross section. These two results use the determination of luminosity, which is an independent result. The measurement of the $|t|$ dependency of the J/ψ photonuclear cross section is the very first of its kind and gives us a new tool to explore QCD.

The measured cross sections are presented and discussed in Chapter 6; they put new constraints on the available models, giving an opportunity to reconsider current theories and improve them. A clear indication of the existence of nuclear shadowing was found. Models based on gluon saturation are able to describe most of the data. The same can be said of models based on the leading-twist approximation.

Although the primarily design of the ALICE apparatus is to study the quark-gluon plasma created in head-on collisions of heavy ions, analyses of Run 1 data have proved the possibility to also employ UPCs to study the inner structure of hadrons and nuclei with ALICE. The higher energy, better detector performance and a larger amount of collected data in Run 2 opened the doors for new measurements, which delivered results on the structure of Pb nuclei approaching the quality as those on the structure of protons from HERA [120, 121].

7.1 Outlook

Clearly, decommissioning of HERA in 2007 did not stop scientists to investigate the structure of matter, even though the available tools are not ideal. The time before the Electron-Ion Collider, the next ideal tool [1], becomes operational, will be filled with more Pb–Pb collisions at $\sqrt{s_{\mathrm{NN}}} = 5.02$ TeV delivered by the LHC in the period called Run 3.

Table 7.1: Table of cross sections and expected number of events in 13 nb^{-1} integrated luminosity for the different mesons in Pb–Pb collisions. Taken from Ref. [123] (Table 13).

PbPb				
Meson	σ	All Total	Central 1 Total	Central 2 Total
$\rho \to \pi^+\pi^-$	5.2b	68 B	5.5 B	21B
$\rho' \to \pi^+\pi^-\pi^+\pi^-$	730 mb	9.5 B	210 M	2.5 B
$\phi \to K^+K^-$	0.22b	2.9 B	82 M	490 M
$J/\psi \to \mu^+\mu^-$	1.0 mb	14 M	1.1 M	5.7 M
$\psi' \to \mu^+\mu^-$	30μb	400 K	35 K	180 K
$\Upsilon(1S) \to \mu^+\mu^-$	2.0 μb	26 K	2.8 K	14 K

The delivered luminosity of Pb–Pb in Run 3+4 is expected to be 13 times larger than in Run 2 yielding i.e. more than a million of J/ψ candidates for the analyses (see Tab. 7.1). The improvement in tracking from the upgrades of the ALICE detector [122] promise a much improved accuracy. These will allow us to reduce the statistical and systematic uncertainties in current analyses giving an opportunity to better decide amongst theoretical models or to investigate the effect of amplitude interference. Also, it will be possible to perform new differential measurements, for example to investigate angular dependencies between leptons from the decay of the vector meson.

Ultra-peripheral collisions, and photon-induced processes in general, at the LHC do not only shine light into nuclei, but also illuminate the path to exciting future studies of the nuclear structure.

About author's work

Service Task

One of author's responsibilities as a part of the Ph.D. studies, is to perform a service task for the ALICE collaboration. Since 2017 the task the author performed under the supervision of prof. Martino Gagliardi was to maintain the automatic luminosity and trigger calculation framework, which helped ALICE trigger coordinators to plan data taking. In 2015, in collaboration with the trigger coordinator at that time, Dr. Evgeny Kryshen, this tool was developed as part of the author's Summer Student project. The output of this framework was regularly presented at ALICE run coordination weekly meetings and ALICE collaboration physics weeks.

MFT production database

During the LHC long shutdown between Run 2 and Run 3 the ALICE apparatus was upgraded and a new detector, called the Muon Forward Tracker (MFT), was installed. The detector itself consists of many parts, from a single chip to large staves. These had to be produced and each assembled part had to be tested. Information about these processes had to be stored in a database for future use. The author's contribution was to create a python interface to easily handle these database.

2018 Pb–Pb trigger simulation

The 2018 Pb–Pb data taking period was crucial for the measurements presented in this thesis. Not every collision at the ALICE interaction point is recorded and so-called triggers, which decide which event to keep, are used. There are multiple different trigger classes focusing on different physics topics, which compete for its portion in the limited data output bandwidth. The author's task was to find the best distribution of the bandwidth portions

amongst these triggers to ensure that all ALICE physics tasks would have enough data to fulfil their physics goals. The output of this work was presented at ALICE run coordination meetings and used to plan the trigger settings, which were then used during data taking.

Shifts

The running of the experiment itself needs permanent supervision. This is arranged in shifts, where three operators handle the experiment, each controlling different systems. These shifters work under a shift leader. The author of this thesis took several shifts at different stations during the years of data taking, including the shift when the very first Pb–Pb collisions in 2018, used in this thesis, were taken.

Analysis: Pb–Pb collisions

The main topic of the author's research is the analysis of the production of a J/ψ meson in ultra-peripheral collisions of lead ions at ALICE. The goal, which has been fulfilled, was to measure the cross section dependence of such process on the transferred momentum $|t|$, when the J/ψ was created at midrapidity. The data from 2011 (Run 1 period) have been analysed by ALICE and the cross section dependence on rapidity y was measured [4]. Results were compared to several models and it was found that those with shadowing or with specific saturation prescriptions could successfully describe the measured data. The author's contribution is a new measurement providing an observable which is sensitive to the gluon distribution in the impact-parameter plane. That means, that the author investigated the dependence of the cross section on $|t|$. The p_{T} migration effect takes place during the event reconstruction and the data need to be corrected for it. This is performed using a tool called unfolding. The author tested several different approaches to find the best solution. The description of the problem and the method definitions are given in Chapter 4.

The final result of the analysis is presented in Chapter 6. The result is published in a peer-reviewed scientific journal, Physics Letters B, and is attached to this thesis as Appendix A.

An inclusive analysis of the same data at midrapidity focusing on the y dependency was performed at the same time as the $|t|$ differential analysis. This author has contributed to the y differential analysis with the luminosity calculation, developing the framework for the efficiency calculation and a cross-check of results in the dimuon channel. This analysis has been submitted to a peer-reviewed scientific journal, European Physical Journal C - Particles and Fields, and it is expected to be accepted soon. The article is attached to this thesis as Appendix B.

Analysis: Luminosity determination

An important ingredient to the cross section calculation is the determination of the luminosity of the analysed data sample. The luminosity calculation framework within ALICE is presented in Chapter 3. In order to estimate the correct luminosity, the knowledge of the cross section of a reference detector is needed. This cross section can be measured in a so-called van der Meer scans. The author of this thesis has contributed with luminosity calculations based on the measured cross sections from different reference detectors to investigate the stability of the cross section across the full data taking period and to estimate the corresponding systematic uncertainty. Also, the author has calculated the efficiency of the reference detector for the detection of the inelastic hadronic cross section, which is used to compare the measured values with the theoretical predictions. This measurement has been published as a CERN public note and it will be sent for publication to a peer-reviewed journal, most probably Journal of Instrumentation, soon. The article is attached to this thesis as Appendix C.

List of publications

Publications submitted to peer-reviewed journals

1. S. Acharya *et al.*, "First measurement of the $|t|$-dependence of coherent J/ψ photonuclear production," *Phys. Lett. B*, vol. 817, p. 136280, 2021.

2. S. Acharya *et al.*, "Coherent J/ψ and ψ' photoproduction at midrapidity in ultra-peripheral Pb–Pb collisions at $\sqrt{s_{\mathrm{NN}}} = 5.02$ TeV," arXiv:2101.04577 [nucl-ex], 2021.

3. S. Acharya *et al.*, "ALICE luminosity determination for Pb–Pb collisions at $\sqrt{s_{\mathrm{NN}}} = 5.02$ TeV," tech. rep., CERN, January 2021. ALICE-PUBLIC-2021-001.

Proceedings from conferences

1. R. Lavicka, "Coherent J/ψ photoproduction in ultra-peripheral Pb–Pb collisions with ALICE at the LHC," *J. Phys. Conf. Ser.*, vol. 1390, no. 1,p. 012024, 2019.

Bibliography

[1] A. Accardi et al. "Electron Ion Collider: The Next QCD Frontier: Understanding the glue that binds us all". In: *Eur. Phys. J. A* 52.9 (2016). Ed. by A. Deshpande, Z. E. Meziani, and J. W. Qiu, p. 268. DOI: 10.1140/epja/i2016-16268-9. arXiv: 1212.1701 [nucl-ex].

[2] "LHC Machine". In: *JINST* 3 (2008). Ed. by Lyndon Evans and Philip Bryant, S08001. DOI: 10.1088/1748-0221/3/08/S08001.

[3] Nestor Armesto. "Nuclear shadowing". In: *J. Phys. G* 32 (2006), R367–R394. DOI: 10.1088/0954-3899/32/11/R01. arXiv: hep-ph/0604108.

[4] Betty Abelev et al. "Coherent J/ψ photoproduction in ultra-peripheral Pb-Pb collisions at $\sqrt{s_{\mathrm{NN}}} = 2.76$ TeV". In: *Phys. Lett. B* 718 (2013), pp. 1273–1283. DOI: 10.1016/j.physletb.2012.11.059. arXiv: 1209.3715 [nucl-ex].

[5] E. Abbas et al. "Charmonium and e^+e^- pair photoproduction at mid-rapidity in ultra-peripheral Pb-Pb collisions at $\sqrt{s_{\mathrm{NN}}}$=2.76 TeV". In: *Eur. Phys. J. C* 73.11 (2013), p. 2617. DOI: 10.1140/epjc/s10052-013-2617-1. arXiv: 1305.1467 [nucl-ex].

[6] Jaroslav Adam et al. "Coherent ψ(2S) photo-production in ultra-peripheral Pb Pb collisions at $\sqrt{s_{\mathrm{NN}}} = 2.76$ TeV". In: *Phys. Lett. B* 751 (2015), pp. 358–370. DOI: 10.1016/j.physletb.2015.10.040. arXiv: 1508.05076 [nucl-ex].

[7] Christopher G. Tully. *Elementary particle physics in a nutshell*. Princeton, USA: Univ. Pr., 2011.

[8] Georges Aad et al. "Observation of a new particle in the search for the Standard Model Higgs boson with the ATLAS detector at the LHC". In: *Phys. Lett. B* 716 (2012), pp. 1–29. DOI: 10.1016/j.physletb.2012.08.020. arXiv: 1207.7214 [hep-ex].

[9] Serguei Chatrchyan et al. "Observation of a New Boson at a Mass of 125 GeV with the CMS Experiment at the LHC". In: *Phys. Lett. B* 716 (2012), pp. 30–61. DOI: 10.1016/j.physletb.2012.08.021. arXiv: 1207.7235 [hep-ex].

[10] F. Halzen and Alan D. Martin. *Quarks and Leptons: An Introductory Course in Modern Particle Physics*. New York, USA: Wiley, Jan. 1984. ISBN: 978-0-471-88741-6.

[11] W. N. Cottingham and D. A. Greenwood. *An introduction to the standard model of particle physics*. Cambridge University Press, Apr. 2007. ISBN: 978-0-511-27136-6.

[12] H. David Politzer. "Reliable Perturbative Results for Strong Interactions?" In: *Phys. Rev. Lett.* 30 (1973). Ed. by J. C. Taylor, pp. 1346–1349. DOI: 10.1103/PhysRevLett.30.1346.

[13] David J. Gross and Frank Wilczek. "Ultraviolet Behavior of Nonabelian Gauge Theories". In: *Phys. Rev. Lett.* 30 (1973). Ed. by J. C. Taylor, pp. 1343–1346. DOI: 10.1103/PhysRevLett.30.1343.

[14] H. Abramowicz et al. "Combination of measurements of inclusive deep inelastic $e^{\pm}p$ scattering cross sections and QCD analysis of HERA data". In: *Eur. Phys. J. C* 75.12 (2015), p. 580. DOI: 10.1140/epjc/s10052-015-3710-4. arXiv: 1506.06042 [hep-ex].

[15] J. G. Contreras and J. D. Tapia Takaki. "Ultra-peripheral heavy-ion collisions at the LHC". In: *Int. J. Mod. Phys. A* 30 (2015), p. 1542012. DOI: 10.1142/S0217751X15420129.

[16] S. Munier, A. M. Stasto, and Alfred H. Mueller. "Impact parameter dependent S matrix for dipole proton scattering from diffractive meson electroproduction". In: *Nucl. Phys. B* 603 (2001), pp. 427–445. DOI: 10.1016/S0550-3213(01)00168-7. arXiv: hep-ph/0102291.

[17] J. J. Aubert et al. "Experimental Observation of a Heavy Particle J". In: *Phys. Rev. Lett.* 33 (1974), pp. 1404–1406. DOI: 10.1103/PhysRevLett.33.1404.

[18] J. E. Augustin et al. "Discovery of a Narrow Resonance in e^+e^- Annihilation". In: *Phys. Rev. Lett.* 33 (1974), pp. 1406–1408. DOI: 10.1103/PhysRevLett.33.1406.

[19] P A Zyla et al. "Review of Particle Physics". In: *Prog. Theor. Exp. Phys.* 2020 (2020), p. 083C01. DOI: 10.1093/ptep/ptaa104.

[20] Ramona Vogt. *Ultrarelativistic heavy-ion collisions*. Amsterdam: Elsevier, 2007. ISBN: 978-0-444-52196-5.

[21] Serguei Chatrchyan et al. "Performance of CMS Muon Reconstruction in pp Collision Events at $\sqrt{s} = 7$ TeV". In: *JINST* 7 (2012), P10002. DOI: 10.1088/1748-0221/7/10/P10002. arXiv: 1206.4071 [physics.ins-det].

[22] S. S. M. Wong. *Introductory nuclear physics*. New York, USA: Wiley, 1998.

[23] A. J. Baltz. "The Physics of Ultraperipheral Collisions at the LHC". In: *Phys. Rept.* 458 (2008). Ed. by G. Baur et al., pp. 1–171. DOI: 10.1016/j.physrep.2007.12.001. arXiv: 0706.3356 [nucl-ex].

[24] Carlos A. Bertulani, Spencer R. Klein, and Joakim Nystrand. "Physics of ultra-peripheral nuclear collisions". In: *Ann. Rev. Nucl. Part. Sci.* 55 (2005), pp. 271–310. DOI: 10.1146/annurev.nucl.55.090704.151526. arXiv: nucl-ex/0502005.

[25] Spencer R. Klein and Heikki Mäntysaari. "Imaging the nucleus with high-energy photons". In: *Nature Rev. Phys.* 1.11 (2019), pp. 662–674. DOI: 10.1038/s42254-019-0107-6. arXiv: 1910.10858 [hep-ex].

[26] Gerhard Baur et al. "Coherent gamma gamma and gamma-A interactions in very peripheral collisions at relativistic ion colliders". In: *Phys. Rept.* 364 (2002), pp. 359–450. DOI: 10.1016/S0370-1573(01)00101-6. arXiv: hep-ph/0112211.

[27] J. Cepila, J. G. Contreras, and M. Matas. "Collinearly improved kernel suppresses Coulomb tails in the impact-parameter dependent Balitsky-Kovchegov evolution". In: *Phys. Rev. D* 99.5 (2019), p. 051502. DOI: 10.1103/PhysRevD.99.051502. arXiv: 1812.02548 [hep-ph].

[28] D. Bendova et al. "Solution to the Balitsky-Kovchegov equation with the collinearly improved kernel including impact-parameter dependence". In: *Phys. Rev. D* 100.5 (2019), p. 054015. DOI: 10.1103/PhysRevD.100.054015. arXiv: 1907.12123 [hep-ph].

[29] D. Bendova et al. "Photonuclear J/ψ production at the LHC: proton-based versus nuclear dipole scattering amplitudes". In: *Phys. Lett. B* 817 (2021), p. 136306. DOI: 10.1016/j.physletb.2021.136306. arXiv: 2006.12980 [hep-ph].

[30] Agnieszka Łuszczak and Wolfgang Schäfer. "Coherent photoproduction of J/ψ in nucleus-nucleus collisions in the color dipole approach". In: *Phys. Rev. C* 99.4 (2019), p. 044905. DOI: 10.1103/PhysRevC.99.044905. arXiv: 1901.07989 [hep-ph].

[31] V. Guzey, E. Kryshen, and M. Zhalov. "Coherent photoproduction of vector mesons in ultraperipheral heavy ion collisions: Update for run 2 at the CERN Large Hadron Collider". In: *Phys. Rev. C* 93.5 (2016), p. 055206. DOI: 10.1103/PhysRevC.93.055206. arXiv: 1602.01456 [nucl-th].

[32] K. J. Eskola, H. Paukkunen, and C. A. Salgado. "EPS09: A New Generation of NLO and LO Nuclear Parton Distribution Functions". In: *JHEP* 04 (2009), p. 065. DOI: 10.1088/1126-6708/2009/04/065. arXiv: 0902.4154 [hep-ph].

[33] Jan Cepila, Jesus Guillermo Contreras, and Michal Krelina. "Coherent and incoherent J/ψ photonuclear production in an energy-dependent hot-spot model". In: *Phys. Rev. C* 97.2 (2018), p. 024901. DOI: 10.1103/PhysRevC.97.024901. arXiv: 1711.01855 [hep-ph].

[34] L. Frankfurt, V. Guzey, and M. Strikman. "Leading Twist Nuclear Shadowing Phenomena in Hard Processes with Nuclei". In: *Phys. Rept.* 512 (2012), pp. 255–393. DOI: 10.1016/j.physrep.2011.12.002. arXiv: 1106.2091 [hep-ph].

[35] V. P. Goncalves, B. D. Moreira, and F. S. Navarra. "Investigation of diffractive photoproduction of J/Ψ in hadronic collisions". In: *Phys. Rev. C* 90.1 (2014), p. 015203. DOI: 10.1103/PhysRevC.90.015203. arXiv: 1405.6977 [hep-ph].

[36] G. Sampaio dos Santos and M. V. T. Machado. "On theoretical uncertainty of color dipole phenomenology in the J/ψ and Υ photoproduction in pA and AA collisions at the CERN Large Hadron Collider". In: *J. Phys. G* 42.10 (2015), p. 105001. DOI: 10.1088/0954-3899/42/10/105001. arXiv: 1411.7918 [hep-ph].

[37] V. Guzey et al. "Evidence for nuclear gluon shadowing from the ALICE measurements of PbPb ultraperipheral exclusive J/ψ production". In: *Phys. Lett. B* 726 (2013), pp. 290–295. DOI: 10.1016/j.physletb.2013.08.043. arXiv: 1305.1724 [hep-ph].

[38] T. Lappi and H. Mantysaari. "Incoherent diffractive J/ψ-production in high energy nuclear DIS". In: *Phys. Rev. C* 83 (2011), p. 065202. DOI: 10.1103/PhysRevC.83.065202. arXiv: 1011.1988 [hep-ph].

[39] T. Lappi and H. Mantysaari. "J/ψ production in ultraperipheral Pb+Pb and p+Pb collisions at energies available at the CERN Large Hadron Collider". In: *Phys. Rev. C* 87.3 (2013), p. 032201. DOI: 10.1103/PhysRevC.87.032201. arXiv: 1301.4095 [hep-ph].

[40] Spencer Klein and Joakim Nystrand. "Exclusive vector meson production in relativistic heavy ion collisions". In: *Phys. Rev. C* 60 (1999), p. 014903. DOI: 10.1103/PhysRevC.60.014903. arXiv: hep-ph/9902259.

[41] Spencer R. Klein and Joakim Nystrand. "Photoproduction of quarkonium in proton proton and nucleus nucleus collisions". In: *Phys. Rev. Lett.* 92 (2004), p. 142003. DOI: 10.1103/PhysRevLett.92.142003. arXiv: hep-ph/0311164.

[42] Spencer R. Klein et al. "STARlight: A Monte Carlo simulation program for ultra-peripheral collisions of relativistic ions". In: *Comput. Phys. Commun.* 212 (2017), pp. 258–268. DOI: 10.1016/j.cpc.2016.10.016. arXiv: 1607.03838 [hep-ph].

[43] T. H. Bauer et al. "The Hadronic Properties of the Photon in High-Energy Interactions". In: *Rev. Mod. Phys.* 50 (1978). [Erratum: Rev. Mod. Phys. 51, 407 (1979)], p. 261. DOI: 10.1103/RevModPhys.50.261.

[44] R. J. Glauber. "Theory of high energy hadron-nucleus collisions". In: *3rd International Conference on High-Energy Physics and Nuclear Structure*. 1970, pp. 207–264.

[45] Mariusz Przybycien. "Latest results on diffraction at HERA". In: *EPJ Web Conf.* 182 (2018). Ed. by Y. Aharonov, L. Bravina, and S. Kabana, p. 02102. DOI: 10.1051/epjconf/201818202102.

[46] G. D. Alkhazov, S. L. Belostotsky, and A. A Vorobev. "Scattering of 1-GeV Protons on Nuclei". In: *Phys. Rept.* 42 (1978), pp. 89–144. DOI: 10.1016/0370-1573(78)90083-2.

[47] James Lewis Friar and John W. Negele. "The determination of the nuclear charge distribution of pb-208 from elastic electron scattering and muonic x-rays". In: *Nucl. Phys. A* 212 (1973), pp. 93–137. DOI: 10.1016/0375-9474(73)90039-0.

[48] Salma Alrasheed. "Impulse, Momentum, and Collisions". In: *Principles of Mechanics: Fundamental University Physics*. Cham: Springer International Publishing, 2019, pp. 73–85. ISBN: 978-3-030-15195-9. DOI: 10.1007/978-3-030-15195-9_5. URL: https://doi.org/10.1007/978-3-030-15195-9_5.

[49] Geoffrey F. Chew. "The Inelastic Scattering of High Energy Neutrons by Deuterons According to the Impulse Approximation". In: *Phys. Rev.* 80 (1950), pp. 196–202. DOI: 10.1103/PhysRev.80.196.

[50] Geoffrey F. Chew and Gian Carlo Wick. "The Impulse Approximation". In: *Phys. Rev.* 85.4 (1952), p. 636. DOI: 10.1103/PhysRev.85.636.

[51] Yuri L. Dokshitzer et al. *Basics of perturbative QCD*. Gif-sur-Yvette, France: Ed. Frontieres, 1991. ISBN: 2–86332–101–3.

[52] M. G. Ryskin. "Diffractive J/ψ electroproduction in LLA QCD". In: *Z. Phys. C* 57 (1993), pp. 89–92. DOI: 10.1007/BF01555742.

[53] R. J. Glauber. "Cross-sections in deuterium at high-energies". In: *Phys. Rev.* 100 (1955), pp. 242–248. DOI: 10.1103/PhysRev.100.242.

[54] V. N. Gribov. "Glauber corrections and the interaction between high-energy hadrons and nuclei". In: *Sov. Phys. JETP* 29 (1969), pp. 483–487.

[55] John C. Collins. "Proof of factorization for diffractive hard scattering". In: *Phys. Rev. D* 57 (1998). [Erratum: Phys.Rev.D 61, 019902 (2000)], pp. 3051–3056. DOI: 10.1103/PhysRevD.61.019902. arXiv: hep-ph/9709499.

[56] Javier L. Albacete and Cyrille Marquet. "Gluon saturation and initial conditions for relativistic heavy ion collisions". In: *Prog. Part. Nucl. Phys.* 76 (2014), pp. 1–42. DOI: 10.1016/j.ppnp.2014.01.004. arXiv: 1401.4866 [hep-ph].

[57] J. Cepila, J. G. Contreras, and J. D. Tapia Takaki. "Energy dependence of dissociative J/ψ photoproduction as a signature of gluon saturation at the LHC". In: *Phys. Lett. B* 766 (2017), pp. 186–191. DOI: 10.1016/j.physletb.2016.12.063. arXiv: 1608.07559 [hep-ph].

[58] Krzysztof J. Golec-Biernat and M. Wusthoff. "Saturation effects in deep inelastic scattering at low Q**2 and its implications on diffraction". In: *Phys. Rev. D* 59 (1998), p. 014017. DOI: 10.1103/PhysRevD.59.014017. arXiv: hep-ph/9807513.

[59] I. Balitsky. "Operator expansion for high-energy scattering". In: *Nucl. Phys.* B463 (1996), pp. 99–160. DOI: 10.1016/0550-3213(95)00638-9. arXiv: hep-ph/9509348 [hep-ph].

[60] Yuri V. Kovchegov. "Small$-x$ F_2 structure function of a nucleus including multiple pomeron exchanges". In: *Phys. Rev.* D60 (1999), p. 034008. DOI: 10.1103/PhysRevD.60.034008. arXiv: hep-ph/9901281 [hep-ph].

[61] J. Bartels, Krzysztof J. Golec-Biernat, and H. Kowalski. "A modification of the saturation model: DGLAP evolution". In: *Phys. Rev. D* 66 (2002), p. 014001. DOI: 10.1103/PhysRevD.66.014001. arXiv: hep-ph/0203258.

[62] V. N. Gribov and L. N. Lipatov. "Deep inelastic e p scattering in perturbation theory". In: *Sov. J. Nucl. Phys.* 15 (1972), pp. 438–450.

[63] Guido Altarelli and G. Parisi. "Asymptotic Freedom in Parton Language". In: *Nucl. Phys. B* 126 (1977), pp. 298–318. DOI: 10.1016/0550-3213(77)90384-4.

[64] E. Iancu, K. Itakura, and S. Munier. "Saturation and BFKL dynamics in the HERA data at small x". In: *Phys. Lett. B* 590 (2004), pp. 199–208. DOI: 10.1016/j.physletb.2004.02.040. arXiv: hep-ph/0310338.

[65] H. Kowalski, L. Motyka, and G. Watt. "Exclusive diffractive processes at HERA within the dipole picture". In: *Phys. Rev. D* 74 (2006), p. 074016. DOI: 10.1103/PhysRevD.74.074016. arXiv: hep-ph/0606272.

[66] I. I. Balitsky and L. N. Lipatov. "The Pomeranchuk Singularity in Quantum Chromodynamics". In: *Sov. J. Nucl. Phys.* 28 (1978), pp. 822–829.

[67] E. A. Kuraev, L. N. Lipatov, and Victor S. Fadin. "The Pomeranchuk Singularity in Nonabelian Gauge Theories". In: *Sov. Phys. JETP* 45 (1977), pp. 199–204.

[68] N. Armesto. "A Simple model for nuclear structure functions at small x in the dipole picture". In: *Eur. Phys. J. C* 26 (2002), pp. 35–43. DOI: 10.1007/s10052-002-1021-z. arXiv: hep-ph/0206017.

[69] Henri Kowalski and Derek Teaney. "An Impact parameter dipole saturation model". In: *Phys. Rev. D* 68 (2003), p. 114005. DOI: 10.1103/PhysRevD.68.114005. arXiv: hep-ph/0304189.

[70] K. Aamodt et al. "The ALICE experiment at the CERN LHC". In: *JINST* 3 (2008), S08002. DOI: 10.1088/1748-0221/3/08/S08002.

[71] Betty Bezverkhny Abelev et al. "Performance of the ALICE Experiment at the CERN LHC". In: *Int. J. Mod. Phys. A* 29 (2014), p. 1430044. DOI: 10.1142/S0217751X14300440. arXiv: 1402.4476 [nucl-ex].

[72] Shreyasi Acharya et al. *ALICE Figure Repository (2021, May 18)*. ALICE Collaboration web. URL: https://alice-figure.web.cern.ch.

[73] A. Kluge et al. "The ALICE on-detector pixel PILOT system - OPS". In: *7th Workshop on Electronics for LHC Experiments*. Sept. 2001.

[74] E.C. Villar. "The AD detector array: a new tool for studying diffractive physics at the ALICE experiment". MA thesis. Pontifical Catholic University of Peru, Lima, 2015. URL: http://hdl.handle.net/20.500.12404/6155.

[75] E. Cerron Zeballos et al. "A New type of resistive plate chamber: The Multigap RPC". In: *Nucl. Instrum. Meth. A* 374 (1996), pp. 132–136. DOI: 10.1016/0168-9002(96)00158-1.

[76] E. Abbas et al. "Performance of the ALICE VZERO system". In: *JINST* 8 (2013), P10016. DOI: 10.1088/1748-0221/8/10/P10016. arXiv: 1306.3130 [nucl-ex].

[77] Betty Abelev et al. "Measurement of the Cross Section for Electromagnetic Dissociation with Neutron Emission in Pb-Pb Collisions at $\sqrt{s_{NN}} = 2.76$ TeV". In: *Phys. Rev. Lett.* 109 (2012), p. 252302. DOI: 10.1103/PhysRevLett.109.252302. arXiv: 1203.2436 [nucl-ex].

[78] K. Akiba et al. "LHC Forward Physics". In: *J. Phys. G* 43 (2016), p. 110201. DOI: 10.1088/0954-3899/43/11/110201. arXiv: 1611.05079 [hep-ph].

[79] M. Broz et al. "Performance of ALICE AD modules in the CERN PS test beam". In: (June 2020). arXiv: 2006.14982 [physics.ins-det].

[80] R. Brun and F. Rademakers. "ROOT: An object oriented data analysis framework". In: *Nucl. Instrum. Meth. A* 389 (1997). Ed. by M. Werlen and D. Perret-Gallix. See also "ROOT" [software], Release v6.18/04, 22/09/2019, pp. 81–86. DOI: 10.5281/zenodo.3457396. URL: https://zenodo.org/record/3457396#.YAf57tYo9jE.

[81] Shreyasi Acharya et al. *The list of ALICE Physics Working Groups (2021, January 20)*. ALICE Collaboration web. URL: https://alice-collaboration.web.cern.ch/organization/phb/index.html.

[82] René Brun et al. *GEANT: detector description and simulation tool; Oct 1994*. CERN Program Library. Long Writeup W5013. Geneva: CERN, 1993. DOI: 10.17181/CERN.MUHF.DMJ1. URL: http://cds.cern.ch/record/1082634.

[83] Shreyasi Acharya et al. *ALICE Data Preparation Group (DPG) (2021, March 17)*. ALICE Collaboration web. URL: https://alice-offline.web.cern.ch/Activities/alice-data-preparation-group.

[84] Christian Møller. "General Properties of the Characteristic Matrix in the Theory of Elementary Particles". In: *D. Kgl. Danske Vidensk. Selsk. Mat.-Fys. Medd.* 23.1 (1945).

[85] Olivier Napoly. "The Luminosity for beam distributions with error and wake field effects in linear colliders". In: *Part. Accel.* 40 (1993), pp. 181–203.

[86] W. Herr and B. Muratori. "Concept of luminosity". In: *CERN Accelerator School and DESY Zeuthen: Accelerator Physics*. Sept. 2003, pp. 361–377.

[87] P. Antonioli, A. Kluge, and W. Riegler. *Upgrade of the ALICE Readout & Trigger System*. Tech. rep. 2013. ISRN: CERN-LHCC-2013-019, ALICE-TDR-015.

[88] Roy D. Yates and David J. Goodman. *Probability and Stochastic Processes: A Friendly Introduction for Electrical and Computer Engineers (2nd ed.)* New York, USA: Wiley, 2014.

[89] Alex Gurevich. "Theory of RF superconductivity for resonant cavities". In: *Supercond. Sci. Technol.* 30.3 (2017), p. 034004. DOI: 10.1088/1361-6668/30/3/034004.

[90] Shreyasi Acharya et al. *ALICE luminosity determination for Pb–Pb collisions at $\sqrt{s_{\mathrm{NN}}}$ = 5.02 TeV*. Tech. rep. CERN, Jan. 2021. ISRN: ALICE-PUBLIC-2021-001. URL: https://cds.cern.ch/record/2749127.

[91] S. van der Meer. *Calibration of the Effective Beam Height in the ISR*. Tech. rep. June 1968. ISRN: CERN-ISR-PO-68-31.

[92] Vladislav Balagura. "Notes on van der Meer Scan for Absolute Luminosity Measurement". In: *Nucl. Instrum. Meth. A* 654 (2011), pp. 634–638. DOI: 10.1016/j.nima.2011.06.007. arXiv: 1103.1129 [physics.ins-det].

[93] Vladislav Balagura. "Van der Meer scan luminosity measurement and beam–beam correction". In: *Eur. Phys. J. C* 81.1 (2021), p. 26. DOI: 10.1140/epjc/s10052-021-08837-y. arXiv: 2012.07752 [hep-ex].

[94] C. J. Clopper and E. S. Pearson. "The use of confidence or fiducial limits illustrated in the case of the binomial". In: *Biometrika* 26.4 (Dec. 1934), pp. 404–413. ISSN: 0006-3444. DOI: 10.1093/biomet/26.4.404. eprint: https://academic.oup.com/biomet/article-pdf/26/4/404/823407/26-4-404.pdf. URL: https://doi.org/10.1093/biomet/26.4.404.

[95] V. Guzey, M. Strikman, and M. Zhalov. "Accessing transverse nucleon and gluon distributions in heavy nuclei using coherent vector meson photoproduction at high energies in ion ultraperipheral collisions". In: *Phys. Rev. C* 95.2 (2017), p. 025204. DOI: 10.1103/PhysRevC.95.025204. arXiv: 1611.05471 [hep-ph].

[96] G. Cowan. *Statistical data analysis*. Oxford Science Publications, 1998. ISBN: 978-0-19-850156-5.

[97] G. Cowan. "A survey of unfolding methods for particle physics". In: *Conf. Proc. C* 0203181 (2002). Ed. by M. R. Whalley and L. Lyons, pp. 248–257.

[98] Florian Huber. "Elastic and Proton Dissociative J/ψ Photoproduction at low $W_{\gamma p}$ with the H1 Detector at HERA". PhD thesis. Heidelberg U., 2012.

[99] Andreas Hocker and Vakhtang Kartvelishvili. "SVD approach to data unfolding". In: *Nucl. Instrum. Meth. A* 372 (1996), pp. 469–481. DOI: 10.1016/0168-9002(95)01478-0. arXiv: hep-ph/9509307.

[100] G. D'Agostini. "A Multidimensional unfolding method based on Bayes' theorem". In: *Nucl. Instrum. Meth. A* 362 (1995), pp. 487–498. DOI: 10.1016/0168-9002(95)00274-X.

[101] G. D'Agostini. "Improved iterative Bayesian unfolding". In: *Alliance Workshop on Unfolding and Data Correction*. Oct. 2010. arXiv: 1010.0632 [physics.data-an].

[102] Georgios Choudalakis. "Fully Bayesian Unfolding". In: (Jan. 2012). arXiv: 1201.4612 [physics.data-an].

[103] Stefan Schmitt. "TUnfold: an algorithm for correcting migration effects in high energy physics". In: *JINST* 7 (2012), T10003. DOI: 10.1088/1748-0221/7/10/T10003. arXiv: 1205.6201 [physics.data-an].

[104] Tim Adye. "Unfolding algorithms and tests using RooUnfold". In: *PHYSTAT 2011*. Geneva: CERN, 2011, pp. 313–318. DOI: 10.5170/CERN-2011-006.313. arXiv: 1105.1160 [physics.data-an].

[105] Volker Blobel. "An Unfolding method for high-energy physics experiments". In: *Conference on Advanced Statistical Techniques in Particle Physics*. Aug. 2002, pp. 258–267. arXiv: hep-ex/0208022.

[106] David L. Phillips. "A Technique for the Numerical Solution of Certain Integral Equations of the First Kind". In: *J. Assoc. Comput. Machinery* 9.1 (1962), pp. 84–97. DOI: 10.1145/321105.321114.

[107] Harrison B. Prosper and Louis Lyons, eds. *Proceedings, PHYSTAT 2011 Workshop on Statistical Issues Related to Discovery Claims in Search Experiments and Unfolding, CERN,Geneva, Switzerland 17-20 January 2011*. CERN Yellow Reports: Conference Proceedings. Geneva: CERN, Jan. 2011. DOI: 10.5170/CERN-2011-006.

[108] Thomas Bayes Rev. "An essay toward solving a problem in the doctrine of chances". In: *Phil. Trans. Roy. Soc. Lond.* 53 (1764), pp. 370–418. DOI: 10.1098/rstl.1763.0053.

[109] Doreen Wackeroth and Leila Belkora. *High Energy Physics Made Painless: Cross Section (2021, March 12)*. Fermilab Collaboration web. https://ed.fnal.gov/painless/pdfs/cross.pdf.

[110] M. Oreglia. "A Study of the Reactions $\psi' \to \gamma\gamma\psi$". SLAC Report SLAC-R-236, Appendix D. PhD thesis. Stanford University, 1980. URL: https://www.slac.stanford.edu/cgi-bin/getdoc/slac-r-236.pdf.

[111] C. Alexa et al. "Elastic and proton-dissociative photoproduction of J/ψ mesons at HERA". In: *Eur. Phys. J.* C73.6 (2013), p. 2466. DOI: 10.1140/epjc/s10052-013-2466-y. arXiv: 1304.5162 [hep-ex].

[112] I.A. Pshenichnov et al. "Particle emission following Coulomb excitation in ultrarelativistic heavy ion collisions". In: *Phys. Rev. C* 60 (1999), p. 044901. DOI: 10.1103/PhysRevC.60.044901. arXiv: nucl-th/9901061.

[113] I. A. Pshenichnov. "Electromagnetic excitation and fragmentation of ultrarelativistic nuclei". In: *Phys. Part. Nucl.* 42 (2011), pp. 215–250. DOI: 10.1134/S1063779611020067.

[114] Kai Hencken, Dirk Trautmann, and Gerhard Baur. "Photon-photon luminosities in relativistic heavy ion collisions at LHC energies". In: *Z. Phys. C* 68 (1995), pp. 473–480. DOI: 10.1007/BF01620724. arXiv: nucl-th/9503004.

[115] B.I. Abelev et al. "Observation of Two-source Interference in the Photoproduction Reaction Au Au —> Au Au rho0". In: *Phys. Rev. Lett.* 102 (2009), p. 112301. DOI: 10.1103/PhysRevLett.102.112301. arXiv: 0812.1063 [nucl-ex].

[116] J. G. Contreras. "Gluon shadowing at small x from coherent J/ψ photoproduction data at energies available at the CERN Large Hadron Collider". In: *Phys. Rev. C* 96.1 (2017), p. 015203. DOI: 10.1103/PhysRevC.96.015203. arXiv: 1610.03350 [nucl-ex].

[117] Shreyasi Acharya et al. "Coherent J/ψ photoproduction at forward rapidity in ultra-peripheral Pb-Pb collisions at $\sqrt{s_{\mathrm{NN}}} = 5.02$ TeV". In: *Phys. Lett. B* 798 (2019), p. 134926. DOI: 10.1016/j.physletb.2019.134926. arXiv: 1904.06272 [nucl-ex].

[118] Shreyasi Acharya et al. "First measurement of the $|t|$-dependence of coherent J/ψ photonuclear production". In: *Phys. Lett. B* 817 (2021), p. 136280. DOI: 10.1016/j.physletb.2021.136280. arXiv: 2101.04623 [nucl-ex].

[119] Shreyasi Acharya et al. "Coherent J/ψ and ψ' photoproduction at midrapidity in ultra-peripheral Pb-Pb collisions at $\sqrt{s_{\mathrm{NN}}} = 5.02$ TeV". In: (Jan. 2021). arXiv: 2101.04577 [nucl-ex].

[120] B. H. Wiik. "HERA: Accelerator performance and physics results". In: *International School of Subnuclear Physics: 31st Course: From Supersymmetry to the Origin of Space-Time*. 1993.

[121] Paul Newman and Matthew Wing. "The Hadronic Final State at HERA". In: *Rev. Mod. Phys.* 86.3 (2014), p. 1037. DOI: 10.1103/RevModPhys.86.1037. arXiv: 1308.3368 [hep-ex].

[122] B Abelev et al. “Upgrade of the ALICE Experiment: Letter Of Intent”. In: *J. Phys. G* 41 (2014), p. 087001. DOI: 10.1088/0954-3899/41/8/087001.

[123] Z. Citron et al. “Report from Working Group 5: Future physics opportunities for high-density QCD at the LHC with heavy-ion and proton beams”. In: *CERN Yellow Rep. Monogr.* 7 (2019). Ed. by Andrea Dainese et al., pp. 1159–1410. DOI: 10.23731/CYRM-2019-007.1159. arXiv: 1812.06772 [hep-ph].

Appendix A

Published work: $|t|$-dependent photoproduction

Physics Letters B 817 (2021) 136280

Contents lists available at ScienceDirect

Physics Letters B

www.elsevier.com/locate/physletb

First measurement of the $|t|$-dependence of coherent J/ψ photonuclear production

ALICE Collaboration *

ARTICLE INFO

Article history:
Received 24 January 2021
Received in revised form 17 March 2021
Accepted 6 April 2021
Available online 15 April 2021
Editor: M. Doser

ABSTRACT

The first measurement of the cross section for coherent J/ψ photoproduction as a function of $|t|$, the square of the momentum transferred between the incoming and outgoing target nucleus, is presented. The data were measured with the ALICE detector in ultra-peripheral Pb–Pb collisions at a centre-of-mass energy per nucleon pair $\sqrt{s_{\rm NN}} = 5.02$ TeV with the J/ψ produced in the central rapidity region $|y| < 0.8$, which corresponds to the small Bjorken-x range $(0.3 - 1.4) \times 10^{-3}$.

The measured $|t|$-dependence is not described by computations based only on the Pb nuclear form factor, while the photonuclear cross section is better reproduced by models including shadowing according to the leading-twist approximation, or gluon-saturation effects from the impact-parameter dependent Balitsky–Kovchegov equation. These new results are therefore a valid tool to constrain the relevant model parameters and to investigate the transverse gluonic structure at very low Bjorken-x.

1. Introduction

Photonuclear reactions can be studied in ultra-peripheral collisions (UPCs) of heavy ions where the two projectiles pass each other with an impact parameter larger than the sum of their radii. In this case, purely hadronic interactions are suppressed and electromagnetically induced processes occur via photons with typically very small virtualities, of the order of tens of MeV^2. The intensity of the photon flux is proportional to the square of the electric charge of the nuclei, resulting in large cross sections for the coherent photoproduction of a vector meson in UPCs of Pb ions at the LHC. This process has a clear experimental signature: the decay products of the vector meson are the only particles detected in an otherwise empty detector.

The physics of vector meson photoproduction is described, e.g., in Refs. [1–4]. Two vector meson photoproduction processes, coherent and incoherent, are relevant for the results presented here. In the former, the photon interacts with all nucleons in a nucleus, while in the latter it interacts with a single nucleon. In both cases a single vector meson is produced. Experimentally, one can distinguish between these two production types through the transverse momentum $p_{\rm T}$ of the vector meson which is related to the transverse size of the target. While coherent photoproduction is characterised by an average transverse momentum $\langle p_{\rm T} \rangle \sim 60$ MeV/c, incoherent production leads to higher average transverse momenta: $\langle p_{\rm T} \rangle \sim 500$ MeV/c. Incoherent photoproduction can also be accompanied by the excitation and dissociation of the target nucleon resulting in an even higher transverse momentum of the produced vector meson [5].

Shadowing, the observation that the structure of a nucleon inside nuclear matter is different from that of a free nucleon [6], is not yet completely understood and several processes may have a role in different kinematic regions. In this context, coherent heavy vector meson photoproduction is of particular interest, because it is especially sensitive to the gluon distribution in the target, and thus to gluon shadowing effects at low Bjorken-x [7,8]. One of the effects expected to contribute to shadowing in this kinematic region is saturation, a dynamic equilibrium between gluon radiation and recombination [9]. The momentum scale of the interaction (Q^2) is related to the mass m_V of the vector meson as $Q^2 \sim m_V^2/4$, corresponding to the perturbative regime of quantum chromodynamics (QCD) in the case of charmonium states. The rapidity of the coherently produced $c\bar{c}$ states is related to the Bjorken-x of the gluonic exchange as $x = \left(m_V/\sqrt{s_{\rm NN}}\right) \exp(\pm y)$, where the two signs indicate that either of the incoming ions can be the source of the photon. Thus, the charmonium photoproduction cross section at midrapidity in Pb–Pb UPCs at the LHC Run 2 centre-of-mass energy per nucleon pair of $\sqrt{s_{\rm NN}} = 5.02$ TeV is sensitive to $x \in (0.3, 1.4) \times 10^{-3}$ at ALICE. It thereby provides information on the gluon distribution in nuclei in a kinematic region where shadowing could be present and saturation effects may be important [10,11].

Charmonium photoproduction in ultra-peripheral Pb–Pb collisions was previously studied by the ALICE Collaboration at $\sqrt{s_{\rm NN}} = 2.76$ TeV [12–14]. The coherent J/ψ photoproduction cross section was measured both at midrapidity $|y| < 0.9$ and at forward

* *E-mail address:* alice-publications@cern.ch.

https://doi.org/10.1016/j.physletb.2021.136280

rapidity $-3.6 < y < -2.6$. Recently, a measurement of the rapidity dependence of coherent J/ψ photoproduction at forward rapidity at the higher energy of $\sqrt{s_{\rm NN}} = 5.02$ TeV was also published by the ALICE Collaboration [15]. In addition, the CMS Collaboration studied the coherent J/ψ photoproduction accompanied by neutron emission at semi-forward rapidity $1.8 < |y| < 2.3$ at $\sqrt{s_{\rm NN}} = 2.76$ TeV [16]. These measurements allow for a deeper insight into the rapidity dependence of gluon shadowing, but do not give information on the behaviour of gluons in the impact-parameter plane. The square of the momentum transferred to the target nucleus, $|t|$, is related through a two-dimensional Fourier transform to the gluon distribution in the plane transverse to the interaction [17]; thus the study of the $|t|$-dependence of coherent J/ψ photoproduction provides information about the spatial distribution of gluons as a function of the impact parameter. Thus far, the only measurements in this direction were performed recently by the STAR Collaboration for the case of the ρ^0 vector meson [18] and for the yield of J/ψ in semi-central Au–Au collisions [19].

In this Letter, the first measurement of the $|t|$-dependence of the coherent J/ψ photoproduction cross section at midrapidity in Pb–Pb UPCs at $\sqrt{s_{\rm NN}} = 5.02$ TeV is presented. The J/ψ vector mesons were reconstructed in the rapidity range $|y| < 0.8$ through their decay into $\mu^+\mu^-$, taking advantage of the better mass and momentum resolution of this channel with respect to the e^+e^- channel. The data sample, recorded in 2018, is approximately 10 times larger than that used in previous ALICE measurements at midrapidity at the lower energy of $\sqrt{s_{\rm NN}} = 2.76$ TeV [14]. Cross sections are reported for six $|t|$ intervals and compared with theoretical predictions.

2. Detector description

The ALICE detector and its performance are described in Refs. [20,21]. Three central barrel detectors, the Inner Tracking System (ITS), the Time Projection Chamber (TPC), and the Time-of-Flight (TOF), in addition to two forward detectors, V0 and the ALICE Diffractive (AD) arrays, are used in this analysis. The central barrel detectors are surrounded by a large solenoid magnet producing a magnetic field of $B = 0.5$ T. The V0, AD, ITS, and TOF detectors are used for triggering, the ITS and the TPC for particle tracking, and the TPC for particle identification.

The V0 is a scintillator detector made of two counters, V0A and V0C, installed on both sides of the interaction point. The V0A and V0C cover the pseudorapidity ranges $2.8 < \eta < 5.1$ and $-3.7 < \eta < -1.7$, respectively. Both counters are segmented in four rings in the radial direction, with each ring divided into 8 sections in azimuth.

The AD consists of two scintillator stations, ADA and ADC, located at 16 and -19 m along the beam line with respect to the nominal interaction point and covering the pseudorapidity ranges $4.8 < \eta < 6.3$ and $-7.0 < \eta < -4.9$, respectively [22,23].

The ITS is a silicon based detector and is made of six cylindrical layers using three different technologies. The Silicon Pixel Detector (SPD) forms the two innermost layers of the ITS and covers $|\eta| < 2$ and $|\eta| < 1.4$, respectively. Apart from tracking, the SPD is also used for triggering purposes and to reconstruct the primary vertex.

The ITS is cylindrically surrounded by the TPC, whose main purpose is to track particles and provide charged-particle momentum measurements with good two-track separation and particle identification. The TPC coverage in pseudorapidity is $|\eta| < 0.9$ for tracks with full radial length. The TPC has full coverage in azimuth. It offers good momentum resolution in a large range of the track transverse momentum spanning from 0.1 GeV/c to 100 GeV/c.

The TOF is a large cylindrical gaseous detector based on multi-gap resistive-plate chambers. It covers the pseudorapidity region $|\eta| < 0.8$. The TOF readout channels are arranged into 18 azimuthal sectors which can provide topological trigger decisions.

3. Data analysis

3.1. Event selection

The online event selection was based on a dedicated UPC trigger which selected back-to-back tracks in an otherwise empty detector. This selection required (i) that nothing above the trigger threshold was detected in the V0 and AD detectors, (ii) a topological trigger requiring less than eight SPD chips with trigger signal, forming at least two pairs; each pair was required to have an SPD chip fired in each of the two layers and to be in compatible azimuthal sectors, with an opening angle in azimuth between the two pairs larger than 144°, (iii) a topological trigger in the TOF requiring more than one and less than seven TOF sectors to register a signal; at least two of these sectors should have an opening angle in azimuth larger than 150°.

The integrated luminosity of the analysed sample is 233 μb^{-1}. The determination of the luminosity is obtained from the counts of a reference trigger based on multiplicity selection in the V0 detector, with the corresponding cross section estimated from a van der Meer scan; this procedure has an uncertainty of 2.2% [24]. The determination of the live-time of the UPC trigger has an additional uncertainty of 1.5%. The total relative systematic uncertainty of the integrated luminosity is thus 2.7%.

Additional offline V0 and AD veto decisions were applied in the analysis. The offline veto algorithm improved the signal to background ratio, because it utilised a larger timing window to integrate the signal than its online counterpart. Some good events were lost due to this selection. The loss was taken into account with the correction on veto trigger inefficiency discussed in Sec. 3.4. The systematic uncertainty from the V0 and AD vetoes was estimated as the relative change in the measured J/ψ cross section before and after imposing them and correcting for the losses; it amounts to 3%.

Each event had a reconstructed primary vertex within 15 cm from the nominal interaction point along the beam direction, z, and had exactly two tracks. These tracks were reconstructed using combined tracking in the ITS and TPC. Tracks were requested to have at least 70 (out of 159) TPC space points and to have a hit in each of the two layers of the SPD. Each track had to have a distance of closest approach to the event interaction vertex of less than 2 cm in the z-axis direction. Also, each track was required to have $|\eta| < 0.9$. The relative systematic uncertainty from tracking, which takes into account the track quality selection and the track propagation from the TPC to the ITS, was estimated from a comparison of data and Monte Carlo simulation. The combined uncertainty to reconstruct both tracks is 2.8%.

The particle identification (PID) was provided by the specific ionisation losses in the TPC, which offer a large separation power between muons and electrons from the leptonic decays of the J/ψ in the momentum range (1.0, 2.0) GeV/c, relevant for this analysis. The effect of a possible misidentification was found to be negligible.

An offline SPD decision was also applied in the analysis. The offline topological SPD algorithm ensured that the selected tracks crossed the SPD chips used in the trigger decision. The relative systematic uncertainty from the SPD and TOF trigger amounts to 1.3%, which was estimated using a data-driven method by changing the requirements on the probe tracks.

The selected events were required to have tracks with opposite electric charge, the rapidity of the dimuon candidate was restricted to $|y| < 0.8$ and its $p_{\rm T}$ had to be less than 0.11 GeV/c, in order to obtain a sample dominated by coherent interactions

with just a small contamination from incoherent processes. The measurement was initially carried out in p_{T}^2 intervals, because for collider kinematics $|t| \approx p_{\mathrm{T}}^2$. The corrections needed to obtain the $|t|$-dependence are discussed in Sec. 3.7.

3.2. Signal extraction

As a first step in extracting the coherent J/ψ signal, a fit to the opposite sign dimuon invariant mass distribution was performed. The model used to fit the data consists of three templates: one Crystal Ball function [25] (CB) to describe the J/ψ resonance, a second CB function to describe the ψ' resonance, and an exponential function to describe the continuum production of muon pairs, $\gamma\gamma \to \mu^+\mu^-$.

The parameters of the exponential function were left free. The integral of this exponential in the mass range $(3.0, 3.2)$ GeV/c^2 was used to determine the number of events from the continuum production in this interval.

The CB parameters describing the tails of the measured distribution in data, commonly known as α and n, were fixed to the values obtained while fitting the dimuon invariant mass distribution in an associated Monte Carlo simulation, which is described in Sec. 3.4. These settings were employed for both CB functions.

The number of J/ψ candidates in each p_{T}^2 interval was obtained from an extended maximum likelihood fit to the unbinned invariant mass distribution of all $\mu^+\mu^-$ pairs which survived the selection criteria described in Sec. 3.1. Results of the fits for the six p_{T}^2 intervals are shown in Fig. 1. In all cases a very clear J/ψ resonance is seen over a fairly small background. Note that the effect on the kinematics from a potential dimuon decay including bremsstrahlung is negligible.

The relative systematic uncertainty from the signal extraction was calculated by repeating the fit over different invariant mass ranges, and modifying the CB α and n parameters accordingly. These uncertainties vary in the interval (0.7,2.2)%.

3.3. Corrections for irreducible backgrounds

The selection criteria described above are not sensitive to events which mimic the signature of coherent J/ψ production, but are coming from feed-down of ψ' or incoherent production. The contribution of these events was taken into account with the f_{D} and f_{I} factors, respectively, entering Eq. (1),

$$N_{\mathrm{J}/\psi}^{\mathrm{coh}} = \frac{N^{\mathrm{fit}}}{1 + f_{\mathrm{I}} + f_{\mathrm{D}}} \times \frac{1}{(\mathrm{Acc} \times \varepsilon)_{\mathrm{J}/\psi}^{\mathrm{coh}}}, \tag{1}$$

where N^{fit}, the yield of J/ψ candidates, is the integral of the CB describing the J/ψ signal in the fit of the dimuon invariant mass spectrum, and $(\mathrm{Acc} \times \varepsilon)_{\mathrm{J}/\psi}^{\mathrm{coh}}$ is the acceptance and efficiency correction factor described in Sec. 3.4.

Feed-down refers to the decay of a ψ' to a J/ψ plus anything else, where these additional particles were not detected for some reason. The correction for these events, f_{D}, was estimated with Monte Carlo simulations describing the apparatus $(\mathrm{Acc} \times \varepsilon)$ factor for the following channels: $\mathrm{J}/\psi \to \mu^+\mu^-$, $\psi' \to \mu^+\mu^-$, and $\psi' \to \mathrm{J}/\psi + X$; and the measured ratio of ψ' to J/ψ production cross sections. The details of the method are described in Ref. [15]. The results for each p_{T}^2 interval are summarised in Table 1. Relative systematic uncertainties, estimated by using different cross section ratios, are p_{T}^2-correlated. Their relative effect on the final cross section can be found in Table 2; it is well below 1%.

Most of the incoherent production of J/ψ off nucleons was rejected with the restriction of the phase space in p_{T}, as mentioned in Sec. 3.1. However, around 5% of all incoherent events remained in the region where the measurement was performed. To estimate the f_{I} factor to correct for the remaining incoherent events, a fit to the measured J/ψ p_{T} distribution of data in the invariant mass range $(3.0, 3.2)$ GeV/c^2 was used. The model fitted to the data consists of six templates: coherent J/ψ photoproduction, incoherent J/ψ photoproduction, incoherent J/ψ photoproduction with nucleon dissociation, coherent ψ' photoproduction, incoherent ψ' photoproduction, and continuum production from $\gamma\gamma \to \mu^+\mu^-$. The templates of all, but dissociative J/ψ and continuum, were taken from Monte Carlo simulations. In the fit, the fractions of both ψ' photoproduction processes were fixed to values calculated as described above. These included the modifications that the p_{T} restriction was released and that there was a selection on the invariant mass to be in the range $(3.6, 3.8)$ GeV/c^2. Other fractions were left free in the fit. The normalisation of the continuum was restricted from the invariant mass fit to be the sum of background events in the mass range of the J/ψ. The shape of the continuum was taken from the dimuon p_{T} distribution selecting the invariant mass range between the J/ψ and the ψ', while the shape for the nucleon dissociation process was based on the H1 parameterisation [26]. The global template was fitted to data using an extended maximum likelihood unbinned fit. The results for each p_{T}^2 interval are reported in Table 1. The systematic uncertainties, estimated from a combination of the fit uncertainty and a modification of the coherent template used in the fitting model are p_{T}-correlated. Their relative effect on the final cross section can be found in Table 2.

Table 1
Incoherent correction f_{I}, feed-down correction f_{D} and the $(\mathrm{Acc} \times \varepsilon)_{\mathrm{J}/\psi}^{\mathrm{coh}}$ correction factor for each p_{T}^2 interval. See Eq. (1).

p_{T}^2 interval (GeV$^2/c^2$)	f_{I}	f_{D}	$(\mathrm{Acc} \times \varepsilon)_{\mathrm{J}/\psi}^{\mathrm{coh}}$
(0, 0.00072)	0.0045	0.0039	0.0348
(0.00072, 0.0016)	0.0047	0.0046	0.0352
(0.0016, 0.0026)	0.0047	0.0058	0.0358
(0.0026, 0.004)	0.0072	0.0072	0.0365
(0.004, 0.0062)	0.0120	0.011	0.0379
(0.0062, 0.0121)	0.0300	0.028	0.0412

Table 2
Summary of the identified systematic uncertainties on the coherent J/ψ photoproduction and photonuclear cross sections. The uncertainties to go from the measured cross section in UPCs to the photonuclear process are listed after the line in the middle of the table and their origin depends on the modeling of the photon flux and interference effects. The correlation across p_{T}^2 intervals is discussed in the text.

Source	Uncertainty (%)
Signal extraction	(0.7, 2.2)
f_{D}	(0.1, 0.5)
f_{I}	(1.1, 2.3)
p_{T}^2 migration unfolding	(0.6, 2.3)
Luminosity	2.7
V0 and AD veto	3
EM dissociation	2
ITS-TPC tracking	2.8
SPD and TOF efficiency	1.3
Branching ratio	0.5
Variations in interference strength	(0.3, 1.2)
Value of the photon flux at $y = 0$	2
$p_{\mathrm{T}}^2 \to \lvert t \rvert$ unfolding	(0.1, 5.7)

3.4. Acceptance, efficiency and pile-up corrections

The STARlight 2.2.0 MC generator [27] was used to generate samples of coherent and incoherent events for the production of $\mathrm{J}/\psi \to \mu^+\mu^-$ and $\psi' \to \mu^+\mu^- + \pi^+\pi^-(\pi^0\pi^0)$. GEANT 3.21 [28]

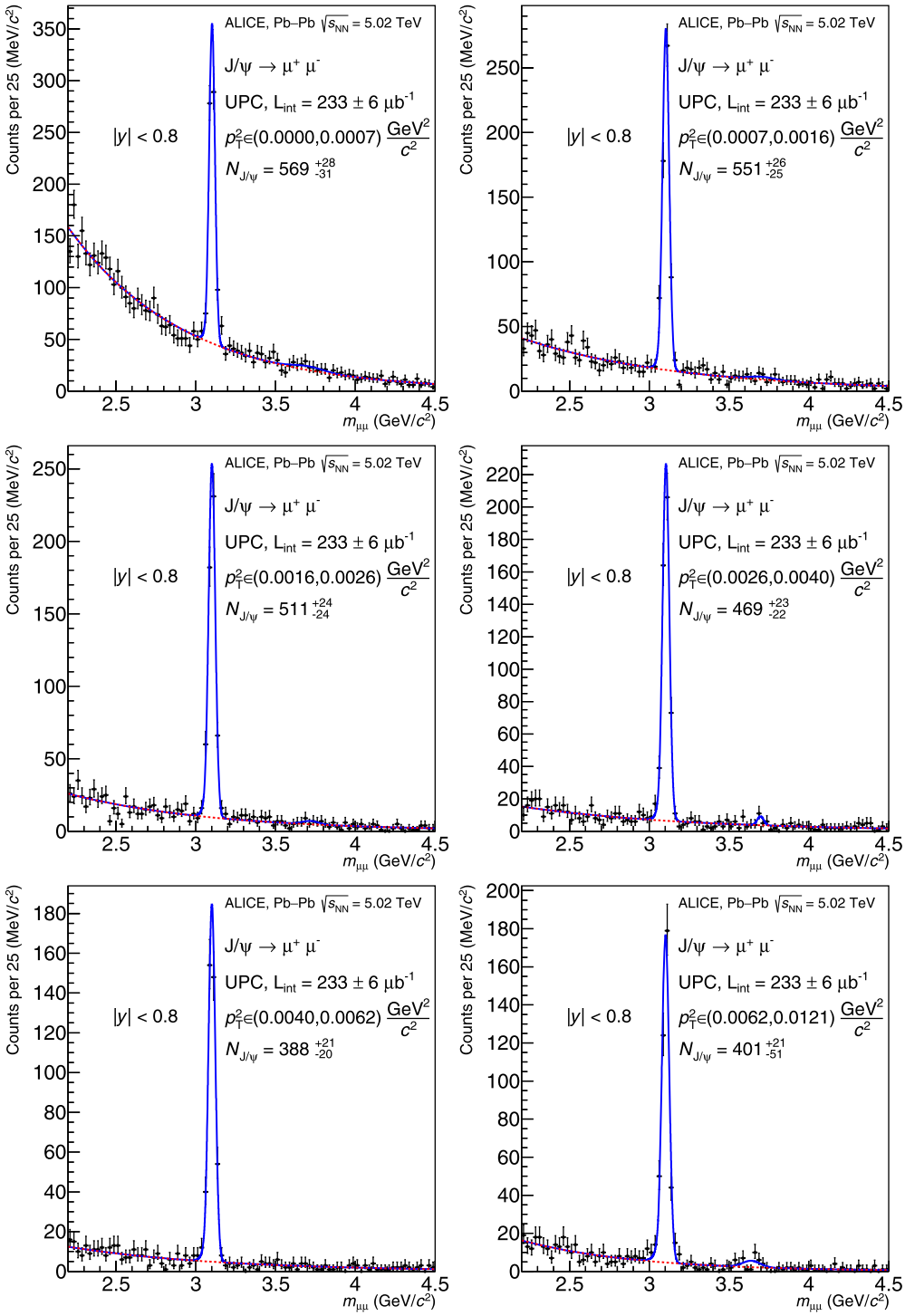

Fig. 1. Invariant-mass distributions for different p_T^2 intervals with the global fit described in the text shown with the blue line. The exponential part of the fit model, representing the $\gamma\gamma \to \mu^+\mu^-$ background, is shown in red.

was used to reproduce the response of the detector. The simulated data were reconstructed with the same software as the real ones, accounting for actual data-taking conditions. Values of the acceptance and efficiency, $(\mathrm{Acc} \times \varepsilon)^{\mathrm{coh}}_{J/\psi}$, are shown in Table 1 for the different p_T^2 intervals used in this analysis.

AD and V0 were used to veto activity at forward rapidity. These detectors were sensitive to signals coming from independent interactions (pile-up), which resulted in the rejection of potentially interesting events. The correction factor for this effect was obtained using a control sample of events collected with an unbiased trigger. These were then used to compute the probability of having a veto from AD or V0 in otherwise empty events. The total veto trigger efficiency $\varepsilon^{\mathrm{VETO}}$ used in Eq. (2) was determined to be 0.94. The corresponding systematic uncertainty is included in the AD and V0 value of 3% mentioned in Sec. 3.1.

Electromagnetic dissociation (EMD) is another process which may cause the rejection of a good event due to the veto from the forward detectors. EMD can occur when photons excite one or both interacting nuclei. Upon de-excitation, neutrons and sometimes other charged particles are emitted at forward rapidities [29]

and can trigger a V0 or AD veto. Such loss of events was quantified from data gathered with a specialized EMD trigger; the efficiency correction factor to take into account these losses amounts to $\varepsilon^{\mathrm{EMD}} = 0.92$ with a relative systematic uncertainty of 2% given by the statistical uncertainty from the control sample.

3.5. Unfolding of the p_{T}^2 distribution

Cross sections were measured in different p_{T}^2 intervals. In order to account for the migration of about 45% of the events across p_{T}^2 intervals due to the finite resolution of the detector, an unfolding procedure was used. The effect of migrations are much more important than the small difference between the data and MC p_{T}^2 spectra, so no re-weighting has been performed previous to unfolding.

Amongst many available methods, unfolding based on Bayes' theorem [30] was chosen to perform the unfolding, while the singular-value decomposition (SVD) method [31] served to study potential systematic effects. The implementations of these methods as provided by RooUnfold [32] were used in this analysis.

Bayesian unfolding is an iterative method, therefore the result depends on the number of iterations. The size of the data sample is large enough to investigate different numbers of p_{T}^2 ranges. These two parameters, that is the number of iterations and of ranges, were tuned using Monte Carlo simulations by studying the evolution of the statistical uncertainty in each interval as a function of the number of iterations, and by using the relative difference between iteration-adjacent results. It was found that the best combination for this analysis is Bayes' unfolding with three iterations applied to the p_{T}^2 distribution split into six regions. The widths of the p_{T}^2 intervals were chosen to have similar statistical uncertainties in each region.

The Monte Carlo sample used for unfolding contained 600 000 events. An 80% fraction of them was used to train the response matrix which is used to unfold the true distribution from the measured distribution. This matrix was tested on the remaining 20% of the events. The unfolding matrix was able to correct the smeared distribution with high precision. Comparison with results using the SVD method revealed a p_{T}-correlated relative systematic uncertainty with values in the interval $(0.6, 2.3)\%$.

3.6. Cross section for coherent J/ψ photoproduction in UPCs

The differential cross section for coherent J/ψ photoproduction in a given p_{T}^2 interval and a given rapidity range Δy in Pb–Pb UPCs is

$$\frac{\mathrm{d}^2\sigma^{\mathrm{coh}}_{\mathrm{J}/\psi}}{\mathrm{d}y\mathrm{d}p_{\mathrm{T}}^2} = \frac{{}^{\mathrm{unf}}N^{\mathrm{coh}}_{\mathrm{J}/\psi}}{\varepsilon^{\mathrm{VETO}} \times \varepsilon^{\mathrm{EMD}} \times \mathrm{BR}(\mathrm{J}/\psi \to \mu^+\mu^-) \times \mathscr{L}_{\mathrm{int}} \times \Delta p_{\mathrm{T}}^2 \times \Delta y}, \quad (2)$$

where the correction factors $\varepsilon^{\mathrm{VETO}}$ and $\varepsilon^{\mathrm{EMD}}$ are introduced in Sec. 3.4, $\mathrm{BR}(\mathrm{J}/\psi \to \mu^+\mu^-)$ is the branching ratio $(5.961 \pm 0.033)\%$ [33], $\mathscr{L}_{\mathrm{int}}$ is the total integrated luminosity of the data sample, Δp_{T}^2 is the size of the interval where the measurement was performed, and finally, ${}^{\mathrm{unf}}N^{\mathrm{coh}}_{\mathrm{J}/\psi}$ is the number of coherent J/ψ candidates after unfolding the results given by Eq. (1). The corresponding systematic uncertainties are summarised in the upper part of Table 2. With the exception of signal extraction, all other systematic uncertainties mentioned up to here are correlated across p_{T}^2 intervals.

3.7. Corrections for the photonuclear cross section

The cross section described by Eq. (2) is the one measured by ALICE. The main theoretical interest is in the photonuclear process at a fixed energy. To obtain the corresponding cross section, one has to account for several effects. None of these effects is affected by the ALICE detector, they just depend on the kinematics and quantum nature of the process. This means that the uncertainties in going from the UPC to the photonuclear cross sections are of theoretical nature only.

At midrapidity, the UPC cross section corresponds to the γPb cross section multiplied by twice the photon flux averaged over the impact parameter, $n_{\gamma\mathrm{Pb}}(y)$,

$$\left.\frac{\mathrm{d}^2\sigma^{\mathrm{coh}}_{\mathrm{J}/\psi}}{\mathrm{d}y\mathrm{d}p_{\mathrm{T}}^2}\right|_{y=0} = 2n_{\gamma\mathrm{Pb}}(y=0)\frac{\mathrm{d}\sigma_{\gamma\mathrm{Pb}}}{\mathrm{d}|t|}. \quad (3)$$

Since the rapidity dependence of the UPC cross section in the rapidity range studied here is fairly flat, the measurements are taken to represent the value at $y = 0$. In UPCs, there are two potential photon sources, so in principle both amplitudes have to be added and their interference needs to be accounted. This was studied for the first time in Ref. [34] and later measured for the case of ρ^0 coherent photoproduction by the STAR Collaboration [35]. The interference is important only at very small values of $|t|$ (see for example [36]). To account for this effect, the STARlight program, which includes the interference of both amplitudes, was used. It was found that this is an 11.6% effect in the smallest $|t|$ interval, where the effect is concentrated. To estimate the potential uncertainty on this procedure, the interference effects with the nominal strength were compared to those with a 25% reduction of the strength. The relative change in the photonuclear cross section varied from 0.3 to 1.2% with the largest uncertainty being assigned to the smallest $|t|$ interval.

The photon flux was computed in the semiclassical formalism following the prescription detailed in Ref. [37] and cross checked with that of Ref. [38]. The flux amounts to 84.9 with an uncertainty of 2% coming from variations of the geometry of the Pb ions.

Although the value of p_{T}^2 is a good approximation to that of $|t|$, it is not exact due to the fact that the photon also has a transverse momentum in the laboratory frame. To account for this effect, the cross section was unfolded with a response matrix built from p_{T}^2- and $|t|$-distributions. Two sources for the distributions were used: (i) the STARlight generator which includes the transverse momenta of the photons, but does not describe so well the shape of the measured p_{T}^2 distribution in data, and (ii) measured p_{T}^2 values coupled to photon momenta randomly generated using the transverse momentum distribution of photons from Refs. [39,40]. The average of the corresponding unfolded results was used for the cross section, while half their difference was taken as a systematic uncertainty which varied between 0.1% and 5.7%, with this last value corresponding to the largest $|t|$ interval.

These three uncertainties are reported in the lower part of Table 2. The uncertainty on the value of the photon flux at $y = 0$ is correlated across $|t|$, the uncertainty on the $p_{\mathrm{T}}^2 \to |t|$ unfolding is partially correlated and the uncertainty on the variation of the interference term is anti-correlated in the lowest $|t|$ region and correlated in the other $|t|$ regions. They are added in quadrature for the final result shown in Sec. 4 and Table 3 below.

4. Results

The final result for the cross section measured in each p_{T}^2 interval is reported in Table 3. The statistical uncertainty originates from the error obtained in the fit to the dimuon invariant-mass

Table 3
Measured coherent J/ψ photoproduction cross section in UPCs in different p_{T}^2 intervals as well as the photonuclear cross section in $|t|$-intervals. The first uncertainty is statistical, the second and third systematic, uncorrelated and correlated, respectively. The fourth uncertainty, for the photonuclear cross section case, is the systematic uncertainty on the correction to go from the UPC to the photonuclear cross section. The mean value of $|t|$ in each interval is also shown.

Interval (GeV$^2c^{-2}$)	$\langle\|t\|\rangle$ (GeV$^2c^{-2}$)	$\frac{\mathrm{d}^2\sigma^{\mathrm{coh}}_{J/\psi}}{\mathrm{d}y\mathrm{d}p_{\mathrm{T}}^2}$ ($\frac{\mathrm{mbc}^2}{\mathrm{GeV}^2}$)	$\frac{\mathrm{d}\sigma_{\gamma\mathrm{Pb}}}{\mathrm{d}\|t\|}$ ($\frac{\mathrm{mbc}^2}{\mathrm{GeV}^2}$)
$(0, 0.72) \times 10^{-3}$	0.00032	$1290 \pm 74 \pm 29 \pm 73$	$8.15 \pm 0.50 \pm 0.18 \pm 0.46 \pm 0.20$
$(0.72, 1.6) \times 10^{-3}$	0.00113	$1035 \pm 47 \pm 10 \pm 60$	$5.75 \pm 0.27 \pm 0.06 \pm 0.34 \pm 0.16$
$(1.6, 2.6) \times 10^{-3}$	0.00207	$743 \pm 34 \pm 6 \pm 43$	$4.23 \pm 0.20 \pm 0.03 \pm 0.25 \pm 0.11$
$(2.6, 4.0) \times 10^{-3}$	0.00328	$465 \pm 24 \pm 6 \pm 27$	$2.87 \pm 0.15 \pm 0.04 \pm 0.17 \pm 0.08$
$(4.0, 6.2) \times 10^{-3}$	0.00498	$229 \pm 14 \pm 3 \pm 14$	$1.48 \pm 0.09 \pm 0.02 \pm 0.09 \pm 0.04$
$(6.2, 12.1) \times 10^{-3}$	0.00833	$51 \pm 5 \pm 1 \pm 4$	$0.40 \pm 0.04 \pm 0.01 \pm 0.03 \pm 0.03$

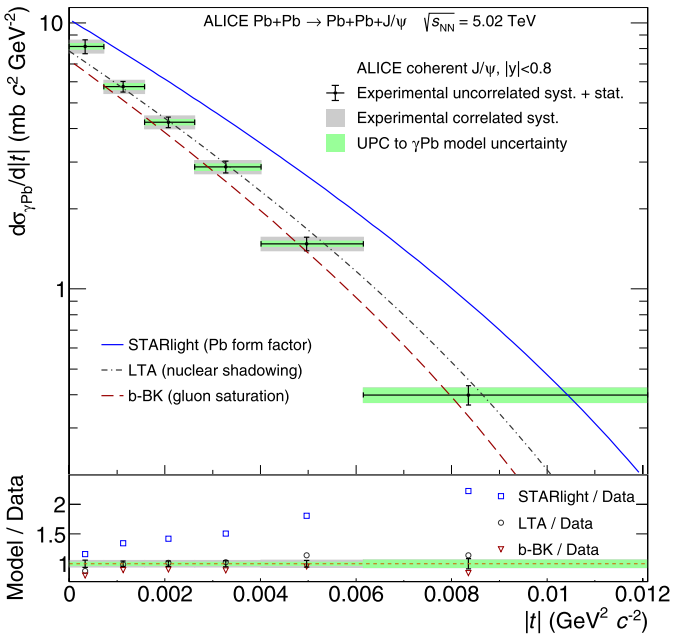

Fig. 2. Dependence on $|t|$ of the photonuclear cross section for the coherent photoproduction of J/ψ off Pb compared with model predictions [10,11,27] (top panel), where for LTA the *low shadowing* case is shown (see text). Model to data ratio for each prediction in each measured point (bottom panel). The uncertainties are split to those originating from experiment and to those originating from the correction to go from the UPC to the photonuclear cross section.

distribution, propagating the uncertainties of the f_{I} and f_{D} corrections, see Eq. (1), and the uncertainty related to the unfolding process. The uncorrelated systematic uncertainty from signal extraction and the quadratic sum of correlated systematic uncertainties are shown in Table 3.

The results for the photonuclear cross section are listed in Table 3 and shown in Fig. 2, where the measurement is compared with several theoretical predictions. The average $|t|$ ($\langle|t|\rangle$) quoted in Table 3 was estimated from the $|t|$-distribution used in the response matrix based on measured data (see above). The mean of the ensuing distribution in a given p_{T}^2 interval was taken to be $\langle|t|\rangle$.

STARlight utilises the vector meson dominance model and a parameterisation of the existing data on exclusive photoproduction of J/ψ off protons coupled with a Glauber-like formalism to obtain the photonuclear cross section. Since the $|t|$-dependence in this model comes from the Glauber calculation, meaning that it does not include explicitly gluon shadowing effects, it is an interesting baseline for comparisons (this approach is quite similar to the impulse approximation used in [41]). STARlight overestimates the measured cross section and the shape of the distribution appears to be wider than that of the measured data.

The LTA prediction by Guzey, Strikman and Zhalov [10] is based on the leading-twist approximation (LTA) of nuclear shadowing based on the combination of the Gribov–Glauber theory and inclusive diffractive data from HERA [42]. There are two LTA predictions; one called *high shadowing* and the other *low shadowing*. The low shadowing prediction is shown in Fig. 2. The shape obtained from this model is similar to that of the data and describes the cross section within experimental uncertainties. As shown in Fig. 3 of [10], the high-shadowing version of the model has a similar shape but the overall normalisation is smaller by factor around 1.7.

The b-BK model by Bendova et al. [11,43,44] is based on the colour dipole approach where the scattering amplitude is obtained from the impact-parameter dependent solution of the Balitsky–Kovchegov equation coupled to a nuclear-like initial condition [45,46] which incorporates saturation effects. This model also predicts the behaviour of the data quite well.

The different predictions of the STARlight and LTA or b-BK models reflect the effects of QCD dynamics (shadowing in LTA, saturation in b-BK) at small values of $x \sim 10^{-3}$ and highlight the importance of measuring the $|t|$-dependence of the photonuclear cross section.

5. Conclusions

The first measurement of the $|t|$-dependence of coherent J/ψ photonuclear production off Pb nuclei in UPCs is presented. The measurement was carried out with the ALICE detector at midrapidity, $|y| < 0.8$, in ultra-peripheral Pb–Pb collisions at $\sqrt{s_{\mathrm{NN}}} = 5.02$ TeV and covers the small-x range $(0.3 - 1.4) \times 10^{-3}$. Photonuclear cross sections in six different intervals of $|t|$ are reported and compared with theoretical predictions. The measured cross section shows a $|t|$-dependent shape different from a model based on the Pb nuclear form factor and closer to the shape predicted by models including QCD dynamical effects in the form of shadowing (LTA) or saturation (b-BK). The difference in shape and magnitude between the LTA and b-BK models is of the same order as the current measurement uncertainties, but the large data sample expected in the LHC Run 3 [47] and the improvement in tracking from the upgrades of the ALICE detector [48] promise a much improved accuracy. These results highlight the importance of observables sensitive to the transverse gluonic structure of particles for extending the understanding of the high-energy limit of QCD.

Declaration of competing interest

The authors declare that they have no known competing financial interests or personal relationships that could have appeared to influence the work reported in this paper.

Acknowledgements

The ALICE Collaboration would like to thank all its engineers and technicians for their invaluable contributions to the construction of the experiment and the CERN accelerator teams for the outstanding performance of the LHC complex. The ALICE Collaboration gratefully acknowledges the resources and support provided by all Grid centres and the Worldwide LHC Computing Grid (WLCG) collaboration. The ALICE Collaboration acknowledges the following funding agencies for their support in building and running the ALICE detector: A. I. Alikhanyan National Science Laboratory (Yerevan Physics Institute) Foundation (ANSL), State Committee of Science and World Federation of Scientists (WFS), Armenia; Austrian Academy of Sciences, Austrian Science Fund (FWF): [M 2467-N36] and Österreichische Nationalstiftung für Forschung, Technologie und Entwicklung, Austria; Ministry of Communications and High Technologies, National Nuclear Research Center, Azerbaijan; Conselho Nacional de Desenvolvimento Científico e Tecnológico (CNPq), Financiadora de Estudos e Projetos (Finep), Fundação de Amparo à Pesquisa do Estado de São Paulo (FAPESP) and Universidade Federal do Rio Grande do Sul (UFRGS), Brazil; Ministry of Education of China (MOEC), Ministry of Science & Technology of China (MSTC) and National Natural Science Foundation of China (NSFC), China; Ministry of Science and Education and Croatian Science Foundation, Croatia; Centro de Aplicaciones Tecnológicas y Desarrollo Nuclear (CEADEN), Cubaenergía, Cuba; Ministry of Education, Youth and Sports of the Czech Republic and Czech Science Foundation, Czech Republic; The Danish Council for Independent Research Natural Sciences, the Villum Fonden and Danish National Research Foundation (DNRF), Denmark; Helsinki Institute of Physics (HIP), Finland; Commissariat à l'Énergie Atomique (CEA) and Institut National de Physique Nucléaire et de Physique des Particules (IN2P3) and Centre National de la Recherche Scientifique (CNRS), France; Bundesministerium für Bildung und Forschung (BMBF) and GSI Helmholtzzentrum für Schwerionenforschung GmbH, Germany; General Secretariat for Research and Technology, Ministry of Education, Research and Religions, Greece; National Research, Development and Innovation Office, Hungary; Department of Atomic Energy, Government of India (DAE), Department of Science and Technology, Government of India (DST), University Grants Commission, Government of India (UGC) and Council of Scientific and Industrial Research (CSIR), India; Indonesian Institute of Sciences, Indonesia; Istituto Nazionale di Fisica Nucleare (INFN), Italy; Institute for Innovative Science and Technology, Nagasaki Institute of Applied Science (IIST), Japanese Ministry of Education, Culture, Sports, Science and Technology (MEXT) and Japan Society for the Promotion of Science (JSPS) KAKENHI, Japan; Consejo Nacional de Ciencia (CONACYT) y Tecnología, through Fondo de Cooperación Internacional en Ciencia y Tecnología (FONCICYT) and Dirección General de Asuntos del Personal Academico (DGAPA), Mexico; Nederlandse Organisatie voor Wetenschappelijk Onderzoek (NWO), Netherlands; The Research Council of Norway, Norway; Commission on Science and Technology for Sustainable Development in the South (COMSATS), Pakistan; Pontificia Universidad Católica del Perú, Peru; Ministry of Science and Higher Education, National Science Centre and WUT ID-UB, Poland; Korea Institute of Science and Technology Information and National Research Foundation of Korea (NRF), Republic of Korea; Ministry of Education and Scientific Research, Institute of Atomic Physics and Ministry of Research and Innovation and Institute of Atomic Physics, Romania; Joint Institute for Nuclear Research (JINR), Ministry of Education and Science of the Russian Federation, National Research Centre Kurchatov Institute, Russian Science Foundation and Russian Foundation for Basic Research, Russia; Ministry of Education, Science, Research and Sport of the Slovak Republic, Slovakia; National Research Foundation of South Africa, South Africa; Swedish Research Council (VR) and Knut & Alice Wallenberg Foundation (KAW), Sweden; European Organization for Nuclear Research, Switzerland; Suranaree University of Technology (SUT), National Science and Technology Development Agency (NSDTA) and Office of the Higher Education Commission under NRU project of Thailand, Thailand; Turkish Atomic Energy Agency (TAEK), Turkey; National Academy of Sciences of Ukraine, Ukraine; Science and Technology Facilities Council (STFC), United Kingdom; National Science Foundation of the United States of America (NSF) and United States Department of Energy, Office of Nuclear Physics (DOE NP), United States of America.

References

[1] C.A. Bertulani, S.R. Klein, J. Nystrand, Physics of ultra-peripheral nuclear collisions, Annu. Rev. Nucl. Part. Sci. 55 (2005) 271–310, arXiv:nucl-ex/0502005.
[2] A. Baltz, The physics of ultraperipheral collisions at the LHC, Phys. Rep. 458 (2008) 1–171, arXiv:0706.3356 [nucl-ex].
[3] J.G. Contreras, J.D. Tapia Takaki, Ultra-peripheral heavy-ion collisions at the LHC, Int. J. Mod. Phys. A 30 (2015) 1542012.
[4] S.R. Klein, H. Mäntysaari, Imaging the nucleus with high-energy photons, Nat. Rev. Phys. 1 (11) (2019) 662–674, arXiv:1910.10858 [hep-ex].
[5] V. Guzey, M. Strikman, M. Zhalov, Nucleon dissociation and incoherent J/ψ photoproduction on nuclei in ion ultraperipheral collisions at the Large Hadron Collider, Phys. Rev. C 99 (1) (2019) 015201, arXiv:1808.00740 [hep-ph].
[6] N. Armesto, Nuclear shadowing, J. Phys. G 32 (2006) R367–R394, arXiv:hep-ph/0604108.
[7] M. Ryskin, Diffractive J/ψ electroproduction in LLA QCD, Z. Phys. C 57 (1993) 89–92.
[8] V. Rebyakova, M. Strikman, M. Zhalov, Coherent ρ and J/ψ photoproduction in ultraperipheral processes with electromagnetic dissociation of heavy ions at RHIC and LHC, Phys. Lett. B 710 (2012) 647–653, arXiv:1109.0737 [hep-ph].
[9] J.L. Albacete, C. Marquet, Gluon saturation and initial conditions for relativistic heavy ion collisions, Prog. Part. Nucl. Phys. 76 (2014) 1–42, arXiv:1401.4866 [hep-ph].
[10] V. Guzey, M. Strikman, M. Zhalov, Accessing transverse nucleon and gluon distributions in heavy nuclei using coherent vector meson photoproduction at high energies in ion ultraperipheral collisions, Phys. Rev. C 95 (2) (2017) 025204, arXiv:1611.05471 [hep-ph].
[11] D. Bendova, J. Cepila, J.G. Contreras, M. Matas, Photonuclear J/ψ production at the LHC: proton-based versus nuclear dipole scattering amplitudes, arXiv:2006.12980 [hep-ph].
[12] ALICE Collaboration, B. Abelev, et al., Coherent J/ψ photoproduction in ultra-peripheral Pb-Pb collisions at $\sqrt{s_{\rm NN}} = 2.76$ TeV, Phys. Lett. B 718 (2013) 1273–1283, arXiv:1209.3715 [nucl-ex].
[13] ALICE Collaboration, E. Abbas, et al., Charmonium and e^+e^- pair photoproduction at mid-rapidity in ultra-peripheral Pb-Pb collisions at $\sqrt{s_{\rm NN}} = 2.76$ TeV, Eur. Phys. J. C 73 (11) (2013) 2617, arXiv:1305.1467 [nucl-ex].
[14] ALICE Collaboration, J. Adam, et al., Coherent $\psi(2S)$ photo-production in ultra-peripheral Pb Pb collisions at $\sqrt{s_{\rm NN}} = 2.76$ TeV, Phys. Lett. B 751 (2015) 358–370, arXiv:1508.05076 [nucl-ex].
[15] ALICE Collaboration, S. Acharya, et al., Coherent J/ψ photoproduction at forward rapidity in ultra-peripheral Pb-Pb collisions at $\sqrt{s_{\rm NN}} = 5.02$ TeV, Phys. Lett. B 798 (2019) 134926, arXiv:1904.06272 [nucl-ex].
[16] CMS Collaboration, V. Khachatryan, et al., Coherent J/ψ photoproduction in ultra-peripheral PbPb collisions at $\sqrt{s_{\rm NN}} = 2.76$ TeV with the CMS experiment, Phys. Lett. B 772 (2017) 489–511, arXiv:1605.06966 [nucl-ex].
[17] J. Bartels, K.J. Golec-Biernat, K. Peters, On the dipole picture in the nonforward direction, Acta Phys. Pol. B 34 (2003) 3051–3068, arXiv:hep-ph/0301192.
[18] STAR Collaboration, L. Adamczyk, et al., Coherent diffractive photoproduction of ρ^0 mesons on gold nuclei at 200 GeV/nucleon-pair at the Relativistic Heavy Ion Collider, Phys. Rev. C 96 (5) (2017) 054904, arXiv:1702.07705 [nucl-ex].
[19] STAR Collaboration, J. Adam, et al., Observation of excess J/ψ yield at very low transverse momenta in Au+Au collisions at $\sqrt{s_{\rm NN}} = 200$ GeV and U+U collisions at $\sqrt{s_{\rm NN}} = 193$ GeV, Phys. Rev. Lett. 123 (13) (2019) 132302, arXiv:1904.11658 [hep-ex].
[20] ALICE Collaboration, K. Aamodt, et al., The ALICE experiment at the CERN LHC, J. Instrum. 3 (2008), S08002.
[21] ALICE Collaboration, B.B. Abelev, et al., Performance of the ALICE Experiment at the CERN LHC, Int. J. Mod. Phys. A 29 (2014) 1430044, arXiv:1402.4476 [nucl-ex].
[22] LHC Forward Physics Working Group Collaboration, K. Akiba, et al., LHC forward physics, J. Phys. G 43 (2016) 110201, arXiv:1611.05079 [hep-ph].
[23] M. Broz, et al., Performance of ALICE AD modules in the CERN PS test beam, arXiv:2006.14982 [physics.ins-det].
[24] ALICE Collaboration, ALICE luminosity determination for Pb–Pb, collisions at $\sqrt{s_{\rm NN}} = 5.02$ TeV, ALICE-PUBLIC-2021-001.

[25] M. Oreglia, A Study of the Reactions $\psi' \to \gamma\gamma\psi$, PhD thesis, Stanford University, 1980, https://www.slac.stanford.edu/cgi-bin/getdoc/slac-r-236.pdf, SLAC Report SLAC-R-236, Appendix D.
[26] H1 Collaboration, C. Alexa, et al., Elastic and proton-dissociative photoproduction of J/ψ mesons at HERA, Eur. Phys. J. C 73 (6) (2013) 2466, arXiv:1304.5162 [hep-ex].
[27] S.R. Klein, J. Nystrand, J. Seger, Y. Gorbunov, J. Butterworth, STARlight: a Monte Carlo simulation program for ultra-peripheral collisions of relativistic ions, Comput. Phys. Commun. 212 (2017) 258–268, arXiv:1607.03838 [hep-ph].
[28] R. Brun, F. Bruyant, F. Carminati, S. Giani, M. Maire, A. McPherson, G. Patrick, L. Urban, GEANT: detector description and simulation tool, Oct 1994, in: CERN Program Library, CERN, Geneva, 1993, http://cds.cern.ch/record/1082634, Long Writeup W5013.
[29] I. Pshenichnov, I. Mishustin, J. Bondorf, A. Botvina, A. Ilinov, Particle emission following Coulomb excitation in ultrarelativistic heavy ion collisions, Phys. Rev. C 60 (1999) 044901, arXiv:nucl-th/9901061.
[30] G. D'Agostini, A multidimensional unfolding method based on Bayes' theorem, Nucl. Instrum. Methods A 362 (1995) 487–498.
[31] A. Hocker, V. Kartvelishvili, SVD approach to data unfolding, Nucl. Instrum. Methods A 372 (1996) 469–481, arXiv:hep-ph/9509307.
[32] T. Adye, Unfolding algorithms and tests using RooUnfold, in: PHYSTAT 2011, CERN, Geneva, 2011, pp. 313–318, arXiv:1105.1160 [physics.data-an].
[33] Particle Data Group Collaboration, P.A. Zyla, et al., Review of particle physics, Prog. Theor. Exp. Phys. 2020 (2020), 083C01.
[34] S.R. Klein, J. Nystrand, Interference in exclusive vector meson production in heavy ion collisions, Phys. Rev. Lett. 84 (2000) 2330–2333, arXiv:hep-ph/9909237.
[35] STAR Collaboration, B. Abelev, et al., Observation of two-source interference in the photoproduction reaction $AuAu \to AuAu\rho^0$, Phys. Rev. Lett. 102 (2009) 112301, arXiv:0812.1063 [nucl-ex].
[36] W. Zha, S.R. Klein, R. Ma, L. Ruan, T. Todoroki, Z. Tang, Z. Xu, C. Yang, Q. Yang, S. Yang, Coherent J/ψ photoproduction in hadronic heavy-ion collisions, Phys. Rev. C 97 (4) (2018) 044910, arXiv:1705.01460 [nucl-th].
[37] J.G. Contreras, Gluon shadowing at small x from coherent J/ψ photoproduction data at energies available at the CERN Large Hadron Collider, Phys. Rev. C 96 (1) (2017) 015203, arXiv:1610.03350 [nucl-ex].
[38] M. Broz, J.G. Contreras, J.D. Tapia Takaki, A generator of forward neutrons for ultra-peripheral collisions: $\mathbf{n}^0_0\mathbf{n}$, Comput. Phys. Commun. 253 (2020) 107181, arXiv:1908.08263 [nucl-th].
[39] M. Vidovic, M. Greiner, C. Best, G. Soff, Impact parameter dependence of the electromagnetic particle production in ultrarelativistic heavy ion collisions, Phys. Rev. C 47 (1993) 2308–2319.
[40] K. Hencken, D. Trautmann, G. Baur, Photon-photon luminosities in relativistic heavy ion collisions at LHC energies, Z. Phys. C 68 (1995) 473–480, arXiv:nucl-th/9503004.
[41] V. Guzey, M. Zhalov, Exclusive J/ψ production in ultraperipheral collisions at the LHC: constrains on the gluon distributions in the proton and nuclei, J. High Energy Phys. 10 (2013) 207, arXiv:1307.4526 [hep-ph].
[42] L. Frankfurt, V. Guzey, M. Strikman, Leading twist nuclear shadowing phenomena in hard processes with nuclei, Phys. Rep. 512 (2012) 255–393, arXiv:1106.2091 [hep-ph].
[43] J. Cepila, J.G. Contreras, M. Matas, Collinearly improved kernel suppresses Coulomb tails in the impact-parameter dependent Balitsky–Kovchegov evolution, Phys. Rev. D 99 (5) (2019) 051502, arXiv:1812.02548 [hep-ph].
[44] D. Bendova, J. Cepila, J.G. Contreras, M. Matas, Solution to the Balitsky–Kovchegov equation with the collinearly improved kernel including impact-parameter dependence, Phys. Rev. D 100 (5) (2019) 054015, arXiv:1907.12123 [hep-ph].
[45] I. Balitsky, Operator expansion for high-energy scattering, Nucl. Phys. B 463 (1996) 99–160, arXiv:hep-ph/9509348 [hep-ph].
[46] Y.V. Kovchegov, Small-x F_2 structure function of a nucleus including multiple pomeron exchanges, Phys. Rev. D 60 (1999) 034008, arXiv:hep-ph/9901281 [hep-ph].
[47] Z. Citron, et al., Report from Working Group 5: future physics opportunities for high-density QCD at the LHC with heavy-ion and proton beams, CERN Yellow Rep. Monogr. 7 (2019) 1159–1410, arXiv:1812.06772 [hep-ph].
[48] ALICE Collaboration, B. Abelev, et al., Upgrade of the ALICE experiment: letter of intent, J. Phys. G 41 (2014) 087001.

ALICE Collaboration

S. Acharya [142], D. Adamová [97], A. Adler [75], J. Adolfsson [82], G. Aglieri Rinella [35], M. Agnello [31], N. Agrawal [55], Z. Ahammed [142], S. Ahmad [16], S.U. Ahn [77], Z. Akbar [52], A. Akindinov [94], M. Al-Turany [109], D.S.D. Albuquerque [124], D. Aleksandrov [90], B. Alessandro [60], H.M. Alfanda [7], R. Alfaro Molina [72], B. Ali [16], Y. Ali [14], A. Alici [26], N. Alizadehvandchali [127], A. Alkin [35], J. Alme [21], T. Alt [69], L. Altenkamper [21], I. Altsybeev [115], M.N. Anaam [7], C. Andrei [49], D. Andreou [92], A. Andronic [145], V. Anguelov [106], T. Antičić [110], F. Antinori [58], P. Antonioli [55], C. Anuj [16], N. Apadula [81], L. Aphecetche [117], H. Appelshäuser [69], S. Arcelli [26], R. Arnaldi [60], M. Arratia [81], I.C. Arsene [20], M. Arslandok [147,106], A. Augustinus [35], R. Averbeck [109], S. Aziz [79], M.D. Azmi [16], A. Badalà [57], Y.W. Baek [42], X. Bai [109], R. Bailhache [69], R. Bala [103], A. Balbino [31], A. Baldisseri [139], M. Ball [44], D. Banerjee [4], R. Barbera [27], L. Barioglio [25], M. Barlou [86], G.G. Barnaföldi [146], L.S. Barnby [96], V. Barret [136], C. Bartels [129], K. Barth [35], E. Bartsch [69], F. Baruffaldi [28], N. Bastid [136], S. Basu [82,144], G. Batigne [117], B. Batyunya [76], D. Bauri [50], J.L. Bazo Alba [114], I.G. Bearden [91], C. Beattie [147], I. Belikov [138], A.D.C. Bell Hechavarria [145], F. Bellini [35], R. Bellwied [127], S. Belokurova [115], V. Belyaev [95], G. Bencedi [70,146], S. Beole [25], A. Bercuci [49], Y. Berdnikov [100], A. Berdnikova [106], D. Berenyi [146], L. Bergmann [106], M.G. Besoiu [68], L. Betev [35], P.P. Bhaduri [142], A. Bhasin [103], I.R. Bhat [103], M.A. Bhat [4], B. Bhattacharjee [43], P. Bhattacharya [23], A. Bianchi [25], L. Bianchi [25], N. Bianchi [53], J. Bielčík [38], J. Bielčíková [97], A. Bilandzic [107], G. Biro [146], S. Biswas [4], J.T. Blair [121], D. Blau [90], M.B. Blidaru [109], C. Blume [69], G. Boca [29], F. Bock [98], A. Bogdanov [95], S. Boi [23], J. Bok [62], L. Boldizsár [146], A. Bolozdynya [95], M. Bombara [39], P.M. Bond [35], G. Bonomi [141], H. Borel [139], A. Borissov [83,95], H. Bossi [147], E. Botta [25], L. Bratrud [69], P. Braun-Munzinger [109], M. Bregant [123], M. Broz [38], G.E. Bruno [108,34], M.D. Buckland [129], D. Budnikov [111], H. Buesching [69], S. Bufalino [31], O. Bugnon [117], P. Buhler [116], P. Buncic [35], Z. Buthelezi [73,133], J.B. Butt [14], S.A. Bysiak [120], M. Cai [28,7], D. Caffarri [92], A. Caliva [109], E. Calvo Villar [114], J.M.M. Camacho [122], R.S. Camacho [46], P. Camerini [24], F.D.M. Canedo [123], A.A. Capon [116], F. Carnesecchi [26], R. Caron [139], J. Castillo Castellanos [139], E.A.R. Casula [23], F. Catalano [31], C. Ceballos Sanchez [76], P. Chakraborty [50], S. Chandra [142], W. Chang [7], S. Chapeland [35], M. Chartier [129], S. Chattopadhyay [142], S. Chattopadhyay [112], A. Chauvin [23], T.G. Chavez [46], C. Cheshkov [137], B. Cheynis [137], V. Chibante Barroso [35], D.D. Chinellato [124], S. Cho [62], P. Chochula [35], P. Christakoglou [92], C.H. Christensen [91], P. Christiansen [82], T. Chujo [135], C. Cicalo [56], L. Cifarelli [26], F. Cindolo [55], M.R. Ciupek [109], G. Clai [55,II], J. Cleymans [126],

Appendix B

Published work: y-dependent photoproduction

EUROPEAN ORGANIZATION FOR NUCLEAR RESEARCH

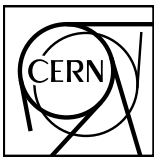

CERN-EP-2021-002
5 January 2021

Coherent J/ψ and ψ' photoproduction at midrapidity in ultra-peripheral Pb–Pb collisions at $\sqrt{s_{NN}} = 5.02$ TeV

ALICE Collaboration*

Abstract

The coherent photoproduction of J/ψ and ψ' mesons was measured in ultra-peripheral Pb–Pb collisions at a center-of-mass energy $\sqrt{s_{NN}} = 5.02$ TeV with the ALICE detector. Charmonia are detected in the central rapidity region for events where the hadronic interactions are strongly suppressed. The J/ψ is reconstructed using the dilepton (l^+l^-) and proton-antiproton decay channels, while for the ψ' the dilepton and the $l^+l^-\pi^+\pi^-$ decay channels are studied. The analysis is based on an event sample corresponding to an integrated luminosity of about 233 μb^{-1}. The results are compared with theoretical models for coherent J/ψ and ψ' photoproduction. The coherent cross section is found to be in a good agreement with models incorporating moderate nuclear gluon shadowing of about 0.65 at a Bjorken-x of around 6×10^{-4}, such as the EPS09 parametrization, however none of the models is able to fully describe the rapidity dependence of the coherent J/ψ cross section including ALICE measurements at forward rapidity. The ratio of ψ' to J/ψ coherent photoproduction cross sections was also measured and found to be consistent with the one for photoproduction off protons.

*See Appendix A for the list of collaboration members

1 Introduction

Photonuclear reactions can be studied in ultra-peripheral collisions (UPCs) of heavy ions where the two nuclei pass by with an impact parameter larger than the sum of their radii. Hadronic interactions are suppressed and electromagnetic interactions are mediated by photons of small virtualities. The intensity of the photon flux is growing with the squared nuclear charge of the colliding ion resulting in large cross sections for the photoproduction of vector mesons in heavy-ion collisions. The photoproduction process has a clear experimental signature: the decay products of vector mesons are the only signal in an otherwise empty detector.

The physics of vector meson photoproduction is described in [1–4]. Photoproduction of vector mesons in ion collisions can either be coherent, i.e. the photon interacts consistently with all nucleons in a nucleus, or incoherent, i.e. the photon interacts with a single nucleon. Experimentally, one can distinguish between these two production types through the typical transverse momentum of the produced vector mesons, which is inversely proportional to the transverse size of the target. While the coherent photoproduction is characterized by the production of mesons with low transverse momentum ($\langle p_{\mathrm{T}} \rangle \sim 60$ MeV/c), the incoherent is dominated by mesons with higher values ($\langle p_{\mathrm{T}} \rangle \sim 500$ MeV/c). In the first case, the nuclei usually do not dissociate, but the electromagnetic fields of ultrarelativistic heavy nuclei are strong enough to develop other independent soft electromagnetic interactions accompanying the coherent photoproduction process and resulting in the excitation of one or both of the nuclei. In the second case, the nucleus breaks up and usually emits neutrons close to the beam rapidities which can be measured in zero-degree calorimeters (ZDC) placed at long distances on both sides of the detector. The incoherent photoproduction can also be accompanied by the excitation and dissociation of the target nucleon resulting in even higher transverse momenta of the produced vector mesons [5].

Coherent heavy vector meson photoproduction is of particular interest because of its connection with the gluon distribution functions (PDFs) in protons and nuclei [6]. At low Bjorken-x values, parton distribution functions are significantly suppressed in the nucleus with respect to free proton PDFs, a phenomenon known as parton shadowing [7]. Shadowing effects are usually attributed to multiple scattering and addressed in various phenomenological approaches based on elastic Glauber-like rescatterings of hadronic components of the photon, Glauber-Gribov inelastic rescatterings, and high-density QCD [8–13]. Besides, different parameterizations of nuclear partonic distributions based on fits to existing data are available [14–17], however these parameterizations are affected by large uncertainties at low Bjorken-x values due to the limited kinematic coverage of the available data samples.

Heavy vector meson photoproduction measurements provide a powerful tool to study poorly known gluon shadowing effects at low x. The scale of the four-momentum transfer of the interaction is related to the mass m_V of the vector meson as $Q^2 \sim m_V^2/4$ corresponding to the perturbative regime in the case of heavy charmonium states. The rapidity of the coherently produced $\mathrm{c\bar{c}}$ states is related to the Bjorken-x of the gluons as $x = \left(m_V/\sqrt{s_{NN}}\right)\exp(\pm y)$, where the sign of the exponent reflects that each of the incoming lead nuclei may act as the photon source. The gluon shadowing factor $R_g(x,Q^2)$, i.e. the ratio of the nuclear gluon density distribution to the gluon distribution in the proton, can be evaluated via the measurement of the nuclear suppression factor defined as the square root of the ratio of the coherent vector meson photoproduction cross section on nuclei to the photoproduction cross section in the impulse approximation that is based on the exclusive photoproduction measurements with the proton target [18, 19]. The square root in this definition is motivated by the fact that the coherent photoproduction cross section is expected to scale as the square of the gluon density in leading order pQCD.

The extraction of the nuclear suppression factor in UPC measurements is complicated by the fact that the measured vector meson cross section in UPCs is expressed as a sum of two contributions since either of the colliding ions can serve as a photon source. At forward rapidities one contribution corresponds to higher photon–nucleus energies while the other to lower energies resulting in ambiguities in the extrac-

tion of the nuclear suppression factor. The midrapidity region has the advantage that both contributions are the same and the suppression factor can be extracted unambiguously in this case.

Charmonium photoproduction in Pb–Pb UPCs was previously studied by the ALICE Collaboration at $\sqrt{s_{\rm NN}} = 2.76$ TeV [20–22]. The coherent J/ψ photoproduction cross section was measured both at midrapidity $|y| < 0.9$ and at forward rapidity $-3.6 < y < -2.6$. In addition, the CMS Collaboration studied the coherent J/ψ photoproduction accompanied by neutron emission at semi-forward rapidity $1.8 < |y| < 2.3$ at $\sqrt{s_{\rm NN}} = 2.76$ TeV [23]. The results were compared with various models and the best description was found amongst those introducing moderate gluon shadowing in the nucleus. The ALICE measurements were used in Ref. [18] to extract the nuclear gluon shadowing factor R_g yielding $R_g(x \sim 10^{-3}) = 0.61^{+0.05}_{-0.04}$ and $R_g(x \sim 10^{-2}) = 0.74^{+0.11}_{-0.12}$ at the scale of the charm quark mass. The ALICE measurement of ψ' photoproduction at midrapidity also supports the moderate-shadowing scenario [22]. A complementary rapidity-differential measurement of the coherent J/ψ and ψ' photoproduction at forward rapidity in Pb–Pb UPCs at $\sqrt{s_{\rm NN}} = 5.02$ TeV by the ALICE Collaboration further underlines the importance of gluon shadowing effects [24]. The gluon shadowing factor $R_g(x \sim 10^{-2}) \sim 0.8$ was obtained under assumption that the contribution from high photon-nucleus energies, i.e. low Bjorken $x \sim 10^{-5}$, can be neglected in the measured cross sections.

In this publication, we present the first measurement of the coherent J/ψ and ψ' photoproduction cross sections at the midrapidity range $|y| < 0.8$ in the Pb–Pb UPCs at $\sqrt{s_{\rm NN}} = 5.02$ TeV, recorded by ALICE in 2018. The J/ψ photoproduction cross section in this measurement is sensitive to $x \in (0.3, 1.4) \times 10^{-3}$, a factor 2 smaller than in the previous midrapidity measurement at $\sqrt{s_{\rm NN}} = 2.76$ TeV [21]. This data sample is approximately 10 times larger than Pb–Pb sample at $\sqrt{s_{\rm NN}} = 2.76$ TeV used for the ALICE results reported in Refs. [21, 22]. The larger data sample allows for a measurement of the J/ψ cross section in three rapidity intervals ($|y| < 0.15$, $0.15 < |y| < 0.35$, $0.35 < |y| < 0.8$) extending the previous rapidity-differential cross section measurement in the forward range at $\sqrt{s_{\rm NN}} = 5.02$ TeV [24]. J/ψ decays to $\mu^+\mu^-$, e^+e^- and $\rm p\overline{p}$ and ψ' decays to $\mu^+\mu^-\pi^+\pi^-$, $e^+e^-\pi^+\pi^-$ and l^+l^- are investigated. The coherent J/ψ production in the $\rm p\overline{p}$ channel in UPCs is measured for the first time. The ratio of the ψ' and J/ψ cross sections is also measured and compared with earlier ALICE measurements [22, 24]. The measured cross sections are compared to models assuming no gluon shadowing as well as to predictions that employ moderate gluon shadowing. Shadowing models are based on a parametrization of previously available data, the leading twist approximation and several variations of the color dipole approach.

2 Detector description

The ALICE detector and its performance are described in [25, 26]. The main components of the ALICE detector are a central barrel placed in a large solenoid magnet ($B = 0.5$ T), covering the central pseudorapidity region, and a muon spectrometer at forward rapidity, covering the range $-4.0 < \eta < -2.5$. Three central barrel detectors, the Inner Tracking System (ITS), the Time Projection Chamber (TPC), and the Time-of-Flight detector (TOF), are used in this analysis.

The ITS is made of six silicon layers and is used for particle tracking and interaction vertex reconstruction [27]. The Silicon Pixel Detector (SPD) makes up the two innermost layers of the ITS with about 10^7 pixels covering the pseudorapidity intervals $|\eta| < 2$ and $|\eta| < 1.4$ for the inner (radius 3.9 cm) and outer (radius 7.6 cm) layers, respectively. The SPD is read out by 400 (800) chips in the inner (outer) layer with each of the readout chips also providing a trigger signal if at least one of its pixels is fired. When projected into the transverse plane, the chips are arranged in 20 (40) azimuthal regions in the inner (outer) layer allowing for a topological selection of events at the trigger level.

The TPC is used for tracking and for particle identification [28]. A 100 kV central electrode separates the two drift volumes, providing an electric field for electron drift. The two end-plates, at $|z| = 250$ cm, are instrumented with Multi-Wire-Proportional-Chambers (MWPCs) with 560,000 readout pads, allowing

high precision track measurements in the transverse plane. The z coordinate is given by the time of drift in the TPC electric field. The TPC acceptance covers the pseudorapidity region $|\eta| < 0.9$. Ionization measurements of individual track clusters are used for particle identification.

The TOF detector is a large cylindrical barrel of multigap resistive plate chambers with about 150,000 readout channels surrounding the TPC and providing very high precision timing measurement [29]. The TOF pseudorapidity coverage is $|\eta| < 0.8$. In combination with the tracking system, the TOF detector is used for charged particle identification up to a momentum of about 2.5 GeV/c for pions and kaons and up to 4 GeV/c for protons. The TOF readout channels are grouped into 1608 trigger channels (maxipads) arranged into 18 azimuthal regions and provide topological-trigger decisions.

The measurement also makes use of the three forward detectors. The V0 counters consist of two arrays of 32 scintillator tiles each, covering the interval $2.8 < \eta < 5.1$ (V0A) and $-3.7 < \eta < -1.7$ (V0C) and positioned respectively at $z = 340$ cm and $z = -90$ cm from the interaction point [30]. The ALICE Diffractive (AD) detector consists of two arrays of 8 scintillator tiles each arranged in two layers, covering the range $4.9 < \eta < 6.3$ (ADA) and $-7.0 < \eta < -4.8$ (ADC) and positioned at $z = 17$ m and $z = -19.5$ m from the interaction point, respectively [31]. Both V0 and AD can be used to veto hadronic interactions at the trigger level.

Finally, two zero-degree calorimeters ZNA and ZNC, located at ± 112.5 m from the interaction point, are used for the measurement of neutrons at beam rapidity. They have good efficiency (≈ 0.94) to detect neutrons with $|\eta| > 8.8$ and have a relative energy resolution of about 20% for single neutrons, which allows for a clear separation of events with either zero or a few neutrons at beam rapidity [32].

3 Data analysis

3.1 Event selection

The data analysis in this paper is based on the event sample recorded during the Pb–Pb at $\sqrt{s_{\rm NN}} = 5.02$ TeV data taking period in 2018. A dedicated central barrel UPC trigger consists of topological trigger formed by at least two and up to six TOF maxipads with at least one pair of maxipads having an opening angle in azimuth larger than 150 degrees and a topological trigger formed by at least four triggered SPD chips. The triggered SPD chips are required to form two pairs, each pair with two chips in different SPD layers falling in compatible azimuthal regions. The two pairs of chips are required to have an opening angle in azimuth larger than 153 degrees. It is further vetoed by any activity within the time windows for nominal beam–beam interactions on the V0 and AD detectors on both sides of the interaction point.

The used data sample corresponds to an integrated luminosity of $233\,\mu{\rm b}^{-1}$, derived from the counts of two independent reference triggers, one based on multiplicity selection in the V0 detector and another one based on neutron detection in the ZDC. The reference trigger cross sections were determined from van der Meer scans; this procedure has an uncertainty of 2.2% [33].The determination of the live-time of the UPC trigger has an additional uncertainty of 1.5%. The total relative systematic uncertainty of the integrated luminosity is thus 2.7%.

Additional offline vetoes are applied on the AD and V0 detector signals to ensure the exclusive production of the charmonia. The offline selection in these detectors is more precise than vetoes at the trigger level, because it relies on larger time windows than the trigger electronics and on a more refined algorithm to quantify the signal.

Online and offline V0 and AD veto requirements may result in significant inefficiencies (denoted as veto inefficiencies) in selecting signal events with exclusive charmonium production due to additional activity induced by hadronic or electromagnetic pile–up processes from independent Pb–Pb collisions accompanying the coherent charmonium photoproduction. The probability of hadronic pile–up in the

collected sample does not exceed 0.2%, however there is a significant pile–up contribution from the electromagnetic electron-pair production process. The veto inefficiency induced by these pile–up effects in the V0 and AD detectors is estimated using events selected with an unbiased trigger based only on the timing of bunches crossing the interaction region. The average veto efficiency $\varepsilon_{\rm veto}^{\rm pileup} = 0.920 \pm 0.002$ is applied to raw charmonium yields to account for hadronic and electromagnetic pile-up processes.

Signal events with exclusive charmonium production, accompanied by electromagnetic nuclear dissociation (EMD), can be rejected if, in addition to the forward neutrons, other particles, produced at large rapidities, leave a signal either in the AD or the V0 detectors. These extra particles may come from multifragmentation or pion production processes, and the corresponding cross sections are expected to be large [34]. The amount of good events with neutrons, which are lost due to AD and V0 vetoes, is estimated using control triggers. The fraction of losses for this category of events (EMD) amounts to $26\% \pm 4\%$ for events with a signal either in ZNA or ZNC and reach $43\% \pm 5\%$ for events with a signal in both ZNA and ZNC. The average event loss is computed using fractions of events with and without neutrons on either side. The average veto efficiency correction $\varepsilon_{\rm veto}^{\rm EMD} = 0.92 \pm 0.02$ is applied to raw charmonium yields to account for the EMD process.

The selected events are required to have a reconstructed primary vertex determined using at least two reconstructed tracks and having a longitudinal position within 15 cm of either side of the nominal interaction point. The analysis is aimed at the reconstruction of J/ψ decaying to $\mu^+\mu^-$, e^+e^-, p$\overline{\rm p}$ and of ψ' decaying to $l^+l^-$and J/$\psi\pi^+\pi^-$ followed by J/$\psi \to l^+l^-$. Therefore, events with two or four tracks in the central barrel are required.

Two types of tracks are considered in the analysis: global tracks and ITS standalone tracks. Global tracks are reconstructed using combined tracking in ITS and TPC detectors. Tracks are required to cross at least 70 (out of 159) TPC pad-rows and to have a cluster on each of the two layers of the SPD. Each track must have a distance of closest approach to the primary vertex of less than 2 cm in the direction of z-axis. ITS standalone tracks are reconstructed using ITS clusters not attached to any global track, requiring at least four clusters in the ITS, out of which two must be in the SPD.

The two-body decays are selected by looking for events with exactly two global tracks with opposite electric charge (unlike-sign). The probability to find extra global tracks not passing the standard track selection criteria or being reconstructed only in ITS is found to be negligible. The four-body decays of ψ' are selected by looking for exactly four tracks with at least two being global tracks. The kinematics of the $\psi' \to l^+l^-\pi^+\pi^-$ decay is such that pions and leptons are well separated: leptons have high $p_{\rm T} \approx 1$ GeV/c while pions are much softer with $p_{\rm T} \approx 0.3$ GeV/c. This feature is used to identify the pion pair. Tracks are sorted according to their $p_{\rm T}$ and the two with lowest $p_{\rm T}$ are assumed to be pions, while the other two are assumed to be leptons. The tagged pions and lepton pairs are required to consist of opposite-sign tracks.

To separate the J/$\psi \to \mu^+\mu^-$, e^+e^- and p$\overline{\rm p}$ decays, the particle identification (PID) capabilities of the TPC and TOF detectors are used. The momenta of the tracks from J/ψ decays are $p \in (1.0, 2.0)$ GeV/c for the $\mu^+\mu^-$ and e^+e^- channels and $p \in (0.75, 1.75)$ GeV/c for the p$\overline{\rm p}$ channel. The PID resolution of the TPC allows for complete separation of electrons and muons in the momentum range mentioned above. Since the specific ionization energy loss (dE/dx) of electron and proton become equal at momenta around 1 GeV/c, the TPC PID is not applicable for the identification of protons from coherently produced J/ψ. However, the PID capabilities of the TOF detector allow for the separation of protons from other particle species in the momentum range relevant for this analysis. For the J/$\psi \to$ p$\overline{\rm p}$ channel, at least one track is required to have valid TOF PID information. If no TOF PID is available for the second track, TPC PID is used. The dE/dx in TPC or the Lorentz Beta factor ($\beta = v/c$) of each reconstructed track in TOF is measured in units of the standard deviation (σ) with respect to expected values for $\mu, e,$ p at the given measured momentum. The track pair is accepted if $n_{\sigma+}^2 + n_{\sigma-}^2 < 16$.

The charmonium photoproduction may be accompanied by pile-up from electromagnetic electron-pair production or by noise in the SPD resulting in extra fired SPD trigger chips satisfying the SPD trigger selection topology. In order to exclude contamination of events not triggered by the charmonium decay products, the fired SPD trigger chips are required to match SPD clusters corresponding to the selected tracks. It is found that 11% (7%) of the events with a J/ψ candidate decaying into dimuons (di-electrons) with 4 SPD clusters cannot be matched to the fired trigger chips. The matching requirement has a much stronger effect for the 4-track decay channels of ψ' removing 40% and 22% of the candidates in the $\psi' \to \mu^+\mu^-\pi^+\pi^-$ and $\psi' \to e^+e^-\pi^+\pi^-$channel, respectively.

3.2 Acceptance and efficiency correction

The product of acceptance and efficiency of the J/ψ and ψ' reconstruction (ε) is evaluated using a large Monte Carlo (MC) sample of coherent and incoherent J/ψ and ψ' events generated by STARlight 2.2.0 [35] with decay particles tracked in a model of the experimental apparatus implemented in GEANT 3.21 [36]. The model includes a realistic description of the detector status during data taking and its variation with time.

For this analysis, the primary J/ψ and ψ' vector mesons produced in UPCs are considered to be transversely polarized. This is consistent with expectations from helicity conservation in photo production and consistent with H1 and ZEUS measurements [37–39]. As observed in previous experiments, both J/ψ and the two pions from ψ' decay are in the S-wave state resulting into the full transfer of the ψ' polarisation to the J/ψ [40]. The expected polarization states of primary J/ψ and ψ' as well as of secondary J/ψ from ψ' decays are properly taken into account in the MC simulations used in this analysis. These MC simulations are also used in the evaluation of the feed-down contribution to the two-body decay channels from the $\psi' \to \mathrm{J}/\psi + \pi^+\pi^-$ and $\psi' \to \mathrm{J}/\psi + \pi^0\pi^0$ decays and for modeling the signal shape and different background contributions.

The efficiency of the SPD trigger chips is measured with a data-driven approach using a minimum bias trigger. Tracks selected without requiring hits in both SPD layers are matched to the trigger chips they cross. The obtained efficiency maps are introduced on an event-by-event basis to the MC simulations. The overall effect corresponds to an efficiency of about 0.72 ± 0.01.

The TOF trigger efficiency is also estimated with a data-driven approach and is taken into account in the MC simulations. The average coverage of the active TOF trigger channels is approximately 90%. The average trigger efficiency of the active channels is defined as the probability to find signals in maxipads crossed by extrapolated TPC tracks from minimum bias events and is found to be 97–98%, depending on track arrival times. More than 93% of the active channels are almost 100% efficient. The low efficiency in some channels is caused by timing alignment issues and partially disconnected or broken equipment.

3.3 Signal extraction

The extraction of coherent J/ψ and ψ' yields in all decay channels is performed in the rapidity interval $|y| < 0.8$. In addition, the J/ψ measurements in the dielectron and dimuon channels are performed in three rapidity intervals: $|y| < 0.15$, $0.15 < |y| < 0.35$, and $0.35 < |y| < 0.8$ where the y ranges were chosen to have approximately the same number of candidates per range. An enriched sample of coherent J/ψ and ψ' candidates is obtained by selecting the reconstructed candidates with transverse momentum $p_{\mathrm{T}} < 0.2$ GeV/c.

The invariant mass distributions for dimuon and dielectron pairs reconstructed in the full rapidity range are shown in Fig. 1, left. The inclusive J/ψ yields are obtained by fitting the invariant mass distributions with an exponential function describing the underlying continuum and two Crystal Ball functions to describe the J/ψ and ψ' signals. The J/ψ pole mass and width were left free, while the tail parameters (α and n) in the Crystal Ball function were fixed to the values obtained in MC simulations in order to

gain higher stability of the fits. In the case of the ψ' signal, all the Crystal Ball parameters were fixed to the values obtained in MC simulations.

The raw inclusive J/ψ yields obtained from invariant mass fits contain contributions from the coherent and incoherent J/ψ photoproduction that can be separated via the analysis of the transverse momentum spectra. The inclusive p_{T} distributions for $\mu^+\mu^-$ and e^+e^- candidates around the J/ψ mass are shown in the right panels of Fig. 1. These distributions are fitted with MC templates produced using STARlight, followed by full detector simulation and reconstruction, corresponding to different production mechanisms: coherent and incoherent J/ψ, feed-down J/ψ from decays of coherent and incoherent ψ' and the dilepton continuum from the $\gamma\gamma \to l^+l^-$ process. Incoherent J/ψ production with nucleon dissociation (or dissociative J/ψ) is also taken into account to describe the high-p_{T} tail with the template based on the H1 parametrization [37]. Normalization of feed-down J/ψ from coherent and incoherent ψ' decays is constrained to the normalization of primary J/ψ templates according to the feed-down fractions extracted as described below. The normalization of the dilepton continuum from the $\gamma\gamma \to l^+l^-$ process is fixed by the results for the background description of the invariant mass fits. The combinatorial background, estimated by considering the distribution of like-sign candidates, is found to be negligible in the J/ψ mass region.

The templates are fitted to the data leaving the normalization free for coherent J/ψ, incoherent J/ψ and dissociative J/ψ production. The extracted incoherent J/ψ fraction $f_{\mathrm{I}} = \frac{N^{\mathrm{incoh}}}{N^{\mathrm{coh}}}$ for $p_{\mathrm{T}} < 0.2$ GeV/c is $4.7 \pm 0.3\%$ $(5.0 \pm 0.5)\%$ for the $\mu^+\mu^-(e^+e^-)$ decay channel. The quoted fractions include the contribution of incoherent J/ψ with nucleon dissociation.

The invariant mass and the p_{T} distributions for the J/$\psi \to \mathrm{p\bar{p}}$ decay channel are shown in Fig. 2. The data sample obtained in this channel is too small to fit the p_{T} distribution with MC templates. However, since the difference in resolution of p_{T} shapes of the coherent or incoherent MC samples for the $\mathrm{p\bar{p}}$ and $\mu^+\mu^-$ channels is negligible, one can expect the f_{I} fraction to be the same. This is due to the fact that neither the $\mu^+\mu^-$ nor the $\mathrm{p\bar{p}}$ channels suffer from bremsstrahlung. This is not the case for dielectrons where bremsstrahlung induces the large difference in the mass and momentum resolution which affect the templates and consequently the f_{I} fraction.

As one can see in Fig. 1, the ψ' yields in the $\mu^+\mu^-$ and e^+e^- channels are small and lying on top of a significant background. In order to increase the significance of the ψ' signal and to reduce the statistical uncertainty, the ψ' yield is extracted from the merged l^+l^- sample. Fig. 3 shows the merged dilepton mass spectrum together with the p_{T} distribution of the dilepton candidates in the invariant mass range under the ψ' mass peak. The fit to the invariant mass distribution is performed in the same way as described before.

Fig. 4 shows the invariant mass (left) and the p_{T} distribution (right) for $\psi' \to \mu^+\mu^-\pi^+\pi^-$ and $\psi' \to e^+e^-\pi^+\pi^-$ quadruplets. A coherent peak is clearly visible at low p_{T}. The signal extraction in the $\mu^+\mu^-\pi^+\pi^-$ and $e^+e^-\pi^+\pi^-$ channel is straight-forward since the signal is very clean. The number of candidates is extracted by summing the bin contents in the mass interval $3.6 < \mathrm{m}_{\mu\mu\pi\pi} < 3.8\,\mathrm{GeV}/c^2$ and $3.4 < \mathrm{m}_{\mathrm{ee}\pi\pi} < 3.8\,\mathrm{GeV}/c^2$. The number of candidates with wrong-sign combinations in the same mass interval, representing the level of background, is subtracted afterwards.

The incoherent contamination of the ψ' sample is estimated as follows. The incoherent-to-coherent photoproduction cross section ratio is expected to be similar for 1S and 2S charmonium states [35, 41]. Due to lack of model calculations for the incoherent ψ' cross section in UPCs at $\sqrt{s_{\mathrm{NN}}} = 5.02$ TeV, predicted incoherent-to-coherent cross section ratios for J/ψ from Refs. [5, 13, 35] are used as an estimate of the incoherent-to-coherent cross section ratio for ψ'. The factor $f_{\mathrm{I}} = \frac{N^{\mathrm{incoh}}}{N^{\mathrm{coh}}} \approx 6\%$ is extracted from the predicted cross section ratios, corrected for acceptance and efficiency of coherent and incoherent ψ' states. The difference in the predicted incoherent-to-coherent cross section ratios is used as an estimate of the systematic uncertainty.

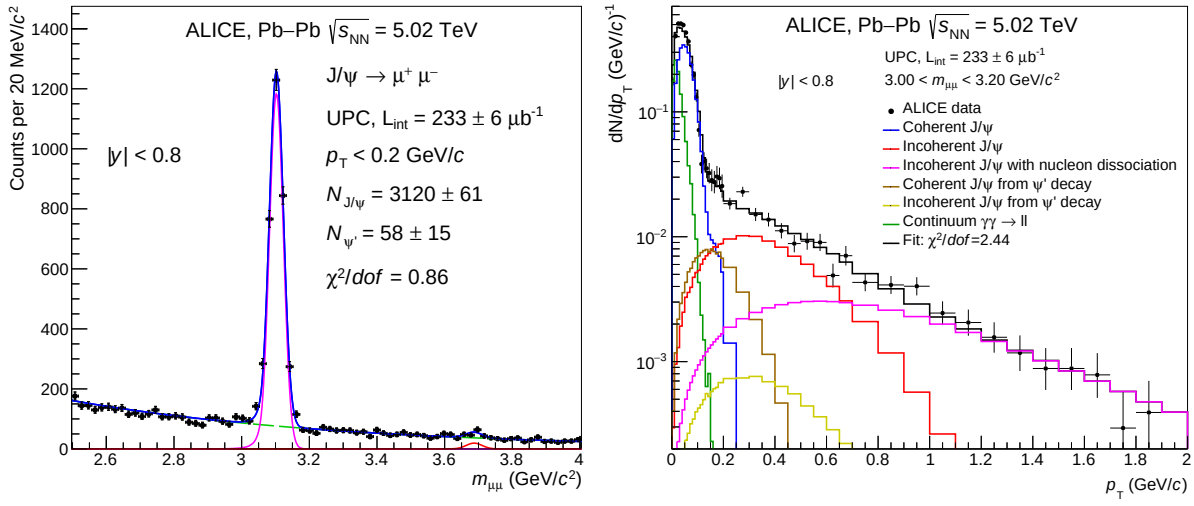

(a) J/$\psi \to \mu^+\mu^-$

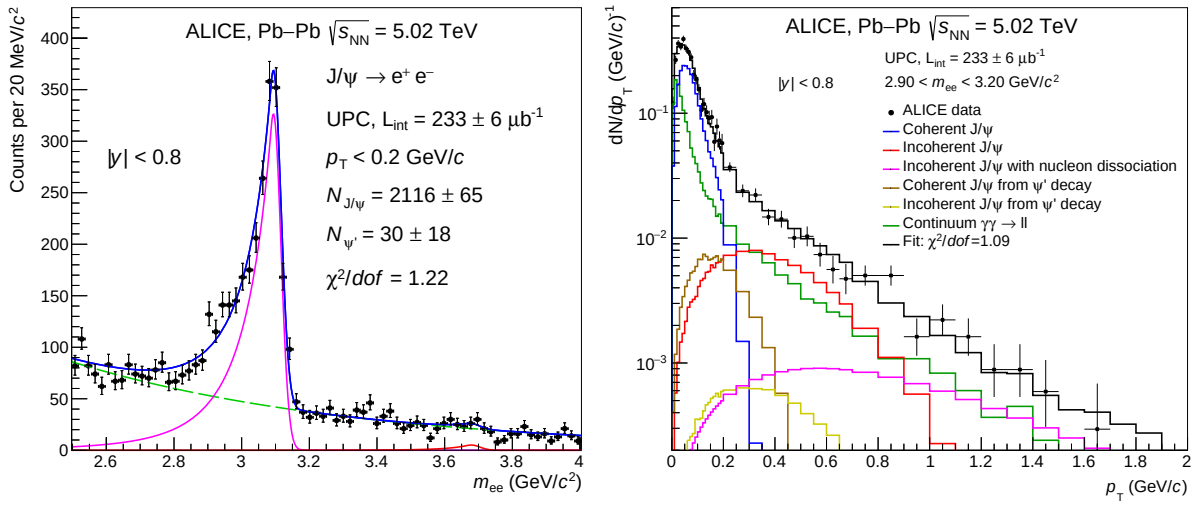

(b) J/$\psi \to e^+e^-$

Figure 1: Left: Invariant mass distribution of l^+l^- pairs. The dashed green line corresponds to the background. The solid magenta and red lines correspond to Crystal Ball functions representing the J/ψ and ψ' signal, respectively. The solid blue line corresponds to the sum of background and signal functions. Right: Transverse momentum distribution of J/ψ candidates in the range quoted in the figure (around the J/ψ nominal mass).

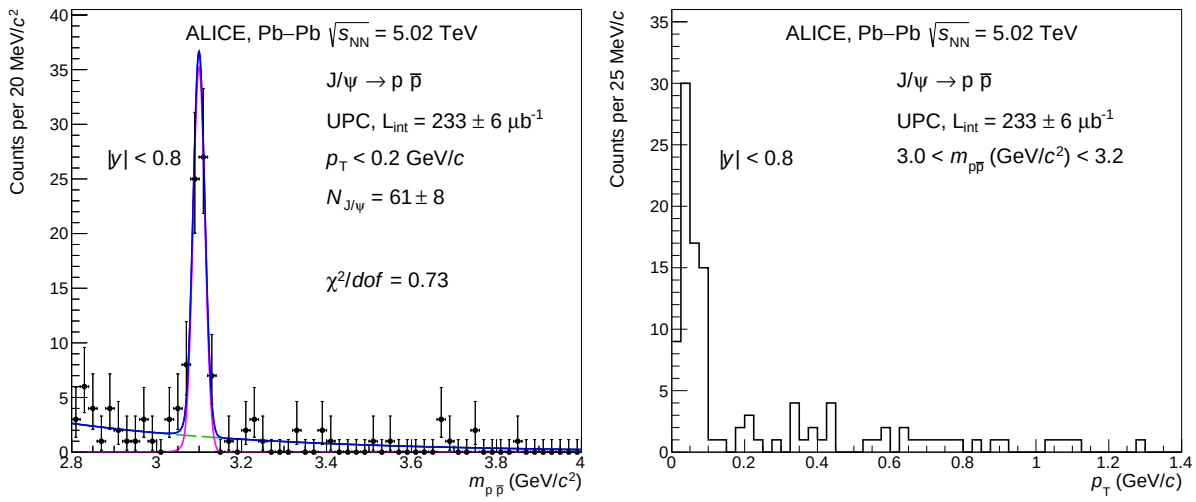

Figure 2: Left: Invariant mass distribution of $p\bar{p}$ pairs. The dashed green line corresponds to the background description. The solid magenta and red lines correspond to Crystal Ball functions representing the J/ψ and ψ' signals, respectively. The solid blue line corresponds to the sum of background and signal functions. Right: Transverse momentum distribution of J/ψ candidates in the range quoted in the figure (around the J/ψ nominal mass).

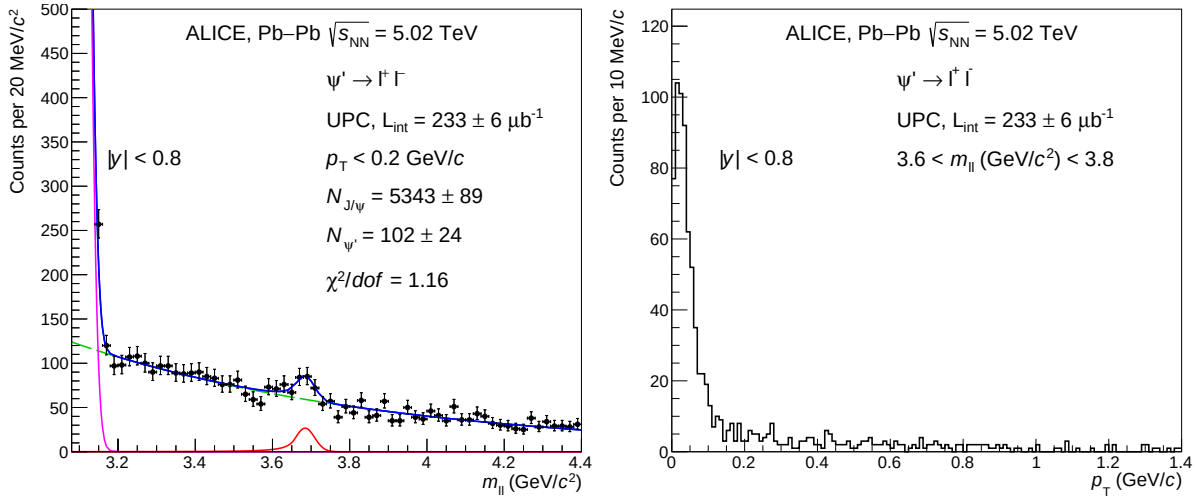

Figure 3: Left: Invariant mass distribution of l^+l^- pairs. The dashed green line corresponds to the background description. The solid magenta and red line correspond to Crystal Ball functions representing the J/ψ and ψ' signals, respectively. The solid blue line corresponds to the sum of background and signal functions. Right: Transverse momentum distribution of ψ' candidates in the mass range quoted in the figure (around the ψ' mass).

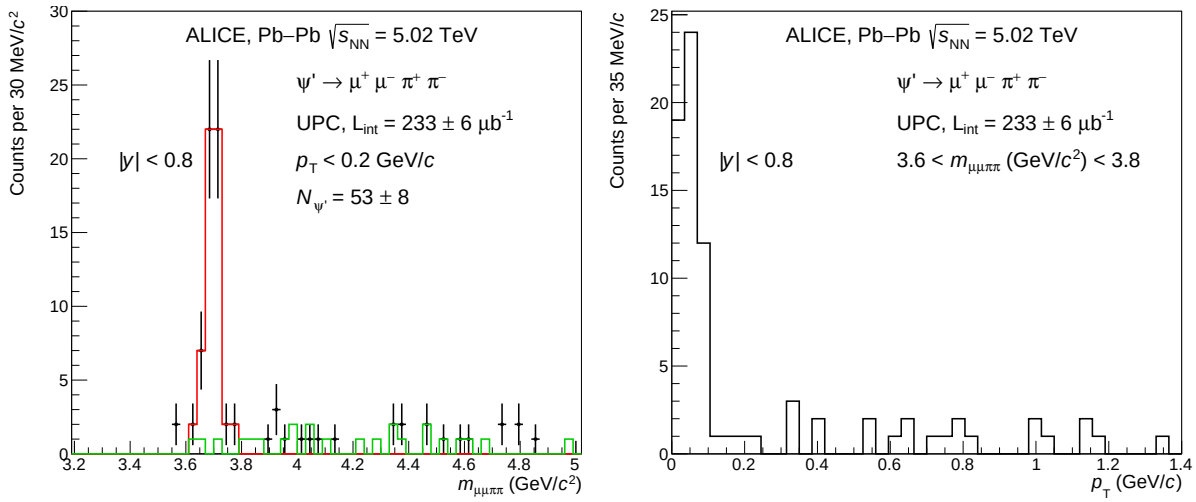

(a) $\psi' \to \mu^+\mu^-\pi^+\pi^-$

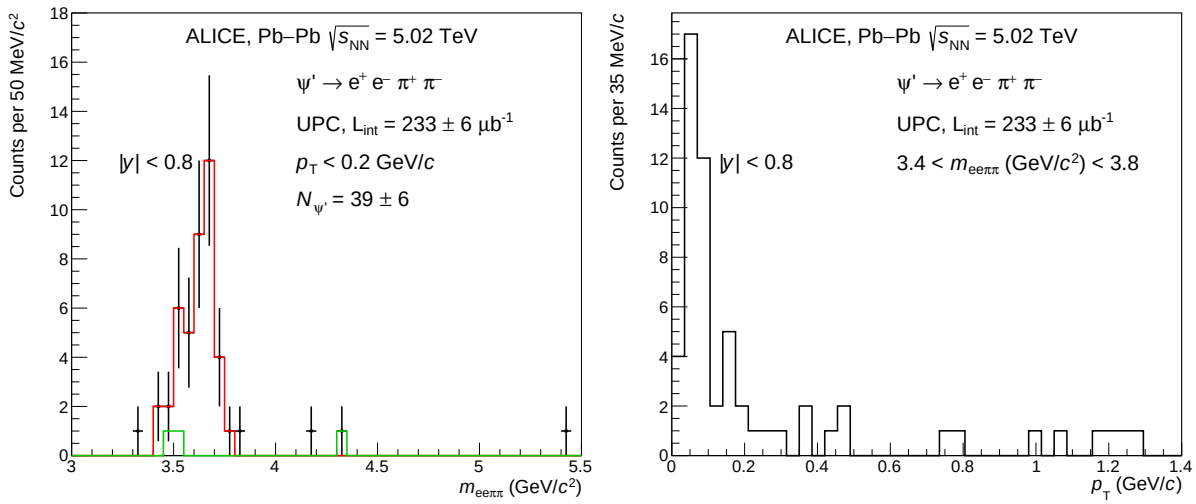

(b) $\psi' \to e^+e^-\pi^+\pi^-$

Figure 4: Left: Invariant mass distribution for $\psi' \to \mu^+\mu^-\pi^+\pi^-$ (upper panel) and $\psi' \to e^+e^-\pi^+\pi^-$ (bottom panel). The green line shows the wrong sign four-track events. The red line shows the ψ' signal as described in the text. Right: Transverse momentum distribution of ψ' candidates in the mass range quoted in the figure (around the ψ' nominal mass).

The raw J/ψ yields contain a significant feed-down contribution originating from decays $\psi' \rightarrow$ J/ψ + anything, dominated by the $\psi' \rightarrow$ J/ψ + $\pi^+\pi^-$ and $\psi' \rightarrow$ J/ψ+ $\pi^0\pi^0$ decay channels. The feed-down fraction $f_{\rm D} = \frac{N(\text{FeedDown})}{N(\text{primary})}$ can be extracted from the ratio of raw J/ψ and ψ' yields:

$$R_N = \frac{N_{\psi'}}{N_{J/\psi}} = 0.0170 \pm 0.0024 (0.0184 \pm 0.0030), \tag{1}$$

for $\mu^+\mu^-(e^+e^-)$. The raw ψ' and J/ψ yields in this ratio contain contributions both from coherent and incoherent photoproduction. However, according to the $p_{\rm T}$ fits, the fraction $f_{\rm I}$ does not exceed 6% and, according to STARlight, the fraction of the incoherent contributions is expected to be similar in the ψ' and J/ψ yields. The R_N ratio can therefore be considered as a good estimate of the ratio of coherent J/ψ and ψ' yields, since the incoherent fractions largely cancel in the ratio. The $f_{\rm D}$ ratio can be expressed via the measured R_N ratio:

$$\left(\frac{1}{f_{\rm D}} + 1\right)^{-1} = \frac{N_{\rm J/\psi}^{\rm feed-down}}{N_{\rm J/\psi}} = \frac{(\text{BR}\cdot\varepsilon)_{\psi'\rightarrow \rm J/\psi\pi^+\pi^-\rightarrow l^+l^-\pi^+\pi^-} + (\text{BR}\cdot\varepsilon)_{\psi'\rightarrow \rm J/\psi\pi^0\pi^0\rightarrow l^+l^-\pi^0\pi^0}}{(\text{BR}\times\varepsilon)_{\psi'\rightarrow l^+l^-}} \times R_N, \tag{2}$$

where $(\text{BR}\times\varepsilon)$ in the corresponding channels denote products of world-average branching ratios [42] and the product of acceptance and efficiency of measuring exactly two leptons. The $f_{\rm D}$ fractions of $3.5\% \pm 0.5\%$ and $4.3\% \pm 0.7\%$ are obtained in the $\mu^+\mu^-$and in e^+e^- channel respectively, with the uncertainty being the quadratic sum of statistical and systematic uncertainties, where the statistical uncertainty dominates. The systematic uncertainty includes contributions from the J/ψ and ψ' signal extraction and the branching ratios.

4 Results

The coherent vector meson differential cross section is given by:

$$\frac{{\rm d}\sigma_{\rm VM}^{\rm coh}}{{\rm dy}} = \frac{N_{\rm VM}^{\rm coh}}{(\text{Acc}\times\varepsilon)_{\rm VM} \times \varepsilon_{\rm veto}^{\rm pileup} \times \varepsilon_{\rm veto}^{\rm EMD} \times \text{BR}(\text{VM}\rightarrow \text{X}+\text{Y}) \times \mathscr{L}_{\rm int} \times \Delta\text{y}} \tag{3}$$

where

$$N_{J/\psi}^{\rm coh} = \frac{N_{\rm yield}}{1 + f_{\rm I} + f_{\rm D}} \tag{4}$$

and

$$N_{\psi'}^{\rm coh} = \frac{N_{\rm yield}}{1 + f_{\rm I}}. \tag{5}$$

The raw J/ψ and ψ' yield values, efficiencies, $f_{\rm I}$ and $f_{\rm D}$ fractions as well as coherent cross sections with statistical and systematic uncertainties are summarized in Table 1 and Table 2. The associated systematic uncertainties are briefly described in the following.

The offline AD and V0 vetoes decreases the J/ψ (ψ') yield by 8% (16%) and also results in a lower $\varepsilon_{\rm veto}^{\rm pileup}$ efficiency. These two effects do not cancel-out completely. A residual discrepancy of 3% (10%) in the cross section of J/ψ (ψ') is included in the systematic uncertainty.

The uncertainty related to the evaluation of the incoherent contamination comes from the shape of the continuum template. By default the $\gamma\gamma \rightarrow l^+l^-$ template from the STARlight MC simulation is used. Alternative way would be to use a data-driven template generated from the side bands of the invariant mass distribution of the J/ψ. These events are, in contrast to the pure MC, supposed to include the same background as under the J/ψ peak. By comparing the $f_{\rm I}$ fraction obtained with the side bands method and the STARlight template, a 0.8 (0.5%) uncertainty of the cross section for the $\mu^+\mu^-$ (e^+e^-) channel is found.

Table 1: Raw J/ψ yields, ε, $f_{\rm D}$ and $f_{\rm I}$ fractions and coherent J/ψ cross sections per decay channel

Decay	$\lvert y\rvert$	$N_{J/\psi}$	ε	$f_{\rm D}$	$f_{\rm I}$	$\mathrm{d}\sigma^{\rm coh}_{\rm J/\psi}/\mathrm{d}y$ (mb)
$\mu^+\mu^-$	(0.00, 0.80)	3120 ± 61	0.037	0.035	0.047 ± 0.003	$4.12 \pm 0.08(\mathrm{stat.}) \pm 0.23(\mathrm{syst.})$
$\mu^+\mu^-$	(0.00, 0.15)	1027 ± 35	0.064	0.035	0.047 ± 0.003	$4.23 \pm 0.15(\mathrm{stat}) \pm 0.24(\mathrm{syst})$
$\mu^+\mu^-$	(0.15, 0.35)	1083 ± 36	0.051	0.035	0.047 ± 0.003	$4.22 \pm 0.14(\mathrm{stat}) \pm 0.23(\mathrm{syst})$
$\mu^+\mu^-$	(0.35, 0.80)	976 ± 33	0.022	0.035	0.047 ± 0.003	$3.85 \pm 0.13(\mathrm{stat}) \pm 0.21(\mathrm{syst})$
e^+e^-	(0.00, 0.80)	2116 ± 65	0.025	0.043	0.050 ± 0.005	$4.05 \pm 0.13(\mathrm{stat.}) \pm 0.24(\mathrm{syst.})$
e^+e^-	(0.00, 0.15)	683 ± 33	0.046	0.043	0.050 ± 0.005	$3.83 \pm 0.19(\mathrm{stat}) \pm 0.23(\mathrm{syst})$
e^+e^-	(0.15, 0.35)	743 ± 34	0.034	0.043	0.050 ± 0.005	$4.20 \pm 0.19(\mathrm{stat}) \pm 0.25(\mathrm{syst})$
e^+e^-	(0.35, 0.80)	643 ± 31	0.014	0.043	0.050 ± 0.005	$3.90 \pm 0.19(\mathrm{stat}) \pm 0.23(\mathrm{syst})$
$\mathrm{p\bar{p}}$	(0.00, 0.80)	61 ± 8	0.023	0.035	0.047 ± 0.003	$3.73 \pm 0.51(\mathrm{stat.}) \pm 0.28(\mathrm{syst.})$

Table 2: Raw ψ' yields, ε, $f_{\rm I}$ fractions and coherent ψ' cross sections per decay channel

Decay	$\lvert y\rvert$	$N_{\psi'}$	ε	$f_{\rm I}$	$\mathrm{d}\sigma^{\rm coh}_{\psi'}/\mathrm{d}y$ (mb)
$\mu^+\mu^-\pi^+\pi^-$	(0.0, 0.8)	53 ± 8	0.0103	0.057	$0.77 \pm 0.11(\mathrm{stat.}) \pm 0.09(\mathrm{syst.})$
$e^+e^-\pi^+\pi^-$	(0.0, 0.8)	39 ± 6	0.0068	0.064	$0.86 \pm 0.15(\mathrm{stat.}) \pm 0.11(\mathrm{syst.})$
l^+l^-	(0.0, 0.8)	102 ± 24	0.0324	0.063	$0.61 \pm 0.15(\mathrm{stat.}) \pm 0.10(\mathrm{syst.})$

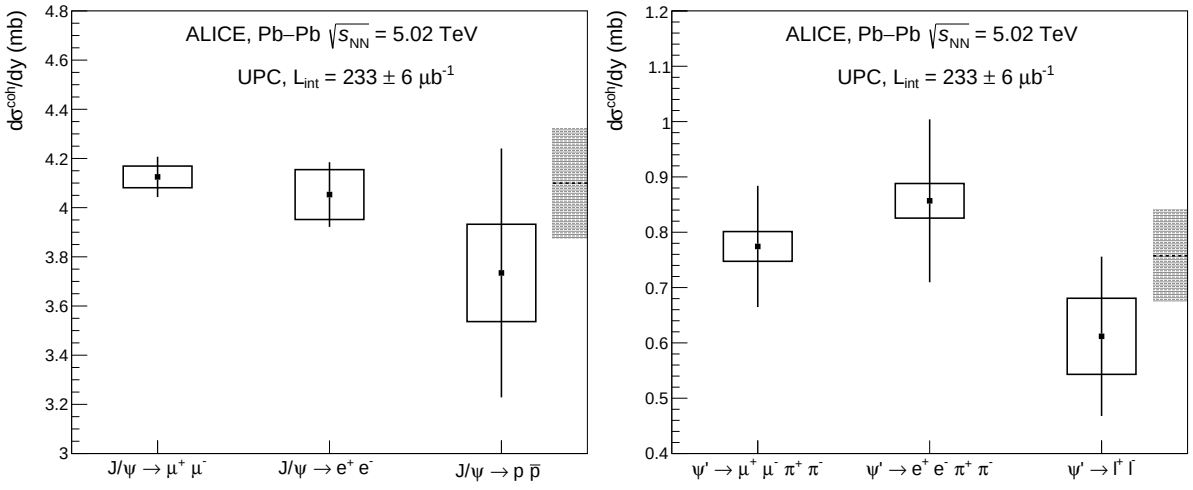

Figure 5: Measured differential cross section of coherent J/ψ (left) and ψ' (right) photoproduction in Pb–Pb UPCs in $|y| < 0.8$. The points show the measurements for different decay channels. The error bars (boxes) represent the statistical (decay channel uncorrelated systematic) uncertainty. The gray box shows the average value (dashed line) and correlated systematic uncertainty.

A systematic uncertainty of the tracking efficiency of 2% per track is estimated by comparing, in data and in MC, the ITS (TPC) hit matching efficiency to the tracks reconstructed with TPC (ITS) hits only. This leads to a 2.8% (4%) systematic uncertainty for two-track (four-track) channels.

For the signal extraction in the J/ψ analysis the goodness of the description of the J/ψ signal by the Crystal Ball function is checked. The yield from the fit is compared to the number of events computed by bin counting in the peak region with the $\gamma\gamma$ contribution subtracted using the exponential background shape from the fit. Half differences of 0.3%, 2.4%, 0.6% were assigned as the systematic uncertainty in the muon, electron and proton channel, respectively.

Another contribution to the signal extraction uncertainties is the difference between the function used in the fit and the true shape of the background. It is estimated by varying the fit range. A systematic uncertainty of 0.4% (0.3%) is determined for the $\mu^+\mu^-$ (e^+e^-) decay channel of the J/ψmeson. The uncertainty in the background subtraction rises rapidly as the signal-to-background ratio drops. A similar study for the l^+l^- decay of the ψ' meson results in a 10% systematic uncertainty.

The uncertainty associated to the determination of the trigger efficiency of the SPD chips is obtained by changing the requirements on the probe tracks used in the data-driven method. Variations include the running conditions, the maximum amount of activity allowed in the event, and the definition of tracks accepted in the efficiency computation. This uncertainty amounts to 1%.

The uncertainty of the TOF trigger efficiency due to the spread of the arrival times of various particle species to TOF is evaluated as 0.5% per track (1% in total). The uncertainty in case of four track decays of ψ' applies only for the lepton tracks since the low-momentum pions do not reach the TOF detector.

In the J/$\psi \to \mathrm{p\bar{p}}$ analysis, at least one track is required to have proton PID from the TOF. Comparing the efficiency of the track matching to TOF in data and MC samples, a 10% disagreement is found. The matching efficiency from MC is used and a half-difference of 5% as an additional systematic uncertainty for the $\mathrm{p\bar{p}}$ channel is assigned.

Tables 3 and 4 show the uncertainties for each source and channel separately as well as quadratic sums of the channel-correlated and uncorrelated sources.

The signal extraction, incoherent contamination and branching ratio are considered as channel-uncorrelated sources of systematic uncertainties. The other sources are fully correlated and are the same for all channels. In the case of the ψ', the four track channels have an extra ITS-TPC matching uncertainty for the pion tracks which is not correlated with the l^+l^- channel, thus it is quoted separately.

The J/ψ and ψ' cross sections for various decay channels computed using Eq. 3 are shown in Fig. 5. The mean values of the J/ψ and ψ' cross sections are obtained as a weighted average of the cross sections per decay channel with weights corresponding to the inverse of the quadratic sum of statistical and channel-uncorrelated systematic uncertainties. The cross section value averaged over the three decay channels of the coherent J/ψ photoproduction measurements is:

$$\frac{\mathrm{d}\sigma^{\mathrm{coh}}_{J/\psi}}{\mathrm{d}y} = 4.10 \pm 0.07(\mathrm{stat.}) \pm 0.23(\mathrm{syst.})\mathrm{mb}. \quad (6)$$

The cross section value averaged over the three channels of coherent ψ' photoproduction measurements is:

$$\frac{\mathrm{d}\sigma^{\mathrm{coh}}_{\psi'}}{\mathrm{d}y} = 0.76 \pm 0.08(\mathrm{stat.}) \pm 0.09(\mathrm{syst.})\mathrm{mb}. \quad (7)$$

Table 3: Sources of systematic uncertainty for the coherent J/ψ cross section measurements per decay channel in percent

	$J/\psi \to \mu^+\mu^-$	$J/\psi \to e^+e^-$	$J/\psi \to p\bar{p}$
Signal Extraction	0.5	2.4	0.7
Incoherent contamination	0.8	0.5	0.8
Branching ratio	0.5	0.5	1.4
TOF matching	–	–	5.0
ITS-TPC matching	2.8	2.8	2.8
AD and V0 veto	3.0	3.0	3.0
SPD trigger efficiency	1.0	1.0	1.0
TOF trigger efficiency	0.7	0.7	0.7
Luminosity	2.7	2.7	2.7
EMD correction	2.0	2.0	2.0
Feed down	0.6	0.6	0.6
Channel uncorrelated	1.1	2.5	5.3
Channel correlated	5.5	5.5	5.5

Table 4: Sources of systematic uncertainty for the coherent ψ' cross section measurements per decay channel in percent

	$\psi' \to \mu^+\mu^-\pi^+\pi^-$	$\psi' \to e^+e^-\pi^+\pi^-$	$\psi' \to l^+l^-$
Signal Extraction	1.0	2.0	10.0
Incoherent contamination	1.4	1.8	1.8
Branching ratio	1.5	1.5	4.8
ITS-TPC matching pions	2.8	2.8	–
ITS-TPC matching leptons	2.8	2.8	2.8
AD and V0 veto	10.0	10.0	10.0
SPD trigger efficiency	1.0	1.0	1.0
TOF trigger efficiency	0.7	0.7	0.7
Luminosity	2.7	2.7	2.7
EMD correction	2.0	2.0	2.0
Channel uncorrelated	3.5	5.8	11.2
Channel correlated	11.0	11.0	11.0

The ratio of the 2S to 1S charmonium states is:

$$\frac{\frac{\sigma^{\mathrm{coh}}_{\psi'}}{\mathrm{d}y}}{\frac{\sigma^{\mathrm{coh}}_{J/\psi}}{\mathrm{d}y}} = 0.18 \pm 0.0185(\mathrm{stat.}) \pm 0.028(\mathrm{syst.}) \pm 0.005(\mathrm{BR}). \quad (8)$$

Many systematic uncertainties of the J/ψ and ψ' cross section measurements are correlated and cancel in the cross section ratio. Since the analysis relies on the same data sample and on the same trigger, the systematic uncertainties of the luminosity evaluation, trigger efficiency, EMD correction and ITS-TPC matching of leptons were considered as fully correlated. The AD and V0 offline veto uncertainty is partially correlated, so the difference of the uncertainties for ψ' and J/ψ is taken into account in the uncertainty of the ratio. The systematic uncertainties connected to the signal extraction, incoherent contamination and the branching ratio are considered uncorrelated between the two measurements. The dominant uncertainty comes from the uncorrelated part of the AD and V0 veto uncertainty for ψ'.

5 Discussion

Figure 6 shows the rapidity-differential cross section of the coherent photoproduction of J/ψ and ψ' vector mesons in Pb–Pb UPCs including previous ALICE measurements of J/ψ at forward rapidity [24]. At midrapidity, J/ψ measurements performed in absolute rapidity ranges are shown at positive rapidities and reflected into negative rapidities. The ALICE measurements are compared to several models which are discussed in the following:

The impulse approximation, taken from STARlight [43], is based on data from exclusive J/ψ photoproduction off protons and neglects all nuclear effects except for the coherence. The square root of the ratio of experimental cross sections to the impulse approximation is 0.65 ± 0.03 for J/ψ and 0.66 ± 0.06 for ψ', where statistical and systematic uncertainties of the ALICE measurements and a conservative 10% uncertainty on the impulse approximation are added in quadrature. The obtained nuclear suppression factor reflects the magnitude of the nuclear gluon shadowing factor at typical Bjorken-x values in the range $(0.3, 1.4) \times 10^{-3}$ and is in good agreement with $R_g(x \sim 10^{-3}) = 0.61^{+0.05}_{-0.04}$ obtained in Ref. [18] from the J/ψ cross section measurement in UPCs at $\sqrt{s_{\mathrm{NN}}} = 2.76$ TeV.

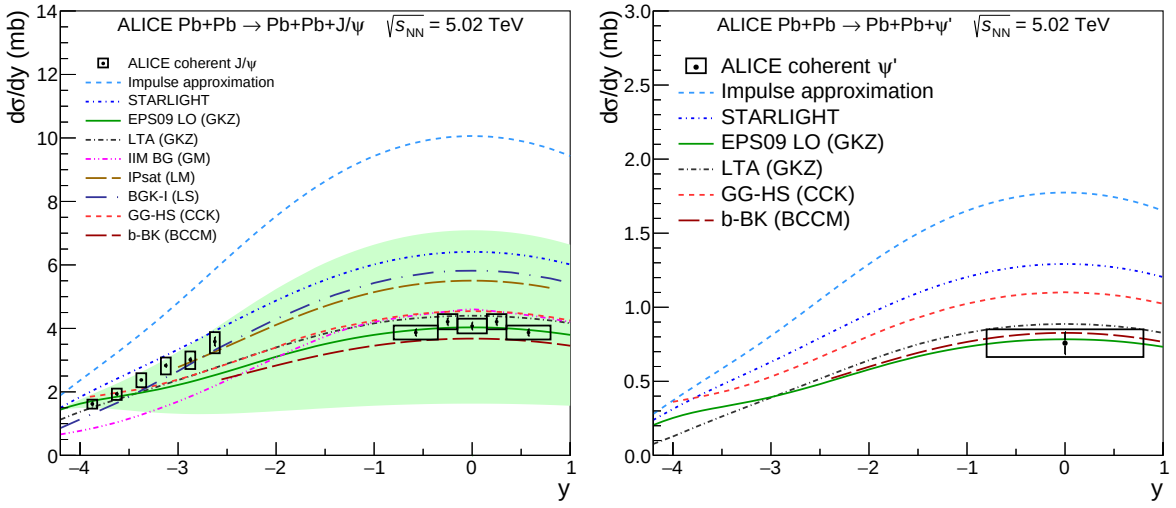

Figure 6: Measured differential cross section of the coherent J/ψ (left) and ψ' (right) photoproduction in Pb–Pb UPC events. The error bars (boxes) show the statistical (systematic) uncertainties. The theoretical calculations are also shown. The green band represents the uncertainties of the EPS09 LO calculation.

STARlight is based on the Vector Meson Dominance model and a parametrization of the existing data on J/ψ photoproduction off protons [35]. A Glauber-like formalism is used to calculate the J/ψ photoproduction cross section in Pb–Pb UPCs accounting for multiple interactions within the nucleus but not accounting for the gluon shadowing corrections. The STARlight model overpredicts the data indicating that Glauber-like rescatterings alone are not enough to explain the observed suppression of the coherent J/ψ cross section.

Guzey, Kryshen and Zhalov [44] provide two calculations (GKZ), one based on the EPS09 LO parametrization of the available nuclear shadowing data [14] and the other on the leading twist approximation (LTA) of nuclear shadowing based on the combination of the Gribov-Glauber theory and the diffractive PDFs from HERA [8]. Both the LTA model and the EPS09 curve, corresponding to the EPS09 LO central set (uncertainties of the EPS09 calculation are represented by the green band), are found to be in a good agreement with the J/ψ and ψ' cross sections measured at midrapidity. However, these models are in tension with the J/ψ data at semi-forward rapidity in the range $2.5 < |y| < 3.5$, indicating that the nuclear shadowing might have a smaller effect at Bjorken $x \sim 10^{-2}$ or $x \sim 5 \times 10^{-5}$ corresponding to this rapidity range.

Calculations by Cepila, Contreras, Krelina and Tapia Takaki (CCK) are based on the colour dipole model with the structure of the nucleon in the transverse plane described by the so-called hot spots, regions of high gluonic density, whose number increases with the increasing energy [13, 45]. Nuclear effects are implemented along the ideas proposed in the energy-dependent hot-spot model with the standard Glauber-Gribov formalism (GG-HS) for the extension to the nuclear case. The GG-HS model agrees with the J/ψ measurements at midrapidity and at most forward rapidities but underpredicts them at semi-forward rapidities. The ψ' measurement at midrapidity is overpredicted by this model.

Calculations by Bendova, Cepila, Contreras, Matas (BCCM) are based on the color dipole approach coupled to the solutions of the impact-parameter dependent Balitsky-Kovchegov equation with initial conditions based on the Woods-Saxon shape of the Pb nucleus [9]. The model is in a reasonable agreement with the J/ψ and ψ' data at midrapidity.

Several theory groups provided predictions for J/ψ within the color dipole approach coupled to the Color Glass Condensate (CGC) formalism with different assumptions on the dipole-proton scattering amplitude. Predictions by Gonçalves, Machado et al. (GM) [10, 46] based on the IIM and b-CGC models for the scattering amplitude agree with the J/ψ data rather well at midrapidity but strongly underpredict the data at forward rapidities. Predictions by Lappi and Mäntysaari (LM) based on the IPsat model [11, 47] overpredict the ALICE measurements at midrapidity, but match them at forward rapidities. Recent predictions by Łuszczak and Schäfer (LS BGK-I) within the color-dipole formulation of the Glauber-Gribov theory [12] are in agreement with the J/ψ data at semi-forward rapidities, $2.5 < |y| < 3$, slightly underpredict the data at more forward rapidities $3 < |y| < 4$ and overpredict the data at midrapidity.

The measured ratio of the ψ' to J/ψ cross section is compatible with the previous ALICE measurement at forward rapidities $R = 0.150 \pm 0.018(\text{stat.}) \pm 0.021(\text{syst.}) \pm 0.007(\text{BR})$ [24], with the exclusive photoproduction cross section ratio $R = 0.166 \pm 0.007(\text{stat.}) \pm 0.008(\text{syst.}) \pm 0.007(\text{BR})$ measured by the H1 collaboration in ep collisions [38] and with the ratio $R \approx 0.19$ measured by the LHCb collaboration in pp collisions [48]. The measured ratio also agrees with the ratio $R \approx 0.20$ predicted in the leading twist approximation [44] for Pb–Pb UPCs at midrapidity. The ψ' to J/ψ coherent cross section ratio is expected to have a mild dependence on the collision energy [44]. Therefore, the measured ratio can be directly compared to the unexpectedly large ψ' to J/ψ coherent cross section ratio $R = 0.34^{+0.08}_{-0.07}$, measured by ALICE at midrapidity in Pb–Pb UPCs at $\sqrt{s_{\text{NN}}} = 2.76$ TeV [22]. The previous measurement is about a factor two larger but is still compatible within 2 standard deviations with the present measurement, owing mainly to the large uncertainties of the previous result.

6 Conclusions

The first rapidity-differential measurement on the coherent photoproduction of J/ψ at midrapidity $|y| < 0.8$ in Pb–Pb UPCs at $\sqrt{s_{\rm NN}} = 5.02$ TeV has been presented and compared to the model calculations. This data complements the ALICE measurement of the coherent J/ψ cross section at forward rapidity $-4 < y < -2.5$ allowing us to provide stringent constraints on nuclear gluon shadowing models.

The nuclear gluon shadowing factor of about 0.65 at Bjorken-x values $x \in (0.3, 1.4) \times 10^{-3}$ is estimated from the comparison of the measured coherent J/ψ cross section with the impulse approximation at midrapidity. This result is in agreement with the gluon shadowing factor extracted from the previous ALICE measurement of the coherent J/ψ cross section at midrapidity in Pb–Pb UPCs at $\sqrt{s_{\rm NN}} = 2.76$ TeV.

None of the models is able to fully describe the measured forward and central rapidity dependence of the coherent J/ψ cross section. The J/ψ measurements at central and most forward rapidities are found to be in agreement with the models based either on the leading twist approximation of nuclear shadowing, or the central value of the EPS09 parameterization as well as with the energy-dependent hot-spot model extended to the nuclear case by the standard Glauber-Gribov formalism and the color dipole approach coupled to the solutions of the impact-parameter dependent Balitsky-Kovchegov equation. However, these models appear to be in tension with the data at semi-forward rapidities in the range $2.5 < |y| < 3.5$. The data might be better explained with a model where shadowing has a smaller effect at Bjorken $x \sim 10^{-2}$ or $x \sim 5 \times 10^{-5}$ corresponding to this rapidity range. On the other hand, the models based on the color dipole approach coupled to the color glass condensate formalism describe either the forward or central measurements depending on the dipole scattering amplitude assumptions but they are not able to describe the measured cross section in the full rapidity range.

The ratio of the ψ' to J/ψ cross sections at midrapidity is in a reasonable agreement with the ratio of photoproduction cross sections off protons measured by the H1 and LHCb collaborations, with the leading twist approximation predictions for Pb–Pb UPCs as well as with the ALICE measurement at forward rapidities.

Acknowledgements

The ALICE Collaboration would like to thank all its engineers and technicians for their invaluable contributions to the construction of the experiment and the CERN accelerator teams for the outstanding performance of the LHC complex. The ALICE Collaboration gratefully acknowledges the resources and support provided by all Grid centres and the Worldwide LHC Computing Grid (WLCG) collaboration. The ALICE Collaboration acknowledges the following funding agencies for their support in building and running the ALICE detector: A. I. Alikhanyan National Science Laboratory (Yerevan Physics Institute) Foundation (ANSL), State Committee of Science and World Federation of Scientists (WFS), Armenia; Austrian Academy of Sciences, Austrian Science Fund (FWF): [M 2467-N36] and Nationalstiftung für Forschung, Technologie und Entwicklung, Austria; Ministry of Communications and High Technologies, National Nuclear Research Center, Azerbaijan; Conselho Nacional de Desenvolvimento Científico e Tecnológico (CNPq), Financiadora de Estudos e Projetos (Finep), Fundação de Amparo à Pesquisa do Estado de São Paulo (FAPESP) and Universidade Federal do Rio Grande do Sul (UFRGS), Brazil; Ministry of Education of China (MOEC) , Ministry of Science & Technology of China (MSTC) and National Natural Science Foundation of China (NSFC), China; Ministry of Science and Education and Croatian Science Foundation, Croatia; Centro de Aplicaciones Tecnológicas y Desarrollo Nuclear (CEADEN), Cubaenergía, Cuba; Ministry of Education, Youth and Sports of the Czech Republic, Czech Republic; Czech Science Foundation; The Danish Council for Independent Research | Natural Sciences, the VILLUM FONDEN and Danish National Research Foundation (DNRF), Denmark; Helsinki Institute of Physics (HIP), Finland; Commissariat à l'Energie Atomique (CEA) and Institut National de Physique Nucléaire et de Physique des Particules (IN2P3) and Centre National de la Recherche Scientifique (CNRS), France;

Bundesministerium für Bildung und Forschung (BMBF) and GSI Helmholtzzentrum für Schwerionenforschung GmbH, Germany; General Secretariat for Research and Technology, Ministry of Education, Research and Religions, Greece; National Research, Development and Innovation Office, Hungary; Department of Atomic Energy Government of India (DAE), Department of Science and Technology, Government of India (DST), University Grants Commission, Government of India (UGC) and Council of Scientific and Industrial Research (CSIR), India; Indonesian Institute of Science, Indonesia; Istituto Nazionale di Fisica Nucleare (INFN), Italy; Institute for Innovative Science and Technology , Nagasaki Institute of Applied Science (IIST), Japanese Ministry of Education, Culture, Sports, Science and Technology (MEXT) and Japan Society for the Promotion of Science (JSPS) KAKENHI, Japan; Consejo Nacional de Ciencia (CONACYT) y Tecnología, through Fondo de Cooperación Internacional en Ciencia y Tecnología (FONCICYT) and Dirección General de Asuntos del Personal Academico (DGAPA), Mexico; Nederlandse Organisatie voor Wetenschappelijk Onderzoek (NWO), Netherlands; The Research Council of Norway, Norway; Commission on Science and Technology for Sustainable Development in the South (COMSATS), Pakistan; Pontificia Universidad Católica del Perú, Peru; Ministry of Science and Higher Education, National Science Centre and WUT ID-UB, Poland; Korea Institute of Science and Technology Information and National Research Foundation of Korea (NRF), Republic of Korea; Ministry of Education and Scientific Research, Institute of Atomic Physics and Ministry of Research and Innovation and Institute of Atomic Physics, Romania; Joint Institute for Nuclear Research (JINR), Ministry of Education and Science of the Russian Federation, National Research Centre Kurchatov Institute, Russian Science Foundation and Russian Foundation for Basic Research, Russia; Ministry of Education, Science, Research and Sport of the Slovak Republic, Slovakia; National Research Foundation of South Africa, South Africa; Swedish Research Council (VR) and Knut & Alice Wallenberg Foundation (KAW), Sweden; European Organization for Nuclear Research, Switzerland; Suranaree University of Technology (SUT), National Science and Technology Development Agency (NSDTA) and Office of the Higher Education Commission under NRU project of Thailand, Thailand; Turkish Atomic Energy Agency (TAEK), Turkey; National Academy of Sciences of Ukraine, Ukraine; Science and Technology Facilities Council (STFC), United Kingdom; National Science Foundation of the United States of America (NSF) and United States Department of Energy, Office of Nuclear Physics (DOE NP), United States of America.

References

[1] C. A. Bertulani, S. R. Klein, and J. Nystrand, "Physics of ultra-peripheral nuclear collisions", *Ann. Rev. Nucl. Part. Sci.* **55** (2005) 271–310, arXiv:nucl-ex/0502005.

[2] A. Baltz, "The Physics of Ultraperipheral Collisions at the LHC", *Phys. Rept.* **458** (2008) 1–171, arXiv:0706.3356 [nucl-ex].

[3] J. G. Contreras and J. D. Tapia Takaki, "Ultra-peripheral heavy-ion collisions at the LHC", *Int. J. Mod. Phys.* **A30** (2015) 1542012.

[4] S. R. Klein and H. Mäntysaari, "Imaging the nucleus with high-energy photons", *Nature Rev. Phys.* **1** no. 11, (2019) 662–674, arXiv:1910.10858 [hep-ex].

[5] V. Guzey, M. Strikman, and M. Zhalov, "Nucleon dissociation and incoherent J/ψ photoproduction on nuclei in ion ultraperipheral collisions at the Large Hadron Collider", *Phys. Rev. C* **99** no. 1, (2019) 015201, arXiv:1808.00740 [hep-ph].

[6] M. Ryskin, "Diffractive J/ψ electroproduction in LLA QCD", *Z. Phys. C* **57** (1993) 89–92.

[7] N. Armesto, "Nuclear shadowing", *J. Phys. G* **32** (2006) R367–R394, arXiv:hep-ph/0604108.

[8] L. Frankfurt, V. Guzey, and M. Strikman, "Leading Twist Nuclear Shadowing Phenomena in Hard Processes with Nuclei", *Phys. Rept.* **512** (2012) 255–393, arXiv:1106.2091 [hep-ph].

[9] D. Bendova, J. Cepila, J. G. Contreras, and M. Matas, "Photonuclear J/ψ production at the LHC: proton-based versus nuclear dipole scattering amplitudes", arXiv:2006.12980 [hep-ph].

[10] V. P. Gonçalves, B. D. Moreira, and F. S. Navarra, "Investigation of diffractive photoproduction of J/ψ in hadronic collisions", *Phys. Rev. C* **90** (Jul, 2014) 015203. https://link.aps.org/doi/10.1103/PhysRevC.90.015203.

[11] T. Lappi and H. Mäntysaari, "Incoherent diffractive J/ψ production in high-energy nuclear deep-inelastic scattering", *Phys. Rev. C* **83** (Jun, 2011) 065202. https://link.aps.org/doi/10.1103/PhysRevC.83.065202.

[12] A. Łuszczak and W. Schäfer, "Coherent photoproduction of J/ψ in nucleus-nucleus collisions in the color dipole approach", *Phys. Rev. C* **99** no. 4, (2019) 044905, arXiv:1901.07989 [hep-ph].

[13] J. Cepila, J. G. Contreras, and M. Krelina, "Coherent and incoherent J/ψ photonuclear production in an energy-dependent hot-spot model", *Phys. Rev. C* **97** no. 2, (2018) 024901, arXiv:1711.01855 [hep-ph].

[14] K. Eskola, H. Paukkunen, and C. Salgado, "EPS09: A New Generation of NLO and LO Nuclear Parton Distribution Functions", *JHEP* **04** (2009) 065, arXiv:0902.4154 [hep-ph].

[15] K. J. Eskola, P. Paakkinen, H. Paukkunen, and C. A. Salgado, "EPPS16: Nuclear parton distributions with LHC data", *Eur. Phys. J. C* **77** no. 3, (2017) 163, arXiv:1612.05741 [hep-ph].

[16] K. Kovarik *et al.*, "nCTEQ15 - Global analysis of nuclear parton distributions with uncertainties in the CTEQ framework", *Phys. Rev. D* **93** no. 8, (2016) 085037, arXiv:1509.00792 [hep-ph].

[17] R. Abdul Khalek, J. J. Ethier, J. Rojo, and G. van Weelden, "nNNPDF2.0: quark flavor separation in nuclei from LHC data", *JHEP* **09** (2020) 183, arXiv:2006.14629 [hep-ph].

[18] V. Guzey, E. Kryshen, M. Strikman, and M. Zhalov, "Evidence for nuclear gluon shadowing from the ALICE measurements of PbPb ultraperipheral exclusive J/ψ production", *Phys. Lett. B* **726** (2013) 290–295, arXiv:1305.1724 [hep-ph].

[19] J. G. Contreras, "Gluon shadowing at small x from coherent J/ψ photoproduction data at energies available at the CERN Large Hadron Collider", *Phys. Rev. C* **96** no. 1, (2017) 015203, arXiv:1610.03350 [nucl-ex].

[20] **ALICE** Collaboration, B. Abelev *et al.*, "Coherent J/ψ photoproduction in ultra-peripheral Pb-Pb collisions at $\sqrt{s_{NN}} = 2.76$ TeV", *Phys. Lett. B* **718** (2013) 1273–1283, arXiv:1209.3715 [nucl-ex].

[21] **ALICE** Collaboration, E. Abbas *et al.*, "Charmonium and e^+e^- pair photoproduction at mid-rapidity in ultra-peripheral Pb-Pb collisions at $\sqrt{s_{\rm NN}}$=2.76 TeV", *Eur. Phys. J. C* **73** no. 11, (2013) 2617, arXiv:1305.1467 [nucl-ex].

[22] **ALICE** Collaboration, J. Adam *et al.*, "Coherent ψ(2S) photo-production in ultra-peripheral Pb–Pb collisions at $\sqrt{s_{\rm NN}}$ = 2.76 TeV", *Phys. Lett. B* **751** (2015) 358–370, arXiv:1508.05076 [nucl-ex].

[23] **CMS** Collaboration, V. Khachatryan *et al.*, "Coherent J/ψ photoproduction in ultra-peripheral PbPb collisions at $\sqrt{s_{NN}} = 2.76$ TeV with the CMS experiment", *Phys. Lett. B* **772** (2017) 489–511, arXiv:1605.06966 [nucl-ex].

[24] **ALICE** Collaboration, S. Acharya *et al.*, "Coherent J/ψ photoproduction at forward rapidity in ultra-peripheral Pb-Pb collisions at $\sqrt{s_{\rm NN}} = 5.02$ TeV", *Phys. Lett.* **B798** (2019) 134926, arXiv:1904.06272 [nucl-ex].

[25] **ALICE** Collaboration, K. Aamodt *et al.*, "The ALICE experiment at the CERN LHC", *JINST* **3** (2008) S08002.

[26] **ALICE** Collaboration, B. B. Abelev *et al.*, "Performance of the ALICE Experiment at the CERN LHC", *Int. J. Mod. Phys. A* **29** (2014) 1430044, arXiv:1402.4476 [nucl-ex].

[27] **ALICE** Collaboration, K. Aamodt *et al.*, "Alignment of the ALICE Inner Tracking System with cosmic-ray tracks", *JINST* **5** (2010) P03003, arXiv:1001.0502 [physics.ins-det].

[28] J. Alme, Y. Andres, H. Appelshäuser, S. Bablok, N. Bialas, R. Bolgen, U. Bonnes, R. Bramm, P. Braun-Munzinger, R. Campagnolo, and et al., "The ALICE TPC, a large 3-dimensional tracking device with fast readout for ultra-high multiplicity events", *Nuclear Instruments and Methods in Physics Research Section A: Accelerators, Spectrometers, Detectors and Associated Equipment* **622** no. 1, (Oct, 2010) 316–367. http://dx.doi.org/10.1016/j.nima.2010.04.042.

[29] A. Akindinov *et al.*, "Performance of the ALICE Time-Of-Flight detector at the LHC", *Eur. Phys. J. Plus* **128** (2013) 44.

[30] **ALICE** Collaboration, E. Abbas *et al.*, "Performance of the ALICE VZERO system", *JINST* **8** (2013) P10016, arXiv:1306.3130 [nucl-ex].

[31] **LHC Forward Physics Working Group** Collaboration, K. Akiba *et al.*, "LHC Forward Physics", *J. Phys. G* **43** (2016) 110201, arXiv:1611.05079 [hep-ph].

[32] **ALICE** Collaboration, B. Abelev *et al.*, "Measurement of the Cross Section for Electromagnetic Dissociation with Neutron Emission in Pb-Pb Collisions at $\sqrt{s_{NN}}$ = 2.76 TeV", *Phys. Rev. Lett.* **109** (2012) 252302, arXiv:1203.2436 [nucl-ex].

[33] **ALICE** Collaboration, S. Acharya *et al.*, "ALICE luminosity determination for Pb–Pb collisions at $\sqrt{s_{\rm NN}} = 5.02$ TeV", tech. rep., CERN, January, 2021. ALICE-PUBLIC-2021-001.

[34] I. A. Pshenichnov, "Electromagnetic excitation and fragmentation of ultrarelativistic nuclei", *Phys. Part. Nucl.* **42** (2011) 215–250.

[35] S. R. Klein, J. Nystrand, J. Seger, Y. Gorbunov, and J. Butterworth, "STARlight: A Monte Carlo simulation program for ultra-peripheral collisions of relativistic ions", *Comput. Phys. Commun.* **212** (2017) 258–268, arXiv:1607.03838 [hep-ph].

[36] R. Brun, F. Bruyant, F. Carminati, S. Giani, M. Maire, A. McPherson, G. Patrick, and L. Urban, *GEANT: Detector Description and Simulation Tool; Oct 1994*. CERN Program Library. CERN, Geneva, 1993. http://cds.cern.ch/record/1082634. Long Writeup W5013.

[37] **H1** Collaboration, C. Alexa *et al.*, "Elastic and Proton-Dissociative Photoproduction of J/ψ Mesons at HERA", *Eur. Phys. J.* **C73** no. 6, (2013) 2466, arXiv:1304.5162 [hep-ex].

[38] **H1** Collaboration, C. Adloff *et al.*, "Diffractive photoproduction of ψ(2S) mesons at HERA", *Phys. Lett. B* **541** (2002) 251–264, arXiv:hep-ex/0205107.

[39] **ZEUS** Collaboration, S. Chekanov *et al.*, "Exclusive photoproduction of J / psi mesons at HERA", *Eur. Phys. J. C* **24** (2002) 345–360, arXiv:hep-ex/0201043.

[40] **BES** Collaboration, J. Z. Bai *et al.*, "$\psi(2S) \to \pi^+\pi^- J/\psi$ decay distributions", *Phys. Rev. D* **62** (Jul, 2000) 032002. https://link.aps.org/doi/10.1103/PhysRevD.62.032002.

[41] M. B. G. Ducati, M. Griep, and M. Machado, "Diffractive photoproduction of radially excited psi(2S) mesons in photon-Pomeron reactions in PbPb collisions at the CERN LHC", *Phys. Rev. C* **88** (2013) 014910, arXiv:1305.2407 [hep-ph].

[42] **Particle Data Group** Collaboration, P. Zyla *et al.*, "Review of Particle Physics", *PTEP* **2020** no. 8, (2020) 083C01.

[43] S. R. Klein and J. Nystrand, "Exclusive vector meson production in relativistic heavy ion collisions", *Phys. Rev. C* **60** (1999) 014903. https://link.aps.org/doi/10.1103/PhysRevC.60.014903.

[44] V. Guzey, E. Kryshen, and M. Zhalov, "Coherent photoproduction of vector mesons in ultraperipheral heavy ion collisions: Update for run 2 at the CERN Large Hadron Collider", *Phys. Rev. C* **93** no. 5, (2016) 055206, arXiv:1602.01456 [nucl-th].

[45] J. Cepila, J. G. Contreras, and J. D. Tapia Takaki, "Energy dependence of dissociative J/ψ photoproduction as a signature of gluon saturation at the LHC", *Phys. Lett. B* **766** (2017) 186–191, arXiv:1608.07559 [hep-ph].

[46] G. Sampaio dos Santos and M. Machado, "On theoretical uncertainty of color dipole phenomenology in the J/ψ and Υ photoproduction in pA and AA collisions at the CERN Large Hadron Collider", *J. Phys. G* **42** no. 10, (2015) 105001, arXiv:1411.7918 [hep-ph].

[47] T. Lappi and H. Mäntysaari, "J/ψ production in ultraperipheral Pb+Pb and p+Pb collisions at energies available at the CERN Large Hadron Collider", *Phys. Rev. C* **87** (Mar, 2013) 032201. https://link.aps.org/doi/10.1103/PhysRevC.87.032201.

[48] **LHCb** Collaboration, R. Aaij *et al.*, "Central exclusive production of J/ψ and $\psi(2S)$ mesons in pp collisions at $\sqrt{s} = 13$ TeV", *JHEP* **10** (2018) 167, arXiv:1806.04079 [hep-ex].

Appendix C

Published work: visible luminosity determination

EUROPEAN ORGANIZATION FOR NUCLEAR RESEARCH

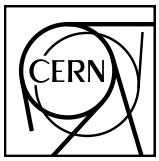

ALICE-PUBLIC-2021-001

ALICE luminosity determination for Pb–Pb collisions at $\sqrt{s_{\mathrm{NN}}} = 5.02$ TeV

ALICE Collaboration*

Abstract

Luminosity determination in ALICE is based on visible cross sections measured in van der Meer scans. In 2015 and 2018, the Large Hadron Collider provided Pb–Pb collisions at a centre-of-mass energy per nucleon pair of $\sqrt{s_{\mathrm{NN}}}$ = 5.02 TeV. Van der Meer scans were performed, in which the cross section was measured for two classes of visible interactions, based on particle detection in the ALICE luminometers: the Zero Degree Calorimeter (ZDC) and the V0 detector. This document describes the experimental set-up and summarises the main features of the analysis procedure. The resulting uncertainty on the ZDC-based (V0-based) luminosity measurement for the full sample is 2.3% (2.2%).

*See Appendix A for the list of collaboration members

1 Introduction

Luminosity determination in ALICE (A Large Ion Collider Experiment) [1] at the Large Hadron Collider (LHC) is based on visible cross sections measured in van der Meer (vdM) scans [2–4]. For collisions of lead ions (Pb–Pb), the visible cross section $\sigma_{\rm vis}$ seen by a detector (or set of detectors) with a given trigger condition has, in general, two components, one hadronic and one electromagnetic: $\sigma_{\rm vis} = \varepsilon_{\rm had}\sigma_{\rm had} + \varepsilon_{\rm EM}\sigma_{\rm EM}$, where $\sigma_{\rm had}$ and $\sigma_{\rm EM}$ are the hadronic and electromagnetic inelastic cross sections and $\varepsilon_{\rm had}$ and $\varepsilon_{\rm EM}$ are, respectively, the fractions of hadronic and electromagnetic inelastic events that satisfy the trigger condition. In the following, a class of events satisfying a given trigger condition will be referred to as a reference process. Once the reference-process cross section ($\sigma_{\rm vis}$) is measured, the luminosity at the ALICE interaction point (IP2) can be determined as the reference-process rate divided by $\sigma_{\rm vis}$. This procedure does not require a knowledge of $\varepsilon_{\rm had}$, $\varepsilon_{\rm EM}$.

In standard vdM scans, the two beams are moved across each other in the transverse directions x (horizontal) and y (vertical). The x and y scans are performed separately, the beams being head-on in the non-scanned direction. The measurement of the rate R of the reference process as a function of the beam separations Δx and Δy, defined as the distance between centroids of the beam bunches, allows one to determine the luminosity L for head-on collisions of a pair of bunches as

$$L = N_1 N_2 f_{\rm rev}/(h_x h_y), \tag{1}$$

where $f_{\rm rev}$ is the accelerator revolution frequency, N_1 and N_2 are the bunch intensities, defined as the number of particles in the bunch, and h_x and h_y are the effective widths of the beam overlap region in the two transverse directions (for head-on collisions). The effective widths h_x and h_y can be measured as the area under the rate curves $R(\Delta x, 0)$ and $R(0, \Delta y)$, respectively, each divided by the head-on rate $R(0,0)$. The cross section $\sigma_{\rm vis}$ for the chosen reference process is then

$$\sigma_{\rm vis} = R(0,0)/L. \tag{2}$$

The standard vdM scans are typically coupled with one or more length-scale calibration scans, whose aim is to determine the global conversion factor from the nominal (as dialled by the accelerator operator) to the actual beam displacement. In these scans, the two beams are kept at constant separation and moved in steps in the same direction, and the interaction vertex position is measured as a function of the nominal beam position.

The formalism of Eq. (1) assumes complete factorisation of the beam profiles in the two transverse directions, such that the beam overlap region is fully described by the product $h_x h_y$. Previous studies performed by ALICE [5–10] and other LHC experiments [11–14] have shown that the actual LHC bunch shapes can violate the factorisation assumption to a non-negligible level. Non-factorisation effects can be studied and quantified by measuring the luminous region parameters, via the distribution of interaction vertices, as a function of the beam separation.

During the so-called Run 2, in 2015 and 2018, the LHC provided Pb–Pb collisions at a centre-of-mass energy per nucleon pair $\sqrt{s_{\rm NN}} = 5.02$ TeV. The ALICE luminosity determination for these data samples is based on a vdM scan session[1] that took place on November 29, 2018, during the LHC fill labelled with number 7483. In this scan session, the cross section was measured for two independent reference processes.

[1] Two more vdM scan sessions, LHC fills 4690 and 7440, were not considered for this analysis. During fill 4690 (December 4, 2015) the LHC orbit feedback system, normally left off during vdM scans in order to not perturb the scan machinery, had to be left on due to beam instabilities; during fill 7440 (November 13, 2018) some of the quadrupole magnets determining the beam optics at IP2 had non-correct settings, leading to coupling between the two transverse directions. Due to the non trivial implications of these peculiar conditions on the vdM scan formalism and analysis, it was decided to base the luminosity normalisation on the vdM scan session of fill 7483 alone.

The rest of this document is organised as follows. Section 2 describes the detectors used for the measurement, along with the relevant machine parameters and the procedure adopted for the scan. Section 3 summarises the analysis procedure and presents the results and uncertainties for the visible cross section and the luminosity measurement. Finally, Sec. 4 presents a brief summary of the work.

2 Experimental set-up

In the vdM scan of fill 7483, the cross section was measured for two reference processes: one is based on the Zero Degree Calorimeter (ZDC), the other on the V0 detector. A detailed description of these detectors is given in [1], and their performance is discussed in [15, 16]. The ZDC system features two neutron calorimeters (ZNA, ZNC), located on opposite sides of IP2, each at a distance of 112.5 m along the beam line. It is completed by two proton calorimeters and two small electromagnetic calorimeters, not used for this measurement. The V0 detector consists of two hodoscopes, with 32 scintillator tiles each, located on opposite sides of the IP2, at distances of 340 cm (V0A) and 90 cm (V0C) along the beam axis, covering the pseudorapidity (η) ranges $2.8 < \eta < 5.1$ (V0A) and $-3.7 < \eta < -1.7$ (V0C). Note that the clockwise (anticlockwise) LHC beam 1 (2) travels from side A (C) to side C (A). The C side is the one hosting the ALICE muon arm [1].

The trigger condition used to define the ZDC-based visible cross section, called ZED in the following, requires a signal in at least one of the neutron calorimeters. Such a trigger condition is sensitive to both electromagnetic dissociation events with (single- or double-sided) neutron emission, and hadronic events [17–21]. The trigger condition for the V0-based visible cross section, called V0M in the following, requires the sum of signal amplitudes in all channels to be above some threshold; during the 2018 Pb–Pb data taking, the threshold was such that the $\sim 50\%$ most central hadronic events (and no electromagnetic events) were selected.

The analysis procedure uses, for the length-scale calibration and non-factorisation corrections, the parameters of the luminous region measured via the distribution of interaction vertices, determined with the ALICE Inner Tracking System (ITS [22]).

During the vdM scan session, each Pb beam consisted of 648 bunches, and 619 bunch pairs were made to collide at IP2. The minimum spacing between two consecutive bunches in each beam was 100 ns. The β^* value[2] at IP2 was 0.5 m. The nominal half vertical crossing angle of the two beams at IP2 was about -60 μrad, the minus sign indicating that the two beams exit the crossing region with negative y coordinate with respect to the beam axis[3]. The current in the ALICE solenoid (dipole) was 30 kA (6 kA), corresponding to a field strength of 0.5 T (0.7 T). The maximum beam separation during the scan was about 100 μm, corresponding to about six times the RMS of the transverse beam profile. The reference-process rates were recorded separately for each colliding bunch pair. Two pairs of horizontal and vertical scans were performed, to obtain two independent cross-section measurements per bunch pair. In addition, in order to provide additional input for non-factorisation studies, two diagonal scans were performed, where the beam separation was varied simultaneously in the two transverse directions. Finally, a set of length-scale calibration scans were performed.

The bunch intensities were of the order of $7–10\times10^7$ Pb ions per bunch. The bunch-intensity measurement is provided by the LHC instrumentation [23]: a DC current transformer (DCCT), measuring the total beam intensity, and a fast beam current transformer (fBCT), measuring the relative bunch intensities. For the relative bunch intensities, data from a second device, the ATLAS beam pick-up system

[2]The $\beta(z)$ function describes the single-particle motion and determines the variation of the beam envelope as a function of the coordinate along the beam orbit (z). The notation β^* denotes the value of the β function at the interaction point.

[3]ALICE uses a right-handed orthogonal Cartesian system whose origin is at the LHC Interaction Point 2 (IP2). The z axis is parallel to the mean beam direction at IP2 and points along the LHC Beam 2 (i.e. LHC anticlockwise). The x axis is horizontal and points approximately towards the centre of the LHC. The y axis is approximately vertical and points upwards.

(BPTX [24]) is also used. The measured beam intensity is corrected for the fraction of ghost and satellite charge. The radio-frequency (RF) configuration of the LHC is such that the accelerator orbit is divided in 3564 slots of 25 ns each. Each slot is further divided in ten buckets of 2.5 ns each. In nominally filled slots, the particle bunch is captured in the central bucket of the slot. Following the convention established in [25], the charge circulating outside of the nominally filled slots is referred to as ghost charge; the charge circulating within a nominally filled slot but not captured in the central bucket is referred to as satellite charge. A measurement of ghost charge is provided independently by the LHCb collaboration, via the rate of beam–gas collisions occurring in nominally empty bunch slots, as described in [11], and by the LHC Longitudinal Density Monitor (LDM), which measures synchrotron radiation photons emitted by the beams [26]. The LDM also provides a measurement of the satellite-charge fraction. For this fill, the combined ghost- and satellite-charge correction to the bunch intensity product (hence to the cross section) is about 13%. The total uncertainty on the bunch intensity is 0.8% and is obtained as the quadratic sum of the uncertainties on the total beam current normalisation from the DCCT (0.5%), on the relative bunch populations (0.2%), and on the ghost and satellite charge (0.6%).

3 Analysis and results

In previous studies, dedicated to luminosity determination in pp and p–Pb collisions [5–10], the trigger rates were corrected for background and pile-up effects, and the corrected rates plotted as a function of beam separation. The fit of the scan curves (separately for the x and y scans) yielded a measurement of $R(0,0)$, h_x, and h_y, which could be plugged directly into Eqs. 1 and 2 to determine $\sigma_{\rm vis}$. In the present analysis, the much smaller collision rate per colliding pair warranted a different approach, aimed to a better treatment of statistical uncertainties at very small numbers of counts. For each colliding bunch pair, the number of triggered events t_i and the number of sampled LHC orbits n_i at scan step i are used as inputs for a binomial likelihood fit:

$$\ln \mathscr{L} = \sum_i \left[t_i \ln P_i + (n_i - t_i) \ln (1 - P_i) \right] \tag{3}$$

where P_i is the probability of having a trigger in a bunch crossing, related to the mean number of triggers per bunch crossing μ_i by Poissonian statistics, $P_i = 1 - e^{-\mu_i}$. The quantity μ_i is modelled by the fit function, according to the following relation:

$$\mu_i = N_{1,i} N_{2,i} \frac{\sigma_{\rm vis}}{h_x h_y} f(\Delta x_i) g(\Delta y_i) + p_{{\rm s},i} + \tilde{p}_1 N_{1,i} + \tilde{p}_2 N_{2,i} + p_0, \tag{4}$$

where: $N_{1,i}$ and $N_{2,i}$ are the intensities of the two colliding bunches; Δx_i and Δy_i are the beam separations, corrected for beam–beam deflection [27, 28] and orbit drifts [29, 30]; f (g) parameterises the luminosity dependence on Δx_i (Δy_i); h_x (h_y) is the integral of f (g), divided by its peak value; $p_{{\rm s},i}$ is the probability that the trigger is fired by a collision between one of the two colliding bunches and a satellite of the other bunch; $\tilde{p}_1$ ($\tilde{p}_2$) is the probability that the trigger is fired by a beam–gas collision of a bunch of beam 1 (beam 2), normalised by the bunch intensity; p_0 is the probability that the trigger is fired in absence of colliding beams. Note that the visible cross section $\sigma_{\rm vis}$ is one of the fit parameters.

The functions $f(\Delta x)$ and $g(\Delta y)$ were chosen to have a Gaussian core with mean value and standard deviation as the only free parameters, the normalisation being constrained by Eqs. 1 and 2. In order to describe the scan-shape tails, the Gaussian function is modified for absolute separations larger than some value, chosen on the basis of fit quality and convergence considerations. For these scan steps, a separation-dependent offset is added to Δx_i or Δy_i, so that there is one additional fit parameter for each scan step beyond the core-tail transition point. Depending on the considered colliding bunch pair and scan, the transition point is located 1.3–2.5 standard deviations away from the peak, and the total number of tail parameters varies between 7 and 13. The function is constrained to be symmetric around the peak by using the same tail parameter for scan steps at opposite nominal separation.

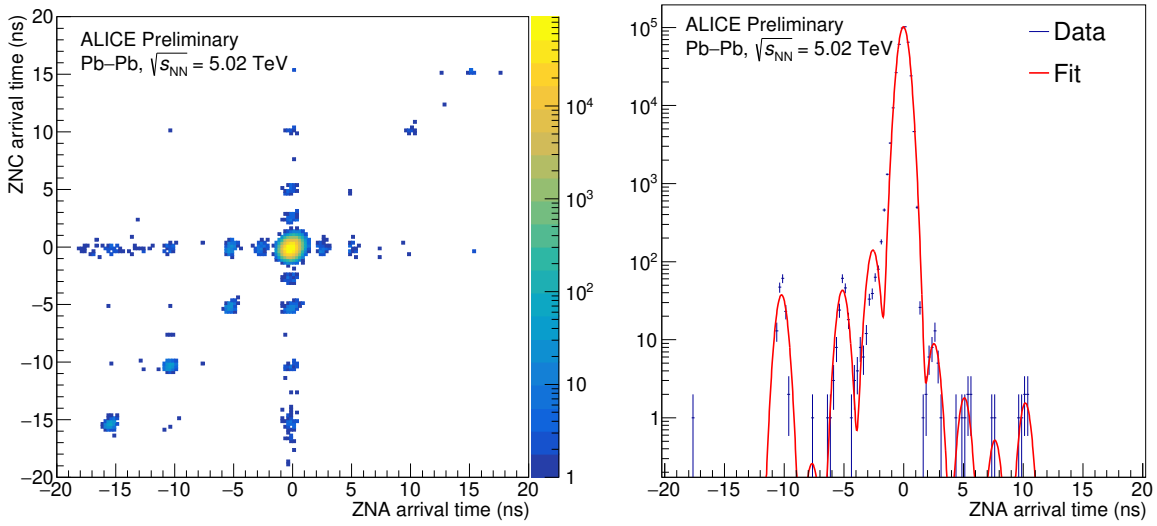

Fig. 1: (Colour online) Left: correlation between the arrival times of neutrons in ZNA and ZNC for events triggered by V0M. Right: arrival time on one of the two neutron calorimeters for ZED-triggered single-neutron events. The line shows a fit with a sum of Gaussian distributions. The nominal beam separation is zero for both figures.

The parameters p_0, $\tilde{p}_1$ and $\tilde{p}_2$ are estimated by means of an independent fit to the trigger rates in non-colliding and empty bunch slots. Owing to the minimum spacing of 100 ns between colliding bunches, the contribution to the trigger counts by after-pulses from a previous collision was found to be negligible for both signals. Hence, the empty bunch slots located immediately after colliding bunch slots, which are affected by background from after-pulses, were excluded from the fit. Because of the ZDC distance from the IP, the background induced on ZNA (ZNC) by beam–gas collisions of a bunch of beam 1(2) happening upstream of the calorimeter results in a signal that is earlier by 31 bunch slots ($\sim$ 750 ns) with respect to beam–beam collisions of the same bunch. For the filling scheme used in the vdM scan, this signal shows up in nominally empty bunch slots, which were excluded from the fit.

The separation-dependent contribution from main–satellite collisions $p_{{\rm s},i}$ is evaluated via the signal arrival time spectra in ZNA and ZNC. All events triggered by V0M have signals in both ZNA and ZNC. The two-dimensional distribution of arrival times in the two calorimeters for these events is shown in the left panel of Fig. 1. The satellite events are tagged by means of a square cut around the main–main peak position. The ZED trigger has a large contribution from events with single-neutron emission, so that most events have signal only in one calorimeter. For this sub-sample of ZED-triggered events, the estimation of the satellite contamination is based on the one-dimensional arrival time distributions in each of the ZNs, and the fraction of satellite collisions is obtained via a fit of the time distribution to a sum of Gaussian functions, with peak positions fixed to the values expected from the LHC radio-frequency structure (right panel of Fig. 1). Note that the signal from a single neutron emitted in a main–satellite collision has the same arrival time as that from a main–main collision if the neutron is emitted by an ion in the main bunch, while it is early or late if the neutron is emitted by an ion in the satellite bunch. Therefore, only half of the single neutrons from main–satellite collisions are identified as such, hence a correction factor of two is applied to the satellite-collision fractions obtained from the single-neutron event sample. Due to the dead time of the detector electronics, the timing information is only available for a fraction of the triggered events during the scan. Moreover, the size of the recorded sample does not allow for a bunch-by-bunch determination of satellite-collision fractions. In order to improve the statistical precision of the satellite estimation, the fit procedure is therefore extended with a joint likelihood maximisation, based on both timing and trigger data, at each separation step. Be S_i the number of events identified as main–satellite collisions in T_i acquired triggers, the joint binomial likelihood can be written

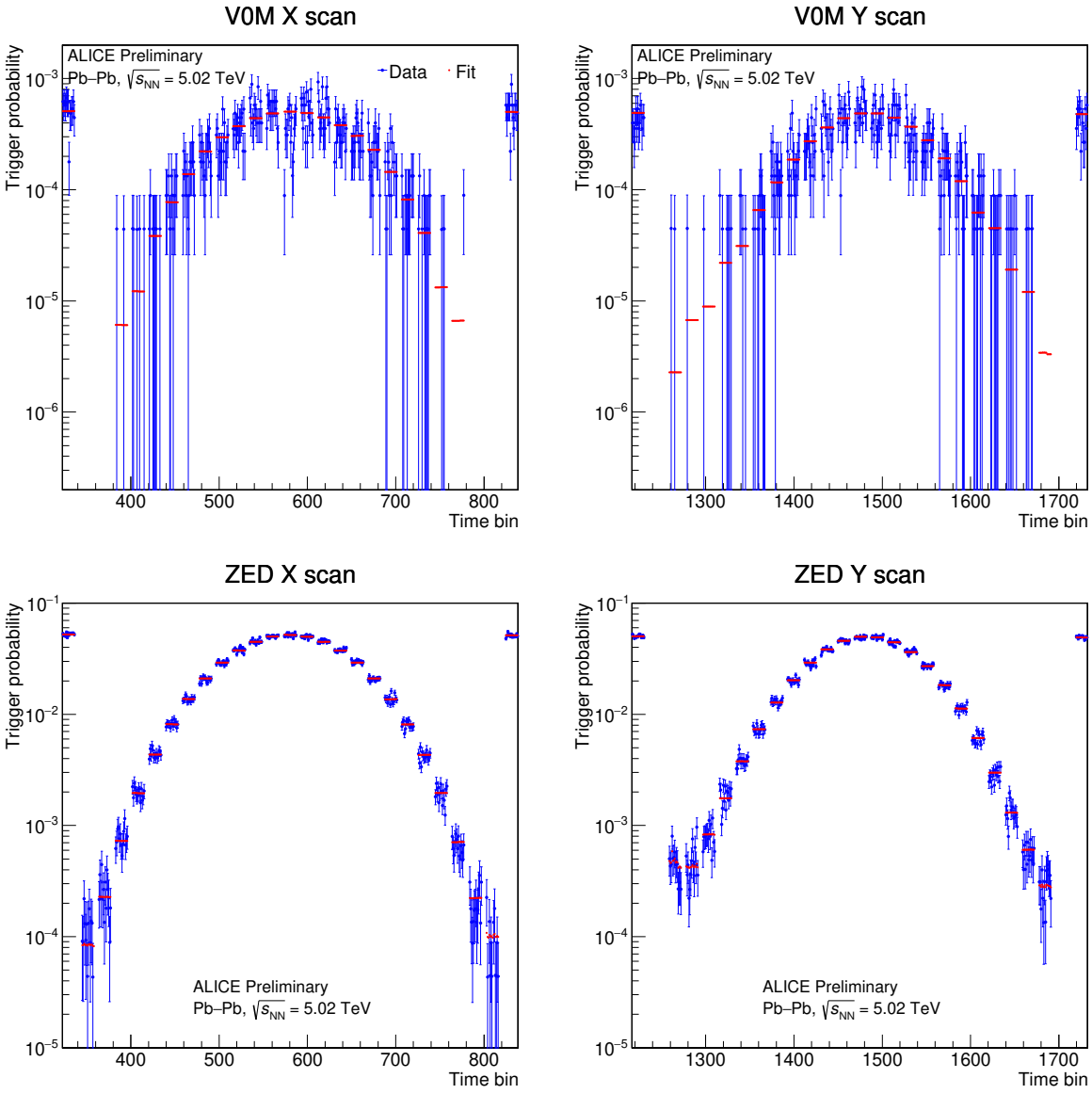

Fig. 2: (Colour online) V0M and ZED trigger probabilities per bunch crossing for a typical colliding bunch pair, as a function of time, during the first horizontal and vertical vdM scan. Each time bin corresponds to an acquisition window of $\sim$ 2 s. The uncertainties are statistical only. The fit expectation values are also shown. Time bins during which the beams are being displaced, not considered in the analysis, are not shown.

as

$$\ln \mathscr{L}_i = t_i \ln P_i + (n_i - t_i) \ln (1 - P_i) + S_i \ln \left(\frac{p_{\mathrm{s},i}}{P_i} \right) + (T_i - S_i) \ln \left(\frac{P_i - p_{\mathrm{s},i}}{P_i} \right). \quad (5)$$

The maximisation procedure determines the most probable value for $p_{\mathrm{s},i}$ for the measured values of n_i, t_i, T_i and S_i and the current expected P_i. The obtained $p_{\mathrm{s},i}$ is then fed into the global likelihood according to Eqs. 3 and 4.

In Fig. 2 the measured trigger probability per bunch crossing as a function of time during the vdM scan is shown for one pair of colliding bunches, together with the expectation from the fit. The quality of the fit is satisfactory, the values of χ^2/ndf being typically close to unity.

The V0M and ZED analyses provide independent estimates of the effective convolved beam widths h_x and h_y, via the fitted parameters of $f(\Delta x)$ and $g(\Delta y)$. The $h_x h_y$ products obtained in the V0M and in the

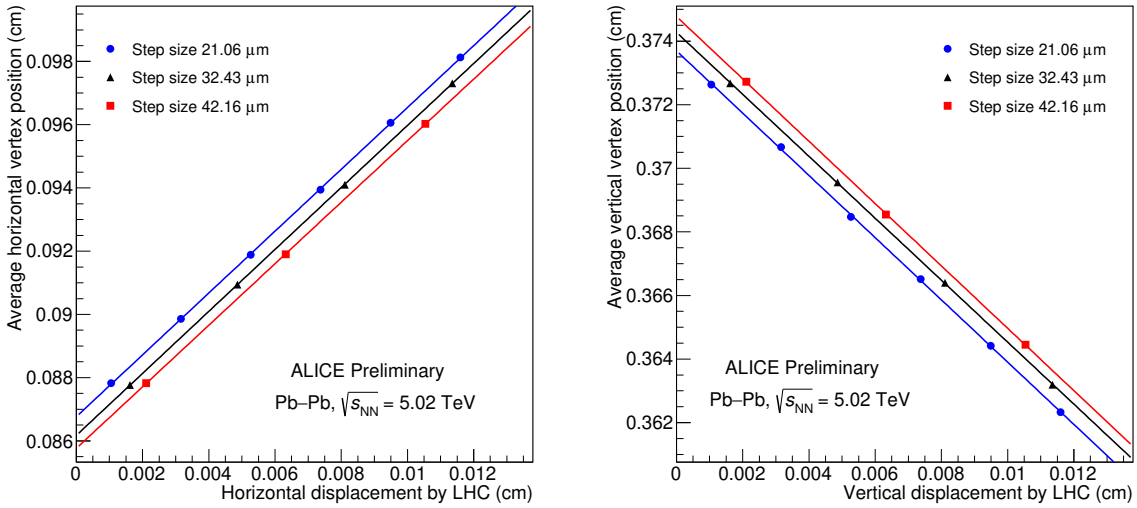

Fig. 3: (Colour online) Nominal versus measured displacements in the horizontal (left) and vertical (right) length-scale calibration scans. Data is represented by symbols, while a linear fit by the solid lines. The uncertainties are smaller than the symbol sizes. The blue (black, red) lines and solid circles (triangles, squares) correspond to a nominal displacement step size of 21.06 μm (32.43 μm, 42.16 μm).

ZED analysis are consistent within 0.13%, showing that detector-dependent effects are reasonably under control.

Three length-scale calibration scans were performed for each direction, with different displacement step size, in order to test a possible dependence on such a parameter. The horizontal (vertical) calibration factor is determined as the slope parameter of a linear fit to the measured horizontal (vertical) vertex displacement versus the nominal one, as illustrated in Fig. 3. The vertex position is determined using tracks reconstructed in the ITS. The resulting (multiplicative) correction factor to the fitted $\sigma_{\rm vis}$ is the product of the horizontal and vertical calibration factors, and was found to be 0.964 ± 0.010. The uncertainty is mostly systematic and accounts for deviations from the linear trend in the individual fits, for the dependence of the results on the displacement step size, and for the dependence of the results on the track and event selection criteria used in the vertex determination procedure.

The impact of non-factorisation effects is evaluated by simultaneously fitting the rates and the luminous-region parameters (positions, sizes, transverse tilt) during both the standard and the diagonal scans with a three-dimensional non-factorisable double-Gaussian model [6, 31], and computing the bias on the head-on luminosity with respect to a factorisable model. The resulting (multiplicative) correction factor to the fitted $\sigma_{\rm vis}$ is 1.011 ± 0.011, where an uncertainty as large as the correction is assigned to account for the non accurate description of some of the luminous-region parameters by the model.

The V0M and ZED cross sections measured for all colliding bunch pairs and scans are shown as a function of the product of bunch intensities N_1N_2 in Fig. 4. For both luminometers and scans, no significant dependence of $\sigma_{\rm vis}$ on N_1N_2 is observed. However, non-statistical fluctuations of the cross section are present in particular for ZED. In order to take these into account, a systematic uncertainty of $\sim 0.1\%$ (0.4%) for V0M (ZED) is assigned, computed as $\sqrt{\chi^2/ndf - 1}$ times the statistical uncertainty of the average cross section, where χ^2/ndf is obtained from the constant-value fits to the bunch-by-bunch cross sections shown in Fig. 4. The bunch-averaged cross sections measured in the two scans agree within 1%, which is considered as an additional systematic uncertainty. The measured visible cross sections, obtained by averaging the results from the two scans, are $\sigma_{\rm ZED}$ = 420.5 b $\pm$ 0.2 b (stat.) and

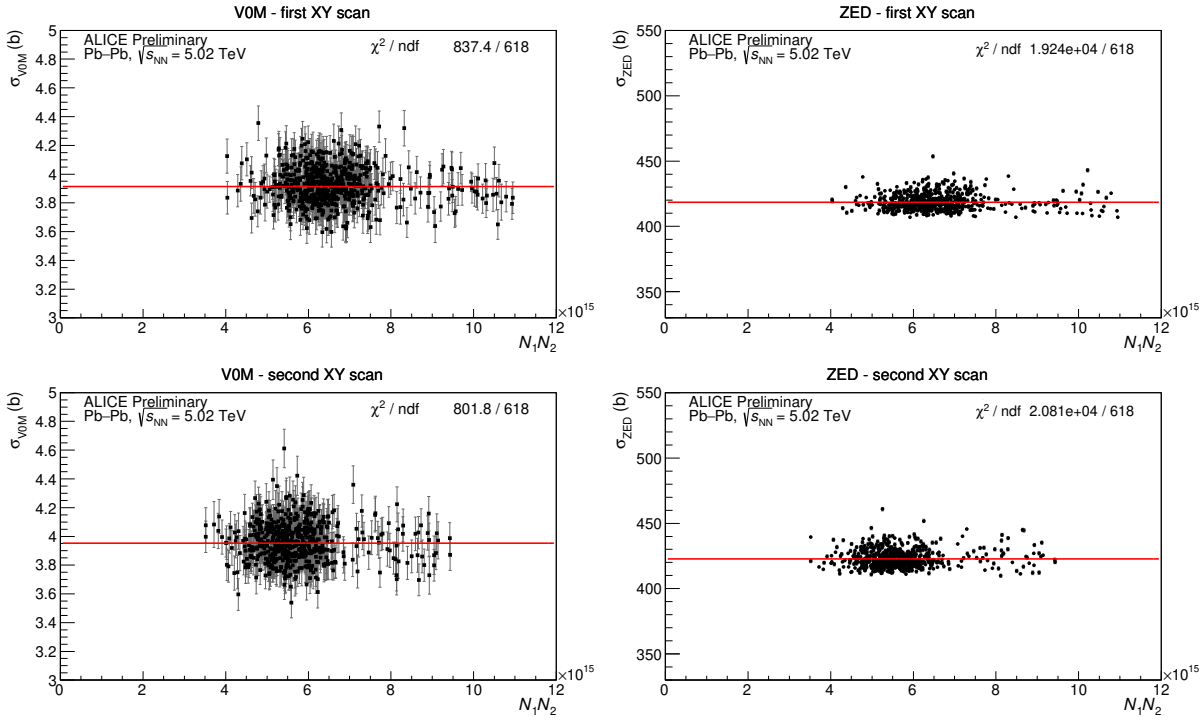

Fig. 4: (Colour online) V0M (left) and ZED (right) visible cross sections as a function of the product of the ion bunch intensities, for the first (top) and second vdM scan (bottom). Uncertainties are statistical only. The solid line represents a fit to a constant value.

$\sigma_{\mathrm{V0M}} = 3.933\ \mathrm{b} \pm 0.004\ \mathrm{b}$ (stat.).

The combined impact of the subtraction of background from beam–gas collisions, electronic noise, and satellite collisions on the final cross section is about 1% for V0M and 1.5% for ZED, largely dominated by satellite collisions. The systematic uncertainty on the background estimation from non-colliding and empty bunch slots is obtained by fitting the p_0, $\tilde{p}_1$ and $\tilde{p}_2$ parameters independently for each separation step, and computing the maximum difference with respect to the values obtained from a global fit to all separations. When the measured differences are propagated to the visible cross section, the resulting uncertainty is of the order of 0.1%. An additional systematic uncertainty arises from the fact that the subtraction of background from beam–satellite collisions is based on bunch-integrated timing data, neglecting differences in the bunch-by-bunch satellite fraction. In order to address this effect, the scan-step-averaged fraction of satellite collisions is evaluated for each colliding bunch pair, and found to fluctuate by about 40% (RMS). The satellite fractions S_i were therefore varied by this amount, resulting in a variation of the visible cross section by about 0.8% (0.5%) for ZED (V0M).

Possible non-linearities in the steering magnet behaviour during the scan, e.g. due to hysteresis, were considered as a source of systematic uncertainty. A preliminary hysteresis model[4] developed for the LHC was used to obtain an upper limit for the variations with respect to the nominal separation at each scan step; these variations, when propagated to the cross section, result in a 0.2% effect.

The uncertainty on the orbit drift correction was conservatively taken to be as large as the effect of the correction (0.15%). The uncertainty on the beam–beam deflection correction was evaluated by varying the input parameters to the deflection calculation within a reasonable range, as described in [6], and found to be less than 0.1%. The effect of distortions of the bunch shapes due to mutual interaction between the two beams was also evaluated, within the framework outlined in [28], and found to be less than 0.1%.

[4]M. Hofstettler and E. Todesco, 2020, presentations at the LHC Luminosity Calibration and Monitoring Working Group, November 16, and private communication, December 9.

The systematic uncertainty associated with the choice of the fitting strategy was evaluated by varying the range of beam separation described by the Gaussian core, by discarding the last scan step, where the satellite contribution is dominant, and by extracting the visible cross section from a simultaneous fit to all colliding bunch pairs instead of averaging the results from individual fits. The resulting uncertainty is 0.4%.

In order to test the stability and mutual consistency of the V0M and ZED calibration, the luminosities measured by the two devices throughout the 2015 and 2018 data-taking periods are compared. For each run[5] the trigger counts, integrated over colliding bunch slots, were corrected by subtracting the estimated beam–gas background, detector noise, and background from main–satellite collisions. The beam–gas background was estimated by means of the counts in non-colliding bunch slots, rescaled by the relative fractions of beam intensities. The contribution from detection noise was estimated via the counts in empty slots. The background from main–satellite collisions was estimated using the ZDC timing data. For each run, the ratio between the ZED- and V0M-based luminosities is computed from the corrected number of trigger counts $N_{\rm V0M}$ and $N_{\rm ZED}$ and from the total number of bunch crossings in the run $N_{\rm BC}$ as

$$\frac{L_{\rm ZED}}{L_{\rm V0M}} = \frac{\ln\left(1 - N_{\rm ZED}/N_{\rm BC}\right)\sigma_{\rm V0M}}{\ln\left(1 - N_{\rm V0M}/N_{\rm BC}\right)\sigma_{\rm ZED}}. \tag{6}$$

While the ZED trigger settings remained unchanged throughout the 2015 and 2018 data-taking periods, the threshold for the V0M trigger was different in 2015 and 2018. Furthermore, in 2018 it was slightly changed a few times during data-taking as the V0M-based centrality trigger was being tuned. For the data-taking periods with different threshold settings with respect to the vdM scan, the V0M trigger efficiency was measured relative to minimum bias collisions and the cross section rescaled by the ratio of the measured efficiency to that measured in the fill containing the van der Meer scans.

The luminosity ratio as a function of time and the distribution of the ratio over all runs, weighted with the run luminosity, is shown in Fig. 5. The mean quadratic difference of the ratio from unity is about 0.7% and is retained as a systematic uncertainty on the stability and mutual consistency of the luminosity calibration. When the analysis is restricted to the 2015 (2018) sample, the mean quadratic difference from unity amounts to 0.9% (0.5%).

In Table 1 a summary of the different contributions to the uncertainty on the visible cross section and the luminosity measurement is presented.

4 Conclusions

In 2015 and 2018, the ALICE Collaboration took data with Pb–Pb collisions at $\sqrt{s_{\rm NN}} = 5.02$ TeV. In order to provide a reference for the luminosity determination, vdM scans were performed and visible cross sections were measured for two processes, ZED and V0M, based on the ZDC and V0 detectors, respectively. The two detectors provide independent measurements of the luminosity, with a total uncertainty, for the full 2015+2018 sample, of 2.3% for the ZED and 2.2% for the V0M reference process. The quantitative contributions of the different sources of uncertainty considered for the visible cross section and the luminosity are shown in Table 1.

Acknowledgements

The ALICE Collaboration would like to thank all its engineers and technicians for their invaluable contributions to the construction of the experiment and the CERN accelerator teams for the outstanding

[5] In the ALICE nomenclature, a run is a set of data collected within a start and a stop of the data acquisition, under stable detector and trigger configurations. For the considered data-taking period, the duration of a run ranges from $\sim$ 5 minutes to $\sim$ 7 hours.

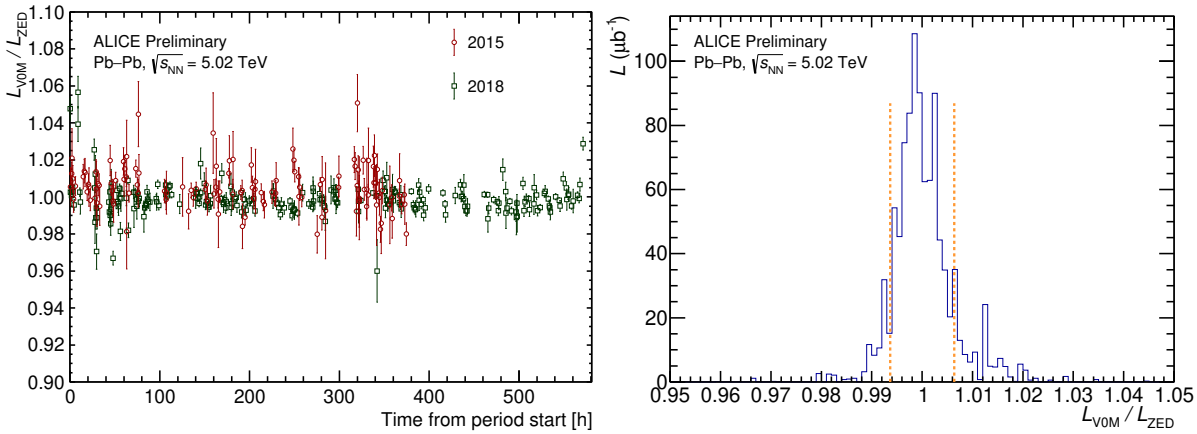

Fig. 5: (Colour online) Left: ratio of V0M and ZED luminosities calculated according to Eq. 6 as a function of time with respect to the beginning of the data-taking periods for 2015 (circles) and 2018 (squares). Right: distribution of the ratios for all runs (2015+2018); the dashed vertical lines are located at $L_{V0M}/L_{ZED} = 1 \pm \alpha$, where α is the mean quadratic difference from unity.

Source	Uncertainty (%) V0M | ZED
Statistical	0.09 | 0.04
Bunch intensity	0.8
$h_x h_y$ consistency (V0M vs ZED)	0.13
Length-scale calibration	1
Non-factorisation	1.1
Bunch-to-bunch consistency	0.1 | 0.4
Scan-to-scan consistency	1
Background subtraction	0.5 | 0.8
Magnetic non-linearities	0.2
Orbit drift	0.15
Beam–beam deflection and distortion	0.1
Fitting scheme	0.4
Total on visible cross section	2.1 | 2.2
Stability and consistency	0.7
Total on luminosity	2.2 | 2.3

Table 1: Relative uncertainties on the measurement of visible cross sections and luminosity in Pb–Pb collisions at $\sqrt{s_{NN}}$ = 5.02 TeV. The stability and consistency and the total luminosity uncertainties refer to the full Run 2 sample (2015+2018); uncertainties for the single periods are given in the text.

performance of the LHC complex. The ALICE Collaboration gratefully acknowledges the resources and support provided by all Grid centres and the Worldwide LHC Computing Grid (WLCG) collaboration. The ALICE Collaboration acknowledges the following funding agencies for their support in building and running the ALICE detector: A. I. Alikhanyan National Science Laboratory (Yerevan Physics Institute) Foundation (ANSL), State Committee of Science and World Federation of Scientists (WFS), Armenia; Austrian Academy of Sciences, Austrian Science Fund (FWF): [M 2467-N36] and Nationalstiftung für Forschung, Technologie und Entwicklung, Austria; Ministry of Communications and High Technologies, National Nuclear Research Center, Azerbaijan; Conselho Nacional de Desenvolvimento Científico e Tecnológico (CNPq), Financiadora de Estudos e Projetos (Finep), Fundação de Amparo à Pesquisa do Estado de São Paulo (FAPESP) and Universidade Federal do Rio Grande do Sul (UFRGS), Brazil; Ministry of Education of China (MOEC) , Ministry of Science & Technology of China (MSTC) and National Natural Science Foundation of China (NSFC), China; Ministry of Science and Education and Croatian Science Foundation, Croatia; Centro de Aplicaciones Tecnológicas y Desarrollo Nuclear (CEADEN), Cubaenergía, Cuba; Ministry of Education, Youth and Sports of the Czech Republic, Czech Republic; The Danish Council for Independent Research | Natural Sciences, the VILLUM FONDEN and Danish National Research Foundation (DNRF), Denmark; Helsinki Institute of Physics (HIP), Finland; Commissariat à l'Energie Atomique (CEA) and Institut National de Physique Nucléaire et de Physique des Particules (IN2P3) and Centre National de la Recherche Scientifique (CNRS), France; Bundesministerium für Bildung und Forschung (BMBF) and GSI Helmholtzzentrum für Schwerionenforschung GmbH, Germany; General Secretariat for Research and Technology, Ministry of Education, Research and Religions, Greece; National Research, Development and Innovation Office, Hungary; Department of Atomic Energy Government of India (DAE), Department of Science and Technology, Government of India (DST), University Grants Commission, Government of India (UGC) and Council of Scientific and Industrial Research (CSIR), India; Indonesian Institute of Science, Indonesia; Istituto Nazionale di Fisica Nucleare (INFN), Italy; Institute for Innovative Science and Technology , Nagasaki Institute of Applied Science (IIST), Japanese Ministry of Education, Culture, Sports, Science and Technology (MEXT) and Japan Society for the Promotion of Science (JSPS) KAKENHI, Japan; Consejo Nacional de Ciencia (CONACYT) y Tecnología, through Fondo de Cooperación Internacional en Ciencia y Tecnología (FONCICYT) and Dirección General de Asuntos del Personal Academico (DGAPA), Mexico; Nederlandse Organisatie voor Wetenschappelijk Onderzoek (NWO), Netherlands; The Research Council of Norway, Norway; Commission on Science and Technology for Sustainable Development in the South (COMSATS), Pakistan; Pontificia Universidad Católica del Perú, Peru; Ministry of Education and Science, National Science Centre and WUT ID-UB, Poland; Korea Institute of Science and Technology Information and National Research Foundation of Korea (NRF), Republic of Korea; Ministry of Education and Scientific Research, Institute of Atomic Physics and Ministry of Research and Innovation and Institute of Atomic Physics, Romania; Joint Institute for Nuclear Research (JINR), Ministry of Education and Science of the Russian Federation, National Research Centre Kurchatov Institute, Russian Science Foundation and Russian Foundation for Basic Research, Russia; Ministry of Education, Science, Research and Sport of the Slovak Republic, Slovakia; National Research Foundation of South Africa, South Africa; Swedish Research Council (VR) and Knut & Alice Wallenberg Foundation (KAW), Sweden; European Organization for Nuclear Research, Switzerland; Suranaree University of Technology (SUT), National Science and Technology Development Agency (NSDTA) and Office of the Higher Education Commission under NRU project of Thailand, Thailand; Turkish Atomic Energy Agency (TAEK), Turkey; National Academy of Sciences of Ukraine, Ukraine; Science and Technology Facilities Council (STFC), United Kingdom; National Science Foundation of the United States of America (NSF) and United States Department of Energy, Office of Nuclear Physics (DOE NP), United States of America.

References

[1] **ALICE** Collaboration, K. Aamodt *et al.*, "The ALICE experiment at the CERN LHC", *JINST* **3**

(2008) S08002.

[2] S. van der Meer, "Calibration of the effective beam height in the ISR", Tech. Rep. CERN-ISR-PO-68-31, CERN, 1968. http://cds.cern.ch/record/296752.

[3] V. Balagura, "Notes on van der Meer Scan for Absolute Luminosity Measurement", *Nucl. Instrum. Meth.* **A654** (2011) 634–638, arXiv:1103.1129 [physics.ins-det].

[4] P. Grafström and W. Kozanecki, "Luminosity determination at proton colliders", *Prog. Part. Nucl. Phys.* **81** (2015) 97–148.

[5] **ALICE** Collaboration, B. Abelev *et al.*, "Measurement of visible cross sections in proton-lead collisions at $\sqrt{s_{\rm NN}}$ = 5.02 TeV in van der Meer scans with the ALICE detector", *JINST* **9** no. 11, (2014) P11003, arXiv:1405.1849 [nucl-ex].

[6] **ALICE** Collaboration, J. Adam *et al.*, "ALICE luminosity determination for pp collisions at $\sqrt{s} = 13$ TeV", Tech. Rep. ALICE-PUBLIC-2016-002, CERN, 2016. https://cds.cern.ch/record/2160174/.

[7] **ALICE** Collaboration, S. Acharya *et al.*, "ALICE luminosity determination for pp collisions at $\sqrt{s} = 8$ TeV", Tech. Rep. ALICE-PUBLIC-2017-002, CERN, 2017. https://cds.cern.ch/record/2255216/.

[8] **ALICE** Collaboration, J. Adam *et al.*, "ALICE luminosity determination for pp collisions at $\sqrt{s} = 5$ TeV", Tech. Rep. ALICE-PUBLIC-2016-005, CERN, 2016. https://cds.cern.ch/record/2202638/.

[9] **ALICE** Collaboration, S. Acharya *et al.*, "ALICE 2017 luminosity determination for pp collisions at $\sqrt{s}$ = 5 TeV", Tech. Rep. ALICE-PUBLIC-2018-014, CERN, 2018. https://cds.cern.ch/record/2648933/.

[10] **ALICE** Collaboration, S. Acharya *et al.*, "ALICE luminosity determination for p-Pb collisions at $\sqrt{s_{\rm NN}}$ = 8.16 TeV", Tech. Rep. ALICE-PUBLIC-2018-002, CERN, 2018. https://cds.cern.ch/record/2314660/.

[11] **LHCb** Collaboration, R. Aaij *et al.*, "Precision luminosity measurements at LHCb", *JINST* **9** no. 12, (2014) P12005, arXiv:1410.0149 [hep-ex].

[12] **ATLAS** Collaboration, G. Aad *et al.*, "Improved luminosity determination in pp collisions at $\sqrt{s}$ = 7 TeV using the ATLAS detector at the LHC", *Eur. Phys. J.* **C73** no. 8, (2013) 2518, arXiv:1302.4393 [hep-ex].

[13] **ATLAS** Collaboration, M. Aaboud *et al.*, "Luminosity determination in pp collisions at $\sqrt{s}$ = 8 TeV using the ATLAS detector at the LHC", *Eur. Phys. J.* **C76** no. 12, (2016) 653, arXiv:1608.03953 [hep-ex].

[14] **CMS** Collaboration, "CMS Luminosity Based on Pixel Cluster Counting - Summer 2013 Update", Tech. Rep. CMS-PAS-LUM-13-001, CERN, 2013. https://cds.cern.ch/record/1598864.

[15] **ALICE** Collaboration, B. Abelev *et al.*, "Performance of the ALICE Experiment at the CERN LHC", *Int. J. Mod. Phys.* **A29** (2014) 1430044, arXiv:1402.4476 [nucl-ex].

[16] **ALICE** Collaboration, E. Abbas *et al.*, "Performance of the ALICE VZERO system", *JINST* **8** (2013) P10016, arXiv:1306.3130 [nucl-ex].

[17] A. J. Baltz, M. J. Rhoades-Brown, and J. Weneser, "Heavy-ion partial beam lifetimes due to Coulomb induced processes", *Physica Review E* **54** (1996) 4233.

[18] **ALICE** Collaboration, B. Abelev *et al.*, "Measurement of the Cross Section for Electromagnetic Dissociation with Neutron Emission in Pb-Pb Collisions at $\sqrt{s_{\mathrm{NN}}}$ = 2.76 TeV", *Phys. Rev. Lett.* **109** (2012) 252302, arXiv:1203.2436 [nucl-ex].

[19] I. A. Pshenichnov, J. P. Bondorf, I. N. Mishustin, A. Ventura, and S. Masetti, "Mutual heavy ion dissociation in peripheral collisions at ultrarelativistic energies", *Physical Review C* **64** no. 2, (Aug, 2001) 249031–2490319, 0101035. http://link.aps.org/doi/10.1103/PhysRevC.64.024903.

[20] I. Pshenichnov, "Electromagnetic excitation and fragmentation of ultrarelativistic nuclei", *Phys. Part. Nucl.* **42** no. 2, (Mar, 2011) 215–250. http://link.springer.com/10.1134/S1063779611020067.

[21] M. Broz, J. G. Contreras, and J. D. Tapia Takaki, "A generator of forward neutrons for ultra-peripheral collisions: $\mathbf{n}^{\mathbf{O}}_{\mathbf{O}}\mathbf{n}$", *Comput. Phys. Commun.* **253** (2020) 107181, arXiv:1908.08263 [nucl-th].

[22] **ALICE** Collaboration, K. Aamodt *et al.*, "Alignment of the ALICE Inner Tracking System with cosmic-ray tracks", *JINST* **5** (2010) P03003, arXiv:1001.0502 [physics.ins-det].

[23] J. J. Gras, D. Belohrad, M. Ludwig, P. Odier, and C. Barschel, "Optimization of the LHC beam current transformers for accurate luminosity determination", Tech. Rep. CERN-ATS-2011-063, CERN, 2011. http://cds.cern.ch/record/1379466.

[24] C. Ohm and T. Pauly, "The ATLAS beam pick-up based timing system", *Nucl. Instrum. Meth.* **A623** (2010) 558–560, arXiv:0905.3648 [physics.ins-det].

[25] A. Alici *et al.*, "Study of the LHC ghost charge and satellite bunches for luminosity calibration.", Tech. Rep. CERN-ATS-Note-2012-029 PERF, CERN, 2012. https://cds.cern.ch/record/1427728.

[26] A. Boccardi, E. Bravin, M. Ferro-Luzzi, S. Mazzoni, and M. Palm, "LHC Luminosity calibration using the Longitudinal Density Monitor", Tech. Rep. CERN-ATS-Note-2013-034 TECH, CERN, 2013. https://cds.cern.ch/record/1556087.

[27] W. Kozanecki, T. Pieloni, and J. Wenninger, "Observation of Beam-beam Deflections with LHC Orbit Data", Tech. Rep. CERN-ACC-NOTE-2013-0006, CERN, 2013. https://cds.cern.ch/record/1581723.

[28] V. Balagura, "Van der Meer Scan Luminosity Measurement and Beam-Beam Correction", arXiv:2012.07752 [hep-ex].

[29] D. Bishop, C. Boccard, E. Calvo-Giraldo, D. Cocq, L. Jensen, R. Jones, J. J. Savioz, and G. Waters, "The LHC Orbit and Trajectory System", Tech. Rep. CERN-AB-2003-057-BDI, 2003. https://cds.cern.ch/record/624190.

[30] J. Wenninger, "Dispersion Free Steering for YASP and dispersion correction for TI8", Tech. Rep. LHC-Performance-Note-005, CERN, 2009. http://cds.cern.ch/record/1156142.

[31] S. N. Webb, *Factorisation of beams in van der Meer scans and measurements of the ϕ^*_η distribution of $Z \to e^+e^-$ events in pp collisions at $\sqrt{s} = 8$ TeV with the ATLAS detector*. PhD thesis, Manchester U., 2015-06-01. https://inspirehep.net/record/1381312/files/CERN-THESIS-2015-054.pdf.